This page intentionally left blank


USGS

Seismicity of the Eruption

Seismicity has long been the key monitoring tool for recognizing precursors to volcanic eruptions. The unrest at Mount St. Helens in 2004 was no different, beginning on September 23 as a seismic swarm that ultimately produced tens of thousands of earthquakes in the days before lava reached the surface on October 11. The sheer number of earthquakes forced adoption of new methods of processing and analyzing the data, as well as new techniques to ensure the rapid dissemination of seismic information over the Internet.

In this eruption, small earthquakes struck a cadence so regular that they became known as drumbeats—a phenomenon that persisted longer at Mount St. Helens than previously described elsewhere. Models to explain drumbeat earthquakes typically invoke stick-slip as the source mechanism. At Mount St. Helens, changes in drumbeat character were unrelated to variations in magma flux at the conduit; thus, drumbeat size and spacing are more likely a function of extrusion mechanics than of extrusion rate.

Also known from other eruptions and seen at Mount St. Helens were multiplets—families of earthquakes—so similar in their waveform that they must have originated from the same source in the shallow crust and traveled along similar paths to the seismometers. Their persistence indicated stationary sources that were stable over long periods of time.

Explosion detection capability was enhanced by the use of microphones to record infrasound. The infrasound signals were subtle, so multiple microphones were required at several sites within 1–2 km of the vent. The six explosions during this eruption lacked seismic precursors, although seismicity dropped after each in response to depressurization of the conduit. Seismic-amplitude values peaked an hour or two before at least one of the explosions, but such instances were too sporadic to serve as a predictive tool.

View west across 1980s dome and deformed glacial ice to explosion of October 1, 2004, the first eruptive event of renewed activity at Mount St. Helens. USGS photo by J.S. Pallister.

A Volcano Rekindled: The Renewed Eruption of Mount St. Helens, 2004–2006
Edited by David R. Sherrod, William E. Scott, and Peter H. Stauffer
U.S. Geological Survey Professional Paper 1750, 2008

Chapter 2

Seismicity Associated with Renewed Dome Building at Mount St. Helens, 2004–2005

By Seth C. Moran[1], Stephen D. Malone[2], Anthony I. Qamar[2*], Weston A. Thelen[2], Amy K. Wright[2], and Jacqueline Caplan-Auerbach[3]

Abstract

The reawakening of Mount St. Helens after 17 years and 11 months of slumber was heralded by a swarm of shallow (depth <2 km) volcano-tectonic earthquakes on September 23, 2004. After an initial decline on September 25, seismicity rapidly intensified; by September 29, M_d >2 earthquakes were occurring at a rate of ~1 per minute. A gradual transition from volcano-tectonic to hybrid and low-frequency events occurred along with this intensification, a characteristic of many precursory swarms at Mount St. Helens before dome-building eruptions in the 1980s. The first explosion occurred October 1, 2004, 8.5 days after the first earthquakes, and was followed by three other explosions over the next four days. Seismicity declined after each explosion and after two energetic nonerruptive tremor episodes on October 2 and 3. Following the last explosion of this series, on October 5, seismicity declined significantly. Over the next ten days seismicity was dominated by several event families; by October 16, spacing between events had become so regular that we dubbed the earthquakes "drumbeats." Through the end of 2005 seismicity was dominated by these drumbeats, although occasional larger earthquakes (M_d 2.0–3.4) dominated seismic energy release. Over time there were significant variations in drumbeat size, spacing, and spectra that correlated with changes in the style of extrusion at the surface. Changes in drumbeat character did not correspond to variations in magma flux at the conduit, indicating that drumbeat size and spacing may be more a function of the mechanics of extrusion than of the extrusion rate.

[1] U.S. Geological Survey, 1300 SE Cardinal Court, Vancouver, WA 98683

[2] Pacific Northwest Seismic Network, Department of Earth and Space Sciences, University of Washington, Box 351310, Seattle, WA 98195

[3] Geology Department, Western Washington University, 516 High Street, Bellingham, WA 98225

* Deceased

Introduction

As of the writing of this paper (2006), more than 26 years of recorded seismic history have accumulated at Mount St. Helens since the Pacific Northwest Seismic Network's (PNSN) digital recording system began operation in March 1980. This 26-year period includes the precursory buildup to the May 18, 1980, eruption (Endo and others, 1981; Malone and others, 1981), post-May 18, 1980, seismicity associated with the 20 eruptions occurring between 1980 and 1986 (Malone, 1983; Malone and others, 1983; Swanson and others, 1985; Swanson and Holcomb, 1990), quiescence between 1987 and 2004 (Moran, 1994; Musumeci and others, 2002), and the onset of the eruption in 2004. This history is made all the richer by its being recorded on a relatively dense seismic network of short-period vertical-component seismometers in place since shortly after the first earthquakes began in late March of 1980 (fig. 1). Seismic data recorded by this network have been used in many studies, including (1) forecasting eruptions and detecting explosions (Endo and others, 1981; Malone and others, 1981; Malone and others, 1983; Swanson and others, 1983; Endo and others, 1990; Jonientz-Trisler and others, 1994); (2) eruption dynamics (Qamar and others, 1983; Weaver and others, 1983; Shemeta and Weaver, 1986); (3) modeling the Mount St. Helens magmatic system (Weaver and others, 1981; Scandone and Malone, 1985; Endo and others, 1990; Barker and Malone, 1991; Moran, 1994; Musumeci and others, 2002); (4) interpreting the structure of the magmatic system through tomography (Lees and Crosson, 1989; Lees, 1992; Moran and others, 1999), earthquake locations (Fehler, 1985; Weaver and others, 1987; Musumeci and others, 2002), and *b* values (Endo and others, 1981; Wiemer and McNutt, 1997); (5) determining the source process responsible for various type of seismic signals recorded at Mount St. Helens (Fehler and Chouet, 1982; Malone, 1983; Fehler, 1985; Norris, 1994); (6) describing the stress field associated with the magmatic system (Barker and Malone, 1991; Moran, 1994;

Giampiccolo and others, 1999; Musumeci and others, 2002); and (7) defining repetitive events (or earthquake families), including the first published study of repetitive events in a volcanic setting (Frémont and Malone, 1987).

As a result of these and other studies, by 2004 we had a fairly good working model of the magmatic system beneath Mount St. Helens. We also had a very good understanding of the character of typical eruptive and noneruptive seismicity. These perspectives proved vital to our ability to correctly assess the significance of seismicity when Mount St. Helens reawakened in 2004.

The reawakening of Mount St. Helens was heralded by a swarm of shallow (depth <2 km) volcano-tectonic (VT) earthquakes beginning at roughly 0200 Pacific daylight time (PDT) on September 23, 2004. More than one million earthquakes were recorded by the end of 2005, with events occurring every 1 to 5 minutes. Of these, roughly 8,000 events were located by the PNSN through the end of 2005. Many will likely never be located, even with sophisticated crosscorrelation and relative relocation techniques (for example, Thelen and others, this volume, chap. 4), because many are small, occur in the coda of previous events, and (or) have nonimpulsive arrivals. With such a sizable dataset we are still very much in discovery mode, and it is likely that at least some of what we present in this paper will be superseded by subsequent research. Our principal purpose is to give an overview of our understanding of seismicity that occurred before and during the eruption in 2004–5, as well as to put the eruption's seismicity in the broader context of the 26 years of seismic history of Mount St. Helens.

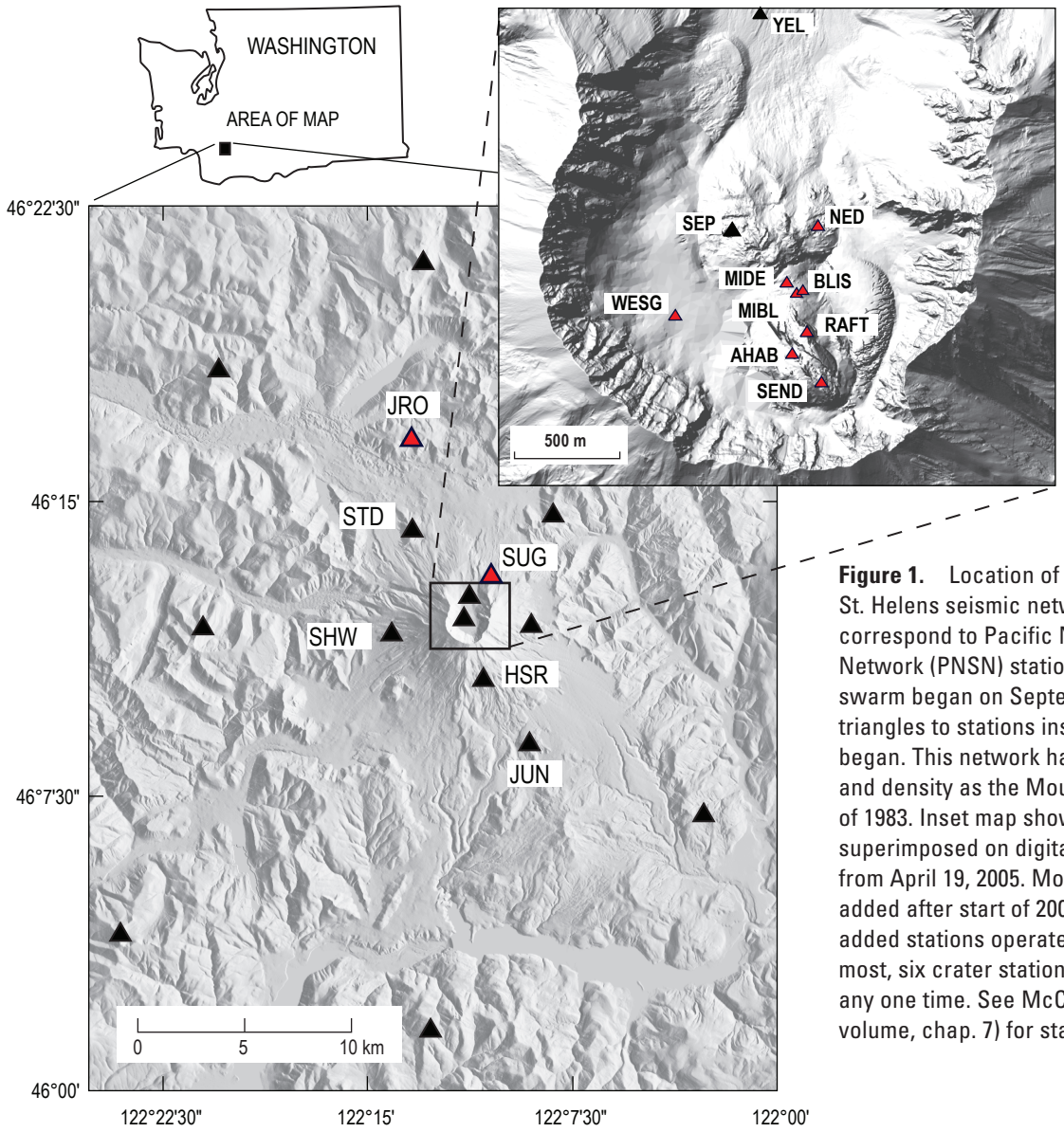

Figure 1. Location of stations in Mount St. Helens seismic network. Black triangles correspond to Pacific Northwest Seismic Network (PNSN) stations in place when swarm began on September 23, 2004, and red triangles to stations installed after eruption began. This network had similar geometry and density as the Mount St. Helens network of 1983. Inset map shows crater stations superimposed on digital elevation model from April 19, 2005. Most crater stations were added after start of 2004 eruption. Many newly added stations operated for short periods; at most, six crater stations were operational at any one time. See McChesney and others (this volume, chap. 7) for station installation details.

Seismicity During Quiescence, 1987–2004

Although short-term precursory seismicity began on September 23, 2004, in a longer term view the first precursory seismicity likely started as early as late 1987 (fig. 2), when the first of several years-long swarms of "deep" (>3 km) VT events began (Moran, 1994). The depth of these swarms contrasted sharply with the exclusively shallow (<3 km) precursory swarms associated with 19 of the 20 post-May 18, 1980, dome-building eruptions (Malone and others, 1983). In map view, the deeper events were concentrated to the north and south of the 1980–86 lava dome (Moran, 1994; Musumeci and others, 2002), in contrast to the east-west orientation of "deep" VT events that extended to 20 km immediately after the May 18, 1980, eruption (Weaver and others, 1981; Shemeta and Weaver, 1986; Barker and Malone, 1991; Moran, 1994). Fault-plane solutions for the post-May 18, 1980, "deep" events had tangentially oriented P axes with respect to the 1980 crater, in contrast to radially oriented P axes for post-1987 "deep" events (Barker and Malone, 1991; Moran, 1994; Musumeci and others, 2002). The changes in stress-field orientation and epicentral distribution are best explained by a pressure decrease in the magmatic plumbing system after 1980 and a pressure increase after 1986 (Barker and Malone, 1991; Moran, 1994; Musumeci and others, 2002). Moran (1994) argued that sizable swarms preceding the last two dome-building eruptions in 1986 were an indication of the formation of a plug in the conduit to the surface, a plug that subsequent batches of magma were unable to penetrate. The occurrence of six phreatic explosions in 1989–91 (Mastin, 1994) and detection of magmatic CO_2 in association with the last significant months-long swarm of deeper seismicity in 1998 (Gerlach and others, this volume, chap. 26) provide further evidence that intrusion of magma may have occurred between 1987 and 2004.

Most seismicity after 1998 was concentrated at depths ~2 km below the crater floor, although occasional deeper and shallower VT events also occurred (fig. 2). The 2-km-deep seismicity band could represent the development of a fracture system in the base of the plug inferred by Pallister and others (1992) and Moran (1994) to extend from the surface down to 2 km. The *b* values for earthquakes in this depth range increased marginally from 0.8–1.0 before 1992 to 1.0–1.4 after 1992 (fig. 3). The *b* values for events between 3 and 10 km showed no such change over the same time period, indicating that the shallow *b*-value change is not a result of a systematic bias in the PNSN catalog. The *b*-value increase, if real, could indicate an increase in the number of small fractures (Mogi, 1962) between 1991 and 1993 and is the type of change that would be expected in association with the

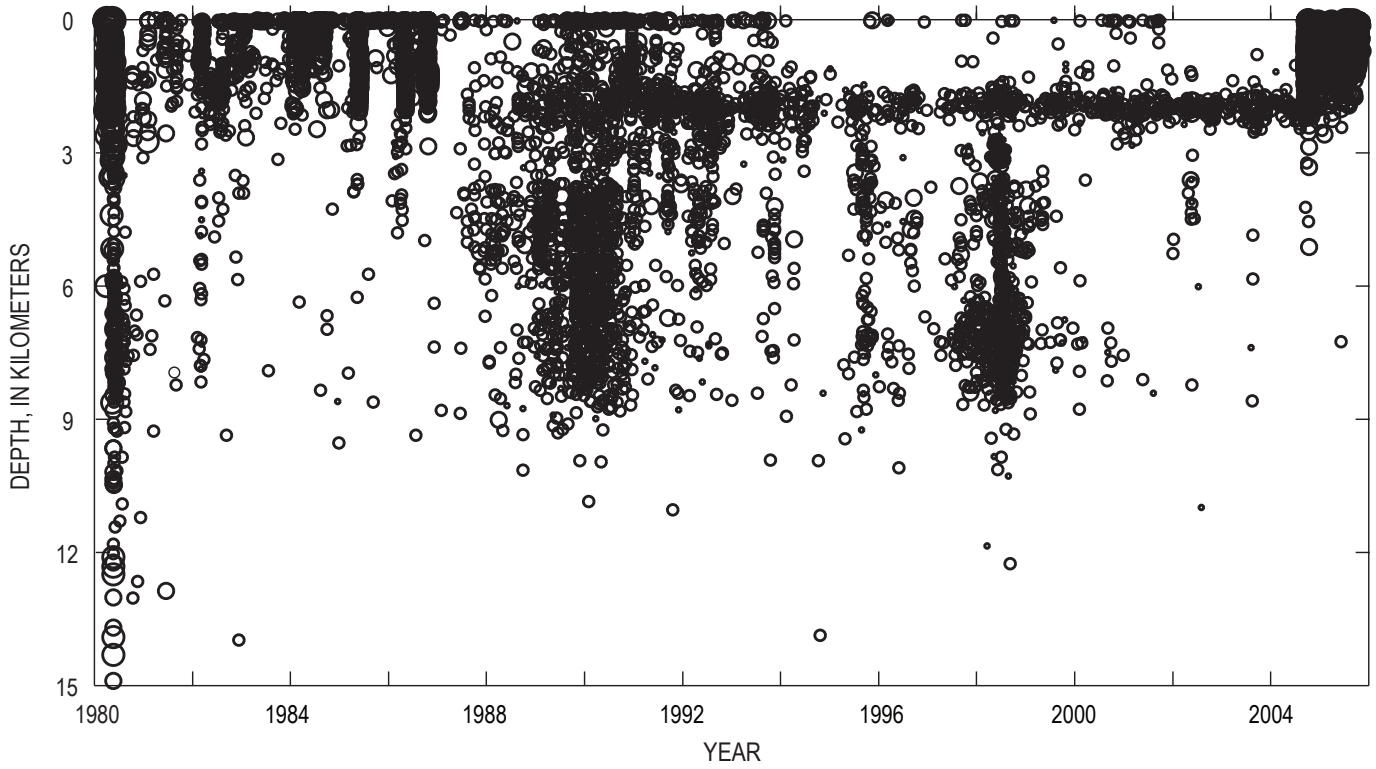

Figure 2. Time versus depth plot showing all earthquakes (circles) with well-constrained locations (gap <135°, nearest station <2 km, and arrival times on at least seven stations) occurring at Mount St. Helens between 1980 and 2005. Depths are relative to a datum corresponding to average altitude of stations in Mount St. Helens network, roughly 1.1 km above sea level. Horizontal-axis tick marks indicate start of a year, with gaps of 2 years between tick marks.

fracturing of the base of a plug (Vinciguerra and others, 2001). However, *b* values remained relatively constant in the subsequent 12 years leading up to the 2004 eruption (fig. 3), despite the evidence for a possible intrusion of magma in 1998.

The last significant earthquake swarm of the 1987–2004 quiescent period occurred on November 2–4, 2001. The swarm began relatively abruptly at around 1730 Pacific standard time (PST) on November 2 and consisted of many small (most with coda-duration magnitudes M_d <0.0, with the largest M_d 1.8) and shallow (<2 km) VT events occurring at a rate of 2–3 per minute. There were also a number of 10–30-minute-long spasmodic bursts of 8–10 VT events per minute. The Cascades Volcano Observatory (CVO) issued an Information Statement at 1800 PST on November 3, 2001, stating that a swarm was underway with no evidence that an eruption was imminent. Following the last spasmodic burst of VTs at 0400 PST on November 4, the number and size of earthquakes declined steadily, reaching background levels by November 5, 2001.

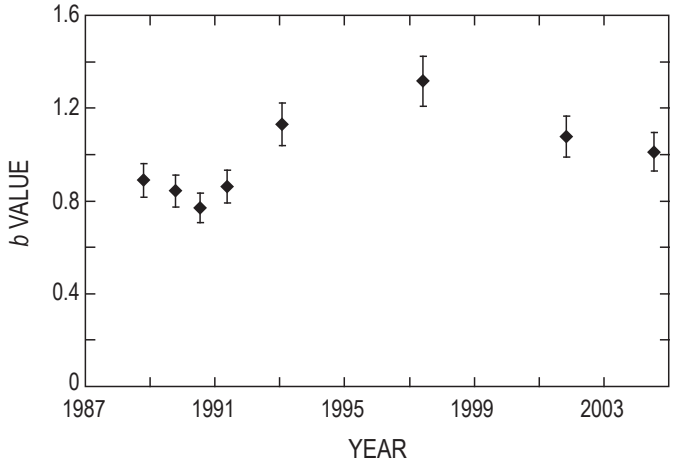

Figure 3. Plot of *b* values for shallow (depths <3 km) earthquakes occurring between 1987 and 09/23/2004, the last day for which the PNSN catalog is complete. Horizontal-axis tick marks indicate start of a year, with gaps of 2 years between tick marks. The *b* values are computed using maximum-likelihood method (Bender, 1983) and are determined for nonoverlapping groups of 150 events with M_d 0.4 (magnitude of completeness for entire interval) selected with same criteria used for earthquakes shown in figure 2.

September 23–October 5, 2004: Vent-Clearing Phase

September 23–September 25, 2004

The first short-term signs of unrest came in the form of a swarm of VT events starting at roughly 0200 PDT on September 23, 2004 (fig. 4), with the onset of unrest defined as the time when hourly event counts reached sustained levels above 1–2 events per hour. The number of earthquakes increased throughout September 23, peaked midday on September 24, and then declined to a minimum early on September 25, roughly 48 hours after the swarm began. By September 24, earthquakes had become so numerous that the PNSN began locating only a subset of them, and real-time seismic amplitude measurement (or RSAM; Endo and Murray, 1991), "webicorder," and spectrogram plots became the principal tools for tracking seismicity (Qamar and others, this volume, chap. 3). All located events were shallow (<2 km) and small, with the largest a M_d 2.2 and most having magnitudes <1.0. The *b* values for catalog locations were ~1, consistent with *b* values before 2004 (fig. 3). Fault-plane solutions from the PNSN catalog show a variety of failure mechanisms and stress-field orientations, with no clear dominant fracture pattern (appendix 1). To this point, seismicity closely resembled the swarm of November 2–4, 2001. This similarity governed initial interpretations by the PNSN and CVO. Although somewhat more energetic than the 2001 swarm, we judged that this swarm was within the bounds of noneruptive seismicity seen during the previous 18 years at Mount St. Helens. An information statement was released on September 24, stating that a seismic swarm was occurring at Mount St. Helens, with no indications that an eruption was imminent (Dzurisin and others, 2005; Scott and others, this volume, chap. 1).

September 25–October 1, 2004

Seismicity departed from the 2001 script midday on September 25, 2004. Instead of continuing to decline, the earthquake rate stabilized and then began to increase (fig. 5). Lower-frequency events, including hybrid and low-frequency (LF) events (previously identified as type "m" and "l" events at Mount St. Helens in the 1980s by Malone, 1983, and Malone and others, 1983) also began occurring alongside the VT events (fig. 6). We elected to refer to these as low-frequency, or "LF," events rather than the commonly used long-period, or "LP," event label, because the definition of an LP event includes a specific source mechanism (that is, the vibration of fluid- or gas-filled cracks; Lahr and others, 1994; Chouet, 1996). Experience with low-frequency events at Mount St. Helens in the 1980s indicated that other source mechanisms might be involved, and so we felt it best to use the purely descriptive "LF event" terminology without presuming a source mechanism. It should be noted that LF events commonly have extended codas at Mount St. Helens, resulting in overly large coda-duration magnitudes relative to amplitude-based magnitudes (Qamar and others, this volume, chap. 3).

The transition from VT to hybrid and LF events took place over several days, as illustrated by the earthquake spectral amplitude (or "ESAM") plot in figure 5 (see appendix 2 for details), with LF events becoming progressively more dominant through October 5. Similar transitions in earthquake types were seen in precursory swarms preceding many dome-building eruptions at Mount St. Helens in the 1980s (Malone,

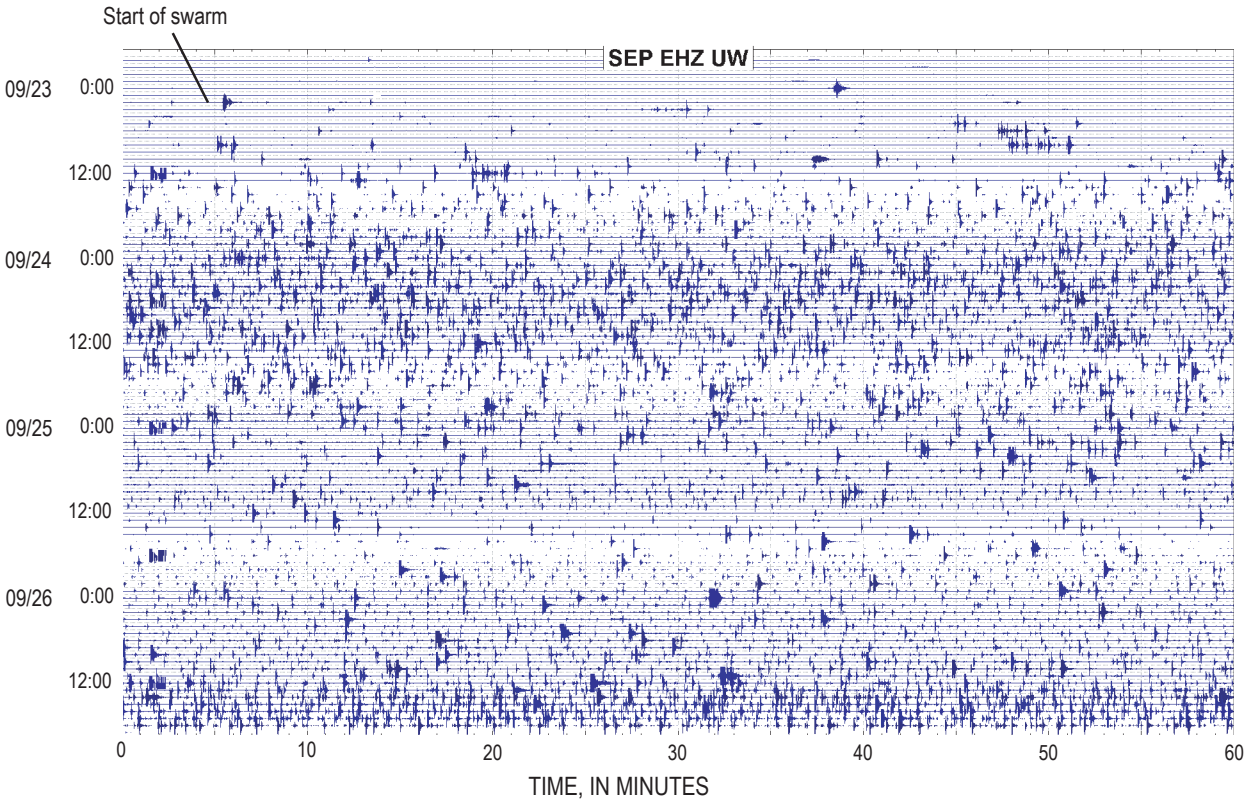

Figure 4. Seismic record from station SEP (~500 m north of the vent; see fig. 1) from 1900 PDT September 22 through 1900 PDT September 26, 2004, showing start of seismic swarm at 0200 PDT September 23 and buildup over next three days.

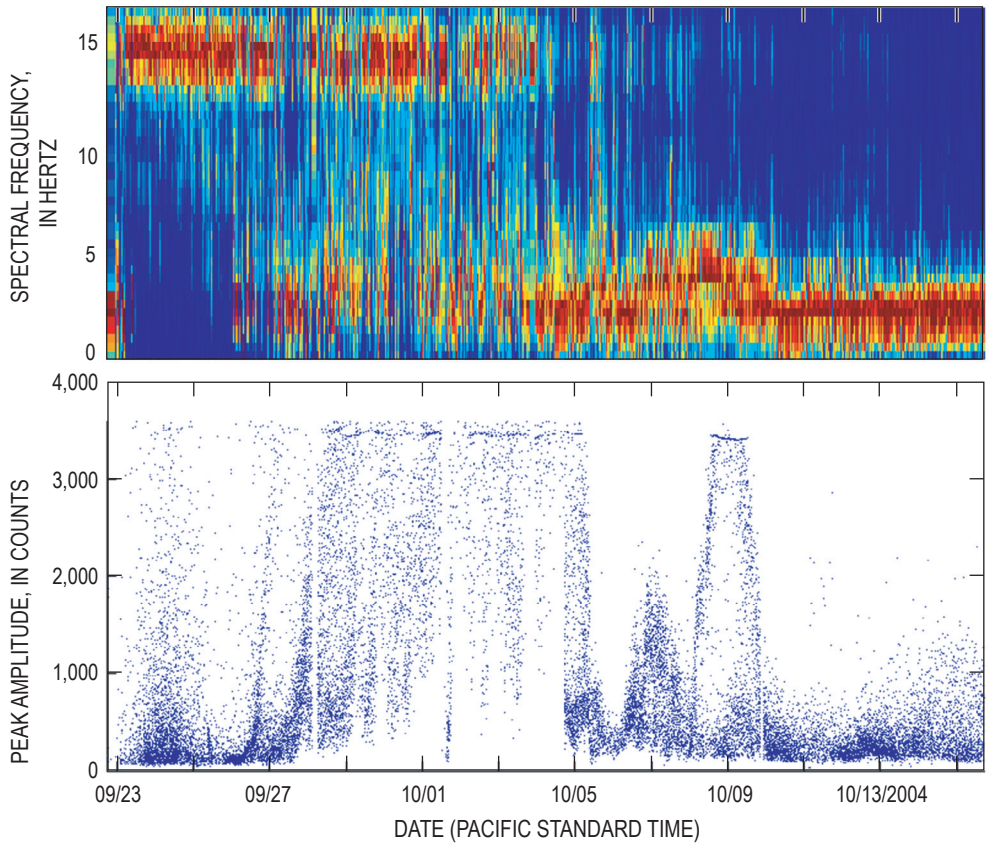

Figure 5. Plot of earthquake spectral amplitudes, or ESAM (top), and peak amplitudes (bottom) for detected events at station HSR (fig. 1) between September 23 and October 15, 2004 (see appendix 2 for event detection details). Horizontal-axis tick marks indicate start of a day, with gaps of 2 days between tick marks. Note that peak amplitudes clip at ~3,400 counts for station HSR.

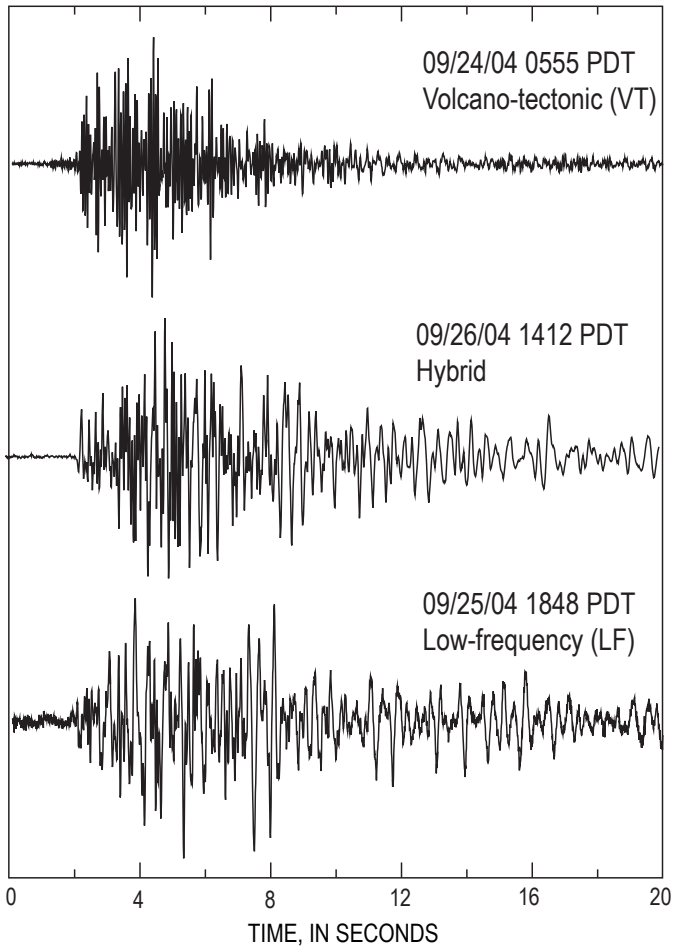

Figure 6. Waveforms for typical volcano-tectonic (VT), hybrid, and low-frequency (LF) events recorded at station HSR (fig. 1) during September 23–26, 2004.

1983; Malone and others, 1983), as well as in the first week of seismicity prior to the May 18, 1980, eruption (Malone and others, 1981; Endo and others, 1981). Those transitions were also gradual, taking place over periods of hours to days. The transitions before the 1980–86 dome-building eruptions were particularly noticeable several hours before eruptions commenced, and they therefore became one of the diagnostic tools that allowed for increasingly precise predictions of eruption onset times (Malone and others, 1983; Swanson and others, 1983; Swanson and others, 1985). Such changes in event character were inferred by Malone and others (1983) to represent a shallowing of the deformation front (as suggested by slightly shallower depths for type "l" events) and to be caused either by the fracturing of different rock types or by a change in source mechanism. In this context, the appearance of lower-frequency events on September 25, 2004, increased the likelihood in our minds that the seismic swarm would ultimately lead to an eruption.

By the morning of September 26 the earthquake rate had further intensified. By midday, maximum event sizes had also started increasing (fig. 5). The increase in event rate and event size and the change in event character caused CVO to issue a Notice of Volcanic Unrest (or Alert Level 1) in the afternoon of September 26. Earthquake locations showed no obvious temporal changes between September 25 and 26, in large part because station density within the crater and the velocity model were insufficient to locate shallow earthquakes in a geologically complex medium with a precision of less than several hundred meters. Between September 25 and 27, however, P-wave arrival-time differences increased between station SEP (fig. 1), located on the 1980–86 lava dome essentially on top of most earthquakes, and other stations located within 4 km of the vent (fig. 7). Daily average arrival-time differences between stations SEP and YEL increased the most (0.13 s), with differences at other stations increasing by 0.07–0.1 s. Arrival-time differences between station pairs not including SEP did not change significantly. We reexamined P-arrival picks and found no evidence that the changes in arrival-time differences were a result of analyst bias (multiple PNSN analysts were involved in picking earthquakes; Qamar and others, this volume, chap. 3) or decreased P-arrival impulsiveness at distant stations (which could result in late picks). The observed pattern is best explained by either a decrease in seismic velocity near station SEP or a decrease in earthquake depths below SEP. Although injection of magma and associated fracturing of country rock could result in lower velocities, shallowing of hypocenters is the simplest explanation for the increase in P-wave arrival-time differences. This shallowing is in part supported by the appearance on September 26 of cracks in the crater glacier (Dzurisin and others, 2005; Scott and others, this volume, chap. 1; Walder and others, this volume, chap. 13).

At roughly 1600 PDT on September 26, a series of earthquakes with similar waveforms (an earthquake "family" or multiplet; for example, see Frémont and Malone, 1987) began, at first mixed with other events with different waveforms (Thelen and others, this volume, chap. 4). By early morning of September 27, seismicity was dominated by this family, with magnitudes increasing through midday and reaching a maximum of M_d 1.9 by late afternoon. This was the first clear instance of repetitive earthquakes, something that was seen frequently before dome-building eruptions at Mount St. Helens in the 1980s (Frémont and Malone, 1987) and has also been observed during other dome-building eruptions, including Usu volcano[4] in Japan (Okada and others, 1981), Augustine Volcano (Power, 1988) and Redoubt Volcano (Power and others, 1994) in Alaska, Guagua Pichincha in Ecuador (Villagómez, 2000), Soufrière Hills volcano in Montserrat (Rowe and others, 2004), and Galeras Volcano in Columbia (R. White, oral commun., 2006). Preliminary fault-plane solutions for the larger events in this family have reverse-faulting

[4] Capitalization of "Volcano" indicates adoption of the word as part of the formal geographic name by the host country, as listed in the Geographic Names Information System, a database maintained by the U.S. Board on Geographic Names. Noncapitalized "volcano" is applied informally—eds.

mechanisms, in contrast to the mix of mechanisms generated during September 23–25 (appendix 1). By 1500 on September 27, the family had become less dominant, but similar events continued through September 28.

The event rate increased relatively rapidly, to 1 event per minute, around 1700 PDT on September 27, as smaller events began occurring between the larger earthquakes (fig. 8). The size of the larger earthquakes also increased, with maximum magnitudes reaching M_d 2.0–2.4 by midday on September 28. Most fault-plane solutions were dip-slip with a steeply dipping fault plane, in contrast to the reverse-faulting mechanisms dominant during the previous 24 hours (appendix 1). At this point, clipping of near-field (<4 km) stations occurred frequently. As a result, smaller events were frequently overwhelmed by the codas of the larger events, making it difficult to distinguish many individual events. It also became increasingly difficult to manually pick earthquakes and determine accurate coda magnitudes, because the coda from one event would be obscured by the onset of the next event. At this point, RSAM became the principal tool for monitoring seismicity (fig. 9), along with helicorder records from stations increasingly distant from Mount St. Helens.

Earthquakes further intensified between 0500 and 0800 on September 29 (fig. 8), when event rates increased to ~3 earthquakes per minute and maximum magnitudes rose to M_d 2.4–2.8, causing CVO to issue a Volcano Advisory (or Alert Level 2) at 1040 PST (Dzurisin and others, 2005). A second rise in RSAM levels occurred 12 hours later, between 1700 and 2100 (fig. 9), when maximum magnitudes increased to M_d 2.8–3.3, with M_d >2 events occurring at a rate of ~1 per minute by the evening of September 29. Most fault-plane solutions for these events had normal-faulting mechanisms, although there were also occasional events with many, or all, down first-motions, consistent with reverse faulting (appendix 1). One side effect of the high rate of larger earthquakes was that they began to dominate seismic recordings at other Cascade volcano seismic networks (in particular at Mount Adams, Mount Hood, Mount Rainier, and Three Sisters), as well as at regional seismic stations in Washington and Oregon, resulting in a temporary reduction in PNSN sensitivity to smaller events in a broad area around Mount St. Helens.

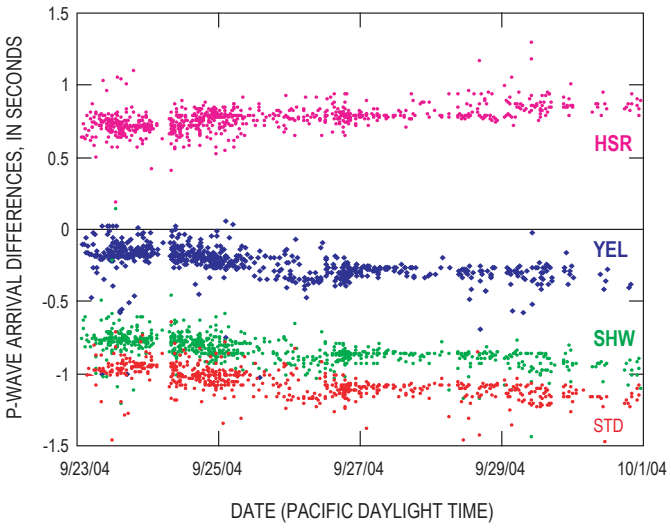

Figure 7. Plot of P-wave arrival-time differences between station SEP (located on the 1980–86 lava dome) and four other stations including HSR (magenta), YEL (dark blue), SHW (green), and STD (red), between September 23 and October 1, 2004. (see fig. 1 for station location). P-wave arrival-time differences were computed only for high-quality picks, with an estimated picking error of ≤0.05 s. Note that the absolute value of differences increases on all station pairs between September 25 and September 27. This increase was not apparent on other non-SEP station pairs and is consistent with shallowing of hypocenters.

Following the second intensification on September 29, the rate of larger earthquakes declined somewhat, resulting in a decline in RSAM values, which reached a relative minimum at roughly 0500 on September 30 (fig. 9). The rate of larger earthquakes increased and decreased two more times on September 30, with RSAM values always between the minimum and maximum levels achieved on September 29. The increases did not correspond with any known changes in the crater, although temporal resolution of visual observations and measurements from other geophysical instrumentation were insufficient to detect changes on an hourly scale. Fault-plane solutions from the PNSN catalog switched from dominantly normal-faulting to reverse-faulting solutions for a short time between 2300 September 30 and 0500 October 1 (appendix 1); then, three hours later at 0800, RSAM levels again increased as a result of an increase in event rate (figs. 8, 9). RSAM values peaked at 1100 at levels similar to previous maxima. The first phreatic explosion occurred an hour later at 1202 PDT, 8.5 days after the first precursory seismicity on September 23. This interval was one day longer than the 7-day interval between the first earthquakes and first phreatic explosion in March of 1980 (Endo and others, 1981; Malone and others, 1981). This similarity could indicate that a characteristic time interval exists between initiation of precursory activity and initial explosive activity at Mount St. Helens. If this is the case, then the time interval presumably is governed by the structure of the shallow conduit system and surrounding country rock, as well as the composition of the intruding magma.

Aside from the RSAM increase, there were no obvious precursors to the October 1 explosion. The explosion began aseismically, with no obvious changes in seismicity associated with the start of the explosion (Moran and others, this volume, chap. 6). Timing constraints for the explosion are excellent, because a CVO crew was flying around the vent when the explosion began (Schneider and others, this volume, chap. 17). The most obvious change in seismicity occurred at 1203, 1 minute after the explosion began, when earthquakes suddenly stopped (figs. 8, 9). This cessation was so dramatic that it caused one CVO crew working at seismic station STD (fig. 1) to look up at the crater when the sound of the earthquakes, heard through a scanner tuned to the frequency of a nearby seismic station, suddenly stopped. A relatively broadband

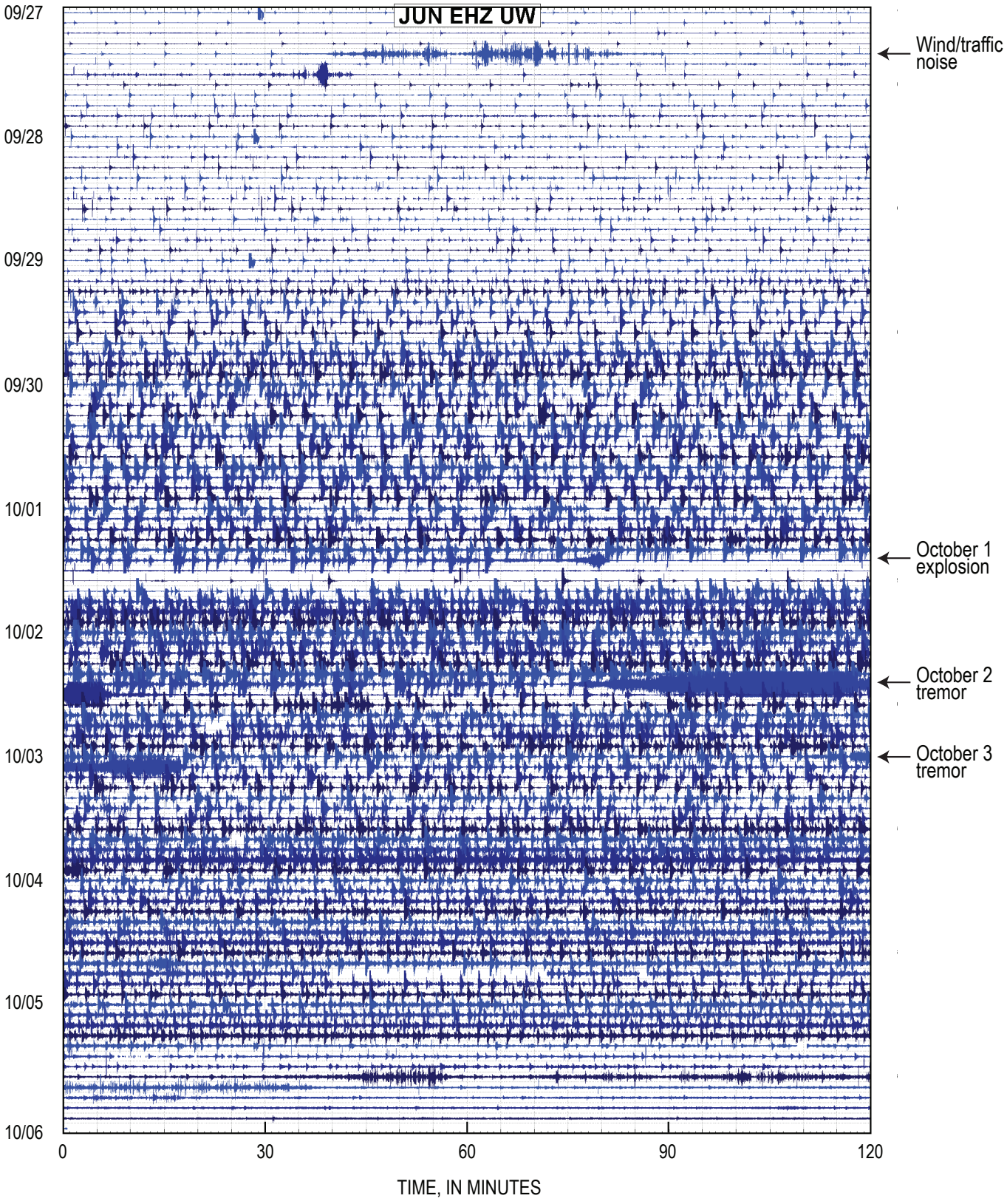

Figure 8. Seismic record from station JUN (6.5 km southeast of vent; fig. 1) from September 27 through October 5, 2004, showing seismicity trends during the vent-clearing phase.

(0.5–3 Hz) tremor signal accompanied the explosion after the last earthquake at 1203 (fig. 8), with tremor amplitudes roughly doubling between 1216 and 1221. At 1221 the tremor and the explosion stopped abruptly.

The October 1 explosion destroyed seismic station SEP, the closest station to the earthquakes (fig. 1). The loss of this station decreased the quality of PNSN catalog locations, with average hypocentral errors for well-constrained earthquakes (P waves on at least 7 stations, azimuthal gap <135°, nearest station within 3 km) increasing from 0.2 km in the 24 hours before October 1 to 0.34 km in the 24 hours after the explosion. This impact illustrates the importance of having seismic stations close to the source. Indeed, the loss of SEP was one of the primary motivations for the development of a seismic sensor package that could be remotely deployed at locations too hazardous for crews to work on the ground (McChesney and others, this volume, chap. 7).

October 1–October 5, 2004

Seismicity levels dropped precipitously following the 1202–1221 explosive event, with the first small earthquake not occurring until roughly 3 hours later at 1515. This drop indicated that seismicity was occurring in response to elevated pressure in the conduit system, pressure that was temporarily reduced by the October 1 explosion. Hybrid earthquakes slowly increased in number and size and then rapidly increased between 1700 and 2000 on October 1, with RSAM levels eventually exceeding those of September 29–October 1. As with previous intensifications, RSAM levels flattened and then gradually declined on October 2 (fig. 9). At roughly 1217 PDT on October 2, earthquakes were replaced abruptly by relatively broadband seismic tremor with dominant frequencies in the 0.5–3-Hz range (fig. 10). Tremor rapidly intensified over a period of 20 minutes, to peak reduced-displacement values of 28–43 cm^2, and was energetic enough to be recorded on seismic stations more than 240 km away. The energetic tremor, in combination with the October 1 explosion and continuing energetic earthquake activity, caused CVO to issue a Volcano Alert, the highest alert level. No explosions or other obvious surficial events (such as increased steaming or small ash emissions) were observed in association with the tremor. Tremor amplitudes began decreasing shortly after the alert level change, and, by 1315, tremor had virtually disappeared. As with the October 1 explosion, earthquake rates and sizes decreased significantly after tremor ceased, although the drop was not as abrupt or as long-lived (figs. 8, 9, 10). Earthquake rates and sizes began increasing again around 1400, and by 1900 RSAM values had returned to levels just below those before the October 2 tremor episode (fig. 9). A smaller tremor episode (reduced displacement 10–20 cm^2, peak frequencies 0.5–2.5 Hz) occurred between 0250–0315 PDT on October

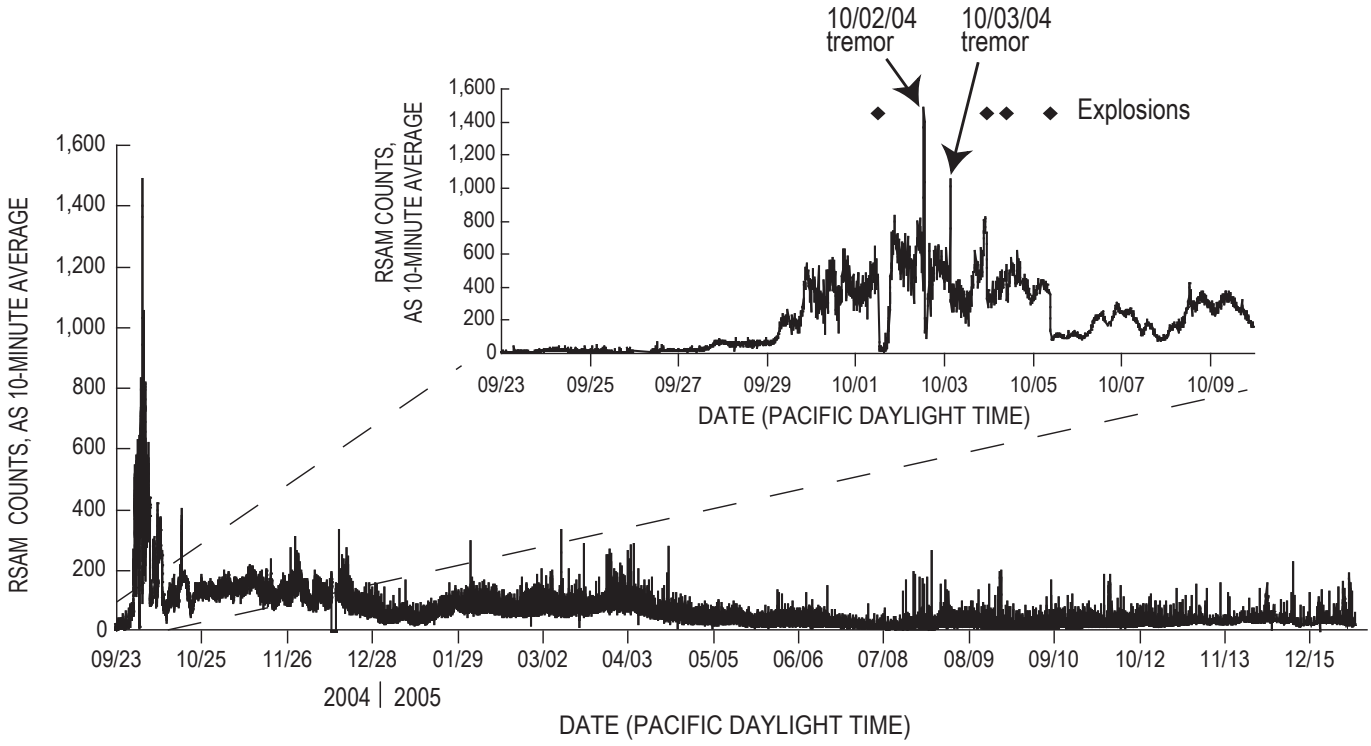

Figure 9. Plot of 10-minute real-time seismic amplitude measurement (RSAM) values from station SHW (3 km west of vent; fig. 1) between September 23, 2004, and December 31, 2005. Inset shows SHW RSAM between September 23 and October 10, timing of four phreatic explosions, and occurrence of two tremor episodes associated with a vent-clearing phase. Horizontal-axis tick marks in inset indicate start of a day, with gaps of 2 days between each tick mark.

3 (fig. 8), and, as with the October 2 episode, no eruptive plume was detected (M. Guffanti, written commun., 2004). In contrast to the October 2 episode, earthquakes continued to occur during the October 3 tremor episode. Although earthquake rates and RSAM levels dropped after the episode and remained low for the next 12 hours, the decrease was not as great as those that followed the October 1 explosion and the October 2 tremor.

Around 1500 PDT on October 3, earthquake rates again began increasing, with RSAM levels peaking at 1650 (fig. 9). After a brief drop, earthquake rates increased again, with seismicity dominated by many small-amplitude events. By 2100, earthquakes were occurring so close together in time that they became difficult to distinguish, forming a spasmodic tremor-like signal (fig. 8). Continuous, small-amplitude tremor was likely also occurring, although this signal can only be seen in the short gaps between individual earthquakes. Earthquake rates and the tremorlike signal decreased substantially around 2305, following a small steam-and-ash explosion at 2240 reported by U.S. Forest Service observers at the Coldwater Ridge Visitor Center, and RSAM dropped to levels similar to those from early in the day on October 3 (fig. 9). Following this small explosion, the number of larger (M_d >2) earthquakes decreased, with many smaller hybrid earthquakes occurring in the gaps between larger events (fig. 8). Earthquake rates and RSAM levels gradually increased again until another steam-and-ash explosion at 0943 PDT on October 4, and, as before, earthquake rates and RSAM levels briefly dropped following the explosion (figs. 8, 9). Shortly afterward, RSAM levels increased again, peaked at 1700 on October 4, and then gradually declined to a relative low at 2330. As with roughly two-thirds of the previous RSAM increases, the peak and subsequent decline were not associated with explosions or other anomalous surface activity. RSAM levels increased once again beginning at 0000 PDT on October 5, reaching a peak at 0600 that was maintained until the final explosion of the vent-clearing stage began at 0903. Earthquake sizes and rates began declining ~15 minutes after the explosion began and continued to decline over the next hour as the explosion continued through 1015. After the explosion, RSAM levels were lower than at any time since September 29, with the exception of the lull following the October 1 explosion. Although RSAM levels increased and decreased several times over subsequent weeks, they never again reached levels achieved before the October 5 explosion (fig. 9).

Between September 29 and October 5, earthquakes were too large and occurring too close together in time for more than a fraction of all earthquakes to be detected and located by the PNSN. Using the average event rates given above, we estimate that ~30,000 earthquakes occurred over these seven days. The largest located event was a M_d 3.9 on October 1, and 9 events had $M_d \geq 3.5$ between October 1 and October 4. To estimate the total amount of seismic energy expended during the vent-clearing phase, we calibrated RSAM values at station FMW (91 km north of Mount St. Helens) using 20 of the largest earthquakes and then integrated RSAM values from FMW between September 23 and October 5. The result was a cumulative magnitude equivalent to a M_d 5.5 earthquake, an order of magnitude lower than the cumulative magnitude of M_d 6.5 estimated for the March 28–May 18, 1980, precursory seismicity.

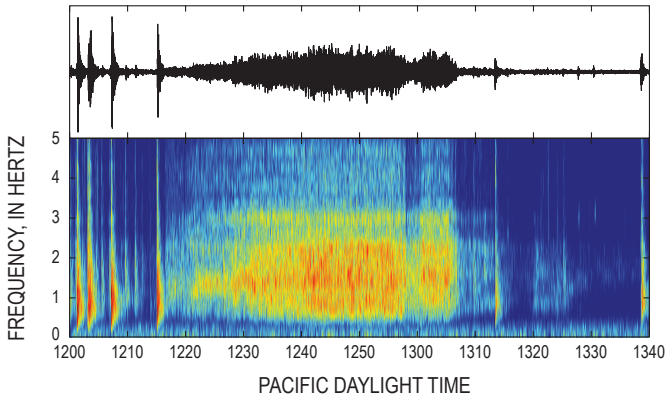

Figure 10. Tremor episode on October 2, 2004, as recorded on vertical component of broadband station JRO (8 km north of the vent; fig. 1). Time series (above) and spectrogram (below) for same time period. Note that discrete earthquakes stopped when tremor started at 1217 PDT and were significantly diminished after it ended at 1310.

October 5, 2004–December 31, 2005: Seismicity Accompanying Dome Building

The steep decline in seismicity following the October 5 explosion caused CVO to lower its alert level to Volcano Advisory (Alert Level 2), where it remained through the end of 2005. Although RSAM levels increased again between October 6–7 and October 8–9, 2004, as a result of increasing event sizes (largest were M_d 2.5–3.0), the increases were much more gradual and didn't reach September 29–October 5 levels (fig. 9). Because there had been a number of more rapid increases in seismicity between September 29 and October 5 that were not directly associated with eruptive activity, we did not change our alert status at the volcano during these more gradual intensifications. We noted during both those periods that earthquakes were dominated by a single event family, an attribute of Mount St. Helens seismicity that continues at the time of this writing (Moran and Malone, 2004; MacCarthy and Rowe, 2005; Thelen and others, this volume, chap. 4).

The October 8–9 earthquakes were a particularly spectacular example of an event family (fig. 11). Event magnitudes systematically increased over a ~12-hour period starting 0200 PDT, then stabilized at M_d 2.5–3.0 for almost 24 hours before systematically declining over a ~12-hour period back to M_d 1–1.5 (fig. 5). We generated hourly event stacks (fig.

11) to increase the signal-to-noise ratio of the P-wave arrivals and found that first motions were down at all stations, consistent with either very shallow reverse faulting or a deeper, nondouble-couple source (such as motion along a curved surface or an implosion). The appearance of event families, taken together with the overall decline in seismic levels, the change in event character to dominantly LF and hybrid events, the relatively low gas levels (Gerlach and others, this volume, chap. 26), and the observed deformation of the crater floor (Dzurisin and others, this volume, chap. 14), led CVO and the PNSN to believe that the most likely outcome was a new episode of lava dome building.

Seismicity declined significantly following the October 8–9 earthquake sequence. From October 10 to October 16, seismicity consisted of small (M_d <1) events occurring at a rate of 1–2 per minute, as well as slightly larger events with longer between-event intervals. At 0200 on October 16 the number of discrete M_d 1–1.5 events started decreasing, and between these events many tiny LF earthquakes appeared, spaced roughly 20 s apart (fig. 12). Event magnitudes of the tiny LF earthquakes steadily increased through October 17 before stabilizing at M_d ~0.5. When first observing these smaller events we noted a strong similarity to short-lived episodes of tiny, closely spaced LF events that were observed at Mount St. Helens in three separate instances associated with the 1983–84 continuous dome-building eruption (R. Norris, oral commun., 2006). On the basis of this similarity, we inferred that these LF events likely represented the extrusion of a new dome.

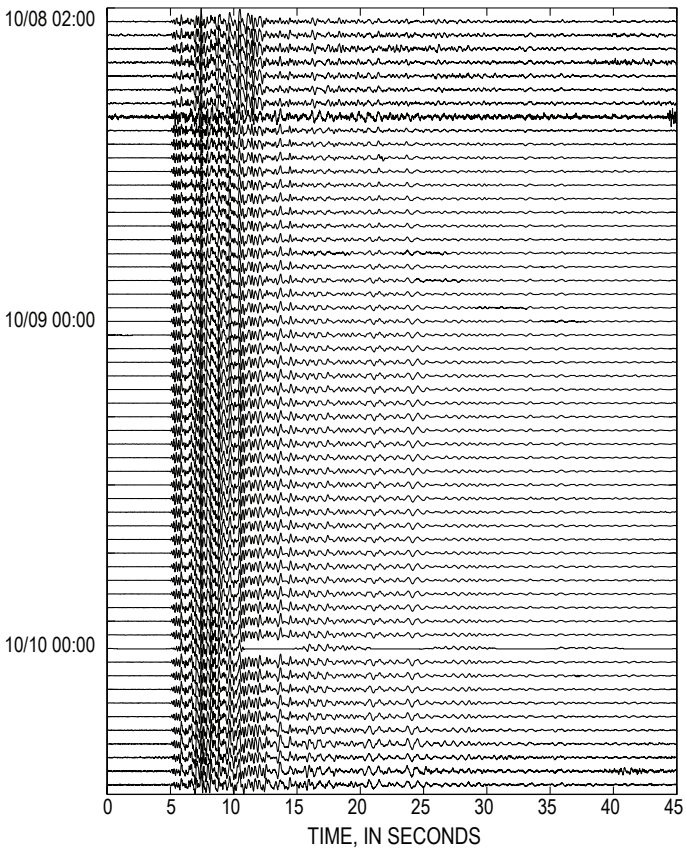

Figure 11. Plot of hourly stacks of events from earthquake family recorded on station HSR (2.5 km south of vent; fig. 1) between October 8 and October 10, 2004.

"Drumbeat" Earthquakes

The appearance of regularly spaced, small earthquakes on October 16, 2004, marked the beginning of the next seismic phase of the eruption, a phase that continues at the time of this writing. Seismicity in this phase was dominated by these events, which occurred at such remarkably constant intervals that we dubbed them "drumbeat" earthquakes. The drumbeats consisted of repetitive LF and hybrid earthquakes and were one of the hallmarks of the eruption in 2004–5. Indeed, we know of no instances at other volcanoes when drumbeatlike events have been observed over such a long period of time. The drumbeats accompanied the regular rate of extrusion of several dacite spines (in this volume: Schilling and others, chap. 8; Vallance and others, chap. 9; Herriott and others, chap. 10; Poland and others, chap. 11; Major and others, chap. 12). Many of the drumbeats had waveforms similar to other drumbeats (Thelen and others, this volume, chap. 4), a similarity that can be used to relatively relocate events within individual earthquake families with high precision, as was done in the 1980s at Mount St. Helens by Frémont and Malone (1987). Thelen and others (this volume, chap. 4) present a thorough analysis of a number of well-recorded families. Identifying and relocating all earthquake families occurring within the million-plus earthquakes of late 2004 and 2005 is a large task that will likely take years to complete, well beyond the scope of this paper.

Several investigators have proposed models that link drumbeats and extrusion rate (Harrington and Brodsky, 2006; Iverson and others, 2006; Iverson, this volume, chap. 21; Mastin and others, this volume, chap. 22), with most invoking stick slip as the source mechanism. Horton and others (this volume, chap. 5) note that spectral peaks from drumbeats recorded on broadband stations deployed in 2004–5 are suggestive of resonance within a structure such as a crack or conduit, with resonance initiated by a stick-slip event (Neuberg and others, 2006) or by a pressure transient in a crack (Chouet, 1996). Research into the drumbeat source mechanism is ongoing, and it is not our intent to present a thorough discussion of possible drumbeat source mechanisms. Instead we focus on describing general trends in drumbeat event spacing, size, and frequency content and how changes in these characteristics correlated with dome extrusion.

Event Spacing

Figure 13 shows that, to a first approximation, the time between drumbeats, or event spacing, changed little between October 16, 2004, and April 11, 2005, with daily averages ranging between 40 and 80 s. An important exception is that

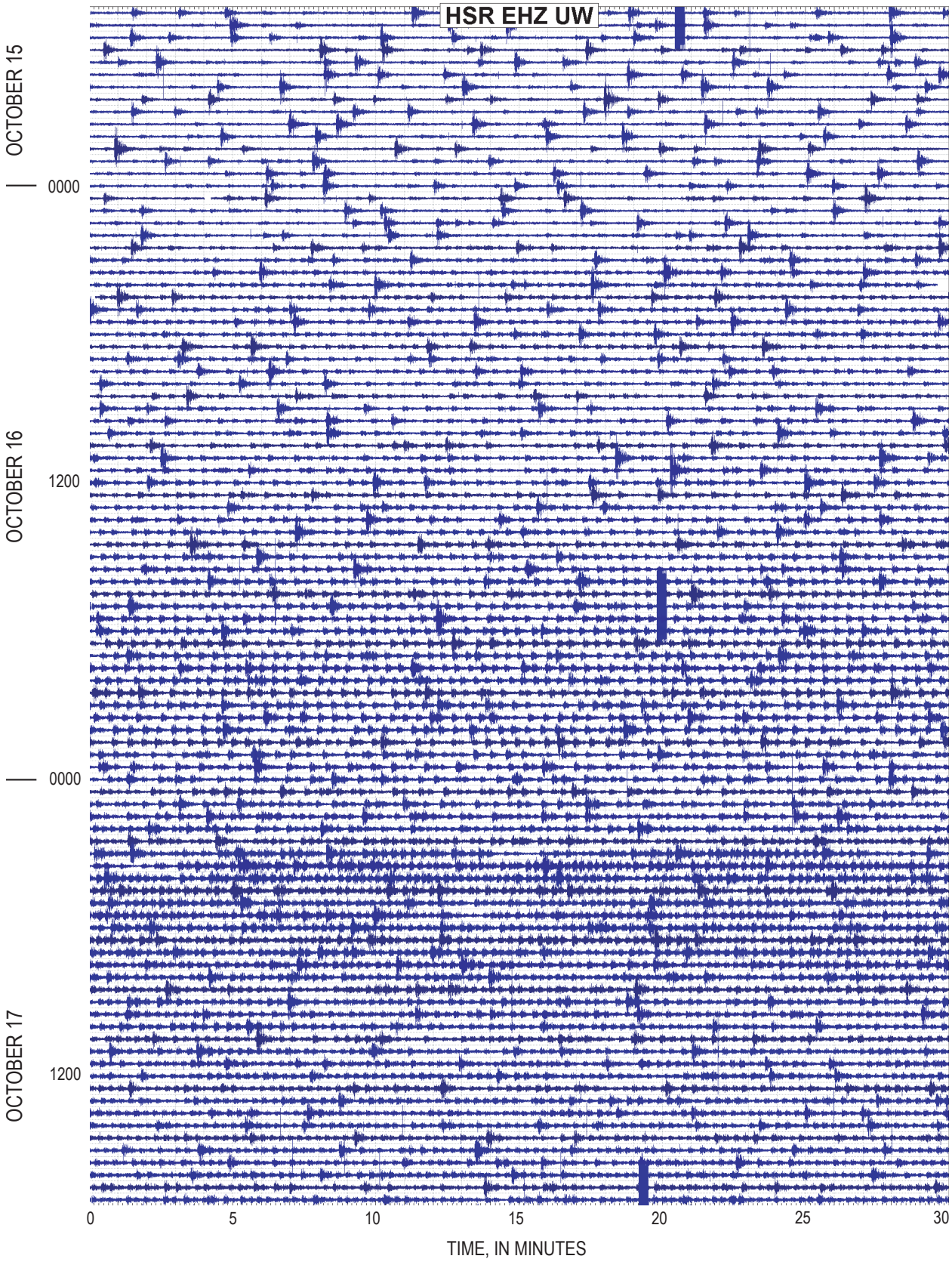

Figure 12. Seismic record from station HSR (2.5 km south of vent; fig. 1) from 1700 PDT on October 15 through 1800 PDT on October 17, 2004, showing onset of small, regularly spaced events ("drumbeats") occurring between larger events early on the morning of October 16. Drumbeat amplitudes increased gradually through the day.

between October 16 and November 12, 2004, events were occurring only ~20 s apart and were small enough that many went undetected by our detection algorithm (appendix 2). After November 12, event spacing increased to ~40 s, and visual inspections show that most events were detected. Between April 12 and July 8–10, 2005, the average event spacing gradually increased to more than 560 s, then briefly got shorter; on July 20 it became irregular, with spacing progressively increasing. In early August the events had become too small to be detected reliably by our algorithm on station HSR. Even on stations located within 1 km of the vent, earthquakes were occurring more as random earthquakes than drumbeats. By early October 2005, they had become so infrequent, emergent, and small that we began questioning whether the seismic events we were seeing were earthquakes or other surface sources, such as ice quakes and rockfalls. However, on October 9, 2005, earthquakes began to increase in size, and event spacing became remarkably regular again, with events occurring every ~70 s. Initially, event sizes were bimodal (fig. 13), with a population of larger-magnitude events (peak magnitude M_d ~2.5) occurring alongside a population of more frequent smaller events. The larger-magnitude events gradually decreased in size until by mid-November 2005 there was just a single dominant event size. Event spacing began increasing in mid-December and, by the end of December 2005, had again become irregular.

One important qualification to the drumbeat story is that many small earthquakes recorded on stations located inside the crater in 2004–5 were not drumbeats. This was particularly the case from May through July of 2005, when the spacing between drumbeats increased significantly (fig. 13). As drumbeats decreased in size and number starting in mid-June, there was a factor of 15 difference between numbers of detected events at station MIDE (located ~200 m from the vent) and station HSR (2.5 km from the vent) between May 20 and July 18, 2005 (fig. 14). Some of the events detected at MIDE were rockfalls, but most were earthquakes that were too small to be recorded on stations >0.5 km from the vent. The

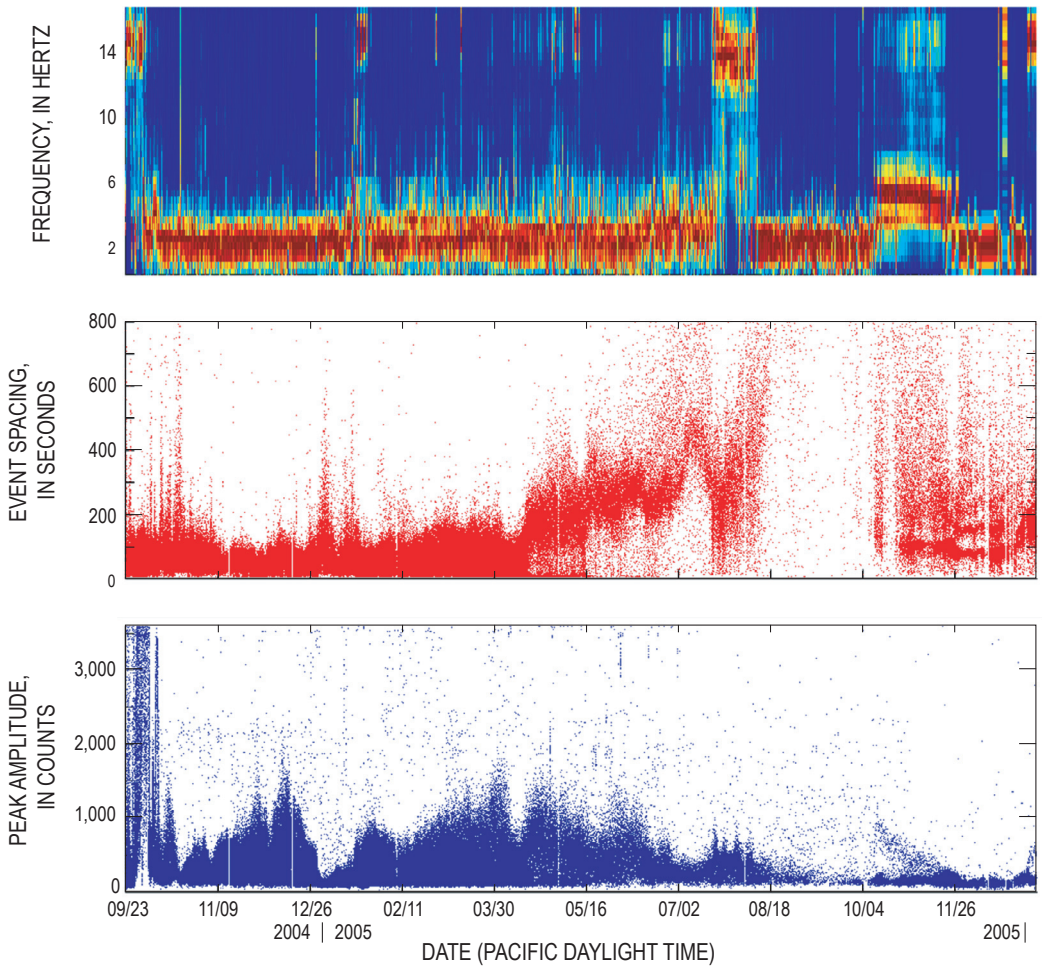

Figure 13. Plot showing ESAM (top), inter-event spacing (middle), and peak amplitudes (bottom) for detected events at station HSR (fig. 1) between September 23, 2004, and December 31, 2005 (see appendix 2 for event detection details). Roughly 370,000 events were detected during this time period, including occasional noise glitches and other false triggers.

events recorded on MIDE and other near-field stations lacked the regular spacing characteristic of drumbeats, and relative amplitudes and arrival-time patterns between MIDE and other near-field stations indicate that many were occurring within the extruded spines.

Event Size Distribution

There was a complex relation between drumbeat event spacing and event size. In general, increases in event spacing corresponded to increases in event size and vice versa (fig. 15). For example, on December 16, 2004, average drumbeat magnitudes were M_d ~1.5 and events were spaced ~90 s apart, whereas on December 23, 2004, average magnitudes had decreased to M_d ~0.5 and events were spaced ~40 s apart (although occasional M_d 1.0–1.5 events still occurred). If drumbeats are a result of stick-slip motion along a common fault plane and the steady extrusion rate corresponds to a constant slip rate (or stress accumulation rate) along the fault plane, then smaller drumbeats must be closer together if extrusion rate and seismic energy release are to remain constant. However, for seismic energy to have remained constant between December 16 and December 23, the event spacing would have had to decrease to ~3 s on December 23, a factor of 13 less than the observed ~40 s spacing. Thus there was a net reduction in seismic energy release between December 16 and December 23. Another drop in seismic energy release occurred in the evening of December 29, 2004, when drumbeat magnitudes dropped to M_d 0.0–0.5 while event spacing remained roughly constant (fig. 13).

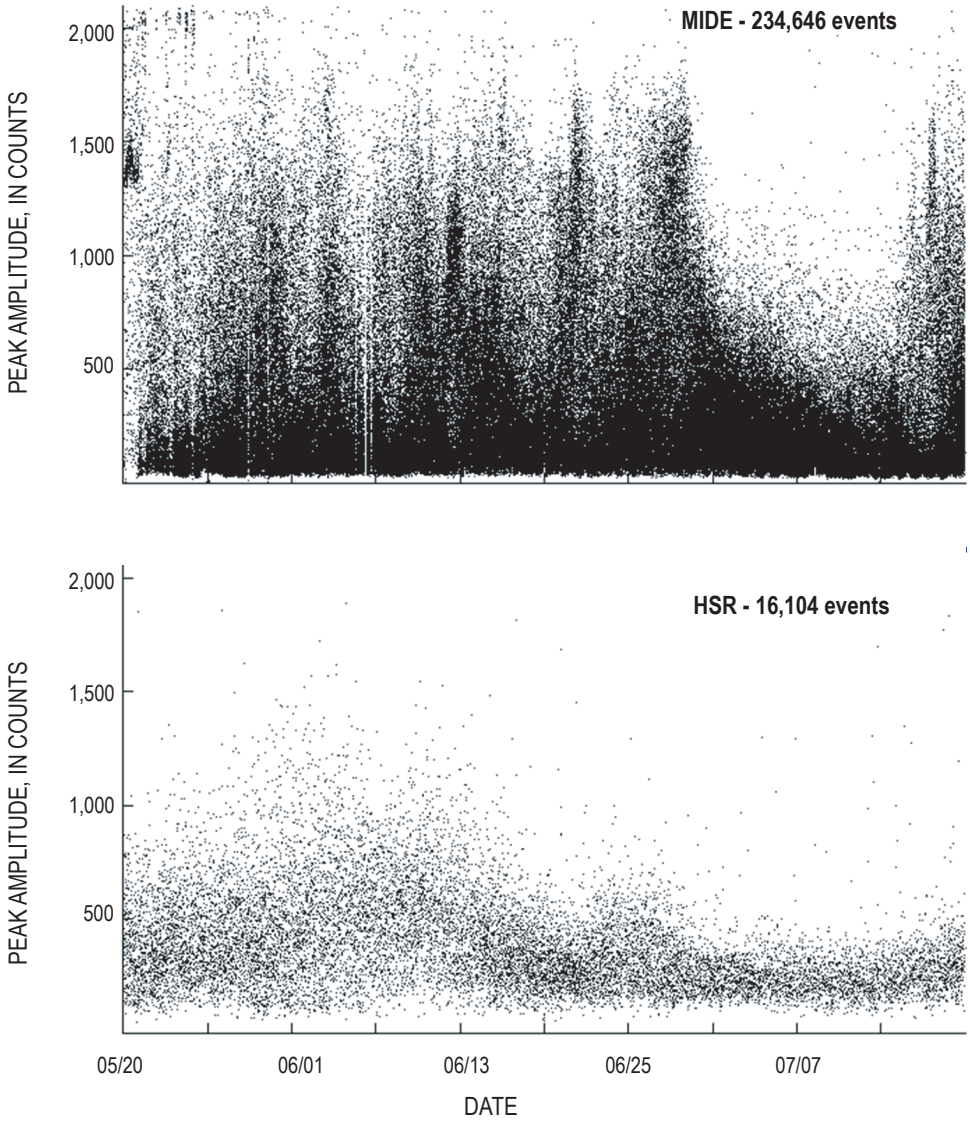

Figure 14. Detected events vs. time at stations MIDE (top) and HSR between May 20 and July 18, 2005. Note that the decline in events at HSR starting around June 13 is not seen at MIDE, evidence that many events detected on MIDE were occurring close to the station and were due to a process distinct from that responsible for the drumbeats.

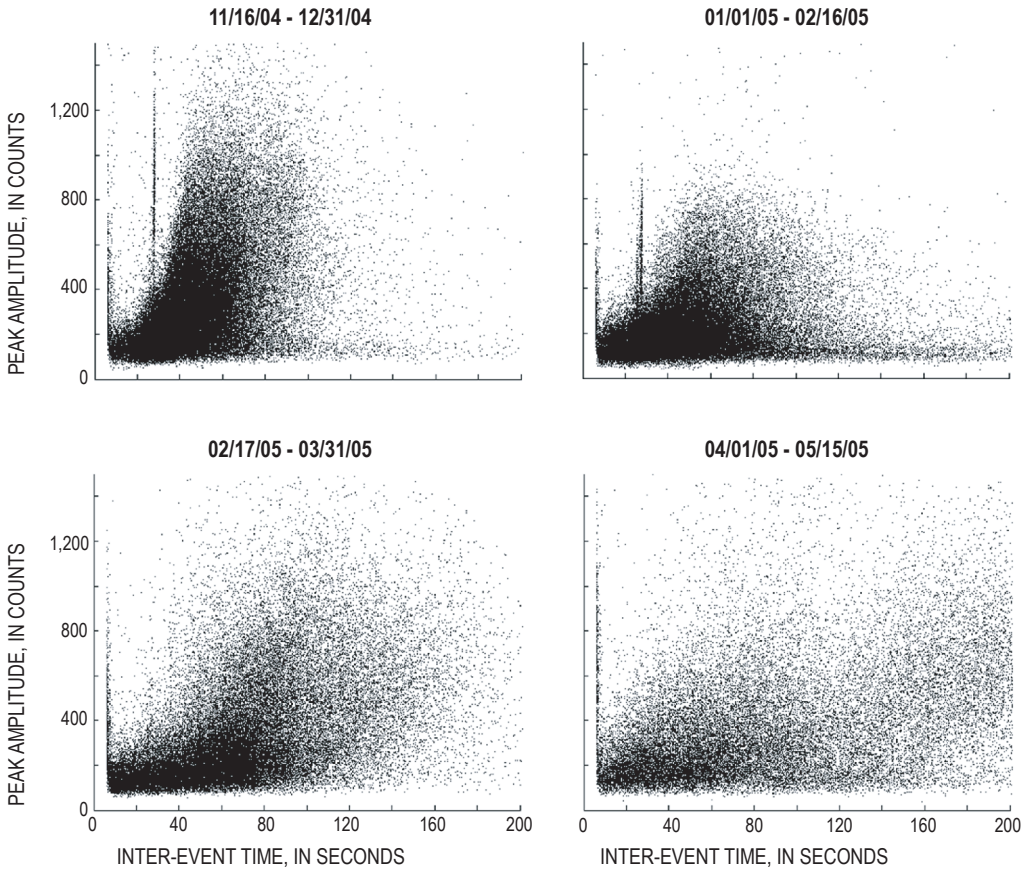

Figure 15. Plot of peak amplitudes vs. event spacing for detected events at HSR (fig. 1) for four time periods (all four plots have same vertical and horizontal scales). Although a general relation is seen between event size and inter-event time, particularly through mid-February (top two plots), the slope decreases over time, indicating that seismic energy release was declining as event spacing was increasing. Two linear features in the top two plots correspond to a sufficiently strong secondary phase arriving ~20 s after the P-wave at HSR to be occasionally detected as an event.

These and other decreases in seismic energy release could have been caused by decreases in extrusion rate, decreases in seismic coupling, or other changes in the mechanics of extrusion. Both December 2004 seismic energy drops (Dec. 23 and Dec. 29) occurred during the breakup of spine 3 and transition to spine 4 as the active locus of extrusion, a transition that began November 16 and continued through mid-January 2005 (Vallance and others, this volume, chap. 9). A mid-April 2005 drop in energy release, when event rates declined noticeably (fig. 13), coincided with the breakup of spine 4 and transition to spine 5, and another energy drop in mid-July coincided with the breakup of spine 5 and transition to spine 6 (Vallance and others, this volume, chap. 9). The correlation between transitions in extrusion style at the surface and changes in seismic energy release suggests that drumbeat seismicity was controlled to a certain extent by the mechanics of extrusion at the surface. Support for this interpretation comes from the observation that extrusion rates determined from digital elevation models (DEM) computed periodically throughout the eruption (Schilling and others, this volume, chap. 8) remained relatively constant despite fairly substantial changes in seismic energy release. In particular, the extrusion of spine 6 was associated with a significant drop in event rate and size from mid-August through early October of 2005, as described above. However, three DEMs spanning August–October 2005 show that the rate of extrusion remained roughly constant during the lull in seismicity. This lack of correspondence indicates that the rate and size of drumbeats may have been more a function of changes in extrusion mechanics than changes in magma flux through the conduit. Changes in extrusion mechanics that could have influenced earthquake occurrence include changes in the angle of extrusion (which would affect clamping forces), changes in the locus of extrusion, and (or) changes in the frictional properties along the conduit margin through rate hardening/softening or other processes.

A further complexity in the relation between event sizes and event spacing is that, although there clearly were extended periods of time when larger drumbeat events were followed by longer gaps, there also were many instances when larger events were followed by short gaps and smaller events followed by larger gaps. This complexity is not predicted by models that marry drumbeats with the regular extrusion rate (Iverson and others, 2006; Iverson, this volume, chap. 21; Mastin and others, this volume, chap. 22). If the drumbeats were a result of a stick-slip source, then this complexity indicates that drumbeats at times occurred at multiple locations within a complex network of shear zones, with individual faults having individual loading and unloading histories somewhat independent of those on other faults. It remains to be seen if individual drumbeat families (Thelen and others, this volume, chap. 4) show a more direct relation between event size and event spacing.

A final general characteristic of drumbeat magnitudes was their magnitude-frequency distribution over time. Most commonly, drumbeats occurred with a single dominant event size and, in general, did not follow a Gutenberg-Richter rela-

tion. This is consistent with the repetitive nature of the drumbeats and implies that source dimensions, as well as location, varied little between individual drumbeats. However, there were also time periods when event amplitudes appeared to follow a Gutenberg-Richter relation (fig. 13), in the sense that a greater number of small events occurred than large events. We note that there is no relation between event size and event spacing during many of these time periods, which also implies that multiple seismic sources were active at the same time.

P-Wave Spectra

With a thousand or more events occurring per day, it was difficult to notice changes in event character over time, although obvious variations from the norm, such as the sporadic occurrence of VT events, were noted, usually within hours. One means we used for tracking changes in drumbeat character was to plot event spectra over time (see appendix 2 for details). Earthquake spectral amplitude (ESAM) plots in figures 5 and 13 show that seismicity transitioned from hybrid events following the October 5 explosion to LF events by October 9 and was dominated by LF events (peak frequencies in the 2–3-Hz range) through early January 2005. Between January 8 and 25, hybrid events occurred along with LF events (fig. 16), with peak hybrid P-wave frequencies of 8–16 Hz on station HSR. Hybrids also occurred with LF events between mid-April and late May 2005 and were the dominant event type between July 20 and August 11, 2005 (fig. 16). In both cases, peak P-wave frequencies were in the 12–16-Hz range on station HSR. Hybrids again occurred alongside LF events between October 9 and November 18, with peak P-wave frequencies in the 4–6-Hz range and a weaker band between 14 and 16 Hz (fig. 13). These frequency changes are most notable on stations HSR and SHW, two stations located 2.5–3 km from the vent. Changes in event appearance are also apparent on station YEL, ~1 km from the vent (the closest station to have operated throughout the entire eruption), but peak frequencies for the hybrid events are 4–5 Hz, suggesting that the path to YEL attenuates much of the high-frequency energy apparent on flank stations.

The four instances of concentrated hybrid occurrence all coincide with transitions in spine extrusion, as well as with several changes in event amplitude and (or) event spacing described above. The best example of this was July–August 2005, when seismicity switched from dominantly LF to dominantly hybrid events. A time-lapse sequence of photos (fig. 17) from a remote camera located on the northeast edge of the crater (Poland and others, this volume, chap. 11; Major and others, this volume, chap. 12) shows that the hybrid events began as the south end of spine 5 stopped moving on July 20, resulting in differential motion within the spine. As time progressed, the resultant shear zone moved northward, until finally spine 6 split away from spine 5 and began moving westwards around August 9–10. Other major spine transitions occurred December 2004–January 2005, mid-April 2005, and early October 2005 (Vallance and others, this volume, chap. 9). Hybrid seismic events occurred to varying degrees during each of these transitions, a correlation that suggests a direct relation between hybrids and motion of the spines after extrusion from the vent. One speculative model is that the hybrids are a result of differential shearing occurring along the base of the spine during spine transitions, whereas the LF events, which do not have as clear a relation to changes in spine motion after extrusion, occur at shallow depths along the conduit margin.

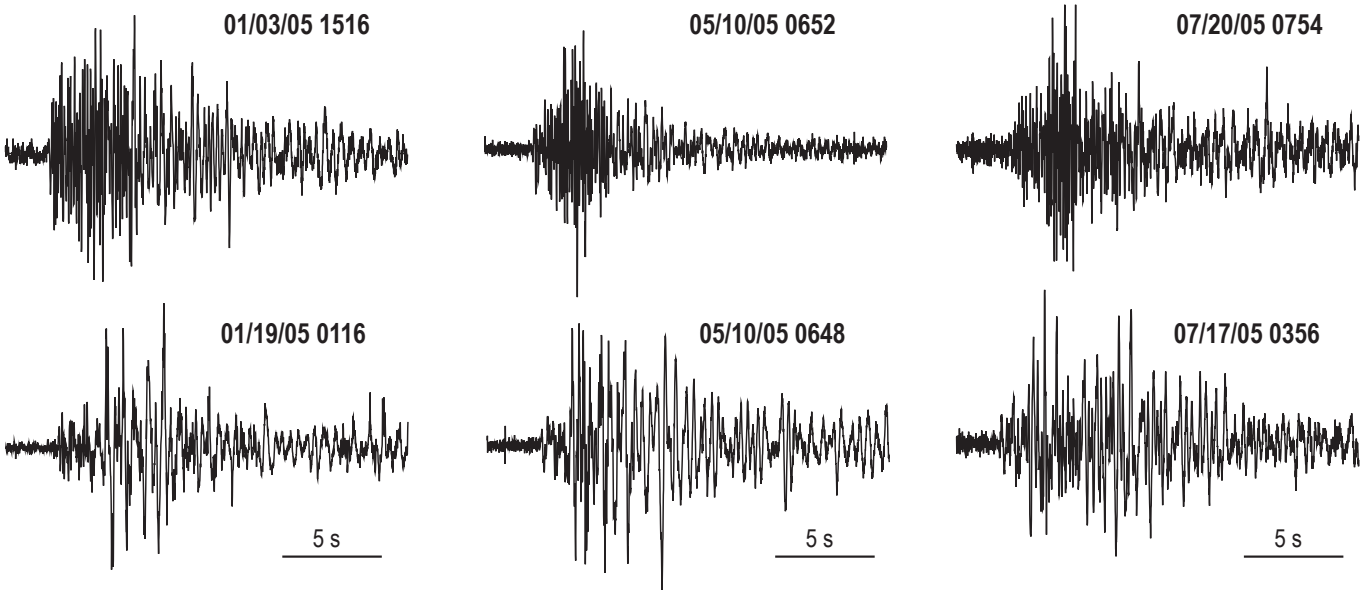

Figure 16. Examples of hybrid (top) and low-frequency drumbeats (bottom) as recorded at station HSR in January, May, and July 2005. Hybrid drumbeats were relatively rare and occurred in temporal clusters that are clearly visible on the ESAM plot in figure 13. Such clusters corresponded to transitional periods when one spine became inactive and a new spine began to grow.

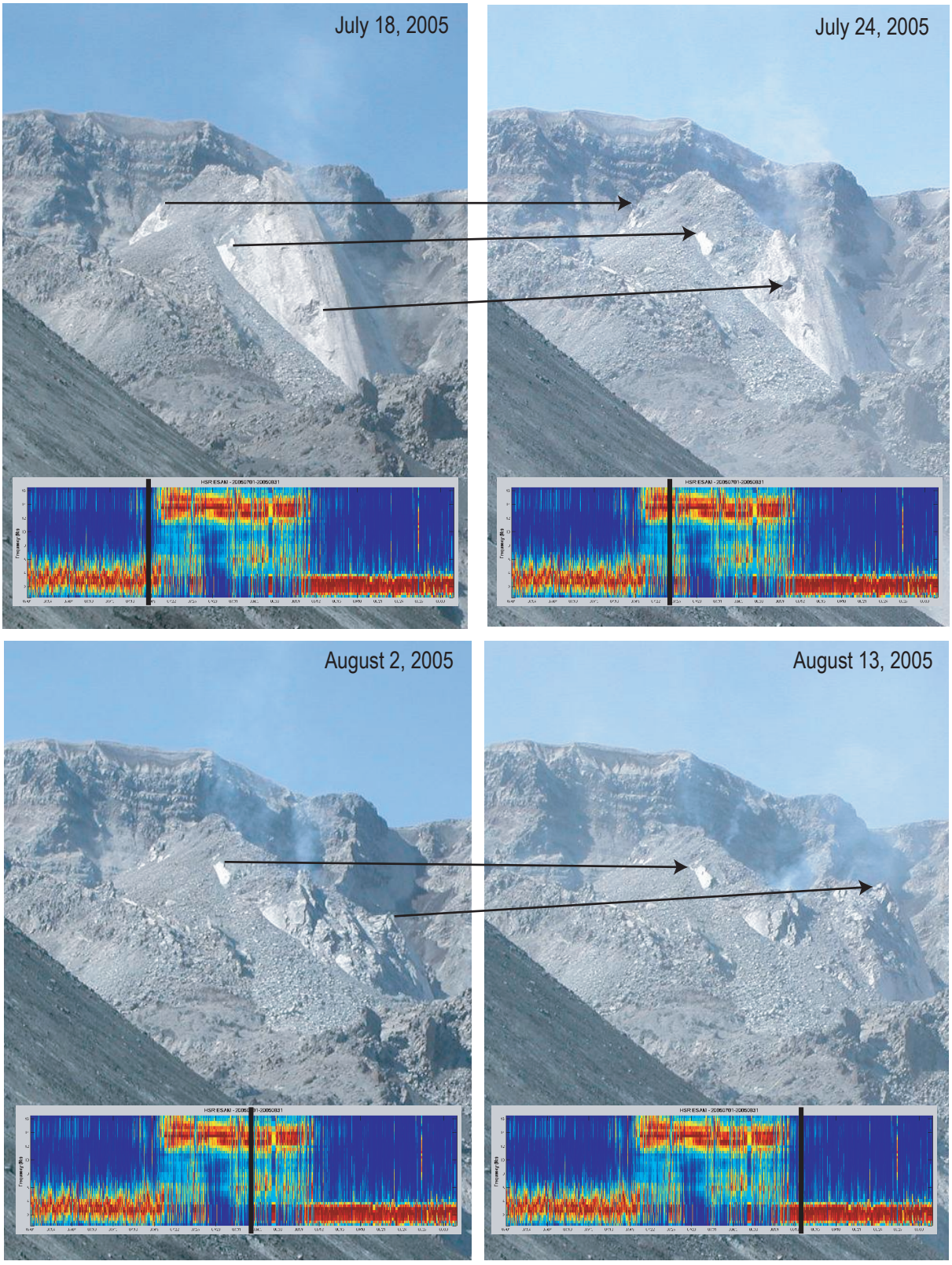

Figure 17. Four pictures taken from a camera station at SUG (fig. 1) showing transition from spine 5 to spine 6 that took place in late July–early August. Arrows indicate relative motion of common spots on spine 5. At bottom of each picture is an ESAM plot showing earthquake spectra between July 1 and August 31, 2005, with frequency ranging from 0 to 16 Hz (identical scale to figs. 5 and 13). Black vertical bar on each ESAM plot corresponds to date on which that picture was taken.

"Big" Earthquakes

Another intriguing aspect of seismicity after October 16, 2004, was the occasional occurrence of larger, or "big" (M_d >2.0, M_{max} = 3.4), shallow earthquakes. The first of these was a M_d 2.4 earthquake at 2048 PST on November 15, 2004, that was followed by 11 others over the next two weeks (fig. 18). These earthquakes were notable because they were much larger than the regular drumbeat events (fig. 19). They generated much interest among scientists and with the public, because they could be seen easily in the real-time digital helicorder plots displayed on the PNSN Web site (Qamar and others, this volume, chap. 3). Also, they often caused large rockfalls that, in turn, generated ash plumes, which frequently rose above the crater rim. The onset of the "big" events coincided with spine 3 encountering the south crater wall, as demonstrated by DEMs (Schilling and others, this volume, chap. 8). Spine 3 was likely in a state of uniaxial compression at this point, and the coincidence of its south-wall impingement and the occurrence of larger events suggests a causal relation.

The larger events cannot be distinguished from larger drumbeat events on the basis of PNSN catalog magnitudes alone, because drumbeats tend to have long codas that yield overly large M_d values relative to magnitudes determined using amplitudes. We therefore arbitrarily define larger events as those post-October 2004 events with amplitudes large enough to clip on station HSR. Through the end of 2005 there were more than 290 larger earthquakes with a cumulative magnitude of M_d 4.4. Most events occurred in one of four temporal clusters: November 15, 2004–January 14, 2005; January 25–March 9, 2005; March 22–April 22, 2005; and July 15–December 31, 2005 (fig. 18). The first and third clusters occurred in association with the breakup of spines 3 and 4, respectively, and the fourth occurred in association with the breakup of spines 5 and 6. In contrast, the second cluster occurred during steady extrusion of spine 4. The ends of the first and second clusters coincided with explosions on January 18, 2005, and March 8, 2005, respectively. The largest number of events in a single day was 11 on March 27, 2005, when several events occurred within an hour of their predecessors, and the largest daily moment release occurred April 4, 2005. Both peaks occurred during the transition in locus of active extrusion from spine 4 to spine 5.

Despite their size, the larger earthquakes are similar in several ways to the drumbeat events. Like the drumbeats, they are classified as either LF or hybrid events. Roughly 40 percent have impulsive arrivals on most stations, and, like the drumbeats, many of the events with impulsive arrivals have most or all down first motions (appendix 1). Many of the impulsive larger earthquakes have higher frequencies at the

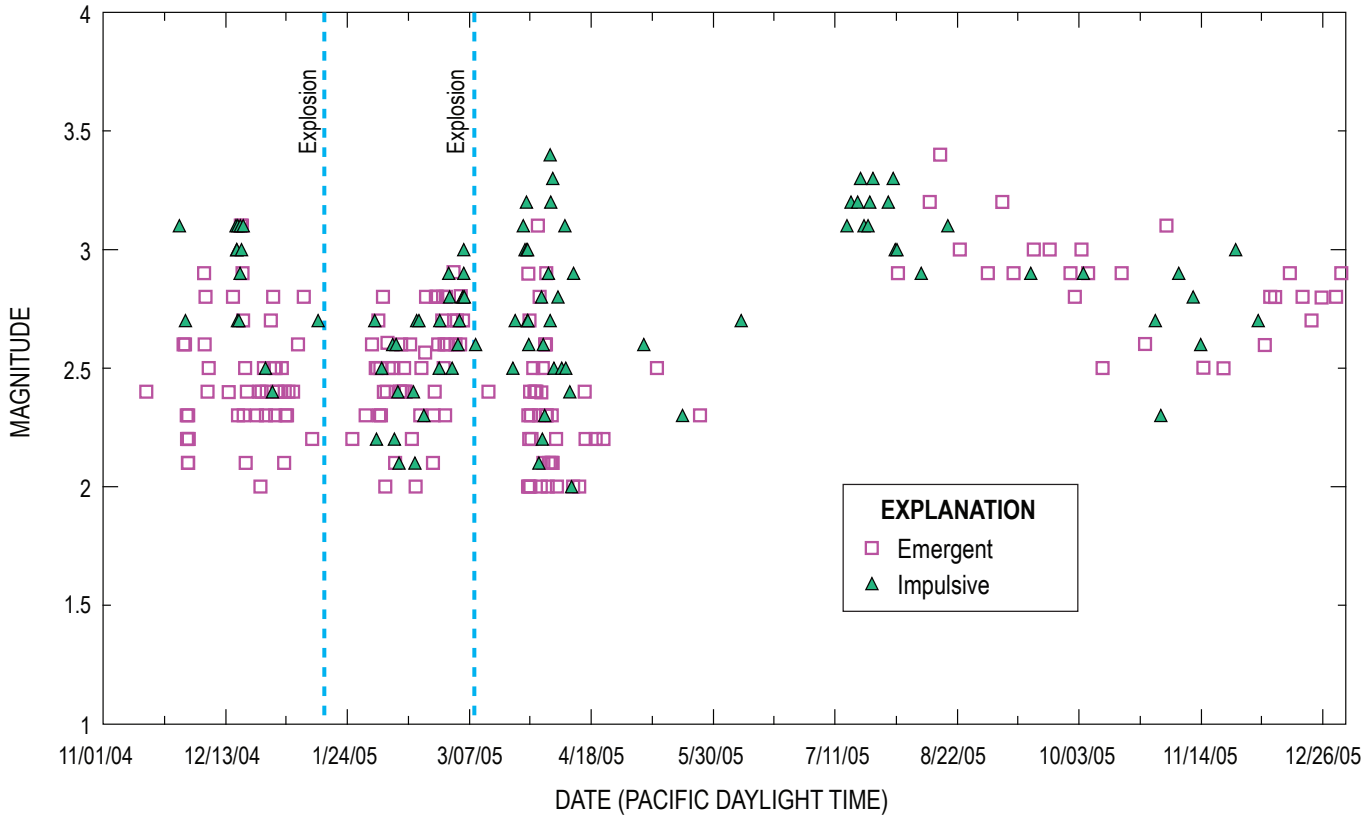

Figure 18. Plot showing occurrence of "big" earthquakes between November 1, 2004, and December 31, 2005. Green triangles correspond to impulsive events, hollow magenta squares to emergent events. Timing of two explosions on January 16 and March 8, 2005, are indicated by dashed blue lines.

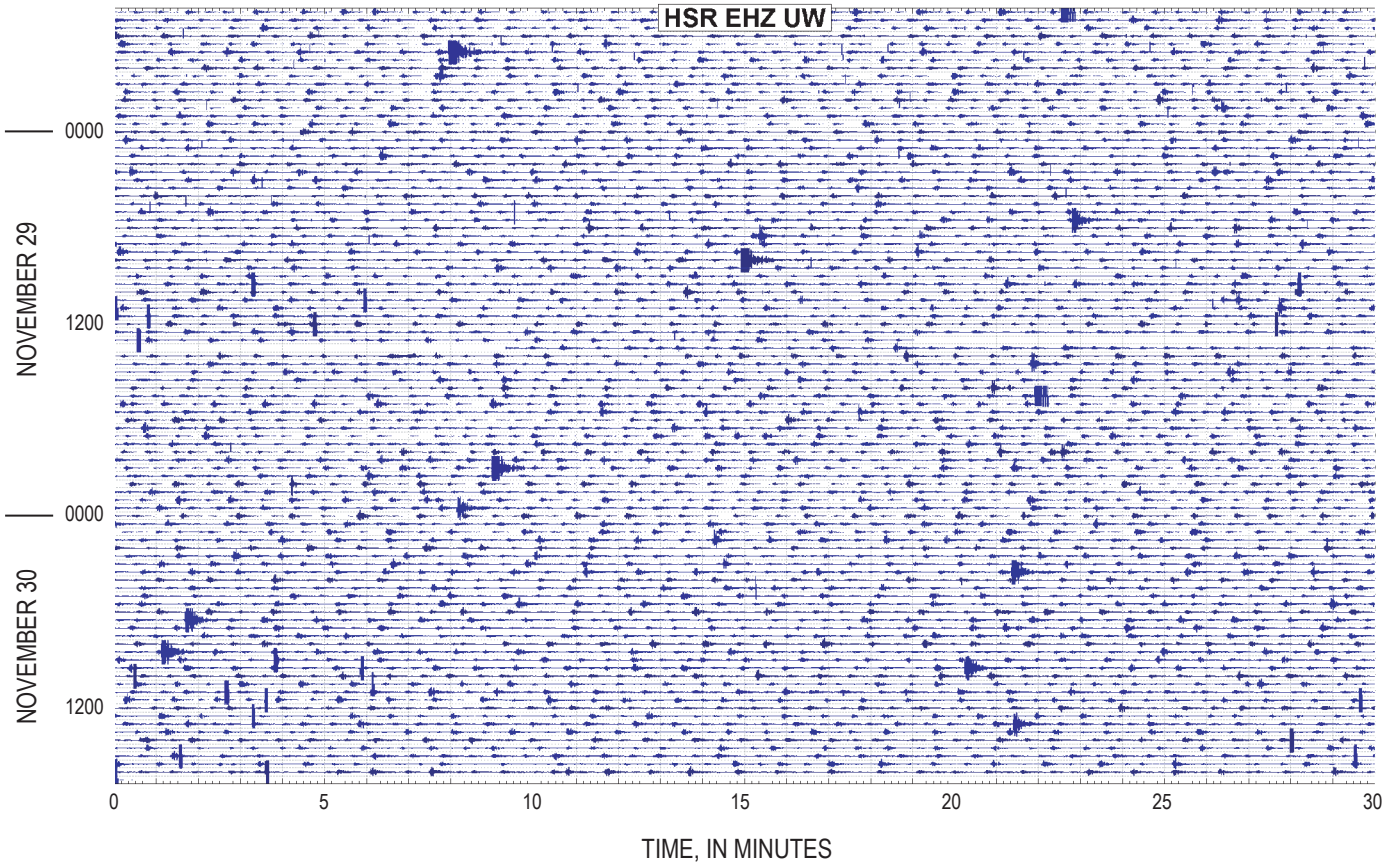

Figure 19. Seismic record from station HSR (see fig. 1) for 48 hours between 1700 PST on November 28 and 1700 PST on November 30, 2004, showing ten "big" earthquakes occurring along with regular drumbeats. Note that no change in drumbeat spacing or size occurs before or after the larger earthquakes, indicating that source processes are separate and distinct from one another.

start of the event and are classified as hybrid events, whereas the emergent events are dominantly LF events. Clipping of near-field sites makes event-family detection difficult, but on-scale recordings at broadband station JRO (~9 km from the vent; fig. 1) show that, although many of the larger events are dissimilar, there was at least one set of events occurring between December 2004 and April 2005 with similar waveforms (fig. 20). The similarity indicates not only that at least some of the larger earthquakes occurred in the same place with the same mechanism, but that the structure on which they occurred remained intact over a 4-month time span.

Spectra for drumbeats and the larger events are also similar. Figure 21 shows a set of waveforms and instrument-corrected spectra for a M_d 1.0 drumbeat and a M_d 3.0 "big" earthquake as recorded on stations plotted in order of distance from the earthquake. Spectra on all stations for both events have relatively flat curves for frequencies <1 Hz, a well-defined corner frequency at 1–2 Hz, and a ω^2 decrease in frequency content at higher frequencies, all characteristics of tectonic earthquake spectra (Brune, 1970). Horton and others (this volume, chap. 5) found similar characteristics for events recorded on their broadband network in 2004–5. Of particular note is the nearly identical corner frequency (F_c in fig. 21) of 1–2 Hz for all spectra, a frequency that is independent of distance and magnitude. One implication of this observation is that if the source is stick slip in nature, then the source duration is independent of source area. A source area independent of event size indicates that event magnitude is primarily a function of source displacement, rather than a combination of fault area and displacement as it is for tectonic earthquakes. This implies that the principal mechanical difference between drumbeats and "big" events is the amount of slip. If the earthquakes reflect stick-slip faulting within or at the periphery of the rising, rapidly solidifying magma plug (Iverson and others, 2006; Thelen and others, this volume, chap. 4; Iverson, this volume, chap. 21), then it is not surprising that the source area for these events is limited, because ruptures cannot propagate far outside of high-strain regions. The source duration of such a stick-slip event would then be a combination of the duration of motion of any part of the rupture surface and the area over which the rupture spreads, with the duration of this spreading being a function of the rupture velocity.

Locations for the impulsive larger events are more concentrated than drumbeat locations (fig. 22), although epicenters are still spread over an area 1 km by 1 km centered on the vent. Some of this scatter is likely due to changes in station

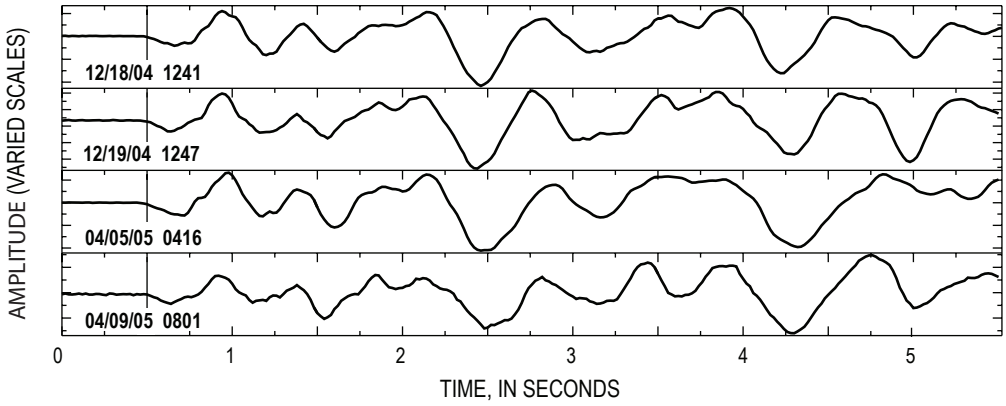

Figure 20. P-wave arrivals at broadband station JRO (fig. 1) for four "big" events occurring in December 2004 (upper two records) and April 2005 (lower two) with similar waveforms. Waveforms are scaled relative to the peak amplitude for each event. Although many "big" events do not have similar waveforms, the fact that some do indicates that these events on occasion occur at the same location with the same source mechanism. The 4-month time span between these four events also indicates that the structure on which these events occurred was not destroyed over that interval.

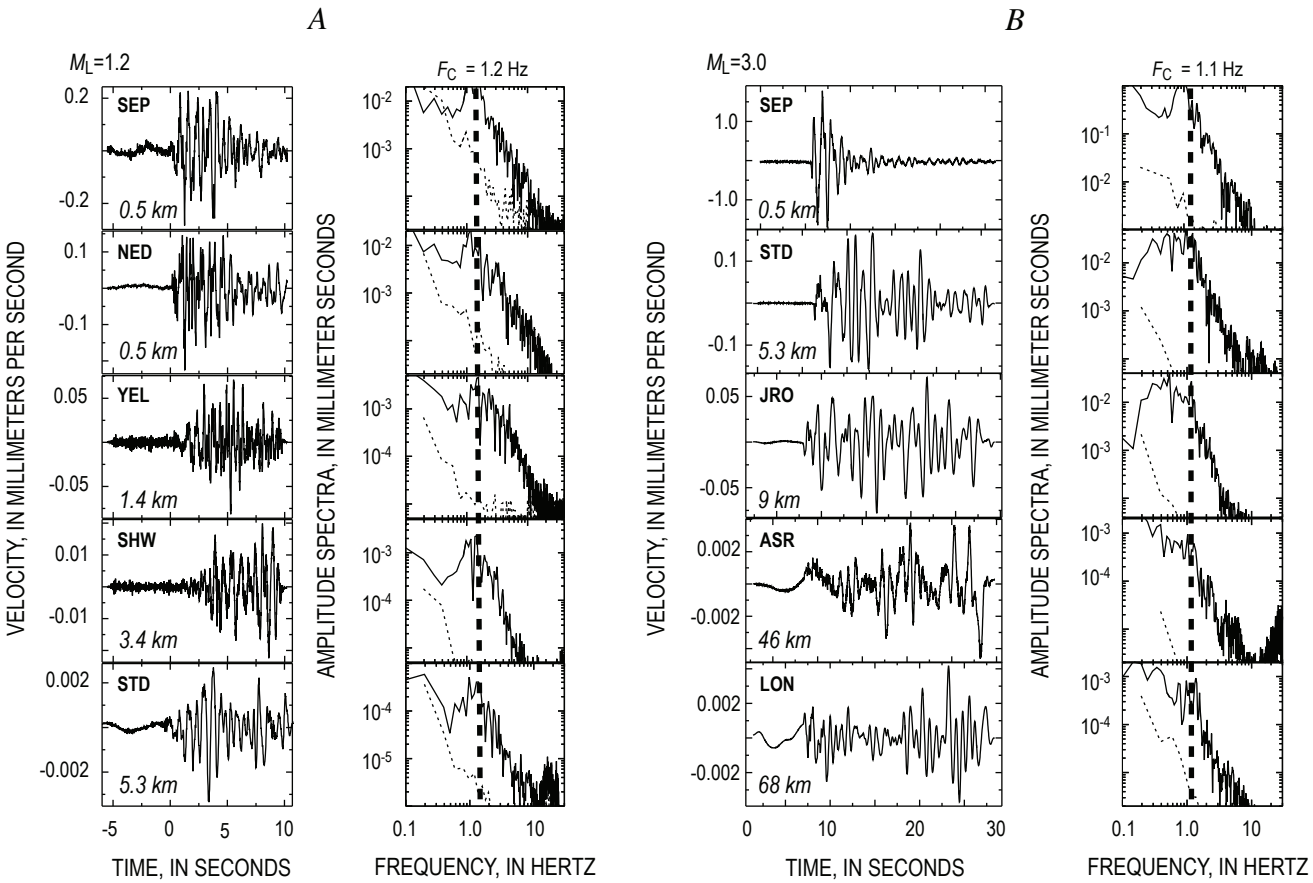

Figure 21. Instrument-corrected seismogram and frequency spectra for typical drumbeat (*A*) and "big" (*B*) seismic events. Stations are arranged in increasing distance from vent, with distance indicated for each station. All stations shown on location map (fig. 1) except ASR, located near Mount Adams, and LON, near Mount Rainier. Spectra are for 10.24-s windows starting with P-wave arrival. Thin dotted line below each spectral plot is noise estimate based on 10.24-s window taken before first arrival. Vertical thick dashed lines indicate corner frequencies (F_c) for each event. *A*, Drumbeat event, M_L 1.2, on August 20, 2005, at 1345 PDT. *B*, "Big" event, M_L 3.0, on March 26, 2005, at 1928 PST.

geometries and inaccuracies in the shallow velocity model (inaccuracies that, because of constantly changing velocity structure caused by the ongoing eruption, varied through time). Some scatter is also due to picking uncertainties, because arrival times, particularly on close-in stations, are difficult to pick to within ~0.1-s accuracy for all but the most impulsive events. However, some of the location scatter is real, the best evidence for which comes from differences in relative P-wave arrival times at stations placed close to the vent. As an example, figure 23 shows records on four crater stations from two events recorded ~9 hours apart on February 10 and 11, 2005. For the February 10 event, the P-wave arrived first at station BLIS (250 m east of the vent) and ~0.4 s later at AHAB (located 250 m southeast of the vent on top of spine 4); whereas for the February 11 event, the P wave arrived only 0.02 s later at AHAB. There was little change in relative P-wave arrivals at stations SEP and NED (~500 m north-northwest and ~500 m north-northeast of the vent, respectively). These patterns indicate that the February 11 event was located midway between AHAB and BLIS (350 m apart, including the altitude difference), whereas the February 10 event was located close to BLIS, a difference of as much as ~175 m (depending on P-wave velocities) between the two events. The 0.4-s difference in arrivals for the first event also implies remarkably low P-wave velocities (<1–2 km/s) at shallow depths, which is likely a result of AHAB and BLIS being placed on top of hot and highly fractured rock and crater-filling deposits (rockfall debris and ashfall deposits from the 1980 eruptions).

Hypotheses for the larger earthquake source include implosive-type mechanisms, fracturing of new rock (formation of new pathways to the surface), fracturing within spines before or after extrusion, and lurching of the active spine in a large-scale stick-slip event. Implosive mechanisms are consistent with all-down first-motion patterns observed for many of the impulsive events. However, none of these events occurred in association with explosions or significant degassing events. In addition, the extremely low levels of magmatic gases emanating from the vent (Gerlach and others, this volume, chap. 26) make it unlikely that sizable gas- or steam-filled cracks or pockets are able to accumulate below the surface and collapse to produce these events. We note, however, that Waite and others (2008) demonstrated that several events occurring in 2005 had a sig-

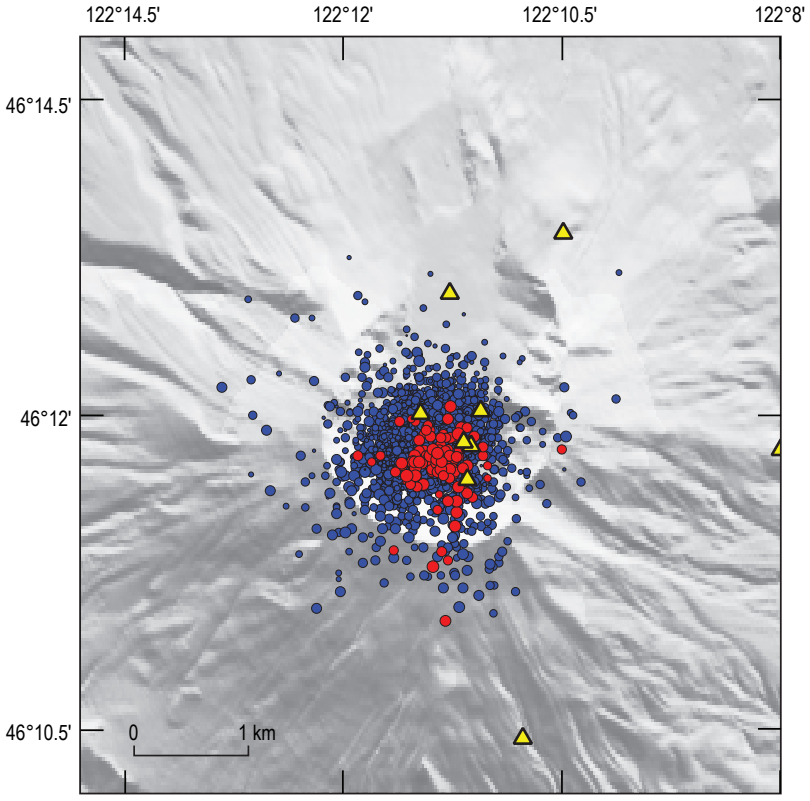

Figure 22. Map showing epicenters of drumbeat events (blue dots) and impulsive "big" events (red dots) occurring between November 1, 2004, and December 31, 2005. Dot sizes vary with magnitude. Drumbeat locations include events with P arrivals on at least seven stations, a nearest station within 2 km, and an azimuthal gap ≤135° (all impulsive "big" event locations meet these same criteria). Yellow triangles correspond to seismic station locations as of July 2005.

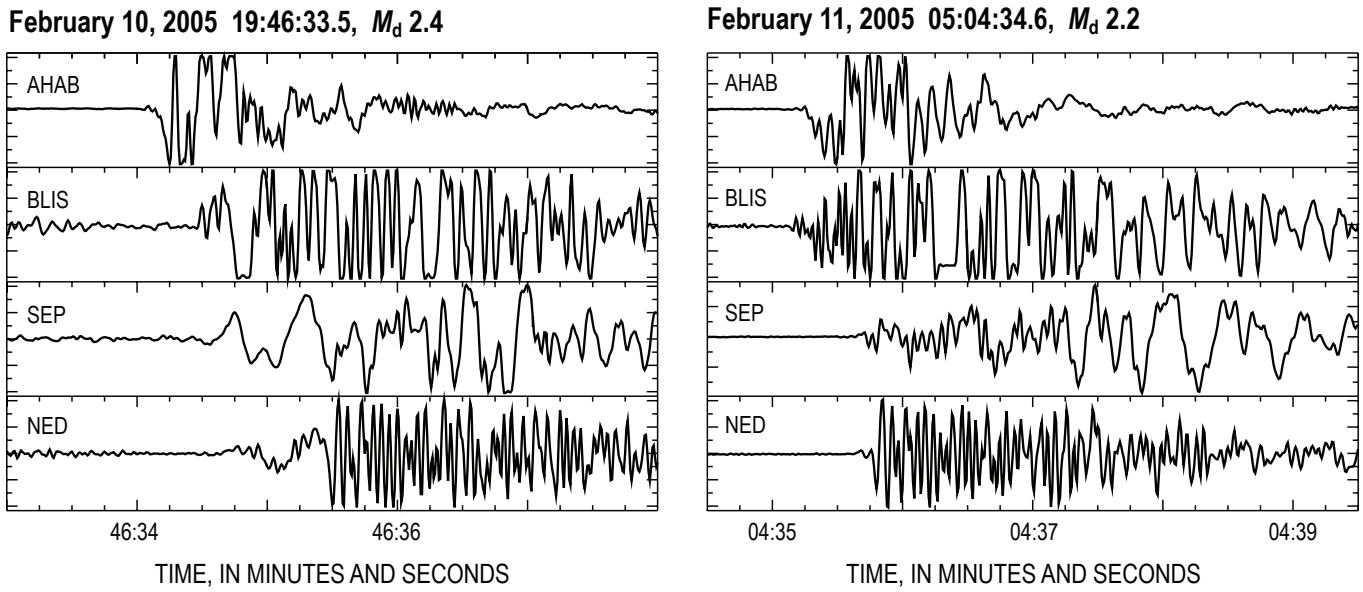

Figure 23. P-wave arrivals from two "big" earthquakes on four stations located within 0.5 km of vent (see fig. 1 for station locations). Note ~0.4-s difference in relative arrival times between stations AHAB and BLIS, indicating epicentral difference of more than one hundred meters for the two events.

nificant volumetric component, and they inferred that the source was a periodically collapsing, horizontal steam-filled crack.

Fracturing of new rock is also an unlikely process, as we would not expect to see repeating events or events with all-down first motions. Also, such a process would presumably not result in the emergent arrivals that we see at most stations in roughly half of the larger events. Fracturing within the spines is consistent with the observation that three of four large seismic-event clusters occur in association with the breakup of individual spines. However, events with all-down first motions are inconsistent with the observed failure mode in the spines, which occurred largely on shear, normal, and tensile fractures. Because the spines were, with one exception, higher than the seismometers, these failure modes would produce either a mixture of first motions or, in the case of normal faulting, dominantly up first motions. In addition, repetitive events spanning several months (and different spines) are incompatible with in-spine fracturing, because the fractures are destroyed in the spine breakup process.

Lurching of the active spine is our preferred hypothesis for the larger events. Lurches are consistent with shallow reverse faulting or upward thrusting of a piston that is indicated by the all-down first motions, as well as with long-lived event families. The fact that at least some events are located beneath the spine away from the vent indicates that they may have occurred along the interface between the base of the spine and the old crater floor. Because the 1980 crater floor is composed largely of ash and rockfall debris that fell from the crater walls in the years following the May 18, 1980, eruption, this interface likely is irregular and separates two poorly consolidated rock bodies. These lithologic and structural aspects could explain the emergent character of many larger seismic events and their low-frequency nature.

Volcano-Tectonic (VT) Earthquakes

Following the initial VT-rich days of the vent-clearing phase, VT events were a minor component of seismicity at Mount St. Helens. On a daily basis we scanned through seismic records in search of VT events, because we felt that VT events, especially those deeper than 2–3 km, might be an indicator either of a surge of new magma entering the system or adjustment of the magmatic system to magma withdrawal—and thus a potential harbinger of the eruption's end. VT events occurred as isolated events throughout the eruption and had small magnitudes (M_d <1), shallow (<2 km) depths, and epicenters similar to those for the drumbeats and larger events. The most notable occurrence of VT events was a swarm of more than 70 small (M_d <0.3) shallow earthquakes occurring between December 27, 2005, and January 4, 2006. The VT events in this swarm occurred independently of the low-frequency drumbeats, in some cases occurring just tens of seconds before or after a drumbeat (fig. 24). This swarm appears quite clearly in figure 13, as only the VT events were large enough to pass our amplitude threshold for the ESAM plot during this time period. Poor weather obscured the volcano from view during this interval, but tiltmeters located on the 1980–86 lava dome showed slight inflation while VT events were occurring, in contrast to deflation before and after (D. Sherrod and M. Lisowski, oral commun., 2006). Other periods of inflation, however, do not coincide with VT events, so we are uncertain whether this relation is coincidental. Given the lack of correspondence of VTs to any obvious changes in eruption dynamics or mechanics of extrusion, our best guess is that the VT events represent fracturing of more competent rock in the crater floor, such as basaltic andesite

lava flows from the Castle Creek period (2,200–1,895 yr B.P.) that underlie much of the 1980 crater (Clynne and others, this volume, chap. 28).

Summary—Patterns and Trends in Mount St. Helens seismicity, 2004–2005

In several intriguing ways the precursory seismic sequence of September 23 to early October 2004 was similar to those before the May 18, 1980, eruption and the 20 eruptions that followed during 1980–86. The 8-day-long interval between the first earthquakes and the first phreatic explosion on October 1, 2004, is close to the 7-day interval seen in March of 1980 (Endo and others, 1981; Malone and others, 1981), suggesting a characteristic time interval for magma to reach the surface once it begins to move. In addition, the transition from VT events to hybrid and LF events starting September 25, 2004, was broadly similar to transitions in event type seen before many of the dome-building eruptions in the 1980s (Malone, 1983). The occurrence of the event families, starting with the first significant family on September 26, 2004, is also similar to occurrence of event families before and during 1983–86 dome-building eruptions (Frémont and Malone, 1987), as well as to those in association with many other dome-building eruptions (for example, Okada and others, 1981; Power, 1988; Power and others, 1994; Villagómez, 2000; Rowe and others, 2004). In retrospect, the combination of event-type transition and occurrence of event families on September 25, 2004, could have given us an early indication of the expected nature of eruptive activity at Mount St. Helens, although that knowledge would likely not have changed how CVO and the PNSN reacted to the developing seismic crisis.

A summary observation from the September 29–October 5 period is that, of the hours-long increases in seismic intensity, only 4 of 12 occurred before explosions (fig. 9). Furthermore, seismic energy levels had stabilized at least an hour before two of the four explosions (October 1 and October 5). Thus we find no statistical basis for using short-term increases in RSAM or other measures of seismic energy to make short-term forecasts of explosive activity.

The drumbeats and “big” earthquakes associated with the dome-building eruption represent a relatively new type of seismicity at Mount St. Helens that, with a few exceptions, was not a dominant characteristic of 1980–86 seismicity. Efforts

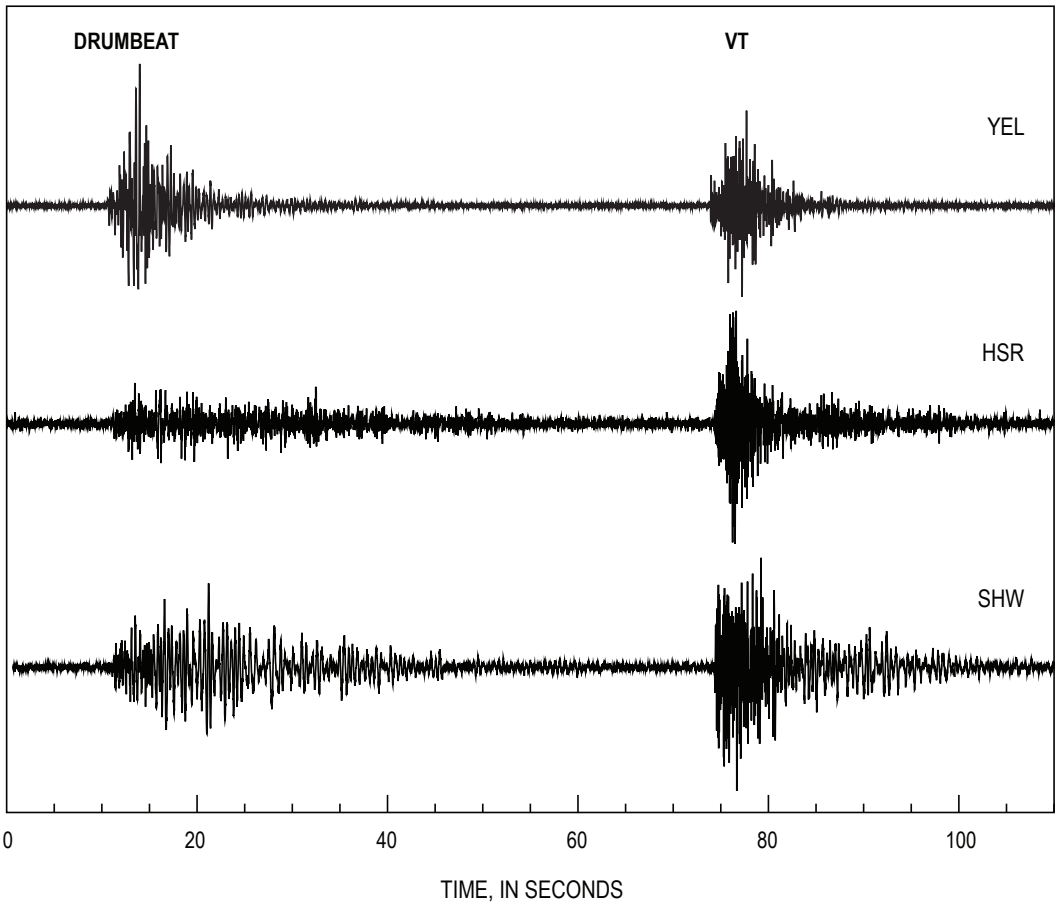

Figure 24. Seismograms from three stations for a drumbeat and a VT event occurring within 50 s of each other on December 29, 2005, at 1643 and 1644 PST, respectively. See figure 1 for station locations.

to characterize the nature of the drumbeat source are ongoing and likely will be the subject of research papers for years to come. Relatively new results with fascinating implications have already emerged from several field experiments run during 2004 and 2005, including the finding of infrasonic pulses associated with some drumbeats (Matoza and others, 2007) and the discovery of very long period (VLP) earthquakes in association with some of the larger drumbeats (Waite and others, 2008). These results provide evidence that processes operating at both deep (~500 m) and shallow (surface) levels are involved in the generation of drumbeats. The complexities in the relation between event spacing, event size, event spectra, and extrusion rate discussed in this paper, as well as in Thelen and others (this volume, chap. 4), further illustrate that the drumbeat source process is complex.

Finally, an important lesson that was reemphasized by the rapid escalation of seismicity during the first week of the eruption is that conditions can quickly become too dangerous to deploy additional seismometers after a volcano awakens. We were fortunate that the Mount St. Helens network installed in 1980–1983, particularly crater stations SEP (formerly REM) and YEL, was still in place and functional in 2004, because many of the events from the first two days were poorly recorded on stations outside of the crater. As the seismic crisis progressed, however, the limited dynamic range of the short-period analog stations was frequently exceeded at seismometers in the crater and on the flanks, resulting in lost information about seismic energy, spectral content, and event similarity. In addition, the absence of broadband three-component instruments in the crater meant that information was lost about the presence or absence of very low frequency signals and about source mechanisms for all types of events. As discussed by McChesney and others (this volume, chap. 7), seismicity intensified so rapidly during the first several days that we were unable to safely install such instruments in the crater. An important goal for seismic monitoring networks at any potentially active volcano should be to have seismometers, including broadband seismometers, installed at locations close to the presumed vent well before unrest begins.

Acknowledgments

The number of people involved in the seismic response to the renewed eruption in 2004–5 was huge, and it is impossible to give proper credit to all who helped us. Peggy Johnson, Josh Jones, Ruth Ludwin, Wendy McCausland, Karen Meagher, Guy Medema, Bob Norris, Bill Steele, George Thomas, and Tom Yelin all played critical roles in the PNSN/CVO seismic monitoring team, particularly with the immense tasks of data processing, production of Web graphics, around-the-clock monitoring of seismicity in the first several months of the eruption, and troubleshooting hardware problems brought on by the immense amount of seismic data and Web traffic. Marv Couchman, Rick LaHusen, Andy Lockhart, Jeff Marso, Pat McChesney, and Tim Plucinski all played critical roles in developing and installing new seismic and telemetry systems on and around the volcano, and we are extremely grateful to each of them for the many hours they devoted to improving real-time seismic monitoring at the volcano. Wendy McCausland calculated reduced displacement estimates for the October 2 and October 3 tremor episodes, and Bob Norris assisted with overnight shifts at CVO for more than a month, provided logistical support in the field, and was the first to recognize the similarity between 2004 drumbeats and “peppercorn” events seen in the 1980s.

We are grateful to Peter Cervelli for providing invaluable assistance in the drafting of all figures showing multiday seismic records and to Dave Ramsey for providing us with the station map showing crater station locations superimposed on the April 19, 2005, DEM in figure 1. We thank Jeff Johnson for his assistance with event-family identification during the first several weeks of the eruption and Helena Buurman for her assistance in processing and error-checking the results from our earthquake detection algorithm. We also thank Phil Dawson, John Power, Stephanie Prejean, and Randy White for their contributions to analysis and discussions of the significance of seismicity during the first critical weeks of renewed activity, for forming invaluable bridges to other researchers in the volcano seismology community when we were too busy to do so, and for providing greatly appreciated moral support during the first incredibly hectic weeks of the eruption. Finally, we are grateful to Charlotte Rowe and Randy White for thorough reviews that significantly improved this paper.

References Cited

Barker, S.E., and Malone, S.D., 1991, Magmatic system geometry at Mount St. Helens modeled from the stress field associated with posteruptive earthquakes: Journal of Geophysical Research, v. 96, no. B7, p. 11883–11894, doi:10.1029/91JB00430.

Bender, B., 1983, Maximum likelihood estimation of *b* values for magnitude grouped data: Bulletin of the Seismological Society of America, v. 73, p. 831–851.

Brune, J.N., 1970, Tectonic stress and the spectra of seismic shear waves from earthquakes: Journal of Geophysical Research, v. 75, no. 23, p. 4997–5009.

Chouet, B.A., 1996, Long-period volcano seismicity; its source and use in eruption forecasting: Nature, v. 380, p. 309–316.

Clynne, M.A., Calvert, A.T., Wolfe, E.W., Evarts, R.C., Fleck, R.J., and Lanphere, M.A., 2008, The Pleistocene eruptive history of Mount St. Helens, Washington, from 300,000 to 12,800 years before present, chap. 28 *of* Sherrod, D.R., Scott, W.E., and Stauffer, P.H., eds., A volcano rekindled;

the renewed eruption of Mount St. Helens, 2004–2006: U.S. Geological Survey Professional Paper 1750 (this volume).

Dzurisin, D., Vallance, J.W., Gerlach, T.M., Moran, S.C., and Malone, S.D., 2005, Mount St. Helens reawakens: Eos (American Geophysical Union Transactions), v. 86, no. 3, p. 25, 29.

Dzurisin, D., Lisowski, M., Poland, M.P., Sherrod, D.R., and LaHusen, R.G., 2008, Constraints and conundrums resulting from ground-deformation measurements made during the 2004–2005 dome-building eruption of Mount St. Helens, Washington, chap. 14 *of* Sherrod, D.R., Scott, W.E., and Stauffer, P.H., eds., A volcano rekindled; the renewed eruption of Mount St. Helens, 2004–2006: U.S. Geological Survey Professional Paper 1750 (this volume).

Endo, E.T., and Murray, T., 1991, Real-time seismic amplitude measurement (RSAM): a volcano monitoring and prediction tool: Bulletin of Volcanology, v. 53, no. 7, p. 533–545.

Endo, E.T., Dzurisin, D., and Swanson, D.A., 1990, Geophysical and observational constraints for ascent rates of dacitic magma at Mount St. Helens, *in* Ryan, M.P., ed., Magma transport and storage: New York, John Wiley, p. 317–334.

Endo, E.T., Malone, S.D., Noson, L.L., and Weaver, C.S., 1981, Locations, magnitudes, and statistics of the March 20–May 18 earthquake sequence, *in* Lipman, P.W., and Mullineaux, D.R., eds., The 1980 eruptions of Mount St. Helens, Washington: U.S. Geological Survey Professional Paper 1250, p. 93–107.

Fehler, M., 1985, Locations and spectral properties of earthquakes accompanying an eruption of Mount St. Helens: Journal of Geophysical Research, v. 90, p. 12729–12740.

Fehler, M., and Chouet, B.A., 1982, Operation of a digital seismic network on Mount St. Helens volcano and observations of long-period seismic events that originate under the volcano: Geophysical Research Letters, v. 9, no. 9, p. 1017–1020.

Frémont, M.J., and Malone, S.D., 1987, High precision relative locations of earthquakes at Mount St. Helens, Washington: Journal of Geophysical Research, v. 92, no. B10, p. 10223–10236.

Gerlach, T.M., McGee, K.A., and Doukas, M.P., 2008, Emission rates of CO_2, SO_2, and H_2S, scrubbing, and preeruption excess volatiles at Mount St. Helens, 2004–2005, chap. 26 *of* Sherrod, D.R., Scott, W.E., and Stauffer, P.H., eds., A volcano rekindled; the renewed eruption of Mount St. Helens, 2004–2006: U.S. Geological Survey Professional Paper 1750 (this volume).

Giampiccolo, E., Musumeci, C., Malone, S.D., Gresta, S., and Privitera, E., 1999, Seismicity and stress-tensor inversion in the central Washington Cascades mountains: Journal of Geophysical Research, v. 89, p. 811–821.

Harrington, R.M., and Brodsky, E.E., 2006, The Mount St. Helens hybrid earthquakes; stick-slip or resonating pipes [abs]: Eos (American Geophysical Union Transactions), v. 87, Fall Meeting Supplement, V52A-02.

Herriott, T.M., Sherrod, D.R., Pallister, J.S., and Vallance, J.W., 2008, Photogeologic maps of the 2004–2005 Mount St. Helens eruption, chap. 10 *of* Sherrod, D.R., Scott, W.E., and Stauffer, P.H., eds., A volcano rekindled; the renewed eruption of Mount St. Helens, 2004–2006: U.S. Geological Survey Professional Paper 1750 (this volume).

Horton, S.P., Norris, R.D., and Moran, S.C., 2008, Broadband characteristics of earthquakes recorded during a dome-building eruption at Mount St. Helens, Washington, between October 2004 and May 2005, chap. 5 *of* Sherrod, D.R., Scott, W.E., and Stauffer, P.H., eds., A volcano rekindled; the renewed eruption of Mount St. Helens, 2004–2006: U.S. Geological Survey Professional Paper 1750 (this volume).

Iverson, R.M., 2008, Dynamics of seismogenic volcanic extrusion resisted by a solid surface plug, Mount St. Helens, 2004–2005, chap. 21 *of* Sherrod, D.R., Scott, W.E., and Stauffer, P.H., eds., A volcano rekindled; the renewed eruption of Mount St. Helens, 2004–2006: U.S. Geological Survey Professional Paper 1750 (this volume).

Iverson, R.M., Dzurisin, D., Gardner, C.A., Gerlach, T.M., LaHusen, R.G., Lisowski, M., Major, J.J., Malone, S.D., Messerich, J.A., Moran, S.C., Pallister, J.S., Qamar, A.I., Schilling, S.P., and Vallance, J.W., 2006, Dynamics of seismogenic volcanic extrusion at Mount St. Helens in 2004–05: Nature, v. 444, no. 7118, p. 439–443, doi:10.1038/nature05322.

Jonientz-Trisler, C., Myers, B., and Power, J.A., 1994, Seismic identification of gas-and-ash explosions at Mount St. Helens—capabilities, limitations, and regional applications, *in* Casadevall, T.J., ed., Volcanic ash and aviation safety; proceedings of the First International Symposium on Volcanic Ash and Aviation Safety: U.S. Geological Survey Bulletin 2047, p. 351–356.

Lahr, J.C., Chouet, B.A., Stephens, C.D., Power, J.A., and Page, R.A., 1994, Earthquake classification, location, and error analysis in a volcanic environment; implications for the magmatic system of the 1989–1990 eruptions at Redoubt Volcano, Alaska: Journal of Volcanology and Geothermal Research, v. 62, nos. 1–4, p. 137–151, doi:10.1016/0377-0273(94)90031-0.

Lees, J.M., 1992, The magma system of Mount St. Helens: non-linear high-resolution P-wave tomography: Journal of Volcanology and Geothermal Research, v. 53, nos. 1–4, p. 103–116.

Lees, J.M., and Crosson, R.S., 1989, Tomographic inversion

for three-dimensional velocity structure at Mount St. Helens using earthquake data: Journal of Geophysical Research, v. 94, p. 5716–5728.

MacCarthy, J.K., and Rowe, C.A., 2005, Automatic scanning detection for characterization of dome-related seismic swarms at Mount St. Helens and their evolution through time [abs]: Eos (American Geophysical Union Transactions), v. 86, Fall Meeting Supplement, V53D-1591.

Major, J.J., Kingsbury, C.G., Poland, M.P., and LaHusen, R.G., 2008, Extrusion rate of the Mount St. Helens lava dome estimated from terrestrial imagery, November 2004–December 2005, chap. 12 *of* Sherrod, D.R., Scott, W.E., and Stauffer, P.H., eds., A volcano rekindled; the renewed eruption of Mount St. Helens, 2004–2006: U.S. Geological Survey Professional Paper 1750 (this volume).

Malone, S.D., 1983, Volcanic earthquakes; examples from Mount St. Helens, *in* Earthquakes—observations, theory and interpretation: Bologna, Italy, Società Italiana di Fisica, p. 436–455.

Malone, S.D., Endo, E.T., Weaver, C.S., and Ramey, J.W., 1981, Seismic monitoring for eruption prediction, *in* Lipman, P.W., and Mullineaux, D.R., eds., The 1980 eruptions of Mount St. Helens, Washington: U.S. Geological Survey Professional Paper 1250, p. 803–813.

Malone, S.D., Boyko, C., and Weaver, C.S., 1983, Seismic precursors to the Mount St. Helens eruptions in 1981 and 1982: Science, v. 221, p. 1376–1378.

Mastin, L.G., 1994, Explosive tephra emissions at Mount St. Helens, 1989–1991; the violent escape of magmatic gas following storms?: Geological Society of America Bulletin, v. 106, no. 2, p. 175–185.

Mastin, L.G., Roeloffs, E., Beeler, N.M., and Quick, J.E., 2008, Constraints on the size, overpressure, and volatile content of the Mount St. Helens magma system from geodetic and dome-growth measurements during the 2004–2006+ eruption, chap. 22 *of* Sherrod, D.R., Scott, W.E., and Stauffer, P.H., eds., A volcano rekindled; the renewed eruption of Mount St. Helens, 2004–2006: U.S. Geological Survey Professional Paper 1750 (this volume).

Matoza, R.S., Hedlin, M.A.H., and Garcés, M.A., 2007, An infrasound array study of Mount St. Helens: Journal of Volcanology and Geothermal Research, v. 160, p. 249–262, doi:10.1016/j.jvolgeores.2006.10.006.

McChesney, P.J., Couchman, M.R., Moran, S.C., Lockhart, A.B., Swinford, K.J., and LaHusen, R.G., 2008, Seismic-monitoring changes and the remote deployment of seismic stations (seismic spider) at Mount St. Helens, 2004–2005, chap. 7 *of* Sherrod, D.R., Scott, W.E., and Stauffer, P.H., eds., A volcano rekindled; the renewed eruption of Mount St. Helens, 2004–2006: U.S. Geological Survey Professional Paper 1750 (this volume).

Mogi, K., 1962, Magnitude-frequency relation for elastic shocks accompanying fractures of various materials and some related problems in earthquakes: Bulletin of the Earthquake Research Institute, v. 40, p. 831–853.

Moran, S.C., 1994, Seismicity at Mount St. Helens, 1987–1992; evidence for repressurization of an active magmatic system: Journal of Geophysical Research, v. 99, no. B3, p. 4341–4354, doi:10.1029/93JB02993.

Moran, S.C., and Malone, S.D., 2004, Seismicity associated with the first month of the 2004 eruption of Mount St. Helens [abs]: Eos (American Geophysical Union Transactions), v. 85, Fall Meeting Supplement, V31E-02.

Moran, S.C., Lees, J.M., and Malone, S.D., 1999, P-wave crustal velocity structure in the greater Mount Rainier area from local earthquake tomography: Journal of Geophysical Research, v. 104, p. 10775–10786.

Moran, S.C., McChesney, P.J., and Lockhart, A.B., 2008, Seismicity and infrasound associated with explosions at Mount St. Helens, 2004–2005, chap. 6 *of* Sherrod, D.R., Scott, W.E., and Stauffer, P.H., eds., A volcano rekindled; the renewed eruption of Mount St. Helens, 2004–2006: U.S. Geological Survey Professional Paper 1750 (this volume).

Musumeci, C., Gresta, S., and Malone, S.D., 2002, Magma system recharge of Mount St. Helens from precise relative hypocenter location of microearthquakes: Journal of Geophysical Research, v. 107, no. B10, 2264, p. ESE 16-1–ESE 16-9, doi:10.1029/2001JB000629.

Neuberg, J.W., Tuffen, H., Collier, L., Green, D., Powell, T., and Dingwell, D., 2006, The trigger mechanism of low-frequency earthquakes on Montserrat: Journal of Volcanology and Geothermal Research, v. 153, nos. 1–2, p. 37–50, doi:10.1016/j.jvolgeores.2005.08.00.

Norris, R.D., 1994, Seismicity of rockfalls and avalanches at three Cascade Range volcanoes; implications for seismic detection of hazardous mass movements: Bulletin of the Seismological Society of America, v. 84, p. 1925–1939.

Okada, H., Watanabe, H. Yamashita, H., and Yokoyama, I., 1981, Seismological significance of the 1977–1978 eruptions and the magma intrusion process of Usu Volcano, Hokkaido: Journal of Volcanology and Geothermal Research, v. 9, p. 311–334.

Pallister, J.S., Hoblitt, R.P., Crandell, D.R., and Mullineaux, D.R., 1992, Mount St. Helens a decade after the 1980 eruptions; magmatic models, chemical cycles, and a revised hazards assessment: Bulletin of Volcanology, v. 54, no. 2, p. 126–146, doi: 10.1007/BF00278003.

Poland, M.P., and Lu, Z., 2008, Radar interferometry observations of surface displacements during pre- and coeruptive

periods at Mount St. Helens, Washington, 1992–2005, chap. 18 *of* Sherrod, D.R., Scott, W.E., and Stauffer, P.H., eds., A volcano rekindled; the renewed eruption of Mount St. Helens, 2004–2006: U.S. Geological Survey Professional Paper 1750 (this volume).

Power, J.A., 1988, Seismicity associated with the 1986 eruption of Augustine Volcano, Alaska: Fairbanks, University of Alaska, M.S. thesis, 142 p.

Power, J.A., Lahr, J.C., Page, R.A., Chouet, B.A., Stephens, C.D., Harlow, D.H., Murray, T.L., and Davies, J.N., 1994, Seismic evolution of the 1989–1990 eruption sequence of Redoubt Volcano, Alaska: Journal of Volcanology and Geothermal Research, v. 62, p. 69–94.

Qamar, A.I., St. Lawrence, W., Moore, J.N., and Kendrick, G., 1983, Seismic signals preceding the explosive eruption of Mount St. Helens, Washington, on 18 May 1980: Bulletin of the Seismological Society of America, v. 73, p. 1797–1813.

Qamar, A.I., Malone, S.D., Moran, S.C., Steele, W.P., and Thelen, W.A., 2008, Near-real-time information products for Mount St. Helens—tracking the ongoing eruption, chap. 3 *of* Sherrod, D.R., Scott, W.E., and Stauffer, P.H., eds., A volcano rekindled; the renewed eruption of Mount St. Helens, 2004–2006: U.S. Geological Survey Professional Paper 1750 (this volume).

Reasenberg, P.A., and Oppenheimer, D., 1985, FPFIT, FPPLOT, and FPPAGE: FORTRAN computer programs for calculating and plotting earthquake fault-plane solutions: U.S. Geological Survey Open-File Report 85–739, 109 p.

Rowe, C.A., Thurber, C.H., and White, R.A., 2004, Dome growth behavior at Soufriere Hills Volcano, Montserrat, revealed by relocation of volcanic event swarms, 1995–1996: Journal of Volcanology and Geothermal Research, v. 134, no. 3, p. 199–221.

Scandone, R., and Malone, S.D., 1985, Magma supply, magma discharge, and readjustment of the feeding system of Mount St. Helens during 1980: Journal of Volcanology and Geothermal Research, v. 23, nos. 3–4, p. 239–262, doi:10.1016/0377-0273(85)90036-8.

Schilling, S.P., Thompson, R.A., Messerich, J.A., and Iwatsubo, E.Y., 2008, Use of digital aerophotogrammetry to determine rates of lava dome growth, Mount St. Helens, Washington, 2004–2005, chap. 8 *of* Sherrod, D.R., Scott, W.E., and Stauffer, P.H., eds., A volcano rekindled; the renewed eruption of Mount St. Helens, 2004–2006: U.S. Geological Survey Professional Paper 1750 (this volume).

Schneider, D.J., Vallance, J.W., Wessels, R.L., Logan, M., and Ramsey, M.S., 2008, Use of thermal infrared imaging for monitoring renewed dome growth at Mount St. Helens, 2004, chap. 17 *of* Sherrod, D.R., Scott, W.E., and Stauffer, P.H., eds., A volcano rekindled; the renewed eruption of Mount St. Helens, 2004–2006: U.S. Geological Survey Professional Paper 1750 (this volume).

Scott, W.E., Sherrod, D.R., and Gardner, C.A., 2008, Overview of the 2004 to 2006, and continuing, eruption of Mount St. Helens, Washington, chap. 1 *of* Sherrod, D.R., Scott, W.E., and Stauffer, P.H., eds., A volcano rekindled; the renewed eruption of Mount St. Helens, 2004–2006: U.S. Geological Survey Professional Paper 1750 (this volume).

Shemeta, J., and Weaver, C.S., 1986, Seismicity accompanying the May 18, 1980, eruption of Mount St. Helens, Washington, *in* Keller, S.A.C., ed., Mount St. Helens, five years later: Cheney, Wash., Eastern Washington University Press, p. 44–58.

Swanson, D.A., and Holcomb, R.T., 1990, Regularities in growth of the Mount St. Helens dacite dome, 1980–1986, *in* Fink, J.H., ed., Lava flows and domes, emplacement mechanisms and hazard implications: Berlin, Springer-Verlag, International Association of Volcanology and Chemistry of the Earth's Interior, Proceedings in Volcanology 2, p. 3–24.

Swanson, D.A., Casadevall, T.J., Dzurisin, D., Malone, S.D., Newhall, C.G., and Weaver, C.S., 1983, Predicting eruptions at Mount St. Helens, June 1980 through December 1982: Science, v. 221, no. 4618, p. 1369–1376.

Swanson, D.A., Casadevall, T.J., Dzurisin, D., Malone, S.D., Holcomb, R.T., Newhall, C.G., and Weaver, C.S., 1985, Forecasts and predictions of eruptive activity at Mount St. Helens, USA; 1975–1984: Journal of Geodynamics, v. 3, p. 397–423.

Thelen, W.A., Crosson, R.S., and Creager, K.C., 2008, Absolute and relative locations of earthquakes at Mount St. Helens, Washington, using continuous data; implications for magmatic processes, chap. 4 *of* Sherrod, D.R., Scott, W.E., and Stauffer, P.H., eds., A volcano rekindled; the renewed eruption of Mount St. Helens, 2004–2006: U.S. Geological Survey Professional Paper 1750 (this volume).

Vallance, J.W., Schneider, D.J., and Schilling, S.P., 2008, Growth of the 2004–2006 lava-dome complex at Mount St. Helens, Washington, chap. 9 *of* Sherrod, D.R., Scott, W.E., and Stauffer, P.H., eds., A volcano rekindled; the renewed eruption of Mount St. Helens, 2004–2006: U.S. Geological Survey Professional Paper 1750 (this volume).

Villagómez, D., 2000, Sismícidad del volcán Guagua Pichincha 1998–1999: Quito, Ecuador, Escuela Politécnica Nacional, M.S. thesis.

Vinciguerra, S., Gresta, S., Barbano, M.S., and Distefano, G., 2001, The two behaviours of Mt. Etna Volcano before and after a large intrusive episode; evidences from *b* value and fractal dimension of seismicity: Geophysical Research Letters, v. 28, p. 2257–2260.

Waite, G.P., Chouet, B.A. and Dawson, P.B., 2008, Eruption dynamics at Mount St. Helens imaged from broadband seismic waveforms; interaction of the shallow magmatic and hydrothermal systems: Journal of Geophysical Research, v. 113, B02305, 22 p., doi:10.1029/2007JB005259.

Walder, J.S., Schilling, S.P., Vallance, J.W., and LaHusen, R.G., 2008, Effects of lava-dome growth on the Crater Glacier of Mount St. Helens, Washington, chap. 13 *of* Sherrod, D.R., Scott, W.E., and Stauffer, P.H., eds., A volcano rekindled; the renewed eruption of Mount St. Helens, 2004–2006: U.S. Geological Survey Professional Paper 1750 (this volume).

Weaver, C.S., Grant, W.G., Malone, S.D., and Endo, E.T., 1981, Post-May 18 seismicity; volcanic and tectonic implications, *in* Lipman, P.W., and Mullineaux, D.R., eds., The 1980 eruptions of Mount St. Helens, Washington: U.S. Geological Survey Professional Paper 1250, p. 109–121.

Weaver, C.S., Zollweg, J.E., and Malone, S.D., 1983, Deep earthquakes beneath Mount St. Helens; evidence for magmatic gas transport?: Science, v. 221, p. 1391–1394.

Weaver, C.S., Grant, W.C., and Shemeta, J.E., 1987, Local crustal extension at Mount St. Helens, Washington: Journal of Geophysical Research, v. 92, no. B10, p. 10170–10178.

Wiemer, S., and McNutt, S.R., 1997, Variations in the frequency-magnitude distribution with depth in two volcanic areas—Mount St. Helens, Washington, and Mt. Spurr, Alaska: Geophysical Research Letters, v. 24, p. 189–192.

Appendix 1. PNSN Fault-Plane Solutions, 09/23/04–12/31/05

This appendix comprises numerous plots showing first motions and preferred fault-plane solutions for well-constrained events (maximum azimuthal gap <135°, nearest station <1 km, and at least 10 picked phase arrivals) (fig. 25) in the PNSN catalog from September 24 to November 27, 2004, and for "big" events from November 27, 2004 to December 31, 2005 (fig. 26). We did not review fault-plane solutions from the PNSN catalog except those for the "big" events. Only those fault-plane solutions with at least 10 polarities are shown. Note that all fault-plane solution times are in Coordinated Universal Time (UTC), in contrast to the local time convention used in the rest of this paper. All fault-plane solutions were determined using the FPFIT computer program (Reasenberg and Oppenheimer, 1985).

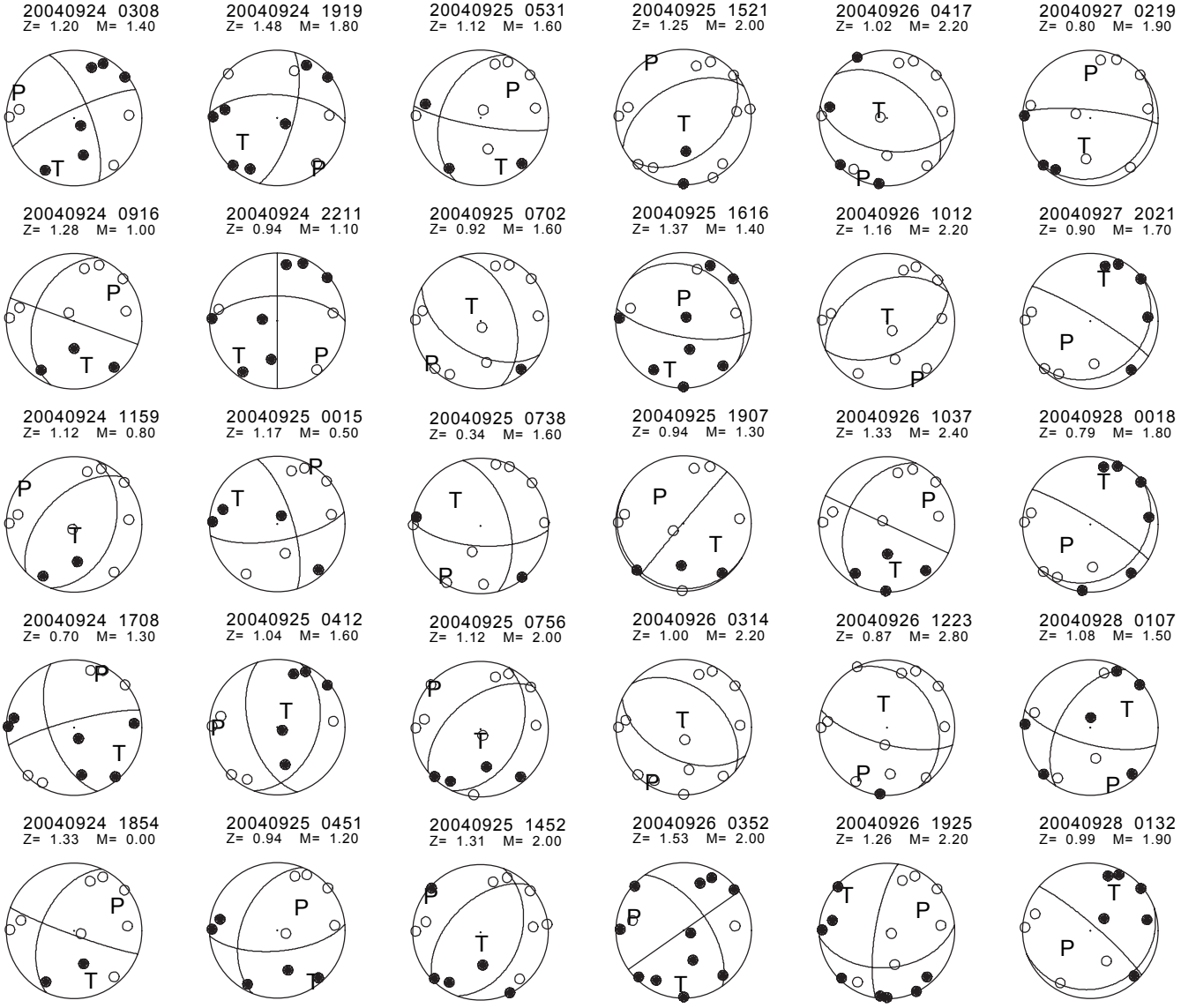

Figure 25. Fault-plane solutions for 161 earthquakes occurring at Mount St. Helens during the period from Sept. 24 to Oct. 11, 2004. P, compressional axis; T, tensional axis. Open circles correspond to dilatational (down) first motions, closed circles to compressional (up) first motions. Each solution is coded for date and time (UTC) in this format: YYYYMMDD hhmm. Z, depth, in kilometers; M, magnitude.

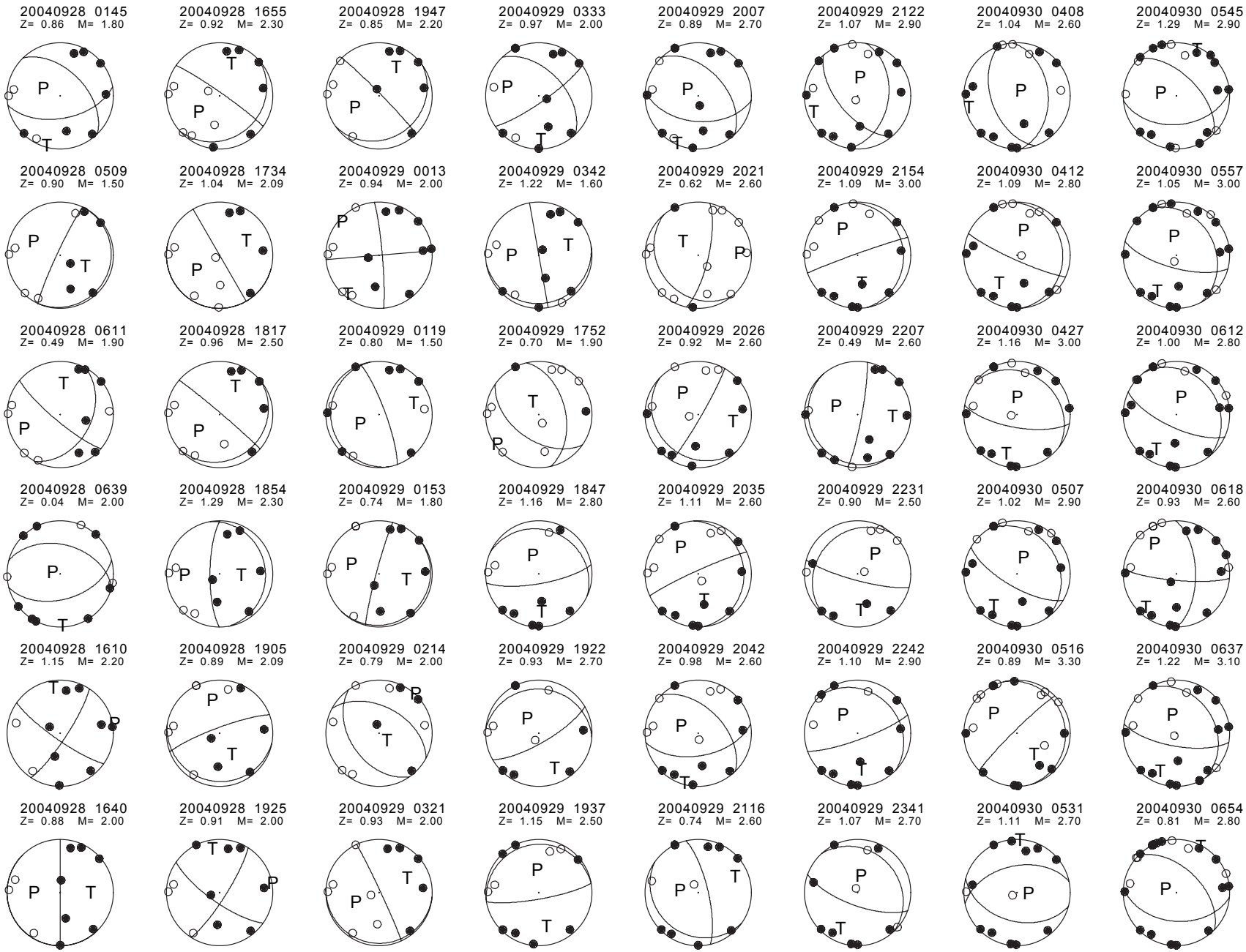

Figure 25—Continued.

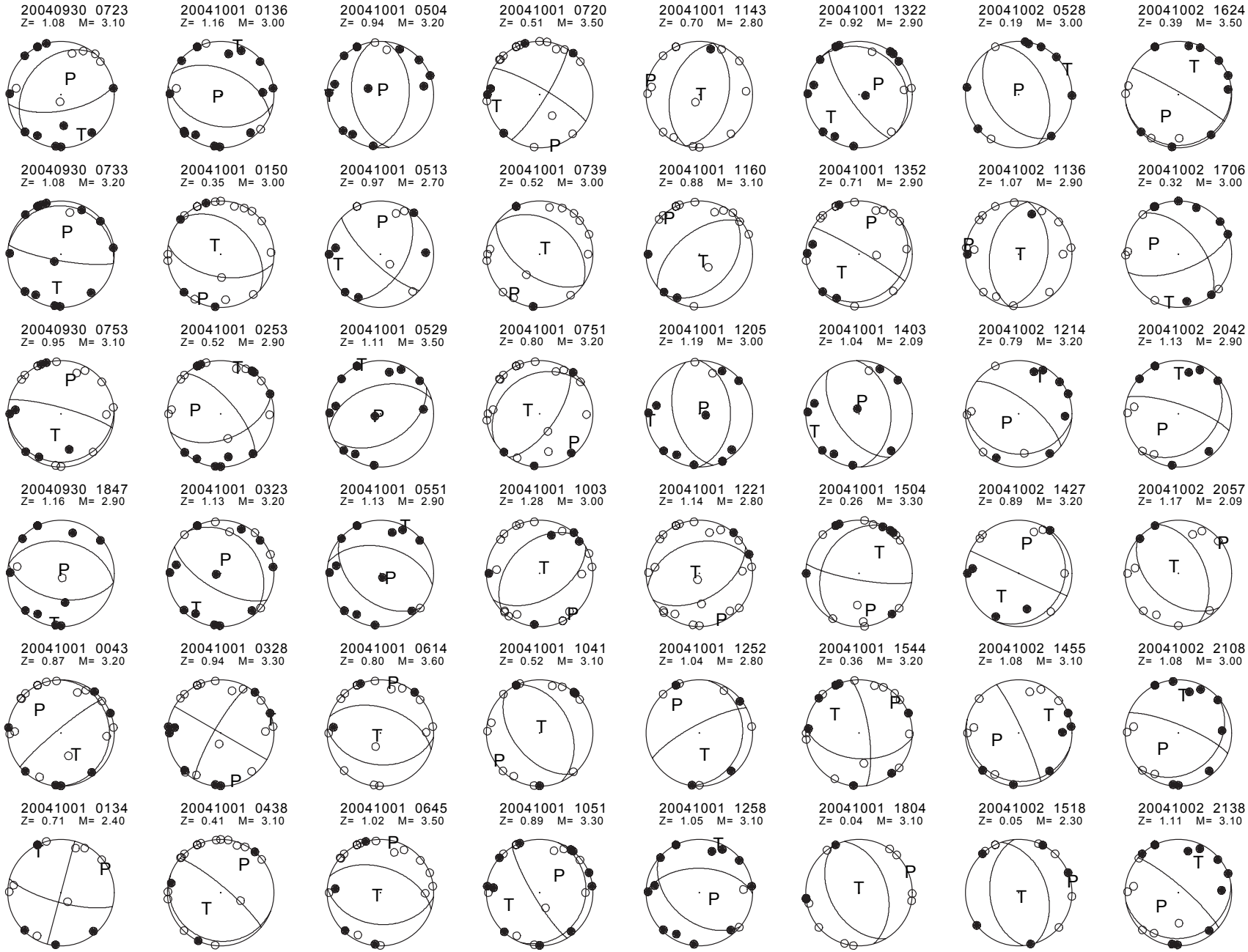

Figure 25—Continued.

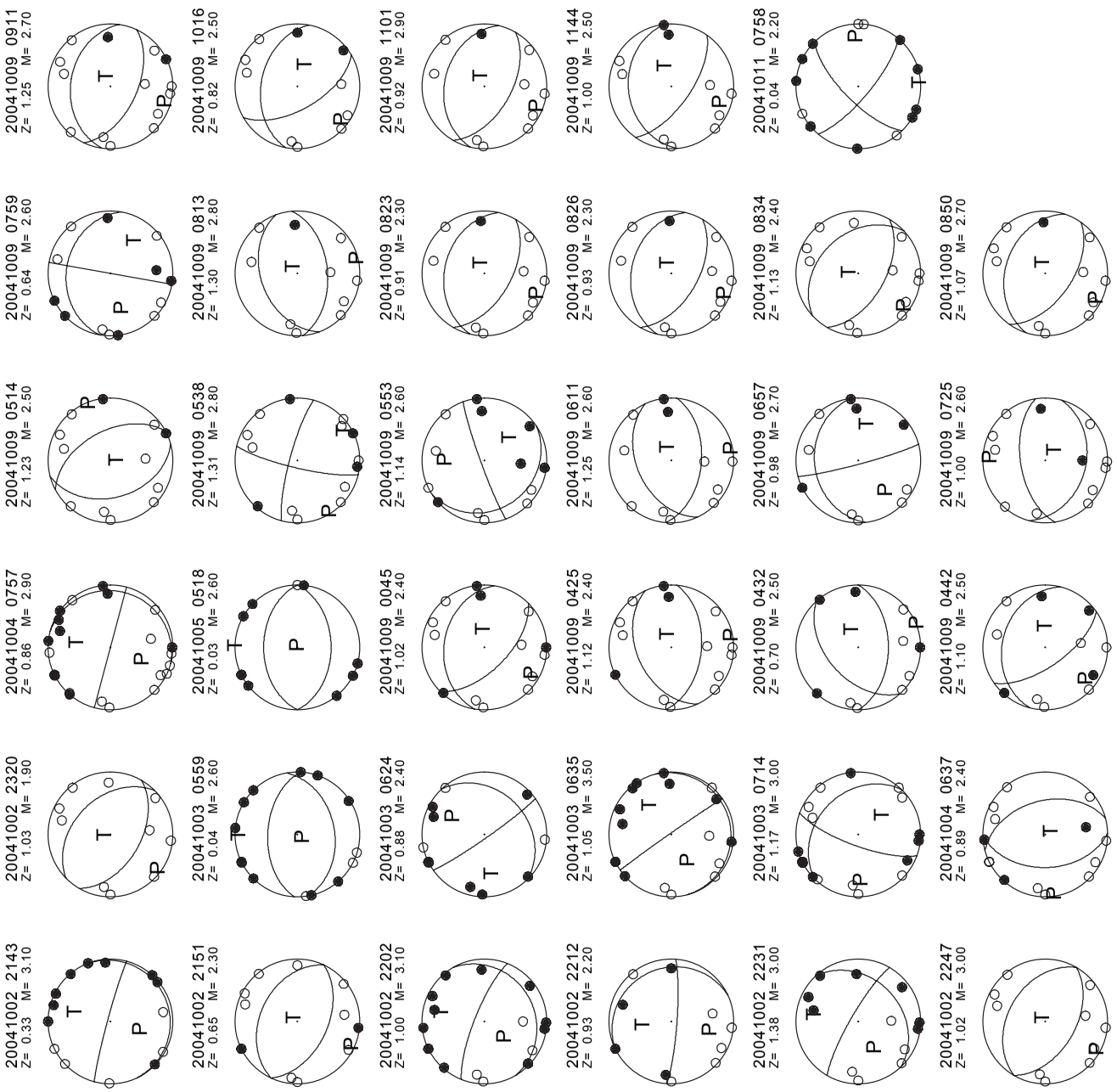

Figure 25—Continued.

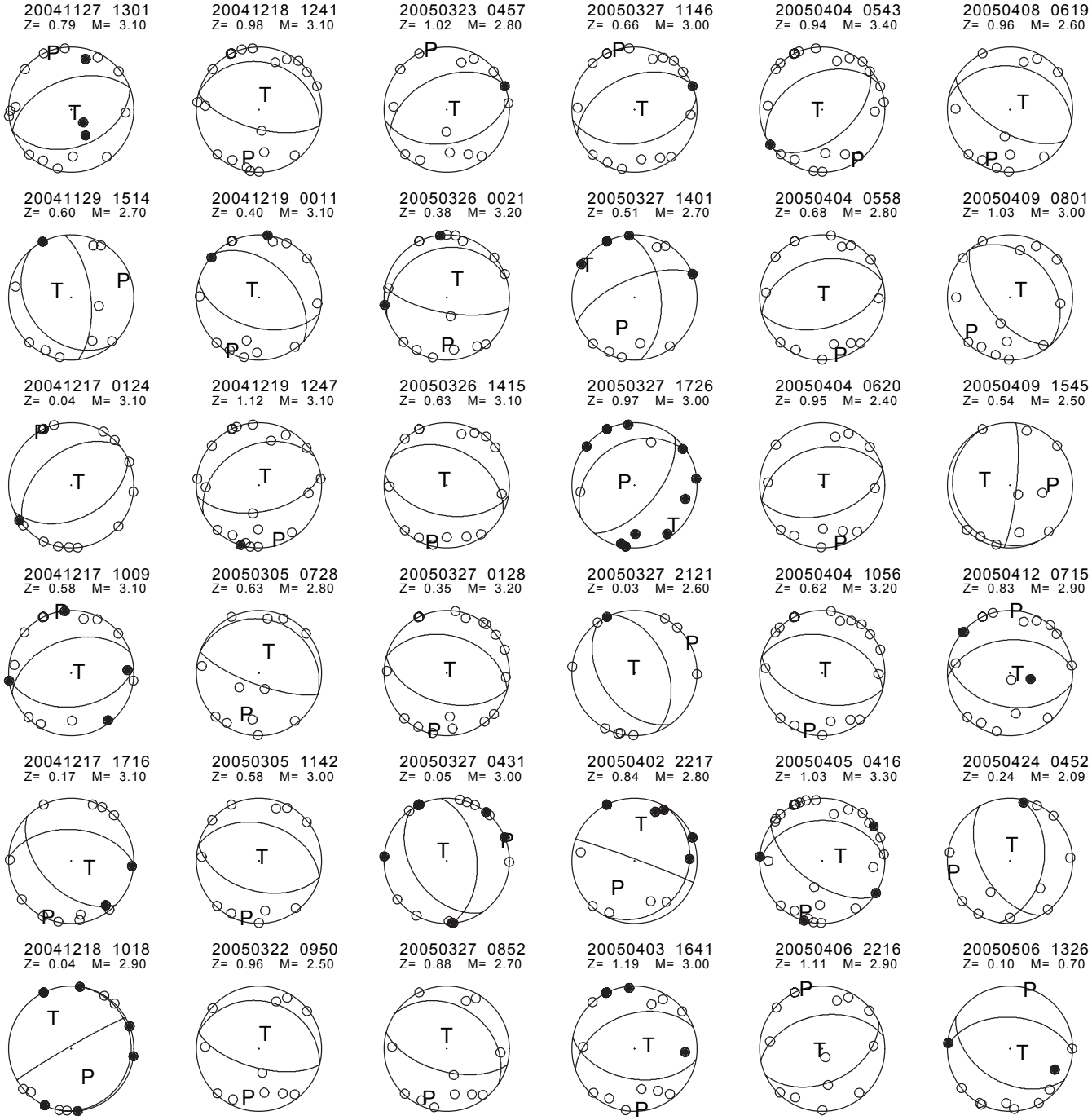

Figure 26. Fault-plane solutions for 55 earthquakes (M_d 0.7–3.4) occurring at Mount St. Helens during the period from Nov. 27, 2004, to Oct. 7, 2005. P, compressional axis; T, tensional axis. Open circles correspond to dilatational (down) first motions, closed circles to compressional (up) first motions. Each solution is coded for date and time (UTC) in this format: YYYYMMDD hhmm. Z, depth, in kilometers; M, magnitude.

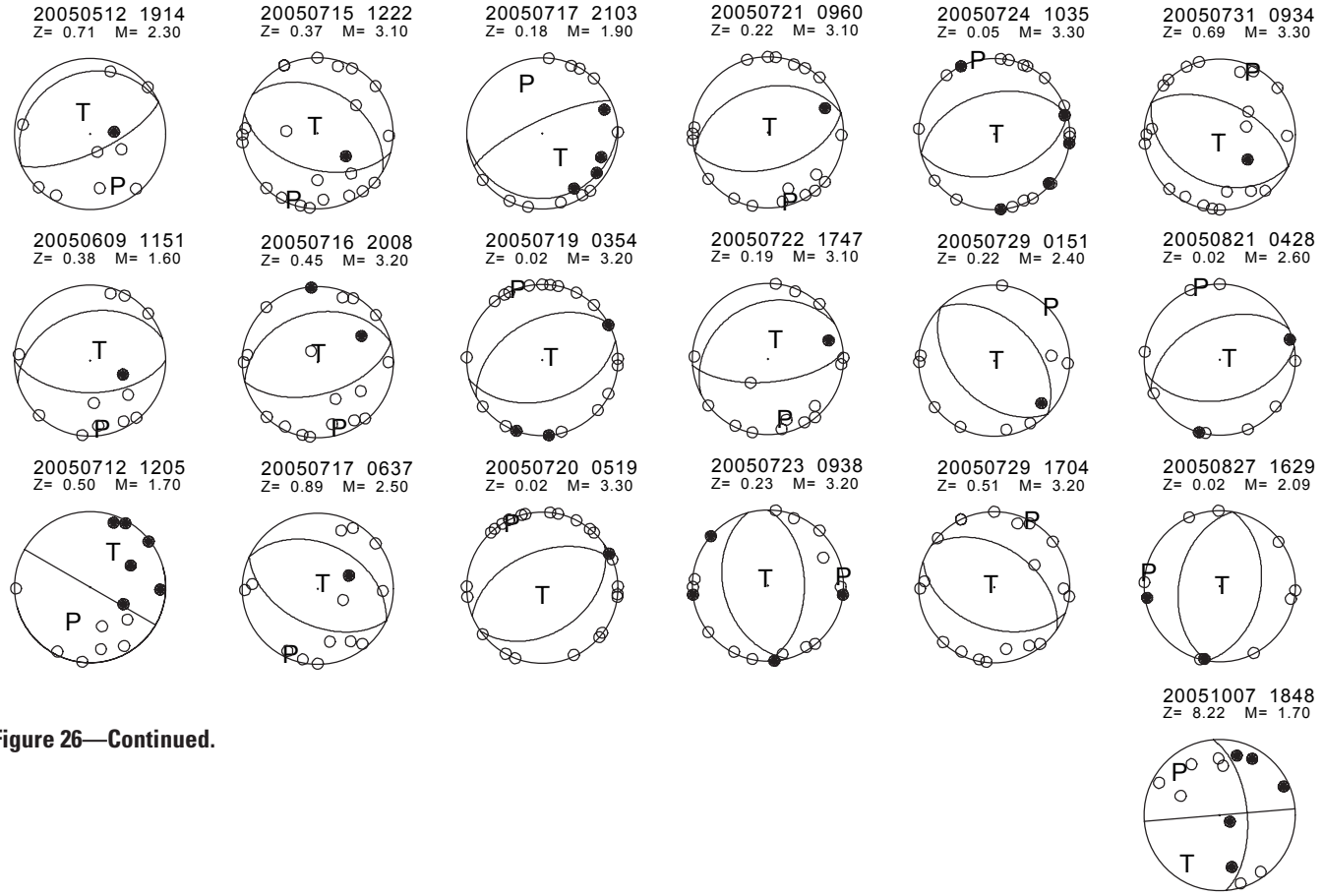

Figure 26—Continued.

Appendix 2. Automated Event Detection

Analyst-driven earthquake location quickly became infeasible as a means for tracking the course of the eruption because it was too slow (Qamar and others, this volume, chap. 3), so over subsequent months we developed methods for automatically detecting events and recording several event parameters of interest. Figures 5, 13, and 14 show results from one such method, a standard triggering algorithm that uses the ratio of average seismic amplitudes computed over short- and long-term time windows, as applied to station HSR (fig. 1). We chose HSR over other stations for three principal reasons: (1) it is a sensitive site that usually records even small earthquakes cleanly; (2) wind noise is usually insignificant; and (3) after a gain reduction on October 4, 2004, no changes were made to the site (McChesney and others, this volume, chap. 7). We used averaging windows of 1 s and 8 s for the short- and long-term averages and a triggering ratio of 2.3 that was determined to be optimal for HSR through trial and error. To avoid multiple triggers from the same event, we skipped forward 6 s after each trigger. We also devised station-specific algorithms for distinguishing between noise glitches (including telemetry and/or Internet dropouts, radio interference, and calibration pulses) and events, although some glitches still made it through our filters. To test the impact of such noise-induced event detections, we visually scanned through helicorder plots for selected time periods and removed glitches that had been recorded as events. Although the resulting plots were cleaner, the fundamental trends were unchanged; in essence, noise was overwhelmed by the shear number of earthquakes.

For each detected event we recorded the peak amplitude over the next 6 s (usually the S wave at HSR), the time gap between successive events, and the normalized power spectra for the first 256 samples following the P-wave arrival (or 2.56 s with the 100-Hz sample rate used by the PNSN and CVO for all short-period stations). We chose to look only at spectra for the first 2.56 s (256 samples) following the event trigger, as full-event spectra were dominated by surface-wave energy and were thus not useful in detecting subtle changes in source spectra, particularly between hybrid and LF events. We only show spectra for events with amplitudes greater than 300 counts (M_d ~1.0), because our algorithm commonly triggered on the S-wave for events smaller than this threshold. The resulting spectra plots, which we referred to as ESAM (Earthquake Spectral AMplitude) plots, proved to be more useful for assessing changes in earthquake source frequency than standard spectrograms of continuous seismic data, particularly because eruption-related seismicity was dominated by discrete seismic events.

A Volcano Rekindled: The Renewed Eruption of Mount St. Helens, 2004–2006
Edited by David R. Sherrod, William E. Scott, and Peter H. Stauffer
U.S. Geological Survey Professional Paper 1750, 2008

Chapter 3

Near-Real-Time Information Products for Mount St. Helens—Tracking the Ongoing Eruption

By Anthony I. Qamar[1]*, Stephen D. Malone[1], Seth C. Moran[2], William P. Steele[1], and Weston A. Thelen[1]

Abstract

The rapid onset of energetic seismicity on September 23, 2004, at Mount St. Helens caused seismologists at the Pacific Northwest Seismic Network and the Cascades Volcano Observatory to quickly improve and develop techniques that summarized and displayed seismic parameters for use by scientists and the general public. Such techniques included webicorders (Web-based helicorder-like displays), graphs showing RSAM (real-time seismic amplitude measurements), RMS (root-mean-square) plots, spectrograms, location maps, automated seismic-event detectors, focal mechanism solutions, automated approximations of earthquake magnitudes, RSAM-based alarms, and time-depth plots for seismic events. Many of these visual-information products were made available publicly as Web pages generated and updated routinely. The graphs and maps included short written text that explained the concepts behind them, which increased their value to the nonseismologic community that was tracking the eruption. Laypeople could read online summaries of the scientific interpretations and, if they chose, review some of the basic data, thereby providing a better understanding of the data used by scientists to make interpretations about ongoing eruptive activity, as well as a better understanding of how scientists worked to monitor the volcano.

Introduction

The renewed activity of Mount St. Helens, which started in September 2004, caused the Pacific Northwest Seismic Network (PNSN) and the U.S. Geological Survey's Cascades Volcano Observatory (CVO) to rapidly adjust routine monitoring procedures and activities in order to accommodate additional data volume, data types, and real-time monitoring requirements. The speed with which the precursory earthquake swarm developed, the sheer number of earthquakes involved, and the need for rapid analysis and interpretation resulted in many changes being made to what had become routine processing procedures developed over the preceding years. The goal of providing accurate and timely interpretation of the evolving sequence was driven by the need of the emergency-response community to mitigate possible hazards and by intense public interest, as indicated by the horde of media that descended on any site where information might be available (Driedger and others, this volume, chap. 24). Through the precursory seismic swarm, the initial minor explosions, and the subsequent dome-building phase, seismic processing and display techniques were developed or expanded to help provide relevant information to the wide variety of users. This paper documents these techniques, focusing on why and how they were developed and what they contributed at the time to monitoring efforts.

Preexistence of Webicorders

Following the end of the previous eruption of Mount St. Helens in October 1986, seismicity at the volcano was monitored using standard seismic techniques, including earthquake locations and visual monitoring of continuous seismic records in the form of helicorders and webicorders. Data from 12 short-period, analog seismic stations were telemetered to the Pacific Northwest Seismic Network (PNSN) headquarters at the University of Washington (UW) for recording and analysis. A subset was also telemetered to the Cascades Volcano Observatory (CVO) for monitoring purposes.

The PNSN routinely processed events from Mount St. Helens through an event-triggered recording system as part

[1] Pacific Northwest Seismic Network, Department of Earth and Space Sciences, University of Washington, Box 351310, Seattle, WA 98195

[2] U.S. Geological Survey, 1300 SE Cardinal Court, Vancouver, WA 98683

* Deceased

of the routine catalog generation for the whole Pacific Northwest. These catalogs were originally only released in quarterly reports and distributed by surface mail. With the rapid evolution of the World-Wide Web, in the early 1990s the PNSN created a public Web site (www.pnsn.org) for online distribution of epicenter catalogs, maps, and other derived information products on earthquakes and volcanoes. As is common for many seismic networks, the PNSN also provided near-real-time Web images of selected seismograms, referred to as webicorder plots (fig. 1).

By 2004, webicorder plots were being produced for more than 60 of the approximately 250 PNSN seismic stations, including several Mount St. Helens stations. As soon as seismic unrest was recognized at Mount St. Helens (September 23, 2004), additional stations there were added to the volcano webicorder list at the expense of stations at other volcanoes; processing constraints limited the total number of webicorders that could be accommodated at any one time.

The webicorder plots were quickly discovered by many members of the public. By September 28, the number of hits on the PNSN departmental Web server was causing a substantial slowing of computer processing and increased Web-page delivery times. Because of the obvious public interest and the PNSN's mission to provide near-real-time information to the public, the PNSN requested assistance from the University of Washington Computers and Communications (CAC) group. Within 18 hours of our request the CAC had a high-capacity Web server connected directly to external high-volume routers to mirror our main pages. Within a few days this server was servicing requests at rates as high as 250,000 per hour, and the CAC group expanded the system to dual server machines with load-balancing routing. The first week's activity totaled more

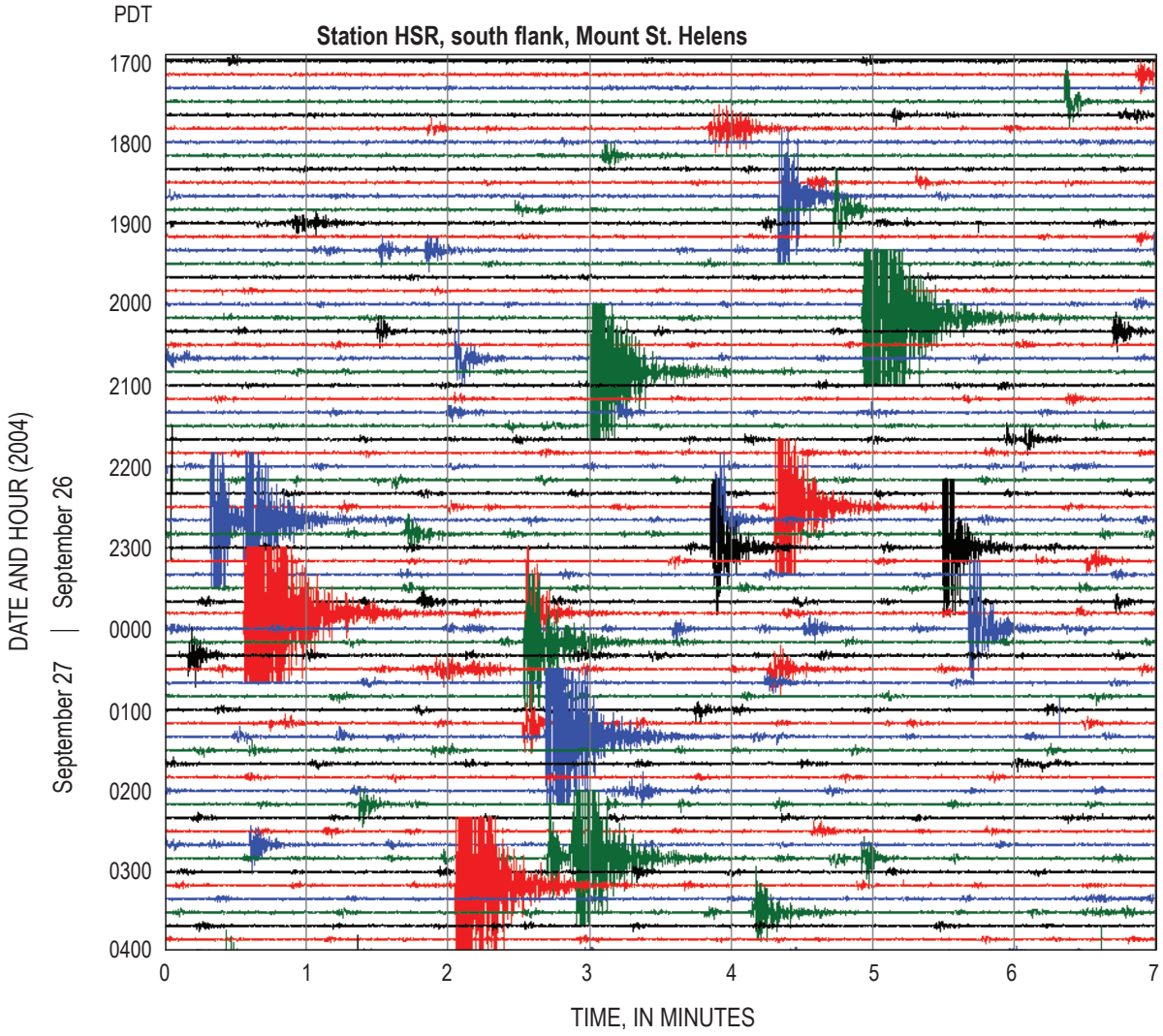

Figure 1. Part of a webicorder plot from station HSR on the south flank of Mount St. Helens from September 26 and 27, 2004. Time advances from left to right and top to bottom, as if reading a book. Each line begins a new 10-minute cycle (the last 3 minutes of each cycle are clipped off here), and gray vertical lines mark 1-minute intervals; color variations are merely to aid the eye in separating traces. Webicorder plots such as this one were updated in real time, available online before and during the 2004 restlessness and ensuing eruption, and were very popular with the public.

than 23 million hits, which translates to roughly 5 million complete pages of information served.

In addition to establishing a mirror site, the PNSN also established a semiprivate (nonlinked but otherwise open) Web server for use by the scientific staff at UW, CVO, and other institutions involved in monitoring the evolving crisis. A password-protected Web server at CVO hosted additional webicorders and other seismicity-related plots. The mix of public and private Web servers enabled us to satisfy the public's need for information while maintaining real-time data-sharing capabilities between CVO and the PNSN. Given the physical separation between the PNSN (located in Seattle, Wash.) and CVO (290 km south in Vancouver, Wash.), the capability for real-time data sharing was critical for effective telephone discussions between CVO and UW staff regarding the evolution of the unrest and eruption.

Real-Time Seismic Amplitude Measurements (RSAM)

Webicorders were valuable for seismologists to qualitatively gauge changes in event type, frequency, and size over the previous minutes to hours, but other tools were necessary to provide a quantitative basis for tracking seismicity changes through time. One such tool, which was quickly implemented at CVO (September 23), was the plotting of real-time seismic amplitude measurement (RSAM) values (Endo and Murray, 1991) (fig. 2). RSAM plots show the rectified amplitude of ground motion averaged over specified time intervals, commonly 10 minutes. Rather than focusing on individual events, RSAM provides a simplified but useful measure of the overall level of seismic activity. RSAM has become a widely used tool in volcano observatories around the world because it readily and quantitatively reflects changes in number and size of earthquakes, tremor, and background noise, each or all of which may be related to changes in volcanic activity. As a result of their previous widespread use, RSAM plots were generally well understood by all scientists at CVO and the PNSN.

The Earthworm seismic-data acquisition and processing system (Johnson and others, 1995; U.S. Geological Survey, 2006) is used both at CVO and at UW for the collection and analysis of seismic data. The "ew2rsam" module, a part of the Earthworm system, was used in the Mount St. Helens crisis to generate RSAM values in real time and plot them on multistation graphs at intervals ranging from several days to several months. Such multistation plots make it easier to determine whether seismic-amplitude changes result from local effects at each station (such as wind noise) or from volcanic processes. The RSAM plots were particularly important for recognizing trends when seismicity intensified on September 26, because webicorder plots for stations on or near the edifice became increasingly saturated and difficult to interpret (Moran and others, this volume, chap. 2).

Root-Mean-Square (RMS) Plots

The usefulness of the RSAM plots inspired the creation at the PNSN of root-mean-square (RMS) plots (fig. 2). Rather than just plotting the average of the rectified signal, these plots show the square root of the sum of squares of the signal averaged over fixed time intervals. Also, different plotting styles for the CVO RSAM and the PNSN RMS were used to emphasize different aspects of seismicity changes. Whereas the RSAM plots connect the points of each average with a line, the RMS plots just show individual averages over a fixed window length as isolated points. Such plots were routinely made for averaging windows of 1 minute and 10 minutes and posted

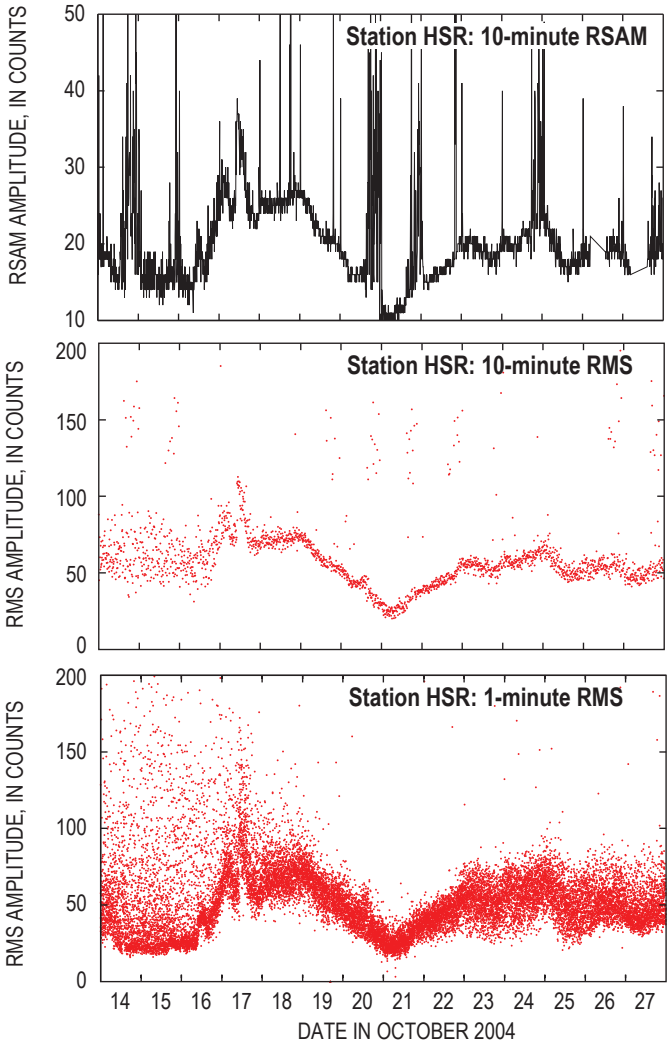

Figure 2. Real-time seismic amplitude measurement (RSAM, top) and root-mean-square (RMS, middle and bottom) plots for seismic signal levels from station HSR during mid- to late October 2004, early in the eruption. Besides the different algorithm to generate the points, plotting characteristics are also different to emphasize different aspects of the activity. Note how the 10-minute and 1-minute RMS plots differ in resolution for the variability of seismic activity.

in nearly real time on the PNSN public Web page. Although the RSAM and RMS plots generally show similar trends, the RMS plots can isolate changes caused by a few large events from cases in which there were an increased number of moderate-size events. From what we know, the inclusion of these plots on the PNSN public Web pages was the first time anywhere that reduced data, other than earthquake locations, were automatically released to the public in real time over the course of a volcanic eruption.

A modification of the RMS plotting routine was developed later in the eruption to show the largest and smallest RMS values determined over a specific time interval. For these plots, RMS values were computed every 5 s and only the largest and smallest during a 30-minute period were selected to plot. In effect these plots track the largest earthquakes and the lowest background level. The maximum-value RMS plots were used for tracking changes in maximum earthquake size over periods of days to weeks, whereas the minimum-value RMS plots were used for detecting elevated background levels that could have represented volcanic tremor (fig. 3).

Spectrograms

Spectrograms, sometimes called "Seismic Spectral Amplitude Measurements" (SSAM) (Rogers and Stephens, 1995) are plots of signal frequency versus time in which color or intensity is used to display the relative strength of a signal in a frequency band (fig. 4). Seismic spectrograms are generated by taking the Fourier spectrum of a fixed time window of signal (1 minute on 12-hour spectrograms at UW and 2.5 s on 10-minute spectrograms at CVO), smoothing the spectrum, and then plotting the amplitude as a color (warm for high amplitude, cool for low) on the vertical frequency axis.

Spectrograms for different sets of stations were being created at UW (12 hours per plot) and at CVO (10 minutes per plot) before September 23, 2004. The spectrograms added little to the interpretation of event types in the first few days of the seismic buildup. By September 26, however, they became useful for recognizing the decrease in higher frequencies as the earthquake sequence progressed from predominantly volcano-tectonic events, with their wide spectrum, through hybrids to dominantly low-frequency events, described by some as long-period (LP) events (Moran and others, this volume, chap. 2; Thelen and others, this volume, chap. 4). These changes of earthquake character were obvious on seismograms of individual events, but the spectrograms allowed us to track changes over time as well. Spectrograms also aided in distinguishing rockfalls, which have broad spectra and long durations, from small, emergent earthquakes. Spectrograms have continued to play an important role in the subsequent years of dome building, because they display variations in seismicity that correspond to different types of events.

Event Processing

At the PNSN, locations and magnitudes of earthquakes in the Pacific Northwest are routinely determined by manual review of waveforms selected by the Earthworm automatic event-triggering-and-recording system. This system uses a detector algorithm that determines a station "trigger" based on the ratio of short-term average over long-term average (STA/LTA) exceeding a specific threshold. Several station triggers must be active at roughly the same time from a subnetwork of nearby stations for the system to declare an event. This criterion helps to discriminate seismic events of real interest from noise bursts on individual stations. The triggering algorithm is tuned to be sensitive, so that very few events of interest are missed, at the cost of having many false triggers. Such a triggering system, in one form or another, has worked well since 1980, having detected for processing more than 100,000 earthquakes between 1980 and 2004.

With the onset of the Mount St. Helens seismic swarm in late September 2004, the routine processing procedures for the PNSN quickly were swamped with data. The automatic system triggered and recorded the early earthquakes with magnitudes as small as $M_d = -1.0$. Event trigger-

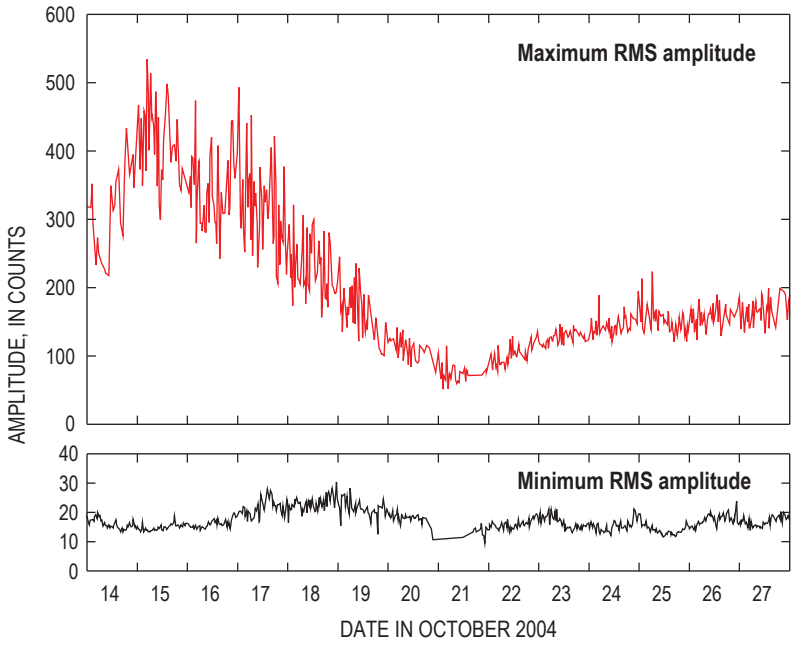

Figure 3. Maximum root-mean-square (RMS, top) and minimum RMS (bottom) plots for seismic-signal levels from station HSR during mid- to late October 2004, early in the eruption. Time period same as in figure 2. Minimum RMS shows background levels, which increased and diminished over roughly weekly intervals. Maximum RMS shows a substantial decrease in large earthquakes during this period.

ing rates for the whole network went from an average of 2–5 events per hour (more than 50 percent noise triggers) before the swarm onset to 6–10 per hour by the end of the second day and to 25–40 per hour by the end of the third day. Soon thereafter the system was in an almost continuously triggered state. By the end of the second day, more than 250 events had been processed, and by the third day the analysis staff could not keep up with manually processing all triggered events. In addition to the burden of reviewing the triggered events, the volume of waveform data was filling available disk space, forcing us to move unprocessed data to tape and other media. Triage was necessary to ensure that at least a reasonable sampling of events were manually reviewed and that no trace data were lost. The task was twofold: first, we trained additional staff and students in the basic process and divided review tasks among them; then we experimented with different trigger parameters to achieve a representative, but not complete selection of events for manual processing.

After the first two months, with seismic activity continuing at a fairly high rate and the potential for a long-lasting eruption becoming evident, we changed the procedures in such a way that we could review the data for significant changes but process in detail only a selection of the larger or impulsive events. For this we started generating hour-long, sequential artificial trigger files of only Mount St. Helens stations, with a display order based on distance from the vent so that the waveforms could be easily scanned for events of interest and for changes in event or background signal characteristics. The trigger threshold for the automatic triggering system was raised for the Mount St. Helens subnet so that only larger events would generate a complete event trigger. This procedure sped up the routine analysis and provided a better way of detecting subtle changes in event types or characteristics, because an analyst could quickly scan through all of the data and easily see changes in both large and small events.

The hypocenter distribution determined by standard processing of well-recorded earthquakes changed very little over the course of the seismic restlessness and ensuing eruptive sequence. Hypocenter depths decreased during the first two weeks of restlessness from 2–3 km deep to less than 1 km. The scatter in epicenters is comparable to variation arising from picking errors. Some of the variation in locations can be attributed to changes in station configuration. Several times during the sequence, no station was located within 1.5 km of the source area because of station outages resulting from explosions, and thus depth control, in particular, was poor. Subsequent specialized analysis shows a much tighter clustering of hypocenters than that determined during the height of the sequence (Thelen and others, this volume, chap. 4).

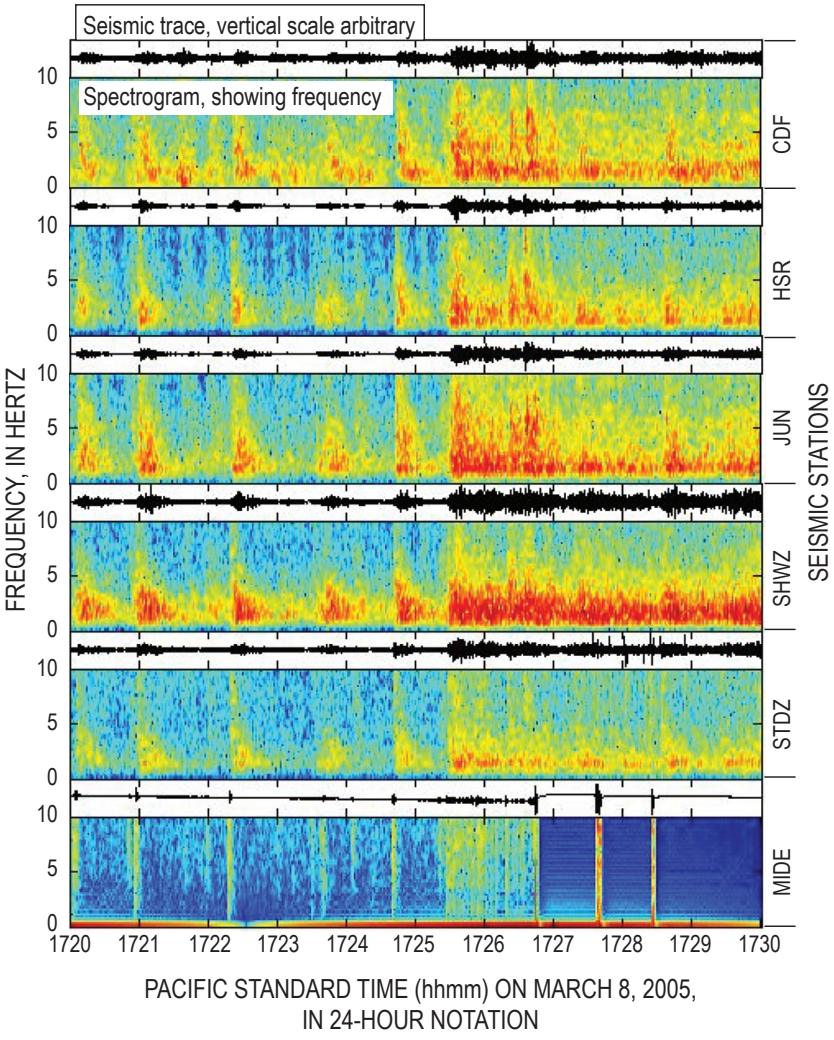

Automatic Trace Processing

Once it became apparent that the dominant seismic signals were from very regular earthquakes—so regular that they were named "drumbeat" earthquakes—we felt a need for tools to track the rate and type of individual earthquakes. A modification of an event-triggering algorithm was developed to detect characteristics of individual events. This algo-

Figure 4. Sample spectrograms from six stations for a 10-minute period on March 8, 2005 (local date). Shown for each station are conventional seismogram (upper line trace) and corresponding spectrogram (color spectrum). Periodic earthquakes characterize the record until about 17:25:30 (1:25:30 UTC), when an explosion at the vent marks onset of sustained, low-frequency tremor. Station MIDE, lowermost of graphs, lost signal sporadically and then completely, owing to thick, airborne ash that interrupted radio transmission.

rithm was based on a ratio of short-term and long-term averages of RMS values computed at 5-s intervals for a key subset of close-in stations with good signal-to-noise ratios. The onset of an event was reliably detected, but determining the end of one event so that the algorithm would de-trigger and be ready for the next event required some tuning of parameters. Once an event was declared, several parameters, including its peak amplitude, average RMS value, and peak frequency, were determined from the original waveforms. The event was not located in the traditional sense, but an effective automatic event catalog was generated that included time, size, and general frequency content.

Focal Mechanisms

Focal mechanisms are traditionally difficult to obtain in volcanic areas because the emergent arrivals typical of low-frequency earthquakes and the high attenuation within the edifice result in low signal-to-noise ratios at more distant stations. Additionally, at Mount St. Helens, earthquakes located at shallow depth in the edifice are mostly small, contributing to poor signal-to-noise ratios. Shallow hypocenters mean that sampling the entire focal sphere, a requirement for a well-constrained focal mechanism, is difficult. Determination of focal mechanisms is therefore restricted to the relatively few large events for which good first motions are available on many stations. Typically focal mechanisms were generated at the PNSN during the event-location process by picking polarities (up or down) of the first motion. A modification of the program "FPFIT"(Reasenberg and Oppenheimer, 1985) was used to fit focal planes for a double-couple solution when there were 10 or more picked polarities. An unusual aspect of Mount St. Helens earthquakes is that a vast majority of first motions are dilatations. Many events have dilatations on all stations, giving the impression of an implosive or tensile source. However, because of poor sampling of the focal sphere, it is sometimes possible to fit a double-couple solution even to these cases. Figure 5 shows examples of four typical events with predominantly "all down" first motions. Of these four events only one clearly does not have a possible double couple solution.

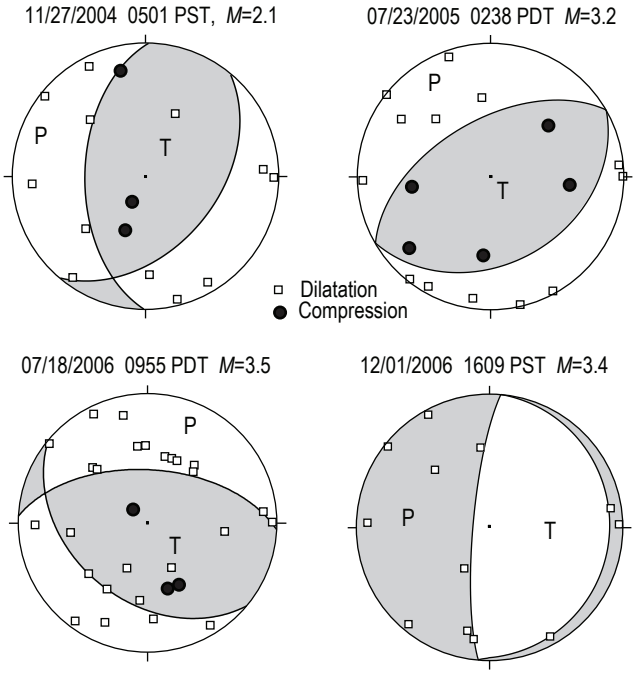

Figure 5. Examples of focal mechanisms determined from four of the many larger, well-recorded events. All such events are located within a few hundred meters of the vent. Note that while almost all polarities are dilatations, double-couple solutions can be fit in some cases. In other cases, such as the event of July 18, 2006, no double-couple solution is possible without many (five) inconsistent polarities.

Event Magnitudes

Routine earthquake processing by the PNSN uses coda duration to compute magnitudes (Crosson, 1972). For most tectonic earthquakes a consistent linear relation exists between the log of the coda duration and the local magnitude, M_L. However, this relation breaks down for earthquakes recorded on Cascade Range volcanoes. For shallow earthquakes in particular, the coda duration is much longer than expected for a given magnitude. Two calibrated broadband stations were installed near Mount St. Helens in October 2004, early in the eruption (McChesney and others, this volume, chap. 7). By deconvolving their known instrument responses and then convolving a Wood-Anderson response, equivalent maximum-trace amplitudes on standardized Wood-Anderson seismograms could be calculated. The resulting local magnitude (M_L) was determined for a suite of earthquakes over the magnitude range 0.5–3.4 (fig. 6). Coda durations for the larger events, mostly picked on stations distant from the volcano, gave duration magnitudes (M_d) comparable to the local magnitude (M_L). For smaller events, however, M_d is often grossly overestimated owing to the extended codas generated by the volcanic earthquakes recorded at stations on volcanic rocks.

Even though the coda duration magnitudes overestimate the true magnitude of the earthquake, coda magnitudes were still measured for located earthquakes to give a quantitative measure of the relative sizes of earthquakes at Mount St. Helens. Codas for the calculation of magnitude are measured only on stations off the edifice (beyond a 5-km radius) to minimize the effect of the extended codas.

Special Web Pages

For many years the PNSN Web site has maintained topical Web pages for all of the monitored Cascade Range volcanoes. Besides some general descriptive text for each volcano and links to the more extensive descriptions on CVO Web

pages, these pages provide plots of epicenters, depth versus time, and energy release versus time at three different time scales. The plots have always been based on routine processing of earthquakes located at a volcano. During inter-eruption periods and for minor seismic swarms, these pages continue to be useful for seismologists and informative for the general public. As the current seismic sequence escalated, however, the plots often became outdated because the routine processing (and thus the catalog) was greatly delayed or incomplete. Thus the utility of these special pages to assist in the interpretation of changes was severely compromised. The automatic RSAM and RMS plots quickly became favored as the data product most used for tracking changes in the seismicity at Mount St. Helens. However, public interest in the special pages remained high, even though we frequently posted disclaimers concerning the accuracy and completeness of these plots.

By adopting the changes already described in this paper, earthquake processing again became routine enough that the special volcano-related pages for Mount St. Helens represented a near-real-time picture of seismicity, even though only a fraction of detected earthquakes were logged in the catalog of located events. For example, time-depth plots (fig. 7) of located events eventually made it obvious that the depths of earthquakes taking place beneath Mount St. Helens since the 1980s changed dramatically with the advent of the 2004 eruption. Earthquakes at depth of 2–3 km, with occasional deeper swarms, had been the norm at Mount St. Helens since the late 1980s. These events, particularly the deeper swarms, were interpreted as representing the repressurization of the magmatic system by recharge (Moran, 1994; Musumeci and others, 2002). With the advent of the 2004 (and ongoing) eruption, these deeper events ceased. This depth-pattern shift hints that if magma recharge is continuing during the eruption, it is not pressurizing the deeper system.

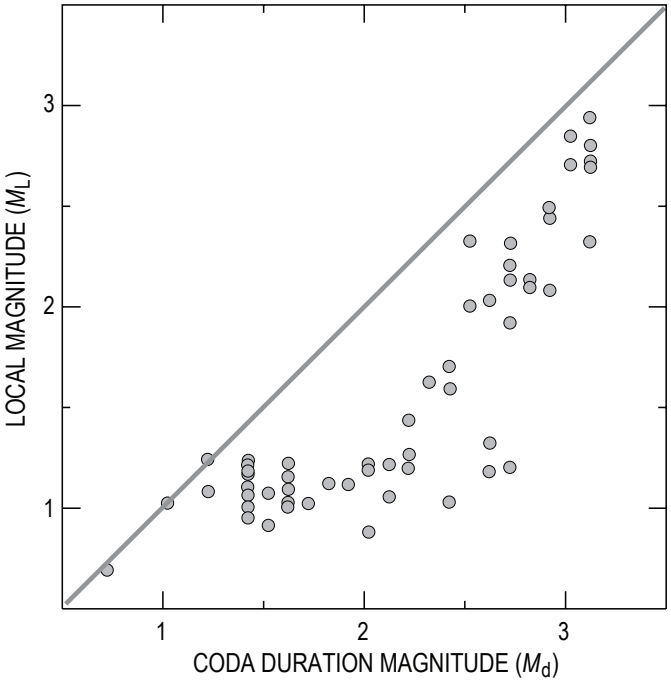

Figure 6. Coda duration magnitude versus local magnitude for a selection of Mount St. Helens earthquakes illustrates how use of coda duration magnitudes overestimates the local magnitudes for these earthquakes, particularly at lower magnitudes.

RSAM Alarms

In addition to magnitude-based earthquake alarms routinely used by the PNSN, several eruption-specific alarms were developed by CVO during the first 6 months of the eruption. RSAM alarms tuned to detect both large, discrete events ("event alarm") and smaller amplitude but longer duration events ("tremor alarm") were employed by CVO in mid-October 2004, shortly after the end of intense seismicity accompanying the vent-clearing phase. These alarms had previously been developed by the USGS Volcano Disaster Assistance Program as part of the "Glowworm" package of modules that operate as an add-on to the Earthworm acquisition system (Marso and others, 2003a). Before 2004, RSAM alarms had been used for more than a year to monitor the eruption of Anatahan volcano in the Commonwealth of the Northern Mariana Islands (Marso and others, 2003b).

The "event alarm" tracks RSAM values determined over a 2.56-s window (for 100-Hz data), with alarms issued if thresholds are exceeded at a prescribed number of stations for longer than 8 s. The "tremor alarm" uses RSAM values for 1-minute windows. When an alarm is issued, a separate module sends alerts via Short Message Service (SMS) to cell phones carried by on-call scientists. A potential weak link in this chain is the use of SMS, which requires that e-mail servers and SMS services be fully functional. Alerts were occasionally delayed by several minutes or even an hour before reaching individual phones. To partly address this limitation, SMS messages were sent to multiple cell phones (13 as of the summer of 2006) using multiple carriers. Nevertheless, these problems kept us from relying completely on SMS messaging, which we augmented by periodic data checks during off-hours.

Alert thresholds for the "event" and "tremor" alarms required refinement throughout the first 6 months of the eruption. Seismicity was so energetic initially that the alarms had to be desensitized to minimize the number of alerts. In mid-November 2004, larger earthquakes began occurring daily (Moran and others, this volume, chap. 2), and the "event alarm" was set so that thresholds were just barely exceeded by these events. Thresholds for the tremor alarm were much harder to determine, as we had no quantitative means for establishing thresholds. They initially were set at nominal values that were sufficiently high to prevent false triggers from wind and other noise sources. As a result, no alarms were issued for the January 16, 2005, explosion, which was accompanied by low-amplitude tremor that was barely detectable on stations outside the crater (Moran and others, this volume, chap. 6). Tremor alarm thresholds were reset on the basis of

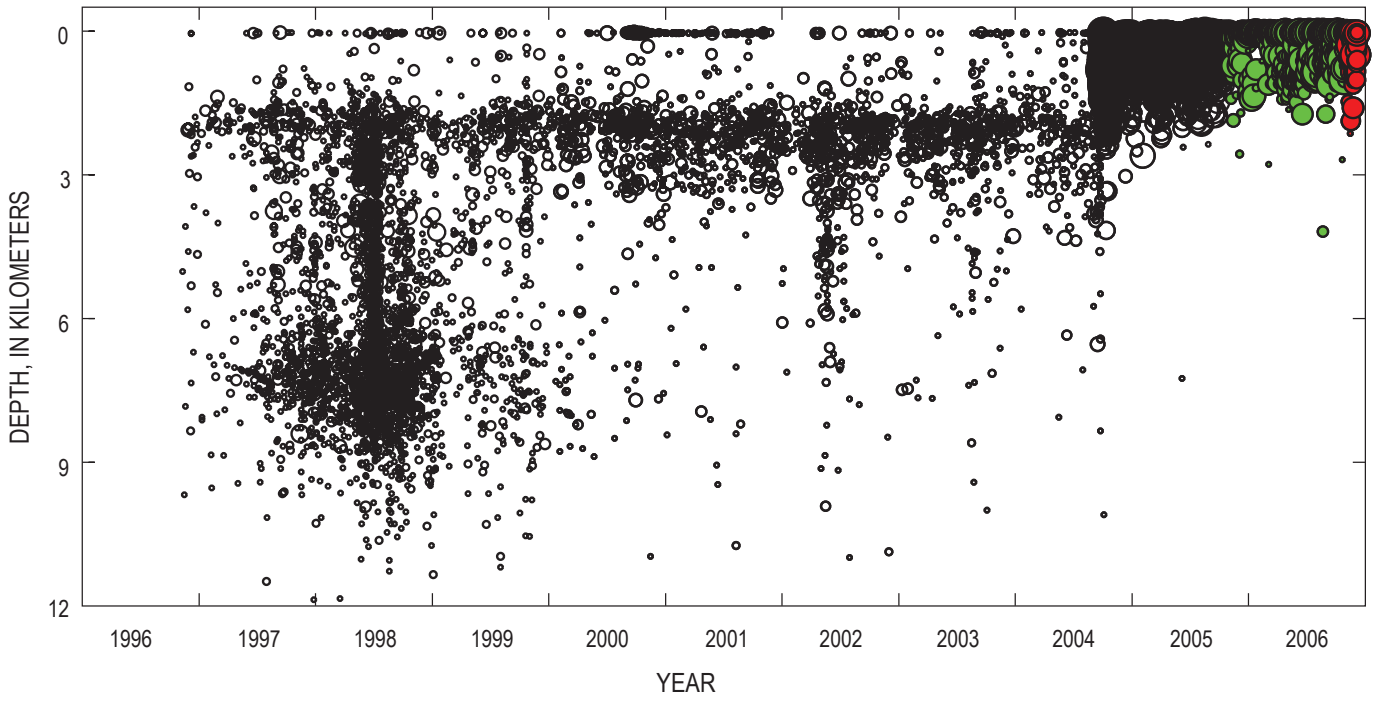

Figure 7. Time versus depth plot for a decade of seismicity at Mount St. Helens. Plot shows approximately 24,000 earthquakes located directly under the volcano (within 6-km radius of the new dome) between January 1997 and the end of 2006. Size of circles is proportional to event magnitude. Green circles, events in 2006; red circles, events in December 2006.

recordings of this explosion on stations located within the crater. However, the closest station became intermittent shortly after the January explosion and had stopped transmitting altogether by the time of the March 8, 2005, explosion. Seismicity associated with the March 8 explosion was more energetic (Moran and others, this volume, chap 6), but thresholds were not exceeded on enough stations to generate an alarm.

The failure of these alarms to generate alerts during explosions motivated us to develop a new alarm in the event of a loss of analog telemetry. Of the six explosions occurring during 2004–5, four, including the January 16 and March 8, 2005, explosions resulted in temporary or permanent loss of telemetry from at least one station. Traditional RSAM alarms have always used RSAM values from which the electronic bias or direct-current (DC) component has been removed, in large part to avoid false alarms resulting from common misalignment problems with analog telemetry circuitry that can impose a small DC offset on seismic data. However, the USGS J120 discriminator includes circuitry that detects the loss of the subcarrier and sets the discriminator output to a static 0.7-V DC level to distinguish loss of telemetry from a quiet seismic signal.

We created a new Earthworm module (based on the Earthworm ew2rsam module) that does not remove the DC component from RSAM values. Named FLOTSAM (not an acronym), this new alarm system sends alerts whenever values exceed a preset threshold at any station. The FLOTSAM system has sent out several alerts, some of which have been generated by loss of telemetry from crater stations destroyed during large rockfalls. Other alerts have resulted from stations that have stopped transmitting because of power outages at the site or weather-related disruptions of the radio signal.

The FLOTSAM alarm has become the alarm that the PNSN and CVO rely upon the most for detecting explosions, because no fine-tuning of amplitude and duration thresholds is required. All that is required is at least one seismometer placed close enough to the vent to have its radio signal disrupted by ash or by physical damage to the station. The event and tremor alarms are employed as well, with the event alarm proving to be a reliable detector of large earthquake-generated rockfalls, which sporadically produce ash clouds that reach from hundreds to several thousand meters above the crater rim.

Real-Time Traces for Remote Use

Early in the Mount St. Helens 2004 eruption, we became aware that researchers at other volcano observatories and academic institutions were interested in our seismic data. Besides the public Web pages, we provided access over the Internet to our real-time trace data wave-servers on a case-by-case basis. We also set up a direct export of selected data to the Alaska Volcano Observatory (AVO), where researchers were interested in following the seismic sequence in detail. At AVO and Stanford University the real-time data integration tool, VALVE (Cervelli and others, 2002), was used to track changes in

seismic activity along with other parameters. The seismic-trace display program, SWARM (Alaska Volcano Observatory, 2006) was used at several different institutions to examine continuous seismic waveforms and their frequency content. In particular, researchers at the following institutions became near-real-time collaborators participating to some degree in the interpretation of specific aspects of Mount St. Helens seismicity:

- Alaska Volcano Observatory (Anchorage and Fairbanks)—event character, multiplet analysis
- U.S. Geological Survey (Menlo Park, Calif.)—event character, frequency shift
- University of California, Los Angeles—strong-motion portable monitoring, explosion analysis
- University of Memphis (Tennessee)—broadband portable monitoring
- Los Alamos National Laboratory (New Mexico)—multiplet analysis
- University of New Hampshire—multiplet analysis, acoustic signals.

Public Use and Response

The availability of relatively detailed information on the Web in nearly real time for this eruption of Mount St. Helens provided a new and powerful tool for public understanding. The availability of near-real-time original data (seismic traces) and analyzed products (RMS plots, maps, and time-depth plots) resulted in a change in the public perception of the eruption and their interaction with scientists. In previous eruption crises, the public has learned about the process primarily through the eyes of the news media, who may witness or photograph the physical events and talk with scientists about their interpretations. In this latest eruption of Mount St. Helens, the public could see for themselves on the Web many of the same data and products that the scientists were using. This availability improves the public understanding in two significant ways: Although the public still obtained the basic summary information from the news media, those wanting more or not trustful of the interpretations they were hearing could look at some of the data themselves.

The current eruption of Mount St. Helens is remarkable for the near absence of rumors and conspiracy theories purporting that critical information was being deliberately withheld from the public by scientists and emergency managers. The public also demonstrated the ability to digest a variety of sophisticated information products in order to follow the course of the eruption. Providing rich, open sources of eruption data enabled the public and media to monitor the ongoing eruption and may have encouraged them to seek further clarification from the scientific community when issues of interpretation arose. This public availability limited the kind of wild speculations that have sometimes occurred in the past.

Acknowledgments

The many staff and students associated with the Pacific Northwest Seismic Network (PNSN) and Cascades Volcano Observatory are too many to acknowledge individually but are greatly appreciated for their tireless help in the field and lab, often going much beyond what was expected to make the acquisition and processing of the huge amount of seismic data possible. Tom Murray, Peter Cervelli, Randy White, Jeff Johnson, Jackie Caplan-Auerbach, Chris Newhall, Giuliana Mele, Stephanie Prejean, and Steve Horton are thanked for their contributions to software, Web design, and general discussions relevant to our information products. David Sherrod and Jackie Caplan-Auerbach provided excellent reviews of our preliminary manuscript. The University of Washington's Office of Computing and Communications is acknowledged for their very rapid and effective Web server upgrades and extra telephone services. Partial support was provided by U.S. Geological Survey Cooperative Agreement 04HQAG005 for the operation of the PNSN.

References Cited

Alaska Volcano Observatory, 2006, Alaska Volcano Observatory software development page, SWARM version 1.2.3: U.S. Geological Survey online-only publication, including tutorial, manual, and software [http://www.avo.alaska.edu/Software/swarm/; last accessed Mar. 17, 2009].

Cervelli, D.P., Cervelli, P., Miklius, A., Krug, R., and Lisowski, M., 2002, VALVE; Volcano Analysis and Visualization Environment [abs.]: Eos (American Geophysical Union Transactions), v. 83, no. 47, Fall Meeting Supplement, U52A-07, p. F3.

Crosson, R.S., 1972, Small earthquakes, structure and tectonics of the Puget Sound region: Seismological Society of America Bulletin, v. 62, p. 1133–1171.

Driedger, C.L., Neal, C.A., Knappenberger, T.H., Needham, D.H., Harper, R.B., and Steele, W.P., 2008, Hazard information management during the autumn 2004 reawakening of Mount St. Helens volcano, Washington, chap. 24 *of* Sherrod, D.R., Scott, W.E., and Stauffer, P.H., eds., A volcano rekindled; the renewed eruption of Mount St. Helens, 2004–2006: U.S. Geological Survey Professional Paper 1750 (this volume).

Endo, E.T., and Murray, T., 1991, Real-time seismic amplitude measurement (RSAM); a volcano monitoring and prediction

tool: Bulletin of Volcanology, v. 53, no. 7, p. 533–545.

Johnson C.E., Bittenbinder, A., Bogaert, B., Dietz, L., and Kohler, W., 1995, Earthworm—a flexible approach to seismic network processing: IRIS Newsletter, v. 14, no. 2, p. 1–4.

Marso, J.N., Murray, T.L., Lockhart, A.B., and Bryan, C.J., 2003a, Glowworm, an extended PC-based Earthworm system for volcano monitoring [abs], *in* Cities on Volcanoes 3: Hilo, Hawaii, International Association of Volcanology and Chemistry of the Earth's Interior (IAVCEI), Hilo, Hawaii, July 14–18, 2003, Abstract volume, p. 82.

Marso, J.N., Lockhart, A.B., White, R.A., Koyanagi, S.K., Trusdell, F.A., Camacho, J.T., and Chong, R., 2003b, The Anatahan volcano-monitoring system [abs.]: Eos (American Geophysical Union Transactions), v. 84, no. 46, Fall Meeting Supplement, V32B-1020.

McChesney, P.J., Couchman, M.R., Moran, S.C., Lockhart, A.B., Swinford, K.J., and LaHusen, R.G., 2008, Seismic-monitoring changes and the remote deployment of seismic stations (seismic spider) at Mount St. Helens, 2004–2005, chap. 7 *of* Sherrod, D.R., Scott, W.E., and Stauffer, P.H., eds., A volcano rekindled; the renewed eruption of Mount St. Helens, 2004–2006: U.S. Geological Survey Professional Paper 1750 (this volume).

Moran, S.C., 1994, Seismicity at Mount St. Helens, 1987–1992: Evidence for repressurization of an active magmatic system: Journal of Geophysical Research, v. 99, no. B3, p. 4341–4354, doi: 10.1029/93JB02993.

Moran, S.C., Malone, S.D., Qamar, A.I., Thelen, W.A., Wright, A.K., and Caplan-Auerbach, J., 2008a, Seismicity associated with renewed dome building at Mount St. Helens, 2004–2005, chap. 2 *of* Sherrod, D.R., Scott, W.E., and Stauffer, P.H., eds., A volcano rekindled; the renewed eruption of Mount St. Helens, 2004–2006: U.S. Geological Survey Professional Paper 1750 (this volume).

Moran, S.C., McChesney, P.J., and Lockhart, A.B., 2008b, Seismicity and infrasound associated with explosions at Mount St. Helens, 2004–2005, chap. 6 *of* Sherrod, D.R., Scott, W.E., and Stauffer, P.H., eds., A volcano rekindled; the renewed eruption of Mount St. Helens, 2004–2006: U.S. Geological Survey Professional Paper 1750 (this volume).

Musumeci, C., Gresta, S., and Malone, S.D., 2002, Magma system recharge of Mount St. Helens from precise relative hypocenter location of microearthquakes: Journal of Geophysical Research, v. 107, no. B10, 2264, p. ESE 16-1–ESE 16-9, doi:10.1029/2001JB000629.

Reasenberg, P.A., and Oppenheimer, D., 1985, FPFIT, FPPLOT, and FPPAGE: FORTRAN computer programs for calculating and plotting earthquake fault-plane solutions: U.S. Geological Survey Open-File Report 85–739, 109 p.

Rogers, J.A., and Stephens, C.D., 1995, SSAM: Real-time seismic spectral amplitude measurement on a PC and its application to volcano monitoring: Seismological Society of America Bulletin, v. 85, no. 2, p. 632–639.

Thelen, W.A., Crosson, R.S., and Creager, K.C., 2008, Absolute and relative locations of earthquakes at Mount St. Helens, Washington, using continuous data; implications for magmatic processes, chap. 4 *of* Sherrod, D.R., Scott, W.E., and Stauffer, P.H., eds., A volcano rekindled; the renewed eruption of Mount St. Helens, 2004–2006: U.S. Geological Survey Professional Paper 1750 (this volume).

U.S. Geological Survey, 2006, Earthworm documentation v. 7.0: U.S. Geological Survey online-only publication, including overview, release notes, and software [http://folkworm.ceri.memphis.edu/ew-doc/; last accessed Nov. 6, 2006].

A Volcano Rekindled: The Renewed Eruption of Mount St. Helens, 2004–2006
Edited by David R. Sherrod, William E. Scott, and Peter H. Stauffer
U.S. Geological Survey Professional Paper 1750, 2008

Chapter 4

Absolute and Relative Locations of Earthquakes at Mount St. Helens, Washington, Using Continuous Data: Implications for Magmatic Processes

By Weston A. Thelen[1], Robert S. Crosson[2], and Kenneth C. Creager[2]

Abstract

This study uses a combination of absolute and relative locations from earthquake multiplets to investigate the seismicity associated with the eruptive sequence at Mount St. Helens between September 23, 2004, and November 20, 2004. Multiplets, a prominent feature of seismicity during this time period, occurred as volcano-tectonic, hybrid, and low-frequency earthquakes spanning a large range of magnitudes and lifespans. Absolute locations were improved through the use of a new one-dimensional velocity model with excellent shallow constraints on P-wave velocities. We used jackknife tests to minimize possible biases in absolute and relative locations resulting from station outages and changing station configurations. In this paper, we show that earthquake hypocenters shallowed before the October 1 explosion along a north-dipping structure under the 1980–86 dome. Relative relocations of multiplets during the initial seismic unrest and ensuing eruption showed rather small source volumes before the October 1 explosion and larger tabular source volumes after October 5. All multiplets possess absolute locations very close to each other. However, the highly dissimilar waveforms displayed by each of the multiplets analyzed suggest that different sources and mechanisms were present within a very small source volume. We suggest that multiplets were related to pressurization of the conduit system that produced a stationary source that was highly stable over long time periods. On the basis of their response to explosions occurring in October 2004, earthquakes not associated with multiplets also appeared to be pressure dependent. The pressure source for these earthquakes appeared, however, to be different from the pressure source of the multiplets.

Introduction

Because more than 1 million earthquakes occurred between the beginning of the latest eruption of Mount St. Helens in 2004 and the end of 2005 (Moran and others, this volume, chap. 2), there is a need to locate a representative set of earthquakes to search for first-order patterns and trends that may aid in future monitoring and research. Although locating most of the 1 million earthquakes would be possible and even somewhat practical with current methods and parallel computing, such a study is beyond the scope of this paper. Herein we concentrate on the seismicity leading up to the early October explosions and through about 1 month of dacitic dome building in order to characterize the seismicity associated with each eruptive phase.

One of the most striking features in this eruption's seismicity was the prominence of earthquake multiplets, or repetitious earthquakes. Earthquake multiplets are characteristically defined by their highly similar waveforms, often exceeding cross-correlation coefficients of 0.8 (Geller and Mueller, 1980; Frémont and Malone, 1987; fig. 1). This phenomenon is likely caused by earthquakes occurring very close to the same location with a similar source process (Geller and Mueller, 1980). Earthquake multiplets are a common occurrence in tectonic and volcanic areas worldwide, and many authors have exploited earthquake multiplets to determine highly precise relative relocations (for example, Poupinet and others, 1984; Fréchet, 1985; Frémont and Malone, 1987; Got and others, 1994; Waldhauser and Ellsworth, 2000). Every relative relocation method operates on the basic idea that closely spaced

[1] Pacific Northwest Seismic Network, Department of Earth and Space Sciences, University of Washington, Box 351310, Seattle, WA 98195

[2] Department of Earth and Space Sciences, University of Washington, Box 351310, Seattle, WA 98195

earthquakes recorded at a common station will have similar path and site effects. As long as the source region is homogeneous (or reasonably so) with respect to the dominant wavelength of the waveforms, the relative time lag between the earthquakes is a measure of the separation distance between the sources (Wolfe, 2002).

The classification and description of large suites of multiplets is also fairly common on volcanoes worldwide. Got and others (1994) relocated 250 earthquakes beneath Kīlauea, Hawai‘i, to define a nearly horizontal plane of seismicity at 8-km depth. Stevens and Chouet (2001) analyzed long-period multiplets beneath Redoubt Volcano before its 1989 eruption and found smooth changes in amplitude and cross-correlation coefficient within multiplets. Rowe and others (2004) relocated approximately 17,000 similar earthquakes on Soufrière Hills volcano, Montserrat, by identifying multiplets through a hierarchical clustering algorithm and using those multiplets as stacks to refine phase picks. On Mount Pinatubo, Philippines, Battaglia and others (2004) used a similar approach to that of Got and others (1994) to relocate almost 11,000 events.

When locating similar earthquakes, a common approach is to use manually phase-picked events to seed stacks of similar events. Short windows of data are normally used, usually between 1.28 and 2.56 s after the P-wave arrival. Often such studies use triggered waveform data (records started by an amplitude trigger at the seismometer) instead of continuous waveform data, which are used here to identify multiplets. Past data sets are thus limited by what is triggered or located manually by the local seismic network and may be largely incomplete (Rowe and others, 2004).

Beginning in 1980, Mount St. Helens has been the most seismically active volcano in the Cascade Range. Increases in moment release in the shallow edifice are characteristically associated with explosive and effusive eruptions (Swanson and others, 1983). Earthquake multiplets at shallow depths were commonly observed at Mount St. Helens after 1982 and were used to obtain highly precise relative locations of earthquakes during the dome-building eruptions of September 10, 1984, and May–June 1985 (Frémont and Malone, 1987). Musumeci and others (2002) used similar events during the late 1990s to establish continuing magma recharge after 1992 into a storage zone at 5.5–10-km depth.

Since the beginning of the latest eruption in September 2004, less than 1 percent of the earthquakes detected have been routinely processed by the Pacific Northwest Seismic Network (PNSN) (Qamar and others, this volume, chap. 3), although care has been taken by PNSN analysts to extract a representative sampling of waveforms for the PNSN earthquake catalog. In this paper we (1) relocate the triggered earthquakes from the PNSN catalog to establish absolute locations, (2) identify and locate multiplets from the continuous seismic record, and (3) discuss the volcanological significance of our findings. We do not claim to classify every earthquake that has occurred during this period; instead, we present the absolute locations of the PNSN catalog data with a new velocity model and the characteristics of a representative set of multiplets that exhibit large populations and/or long lifespans. Especially of interest in this study are the relative locations and characters of the individual multiplets, how those characteristics change through time, and the relation of those characteristics to other phenomena. This information is important because we would like to assess the ability of multiplets to forecast eruptive activity or style.

This paper follows the time divisions used by Moran and others (this volume, chap. 2) to present the seismic evolution of the eruption. As it happens, station outages or station installations necessitated the use of additional time breaks to present consistent locations within a time period. Care has been taken across changes in network configurations to present a consistent and coherent picture of the seismicity.

Methods

Absolute Locations

Mount St. Helens has the densest seismic network of any volcano in the Pacific Northwest. Before the eruption in 2004, there were 13 permanent stations within 20 km of the volcano (fig. 2). Except for 11 days after the first phreatic explosion on October 1, a seismometer was positioned within 1 km of the new vent (McChesney and others, this volume, chap. 7), an arrangement that allowed an unusually accurate determination of absolute locations beneath the edifice compared to standard regional network locations. In this paper, we consider only earthquakes with eight picked P-wave arrival times, a maximum azimuthal gap of 135 degrees, and an arrival time pick within 3 km of the epicenter. The 3-km criterion is necessary for times when stations on the 1980s dome were saturated or destroyed. Additionally, we use a new velocity model (Thelen and others, 2006) to significantly reduce station corrections and improve locations (table 1, appendix 1). Absolute locations are determined with the program “SPONG,” a PNSN adaptation of FASTHYPO (Herrmann, 1979).

Uncertainties in absolute event location are given by the program SPONG, which was benchmarked against Hypoinverse (Klein, 1989; S. Malone, oral commun., 2006). These include uncertainties in phase picks and in the earthquake-location inversion scheme itself. To evaluate the effect of changing station configurations, we performed jackknife tests (Efron and Gong, 1983) by systematically removing seismic stations. Generally, removing crater stations reduced depth constraint but did not change the distribution of epicenters significantly (appendix 2). The reduced resolution in depth often produced “airquakes,” earthquakes with phase picks that resulted in depths above the velocity-model datum used in the solution. Airquakes were common in the existing PNSN earthquake catalog throughout the eruptive sequence at Mount St. Helens beginning in 2004. The uncertainties presented here do not include uncertainties in the velocity model, do not quantitatively account for changes in station configuration, and therefore are likely underestimates, especially in depth.

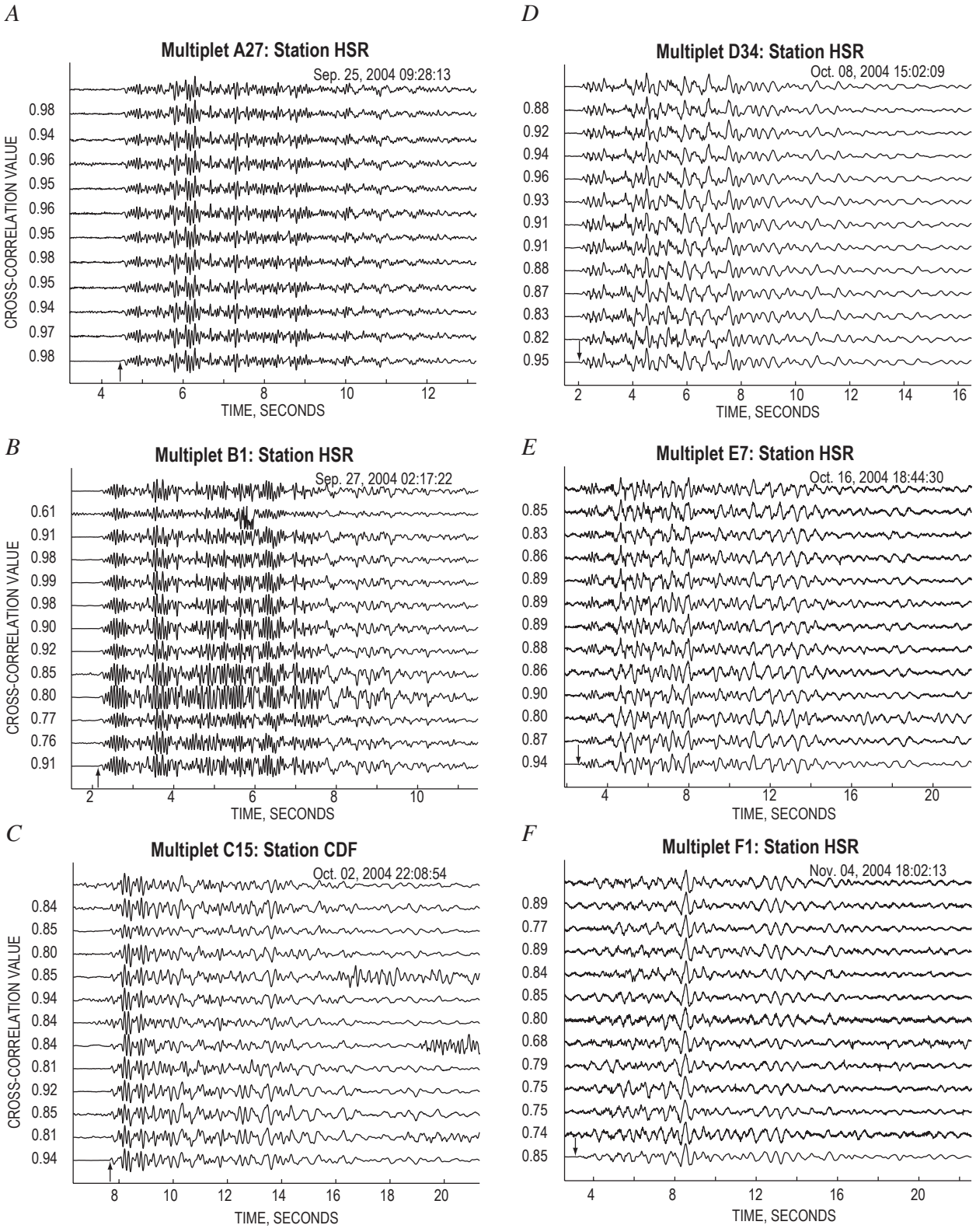

Figure 1. Example of waveforms from six multiplets analyzed in this study. Top trace in each is seed event for multiplet, and last trace is stack of all waveforms within multiplet at given station. Date and time on first trace are when seed event occurred. Arrow in bottom trace shows first arrival with polarity (up is compressional, down is dilatational). Station CDF has reversed polarity, so the first motion in *C* is actually down. Cross-correlation value of each trace with respect to seed event is shown on the y-axis. Waveforms are unfiltered and chosen at constant time intervals within the lifespan of their respective multiplets.

Classification of Multiplets

The PNSN catalog contains less than 1 percent of the total number of earthquakes, so entire groups of earthquakes have no representative in the catalog. As a result, we could not use the PNSN catalog as a starting point in searching for multiplets. Instead, our method for identifying multiplets started with a simple, highly sensitive threshold autopicker for which we selected a window of data around each trigger on the basis of the characteristic length of earthquakes in a given time period (10–20 s). Our autopicker typically missed the P-wave first arrival, so we included an empirically determined amount of time before the trigger (usually 1–3 s) in order to capture the entire event.

After the triggers were selected from the record, we cross-correlated, in the time domain, the first event to all other events at a particular station. Any event that was equal to or above the threshold cross-correlation coefficient (0.8) was considered part of that multiplet. The multiplet was then taken from the triggered events and stored. The next event that was not part of an existing multiplet was cross-correlated against all the remaining events and evaluated for events exceeding the cross-correlation coefficient cutoff. Any event that did not correlate with another event was considered an orphan and stored else-

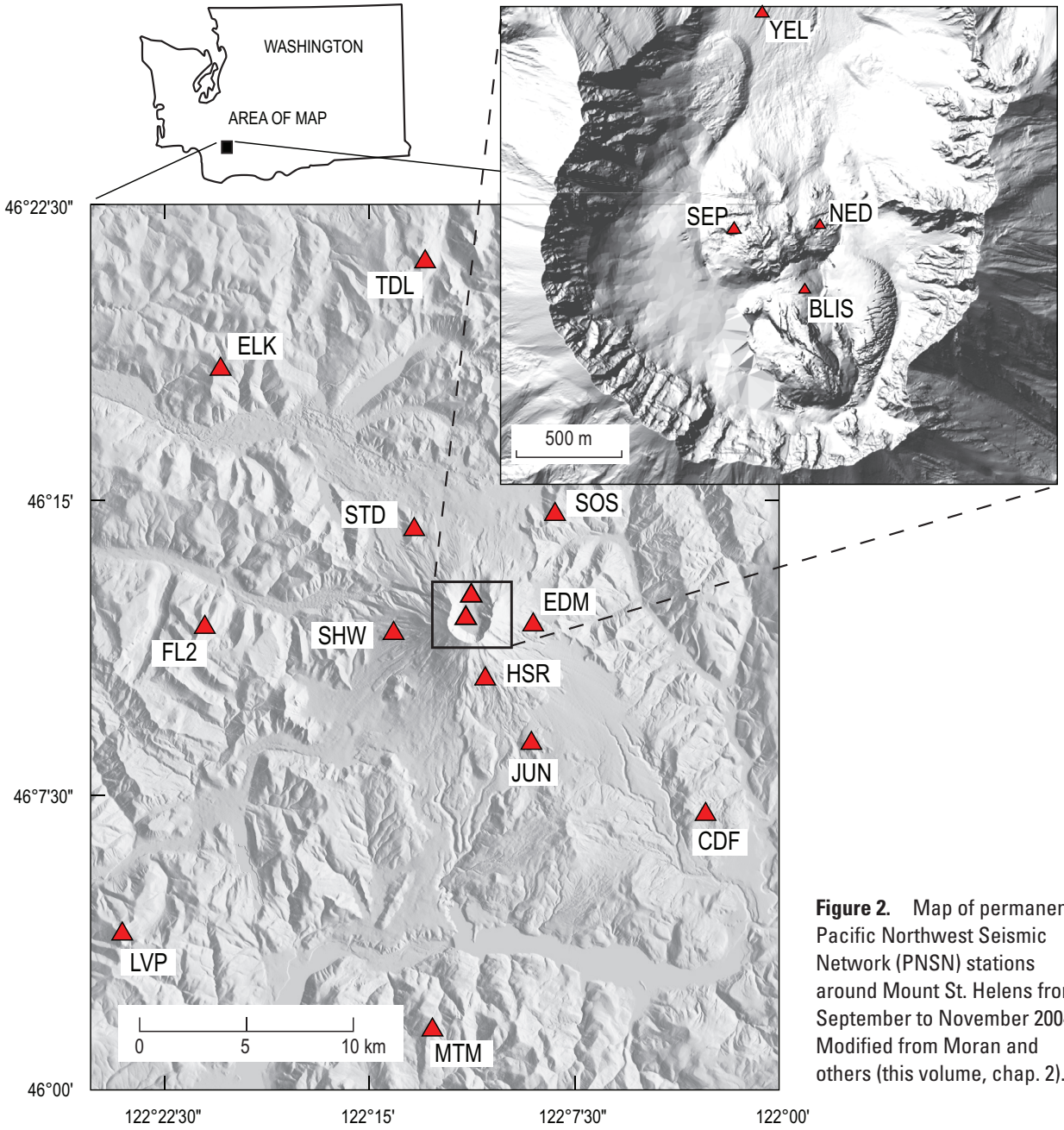

Figure 2. Map of permanent Pacific Northwest Seismic Network (PNSN) stations around Mount St. Helens from September to November 2004. Modified from Moran and others (this volume, chap. 2).

Table 1. Depth and velocity for P-wave model of Thelen and others (2006).

[Depth to top of layers defined by P-wave velocities; datum is altitude 2,200 m above sea level. Column 3 is the velocity model used for the relative locations, which assumes a Poisson solid in order to convert to S-wave velocity from the P-wave velocity of the one-dimensional model (appendix 1).]

Depth (km)	P-wave velocity (km/s)	S-wave velocity (km/s)
0	2.7	1.51
1.0	3.5	1.97
1.3	4.3	2.42
1.6	5.1	2.87
3.9	6.0	3.37
6.5	6.2	3.58
10.5	6.6	3.82
18.5	6.8	3.93
34.5	7.1	4.10
43.5	7.8	4.51

where. This process was repeated until all events were either classified into a multiplet or as an orphan. The multiplets were visually inspected to remove those with systematic noise such as calibration pulses and telemetry spikes, which can produce repeatable waveforms. Computer memory restrictions and the large number of triggers allowed us to process only about 10 days of data at a time. We therefore treated each time period individually and then combined the time periods by stacking multiplets from each time period and running the same analysis described above with event stacks instead of triggered data. This method served to combine time periods; however it also allowed for events with similar stacks to be combined even if individual events did not correlate at the initial threshold level. This technique of tracking multiplets has a disadvantage of using only one station to identify and classify multiplets, which makes it susceptible to near-site effects. However, Stephens and Chouet (2001) successfully used only one station to classify the multiplets before the 1989 eruption of Redoubt Volcano. We also visually checked other stations at the same distance range for the presence of the larger multiplets and ensured that near-site effects were not dominating the multiplet analysis.

Relative Location of Multiplets

After the identification of a multiplet, a representative event from that multiplet was chosen and cross-correlated against each hour of continuous data. Again, cross-correlation windows of 10–20 s were used, a choice based on the length of high signal-to-noise ratios throughout the waveform. Cross-correlation coefficients above a threshold were considered triggers. Three stations were required to have coincident triggers in order for the earthquake to be classified as a valid event. After the triggered events were compiled, all of the events were cross-correlated against each other at each station, and lags were noted at the maximum cross-correlation coefficient. Subsample estimates of lags were achieved in the time domain through polynomial interpolation of the cross-correlation coefficient peak. Lags were weighted by their normalized cross-correlation coefficient, and only lags with a cross-correlation above 0.8 were considered for earthquake locations. The lags for each event were then used to compute double-difference hypocenter locations with the hypoDD software (Waldhauser, 2001). For the initial location of the earthquakes within each multiplet, we stacked the multiplet and picked the first arrival of the stack at each station. Those picks were then applied to each earthquake in the stack on the basis of the lag derived from the cross-correlation. The picks were used to get absolute locations for each earthquake in the multiplet using the identical process as discussed above.

The use of long time windows meant that we were correlating dominantly S waves and Rayleigh waves. Most of the stations used in this study had a difference of 2 s or less between the P- and S-wave arrivals, meaning that at least 80 percent of the correlation window was composed of S waves and Rayleigh waves. Consequently, cross-correlating long time windows produced lags of phases that are traveling at S-wave velocities between the source and the receiver. We therefore elected to use an S-wave model for our relative locations. The S-wave model was obtained by assuming a Poisson's ratio for the crust and applying it to the P-wave model used in the absolute locations (table 1).

Errors in relative locations have several sources of uncertainty. One source is waveform alignment. Poorly aligned waveforms at a particular station may generate lineations in events toward that station (Battaglia and others, 2004). We minimized this source of uncertainty by using large time windows, which minimizes the occurrence of poorly aligned waveforms (Schaff and others, 2004). Another source of error in relative locations is uncertainty in the velocity model that the initial hypocenters start in (Michelini and Lomax, 2004). The path is canceled out by calculating the lag between two events, but the takeoff angle and azimuth are affected by the choice of an initial velocity model. In our analysis, we use a velocity model that is homogenous in the region of our cluster centroid. Changes in velocity, and therefore takeoff angle, only stretch or compress our cloud of hypocenters and do not affect the overall shape (appendix 3). Finally, artifacts in relative earthquake locations can be introduced through inhomogeneous phase lags on all stations in a solution. In other words, some stations will have a larger effect on the earthquake location than others, depending on the number of phase picks on that station. We tested this with the use of a jackknife test (Efron and Gong, 1983), a method in which one station is removed at a time and then all of the earthquakes within the multiplet are relocated, using the reduced station set (appendix 3). The change in location of each earthquake

was tracked, and the maximum offset of all of the stations in the north, east, and vertical directions is presented as the uncertainty in relative location.

September 23–October 5, 2004: Vent-Clearing Phase

Absolute Locations, September 23, 0000 PDT, Through September 25, 1200 PDT

Relocating a subset of catalog PNSN events with the updated velocity model revealed a tight cluster of earthquakes with a radius of 250 m centered immediately southeast of station SEP (fig. 3*A*). The depth cross section showed a cluster of hypocenters that was elongate toward the future vent. The cluster spanned depths of approximately 400 to 1,100 m below the future vent. The average number of phases used in the earthquake location during this time period was 9.32, with a maximum of 52. The mean azimuthal gap in this subset of earthquake locations was 90 degrees. A total of 229 earthquakes were relocated with formal uncertainties averaging 132, 92 and 84 m in the north, east, and vertical directions, respectively. Reductions in estimated uncertainties for the north, east, and vertical directions were 20, 35, and 74 percent when compared to the routine network locations.

Multiplets, September 23, 0000 PDT, Through September 25, 1200 PDT

The buildup of multiplets occurred at an accelerating pace until approximately 0200 on September 24 (fig. 4). All multiplets were composed of volcano-tectonic (VT) events and, in most cases, many multiplets were occurring simultaneously. Here we distinguish VT earthquakes from hybrid and low-frequency earthquakes, as was done by Moran and others (this volume, chap. 2). Examples of frequency spectra of hybrid versus low-frequency earthquakes versus VT earthquakes, as defined in this paper, are shown in figure 5. The maximum number of multiplets with populations greater than 20 occurring concurrently was eight at 0200 PDT on September 24, coincident with the maximum of earthquake amplitudes on station JUN during this time period (fig. 4). After the maximum in earthquake amplitudes on September 24, seismic activity waned until September 26. None of the early multiplets recurred after seismic activity ramped up again on September 26, 2004.

The largest magnitude multiplet during this period, A27 (figs. 1, 6), was a group of 59 VT events that occurred over approximately 3 hours beginning at 1104 PDT on September 25. Picking the first arrivals of the stacked traces of A27 on each station and locating the multiplet with standard absolute-location techniques resulted in a location at the south end of the cluster of epicenters in figure 3*A*, at depths near the top of the cluster. The absolute location of the stack used only six phase picks, giving the location of the hypocentroid the largest uncertainty of any multiplet analyzed. Double-difference relocations of this swarm reveal a tight cluster, spanning less than 10 m in depth and about 5 m horizontally (fig. 6*A*). Orthogonal cross sections show mostly vertical orientations, which are an artifact of different stations' picks being used for different events. Uncertainty estimates are on the order of 3 m horizontally and 20 m vertically. In figure 6, the generally small average errors are masked by a few larger errors as great as 40 m. The cross-correlation values of the first event to subsequent events in the multiplet are nearly constant. Considering the location errors and constant cross-correlation values, we suggest that the earthquakes in this multiplet occurred at nearly the same location. The end of this multiplet coincided with the waning seismic activity of the swarm on September 25 (Moran and others, chap. 2, their figs. 4, 5).

Absolute Locations, September 25, 1200 PDT, Through October 1, 1200 PDT

Absolute locations of 313 PNSN catalog events during this time period showed a distinct shift up and to the south compared to those of the previous period (figs. 3*B*, 7). The decrease in earthquake depth was consistent with phase-pick differences identified by Moran and others (this volume, chap. 2; fig. 7) between September 25 and September 27. This cluster, too, was tightly spaced in depth (250 m radius) and in epicenter (300 m radius), with respect to other absolute locations. The hypocentroid shift compared to the swarm beginning September 23 was 133 m south, 69 m east, and 221 m up. The average number of stations used was 11, the average gap was 78 degrees, and the average distance from the epicenter to the closest station was 115 m. Uncertainties in event locations averaged 109 m north-south, 140 m east-west, and 119 m in depth.

Multiplets, September 25, 1200 PDT, Through October 1, 1659 PDT

Multiplets were present throughout this time period and occurred in two phases before the explosion on October 1 (fig. 4). The multiplets had lifespans of 1–2.5 days. Their first buildup started at approximately 1200 PDT on September 25, 2004. Accompanying an increase in the number and lifespan of the multiplets was an increase in the maximum amplitudes of the continuous data averaged over 1-minute intervals at station JUN (fig. 4). The second buildup started around midday on September 29 and continued until the explosion on October 1. The second phase is identified by the end of multiplets from the first phase of buildup and the occurrence of new multiplets. The transition coincided with a 250 percent increase in the maximum amplitude of signals recorded at station JUN (fig. 4). Thirteen multiplets that

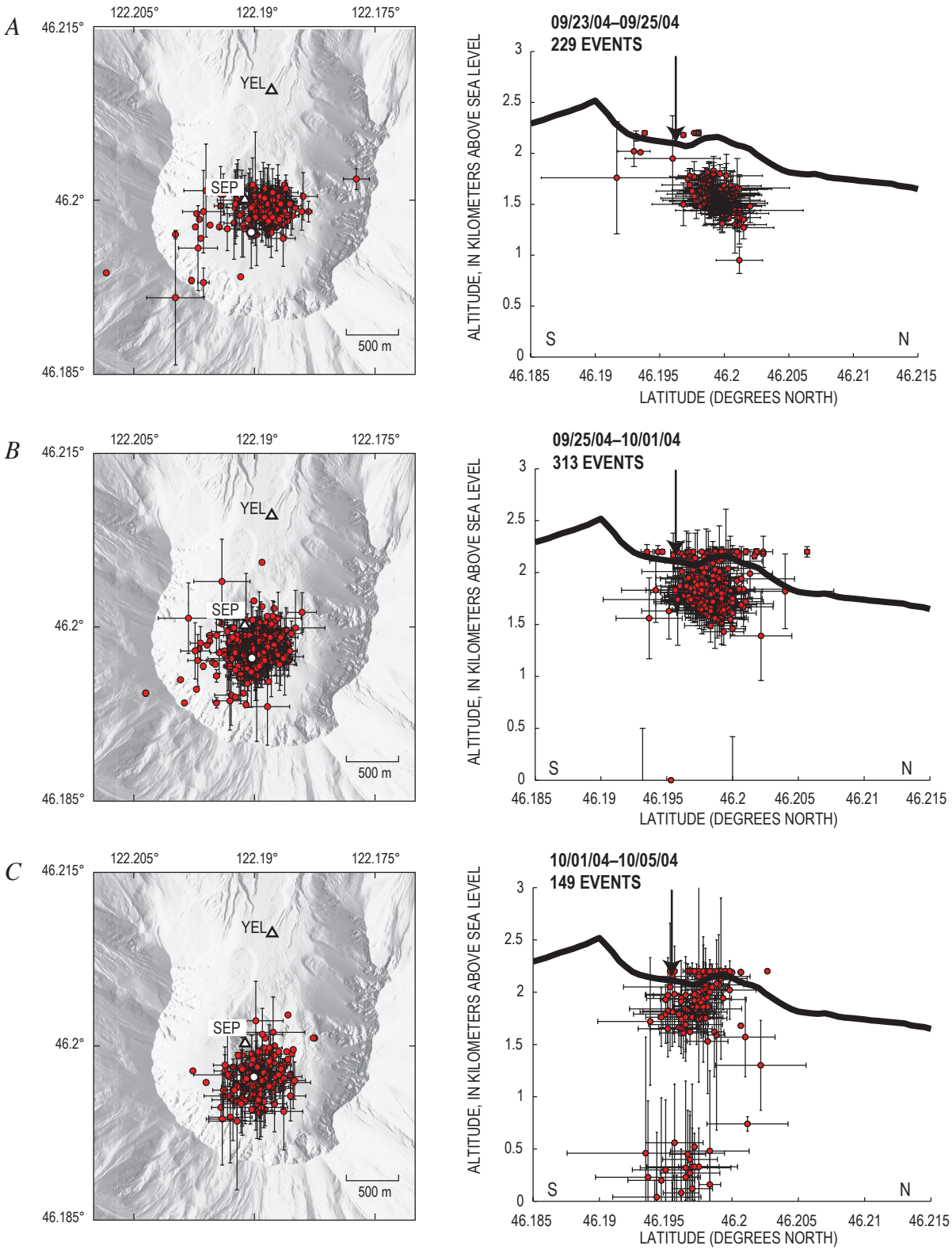

Figure 3. Absolute locations for Pacific Northwest Seismic Network (PNSN) catalog events for three time periods. Earthquakes plotted have eight or more phase picks, azimuthal gap of less than 135 degrees, and a phase pick at a station closer than 3 km from epicenter. Error bars are from SPONG location output. Permanent seismic stations shown on maps by black and white triangles. Cross sections show earthquake depth plots and topographic surface profile north-south through station SEP. White dot in map view and arrow in cross section show approximate location of vent.

were active before the October 1 explosion recurred after the explosion. Multiplets occurring after September 25 at 1200 PDT and through November 2004 were overwhelmingly hybrid and low-frequency earthquakes.

One multiplet, B1, started September 27 and continued for approximately 2.5 days (fig. 6*B*). The absolute location of the stacked traces formed a hypocentroid at 520-m depth, with an epicentroid centered in the cluster in figure 3*B*. The absolute location solution used 12 stations and had impulsive arrivals at all stations, making it one of the most reliable locations of the multiplets studied. The polarity of first arrivals was mixed and was consistent with reverse faulting on a north-striking, vertical or steeply dipping (85º–90º) fault. Relative locations of hypocenters are concentrated inside a sphere less than 15 m in diameter (fig. 6*B*). Location errors derived from jackknife techniques reveal uncertainties in the north, east, and vertical directions of 1.9 m, 1.3 m, and 1.3 m, respectively. The cross-correlation coefficient of the first event relative to each subsequent event decays with time, indicating a systematic temporal change in either the path between the earthquake and the receiver or a very small shift in location (Gret and others, 2005).

Absolute Locations, October 1, 1700 PDT, Through October 5, 1659 PDT

The absolute locations of 149 PNSN catalog events between the October 1 explosion and the end of October 5 apparently varied more widely in depth than those of the two previous time periods (fig. 3). However, with the destruction of station SEP during the October 1 explosion, the depths were less well constrained than in previous earthquake sets. In addition, emergent P-wave arrivals and overlapping codas made picks at the remaining crater station (YEL) and flank stations (HSR, EDM, SHW, and STD) sparse and imprecise, further affecting the depths. The effect of this can be seen as a cluster of seismicity that was falsely centered at 400-m

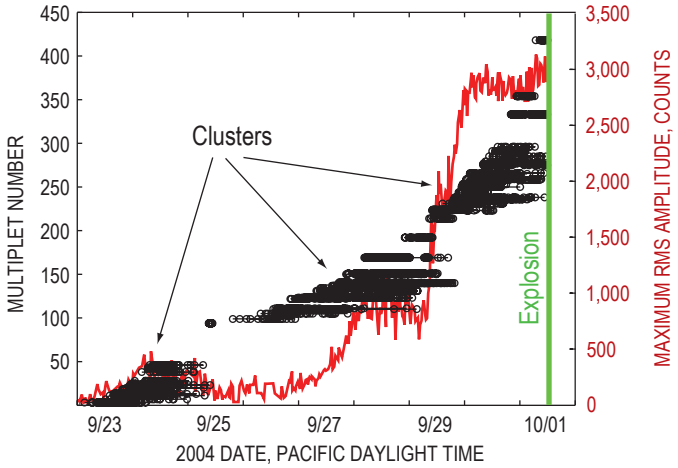

Figure 4. Timeline of multiplets from September 24, 2004, until explosion of October 1, 2004 (green line), detected on station HSR. Each earthquake is plotted as a circle, and multiplets are identified by a horizontal line through events that define multiplet. Only multiplets that have more than 20 events are plotted. Maximum root-mean-squared (RMS) amplitude averaged over 1 minute at station JUN shown in red.

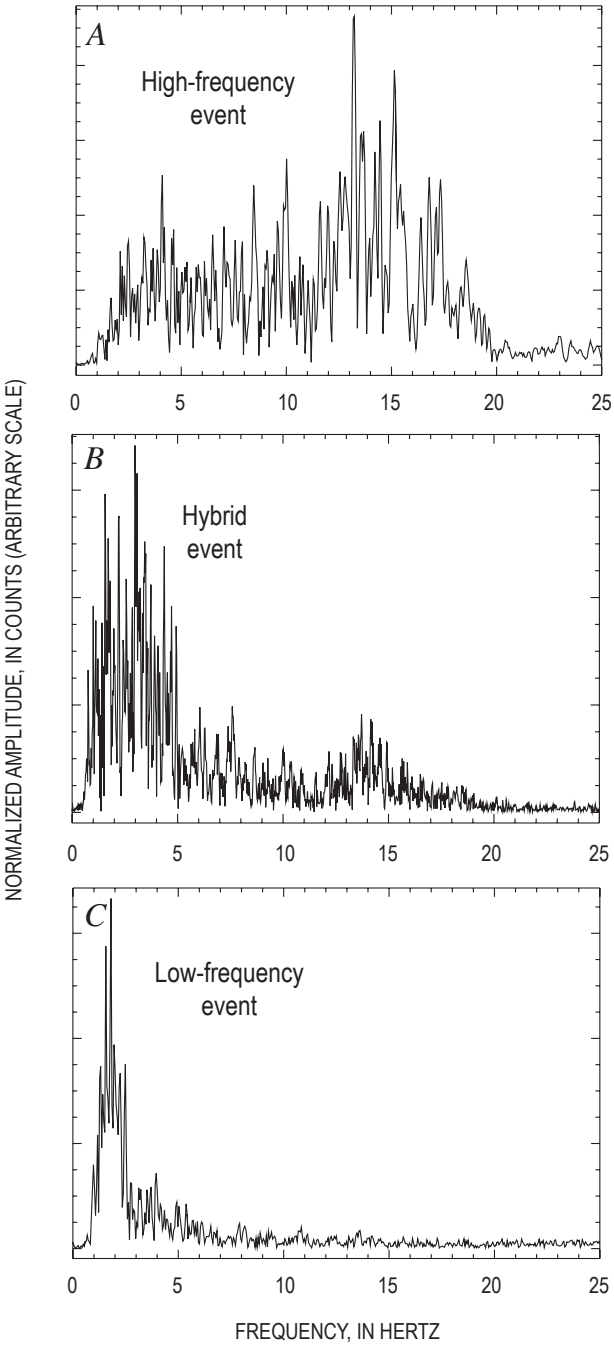

Figure 5. Examples of frequency spectra. High-frequency energy is seen between 12 and 20 Hz in high-frequency and hybrid events but not in low-frequency event. *A*, High-frequency event from September 25, 2004. *B*, Hybrid event from seed event of multiplet B1. *C*, Seed event of low-frequency multiplet F1 on station HSR.

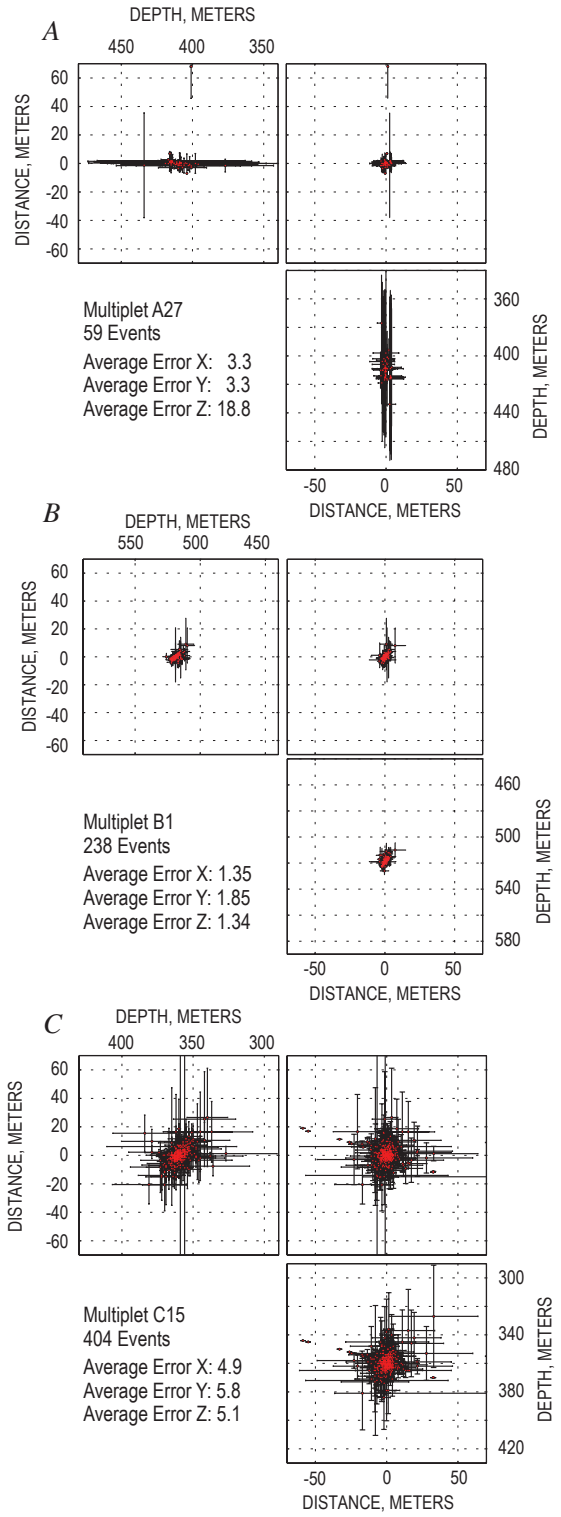

Figure 6. Relative relocations for three multiplets from the beginning of unrest through the period of phreatic explosions. For each, upper right square is map view (north at top), and left and bottom plots are cross sections. Plots are presented as cube with two sides folded out. Errors determined through jackknife techniques. Directions X, Y, and Z correspond to east, north, and vertical, respectively.

altitude owing to a lack of picks at station YEL (fig. 3*C*). Earthquake-location solutions used an average of 10 stations with an average gap of 81 degrees and an average delta of 1.52 km. Uncertainties in x, y, and z were 124, 146, and 244 m, respectively.

Multiplets, October 1, 1700 PDT, Through October 5, 1659 PDT

Several small-population multiplets were present during this time period (fig. 8). These multiplets consist of hybrid and low-frequency event families. There were three explosions and two episodes of tremor during this time period, in some cases concurrent with the start or stop of a multiplet. In most cases, however, multiplets during this time period continued largely unaffected by the occurrence of tremor or explosion.

One large low-frequency multiplet, C15, started 7 hours after the explosion on October 1. The absolute location of this multiplet using event stacks revealed a hypocentroid 100 m south and 160 m shallower than B1. Using a similar station configuration for both event stacks (no station SEP) shows approximately the same offset in location. Polarities from first arrivals of the multiplet stack were all dilatational, a characteristic for other earthquakes in this sequence, especially after October 1 (Moran and others, this volume, chap. 2; Qamar and others, this volume, chap. 3). This multiplet possessed highly stable amplitudes and cross-correlation coefficients in time. The relative relocations of 404 events from the C15 multiplet show a cluster of seismicity spanning approximately 20 m in diameter (fig. 6*C*). Some events of

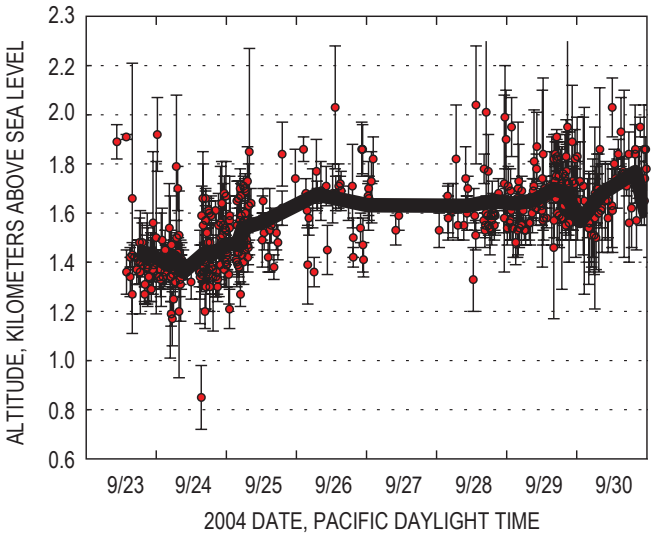

Figure 7. Earthquake altitude as function of time, September 23–30, 2004. Black line is running average altitude of 20 nearest earthquakes in time. The apparent gap in earthquakes between 9/26 and 9/28 is artificial, caused by a lack of earthquakes with location parameters that met our criteria and not by diminished seismicity.

the main cluster may have indicated a south-dipping structure; however, the overwhelming majority (75 percent) of the earthquake hypocenters were within the circular cluster. Using jackknife error techniques, we determined the locational uncertainties in north, east, and depth to be 5.8, 4.9, and 5.1 m, respectively.

October 5–November 20, 2004: Seismicity Associated with Dome Building

Absolute Locations, October 5, 0000 PDT, Through October 11, 1659 PDT

As with those between October 1 and October 5, earthquake arrivals at crater and flank stations were highly contaminated with earthquake codas from previous earthquakes and plagued with emergent signals. Thus, large uncertainties existed in the absolute locations, particularly in depth (fig. 9*A*). The spread of earthquake depth is suspect, owing to the absence of station SEP and the poor character of the first arrivals on station YEL. During this time period the absolute-location solutions of 227 events used an average of 10 stations, with an average gap of 89 degrees. The average distance to the nearest station was 1.15 km. Average uncertainties were 142 m in the north-south direction, 130 m in the east-west direction, and 226 m in depth.

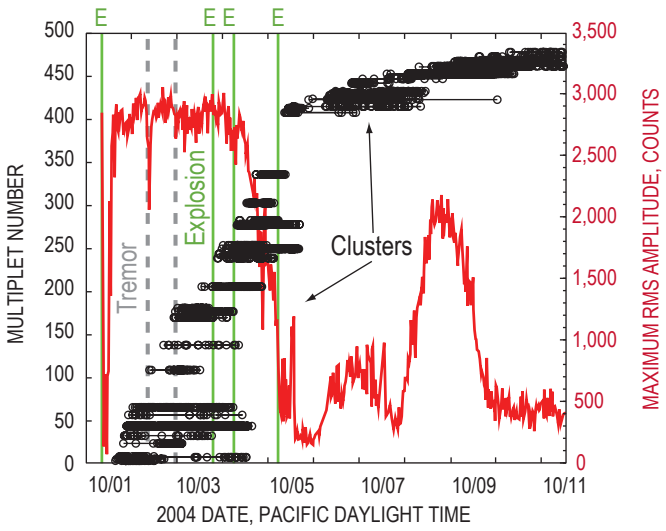

Figure 8. Timeline of multiplets from explosion of October 1 (leftmost green line) through October 11, 2004, detected on station ELK. Each earthquake is plotted as a circle, and multiplets are identified by a horizontal line through events that define multiplet. Only multiplets having more than 20 events are plotted. Maximum root-mean-squared (RMS) amplitude averaged over 1 minute at station JUN shown in red. Explosions, vertical green lines; tremor episodes, vertical gray lines.

Multiplets, October 5, 0000 PDT, Through October 11, 1659 PDT

Although four multiplets continued briefly through the explosion on October 5, a new temporal group of multiplets began about 1200 PDT on October 5. These multiplets generally had longer lifespans than previous multiplets, and fewer multiplets were occurring at the same time. Hybrids and low-frequency earthquakes dominated the seismic record. Multiplets during this time period did not obviously correspond to changes in the maximum amplitudes of signals recorded on station JUN.

The D34 hybrid multiplet discussed by Moran and others (this volume, chap. 2, their fig. 11) occurred during this time period. This multiplet consisted of 681 events starting October 8 at 0200 PDT. Absolute locations determined from the first arrivals of event stacks revealed a hypocentroid in the same location as multiplet C15. As was the case for C15, the polarities of the first arrivals were all dilatational. This multiplet methodically increased its amplitude before reaching a plateau and then decreased again to near the initial amplitude level (Moran and others, this volume, chap. 2). Magnitudes at the beginning were in the range M_d 1–1.5 and at the maximum were M_d 2.5–3.0. The cross-correlation coefficient of the first event to all others declined until the plateau in amplitude, and then remained constant for the rest of the sequence. Relative relocations of this cluster reveal a different pattern from that in previous multiplets. The hypocenter volume was tabular, striking to the southwest (fig. 10*A*). Uncertainties derived from jackknife tests showed errors of 2.7, 2.3, and 2.5 m, in the north-south, east-west, and vertical directions, respectively.

Absolute Locations, October 11, 1700 PDT, Through November 4, 1559 PST

During this period, low-frequency earthquakes dominated the seismic record. These earthquakes possessed emergent arrivals and thus had high uncertainties in absolute locations (fig. 9*B*). Earthquakes were extremely difficult to pick at stations outside the crater because of coda interference from previous events and poor arrivals. On October 12, station BLIS was installed on the saddle between the old and new domes (McChesney and others, this volume, chap. 7; fig. 2 for location). This station was used in less than half of the locations, however, owing to consistently emergent arrivals. Over the period of a month, only 130 earthquakes located by the PNSN met our selection criteria. For these earthquakes, an average of 10 stations were used for location solutions, with an average gap of 96 degrees and an average distance to the closest station of 431 m. Uncertainties in the north-south, east-west, and vertical directions were 142, 130, and 227 m, respectively.

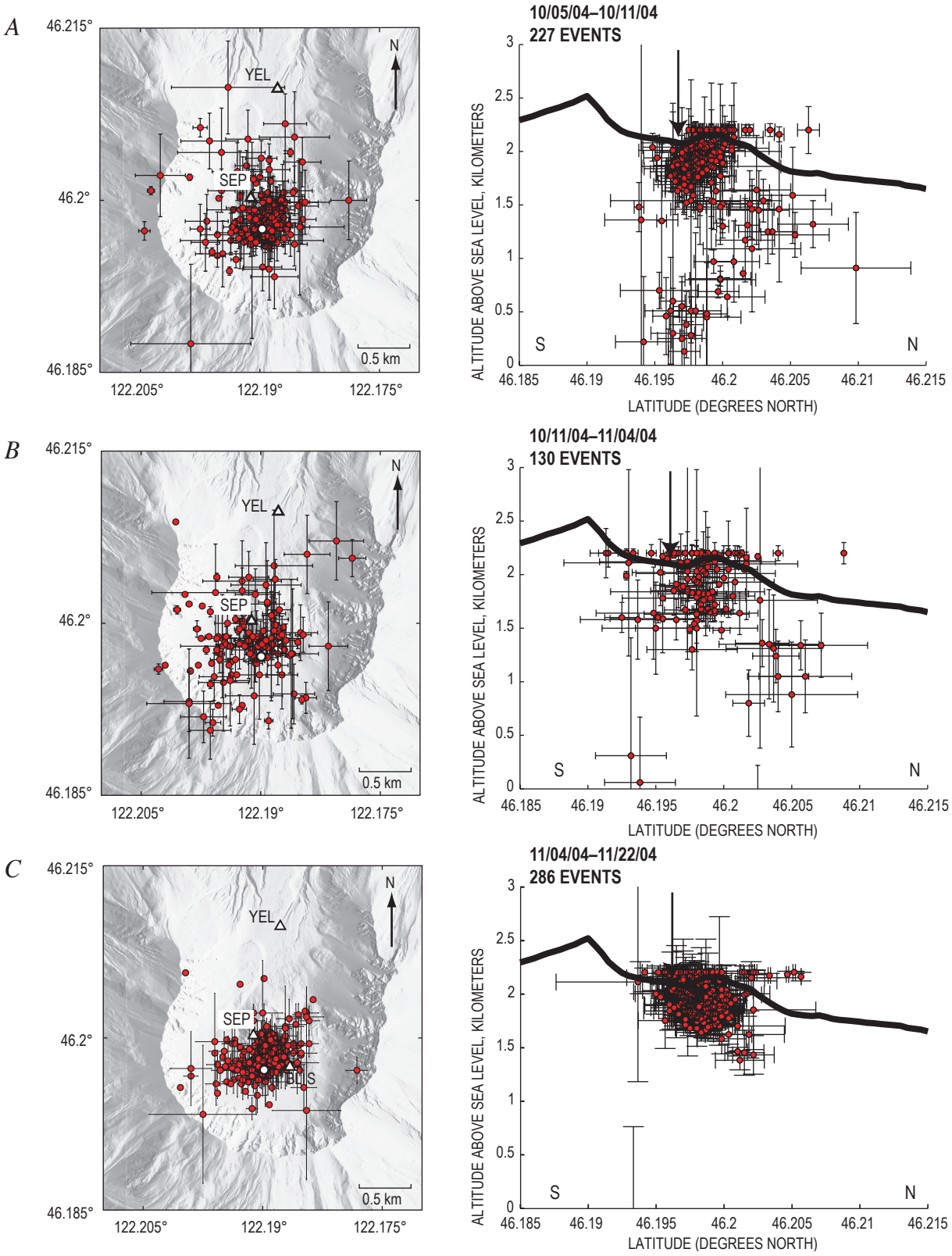

Figure 9. Absolute locations for Pacific Northwest Seismic Network (PNSN) catalog events for given time periods. Map views shown on left, cross sections on right. Permanent PNSN seismic stations shown with white triangles. Cross sections are north-south through station SEP, which was destroyed by explosion on October 1 and not reinstalled until November 5, 2004 (shown in top two plots only for reference). Earthquakes selected using same criteria as in figure 3. White dot (map view) and black arrow (cross section) show approximate location of vent.

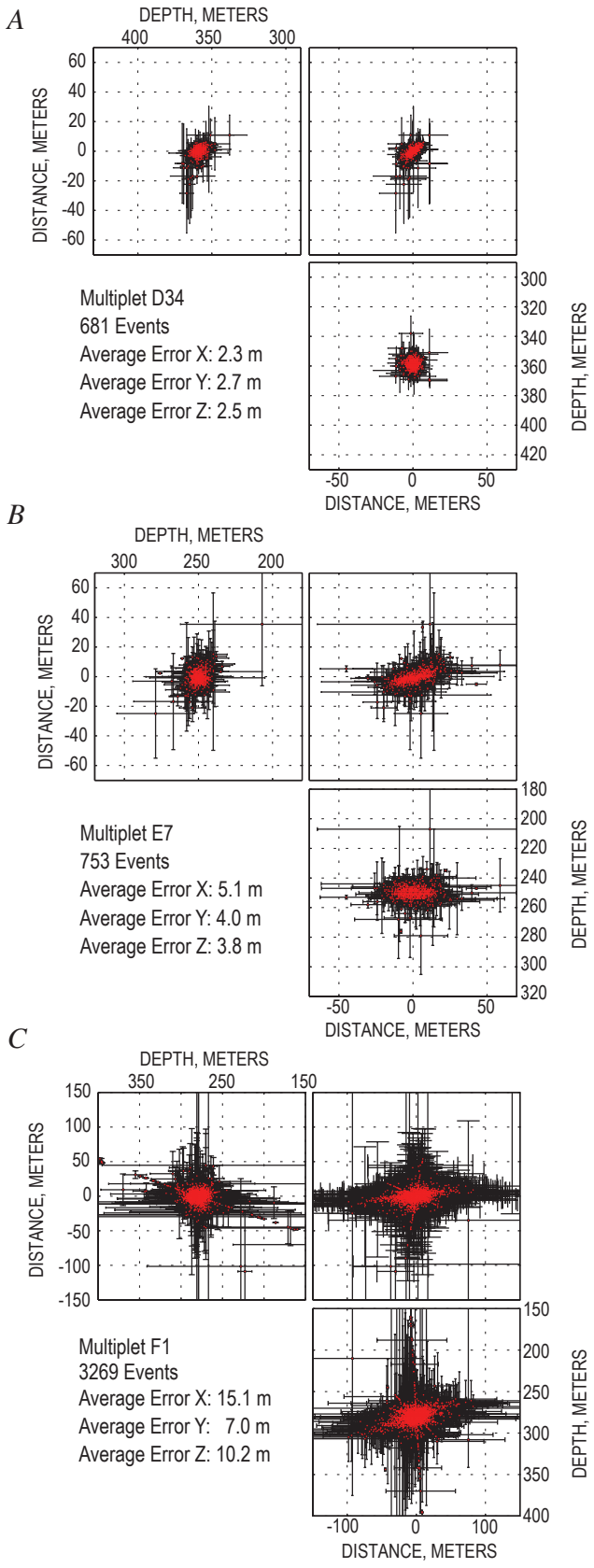

Figure 10. Relative relocations for three multiplets from early October to late November 2004. See figure 6 for explanation of views and errors.

Multiplets, October 11, 1700 PDT, Through November 4, 1559 PST

October 11, 2004, marked the first time new lava was seen at the surface (Vallance and others, this volume, chap. 9). Between then and November 4, three different spines were extruded, accompanied by comparatively low seismicity rates. Multiplets in the beginning of this time period had lifespans comparable to multiplets beginning after the October 5 explosion (figs. 8, 11), but multiplets with lifespans more than 1 month long began to occur later in the study period. In general, multiplets starting after October 22, 2004, had substantially longer lifespans than earlier multiplets. However, there was no obvious correlation between spine extrusion and the occurrence of multiplets during this time period.

One multiplet, E7, consisted of 753 events and started on October 16. Peak-to-peak amplitudes were stable and the cross-correlation coefficients of the first event compared to all others were nearly constant. The absolute hypocentroid from first-arrival picks of event stacks resulted in a location similar to that of multiplets C15 and D34. The polarities of first arrivals from event stacks all showed dilatation. The distribution of hypocenters was tabular, like that of D34, but had a more westerly strike (fig. 10*B*). The tabular distribution of epicenters had a long axis of approximately 40 m and a short axis of 10 m or less. The relative hypocenters spanned depths from 240 to 260 m. Uncertainties derived from jackknife analyses revealed average errors in location of 4.0, 5.1, and 3.8 m in the north-south, east-west, and vertical directions, respectively.

Absolute Locations, November 4, 1600 PST, Through November 22, 1559 PST

On November 5, station SEP was reinstalled (McChesney and others, this volume, chap. 7), increasing to three the number of stations within 2 km of the actively extruding spine. This addition proved important for locating earthquakes, as there were reliable picks from three close-in stations for almost all events. Absolute locations for 286 PNSN catalog events showed a 300-m-radius cluster with an epicentroid located only 160 m from the active vent (fig. 9*C*). The hypocentroid was located less than 400 m below the surface. The addition of the closest station, BLIS, on October 12, improved the sensitivity of the network to earthquakes, but comparing locations determined with and without BLIS is problematic. By ignoring station BLIS, we simulated the station configuration before October 1, 2004. The effect of taking out station BLIS was to make events slightly deeper on average, but the epicenters remained nearly unchanged. Details of these tests can be found in appendix 2. These tests suggest that the hypocentroid during this time period was at the same depth as the hypocentroid for the time period between September 25 and October 1, 2004, within error (figs. 3*B*, 6*C*). During the time period between November 4 and November 22, 2004, the earthquake-location solutions used an average of 10 stations, with an average gap of 96 degrees and

an average distance from the epicenter to the nearest station of 45 m. Average uncertainties in the north-south, east-west, and vertical directions were 134, 107, and 122 m.

Multiplets, November 4, 1600 PST, Through November 22, 1559 PST

As was the case for the previous time period, multiplets during this time period possessed lengthy lifespans that included long periods of quiescence (fig. 11). As before, many multiplets were concurrent. One of the most prominent multiplets during this period, F1, consisted of 3,269 events that began on November 4 at approximately 1700 PST and lasted for more than 20 days. The absolute location derived from first-arrival picks of earthquake stacks resulted in a location south of all other multiplets analyzed in this study. The emergent first arrivals in the earthquake stacks produced large pick uncertainties. Resulting large uncertainties in the absolute locations as a result of the large pick uncertainties means that we cannot distinguish the absolute hypocentroid of F1 from those of other multiplet locations. Relative relocations of F1 formed a tabular volume similar in shape to multiplet E7 (Oct. 16 start) (fig. 10*B*). The epicentral distribution of multiplet F1 had a long axis of approximately 100 m and a short axis of 20 m. The cluster was confined to depths of 260 to 300 m. Average uncertainties derived from jackknife analyses in the north-south, east-west, and vertical directions were 7.0, 15.1, and 10.2 m, respectively.

Discussion

Absolute Locations

The high-frequency nature of the earthquakes between September 23 and September 25, 2004, suggests that the earthquakes during this time period were fracturing brittle rock. Although the uncertainties in latitude and longitude are on the same order of magnitude as the epicentral shift between September 23 and September 25, we believe the phase pick differences outlined by Moran and others (this volume, chap. 2) support the observed shift in epicentroid location. The upward and southward migration of

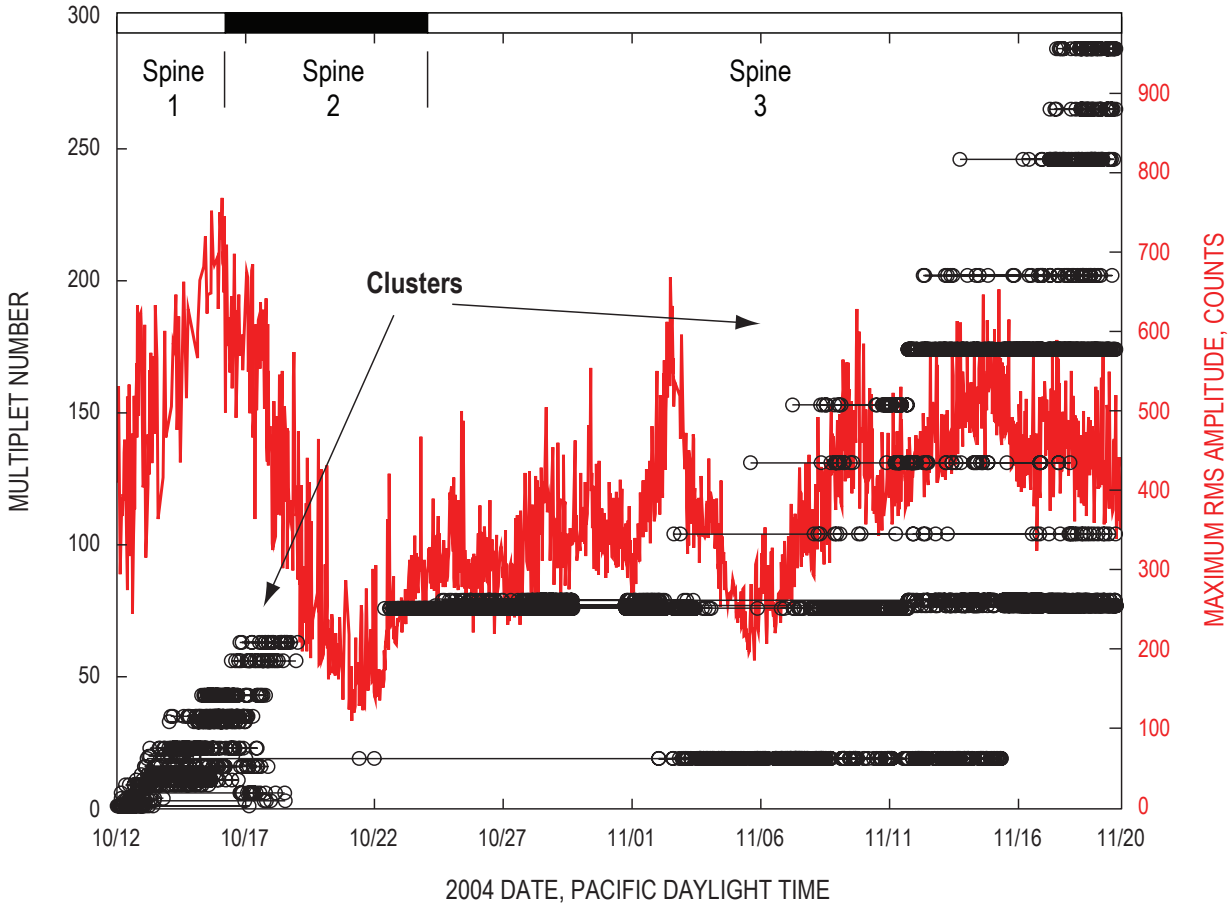

Figure 11. Timeline of multiplets detected on station ELK from October 12 through November 20, 2004. Each earthquake is plotted as a circle, and multiplets are identified by a horizontal line through events that define multiplet. Only multiplets that have more than 20 events are plotted. Maximum root-mean-squared (RMS) amplitude averaged over 1-minute intervals at station JUN shown in red. Date tickmarks are beginning of day, 0000 hr (midnight). Note change in amplitude scale compared to figures 4 and 8. Bar on top shows dome extrusion chronology (from Vallance and others, this volume, chap. 9).

absolute hypocenters between September 24 and September 26 and the shift to dominantly hybrid earthquakes suggest that the seismicity was occurring in response to a magmatic plug moving toward the surface (fig. 7). The shift occurred before any surface deformation near the 1980–86 dome (Dzurisin and others, this volume, chap. 14), although the continuous GPS at Johnston Ridge Observatory (JRO) did detect deflationary movement toward the volcano (Lisowski and others, this volume, chap. 15). An upward shift in hypocenters in the 1989 Ito-oki submarine eruption was explained as an upward propagating dike (Ukawa and Tsukahara, 1996). Their model showed that seismicity could occur above the crack tip in response to the dilatation of the crack below. Although this conclusion is plausible in hindsight at Mount St. Helens, the character and absolute locations of the earthquakes in the swarm between September 23 and September 25 alone probably would have not been enough to forecast an impending eruption.

After the first phreatic explosion on October 1, 2004, the loss of station SEP and consistently high seismic amplitudes on station YEL prevented the precise picking of events on crater stations. The absolute locations thus show greater scatter, have larger uncertainties, and are skewed in depth owing to the lessened station coverage. Jackknife tests performed by removing stations SEP and YEL from earthquake locations from September 25 to October 1 reveal depth patterns in seismicity similar to those seen for absolute earthquake locations calculated between October 1 and November 4. In essence, the precision in depth was poorer with the absence of stations SEP and YEL. This made relatively deep earthquakes deeper and shallow earthquakes become shallower (appendix 2). The locations were also more vertically aligned, similar to the absolute locations from October 1 through October 5 (fig. 3). The epicenter distribution in jackknife tests was nearly unchanged. We therefore suggest that the absolute locations for earthquakes from October 1 through October 5 were similar to those occurring before the first explosion. Similar tests indicate that locations for earthquakes after the October 5 explosion were similar to locations between September 25 and October 1 (appendix 2).

Absolute locations from November 5 to November 22 show that earthquake locations shifted slightly both up and south compared to pre-October 1 seismicity. The character of seismicity did not change significantly between October 16 and November 5, and we suggest that seismicity after the middle of October had similar absolute locations. The hypocentroid of absolute locations from November 5 to November 22 was ~290 m below the surface. Patterns in absolute locations between September 23 and November 22 indicate a conduit plunging 45º–60º northward at shallow depth beneath the old dome. The shape of the pattern is robust to changes in station layout (appendix 2); therefore we are confident the pattern is real.

Multiplets

A striking feature of seismicity during the early months of seismic unrest and eruption was the overwhelming presence of multiplets. Discrete multiplets occurred simultaneously throughout the study period; however, many can be further grouped into multiplet clusters. Here, we define a multiplet cluster as several multiplets that occurred simultaneously. Multiplet clusters often build slowly and end abruptly (figs. 4, 8, 11). On September 25, September 29, October 1, and October 5, the abrupt end of one cluster and the start of another was accompanied by changes in the amplitude of seismic signals recorded at station JUN (figs. 4, 8). No cluster recurred at any point during the study period, but in at least one case a multiplet within a previous cluster recurred after the cluster had ceased. The distinct clustering in time of multiplets may indicate that a particular source region was active during a cluster, with each multiplet having a different mechanism or occurring at a different location within the cluster source region. As each source region was altered or destroyed, a new cluster began from a new source region. Temporal clusters of multiplets were also observed at Soufrière Hills volcano, Montserrat, and were found to be related to the time derivative of the tilt (Green and Neuberg, 2006). Peaks in the real-time seismic amplitude measurement (RSAM), similar to the maximum amplitudes used here, were well correlated with peaks in the tilt at Soufrière Hills volcano; however, the relation between the RSAM and the occurrence of clusters of multiplets was not explicitly stated.

At Mount St. Helens, the absolute hypocentroid of each analyzed multiplet was similar when determined from stacks of each multiplet recorded at each station. All of the analyzed multiplets had locations within ~100 m of station BLIS at depths of 250 to 350 m (fig. 12). Further, the cross-correlation coefficients between each of the analyzed multiplets had values ranging between 0.17 and 0.50. This suggests that highly stable but distinct sources were present within a small source region at shallow depth beneath the 1980–86 dome. Similarly, the absolute location of multiplets that occurred at Soufrière Hills volcano in 1997 clustered tightly together, and Neuberg and others (2006) used this evidence to help argue for a pressure-dependent source for the occurrence of multiplets.

Multiplets also varied in lifespan. Generally, multiplets earlier in the study period had shorter lifespans than those occurring later. Lifespans of more than 1 month were observed for some multiplets during the dome-building phase of the eruption, suggesting a stable and stationary source region. Such long event families have only been reported at Shishaldin Volcano, Alaska (Petersen and others, 2006). However, very few studies have covered periods of time longer than days to weeks with continuous data. Amplitudes of events within individual multiplets were highly variable. However, changes typically varied smoothly with time. The magnitudes of events in large-population multiplets also ranged widely, from M_d –0.2 to M_d 3.0.

A steady decline in the cross-correlation coefficient between the first and subsequent events is observed in many multiplets. An example of this phenomenon is multiplet B1 (fig. 13). This change in cross-correlation coefficient could result from a shift in location or a change in the path between

an earthquake and the recording station. Gret and others (2005) exploited the sensitivity of the coda to changes in path to distinguish changes in location from changes in path at Mount Erebus, Antarctica. They compared the cross-correlation values of event families using windows in different parts of the earthquake waveform. A similar analysis of multiplets here reveals similar patterns in correlation coefficients of the first event to each subsequent event, regardless of the time window used (fig. 13). We therefore interpret the change in cross-correlation values with time to result from small changes in location that are within the uncertainty of our relative locations.

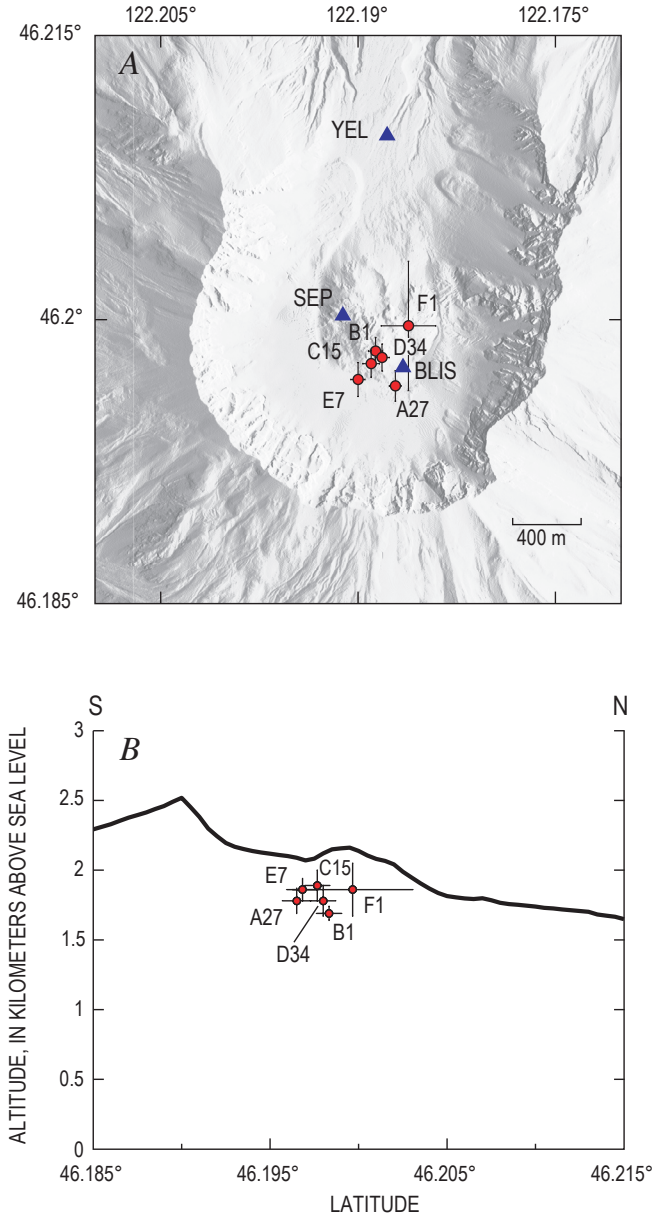

Figure 12. Absolute locations, obtained using first-arrival picks of event stacks, for multiplets depicted in figures 6 and 10. *A*, Map view. Blue triangles, permanent Pacific Northwest Seismic Network (PNSN) seismic stations as of November 4, 2004. *B*, Locations projected on north-south cross section through station SEP.

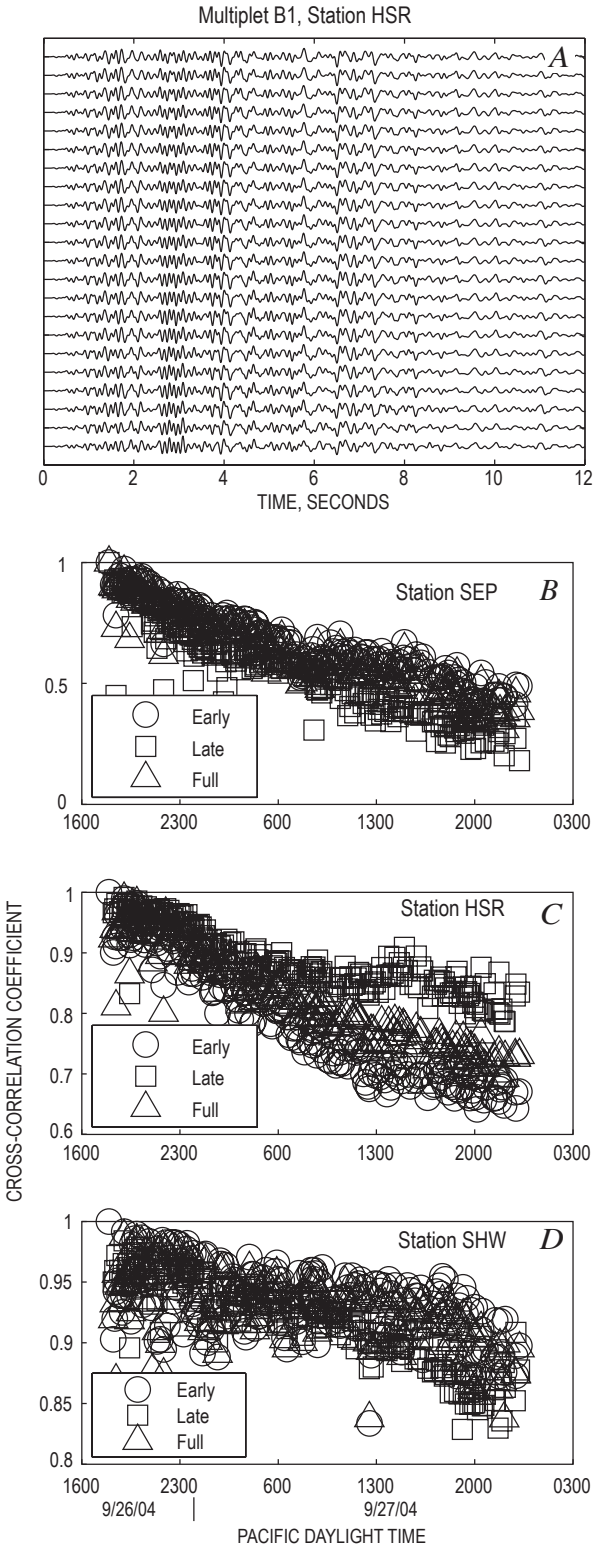

Figure 13. Cross-correlation analysis of first 220 events from multiplet B1. *A*, Waveforms filtered between 1 and 10 Hz of every tenth earthquake recorded on station HSR. *B–D*, Cross-correlation values as a function of time at stations SEP, HSR, and SHW, respectively. Three parts of waveform are used in each plot: first 4 s (early), next 4 s (late), and entire waveform (full).

Only the explosion on October 1 and, to a lesser extent, the explosion on October 5 significantly affected the occurrence of multiplets. After the October 1 explosion, all earthquakes, including multiplets, stopped for more than 3 hours (Moran and others, this volume, chap. 2). Several multiplets then restarted, and new multiplets began as the level of seismicity increased. This process repeated itself during periods of tremor and explosions occurring between October 1 and October 5; some multiplets already present continued and, in many cases, new multiplets began. The reactivation of multiplets and general seismicity after the October 1 explosion suggests that the phenomenon leading to the generation of multiplets during the time period around October 1 may be pressure dependent (Moran and others, this volume, chap. 2). The relation between the October 5 explosion and the occurrence of multiplets is less clear, because four multiplets continued through the explosion and another multiplet cluster started shortly after.

Relative locations of multiplets during the period we studied define a changing source volume. Between September 23 and October 5, hypocenters of multiplets defined a small equidimensional space, but after October 5 they defined larger, more tabular bodies striking west-southwest. In all cases except multiplet F1, depths spanned 20 m or less. The strike of the tabular bodies in E7 and F1 was also approximately perpendicular to the strike of spine 3, which extruded from October 24 to December 20, 2004 (Vallance and others, this volume, chap. 9). Such a progression is interesting in the context of volcanic activity. Moran and others (this volume, chap. 2) suggest that seismicity between September 23 and October 5 was associated with clearing of the conduit to allow subsequent lava extrusion. Smaller, more equidimensional source volumes early in the study period have relatively smaller surface area for gas escape. If the gas could not escape efficiently, excess overpressure may have caused fragmentation to occur in the conduit, resulting in the explosions seen between October 1 and October 5. After October 5, seismic amplitudes decreased, the lifespan of multiplets and source volumes increased, and extrusion of lava at the surface soon began. The tabular shape and orientation of the relative locations after October 1 are suggestive of a dike. Presumably, the larger source volume (and larger surface area) defined by the relative locations facilitated greater gas loss at shallow levels in the conduit, thereby contributing to steady degassing and suppression of explosions.

The cause for earthquakes at the restricted depths indicated by the absolute and relative locations is enigmatic. Seismogenic stresses around a plug of magma are dependent on the diameter, velocity, and viscosity of the plug (Webb and Dingwell, 1990; Goto, 1999). Indeed, it has been shown that stick-slip motion along the edges of an extruding plug can generate earthquakes that match the rates and sizes of observed drumbeat earthquakes at Mount St. Helens (Iverson, this volume, chap. 21). We might expect seismogenic zones at constrictions in the conduit (where the local magma flux increases), and we believe that this may be a reasonable source of seismogenic stress. We might also expect earthquakes in an area where the overburden pressure is low enough to allow solidification of the magma and force the viscosity across some threshold value. The viscosity is dependent mostly on pressure and, to a lesser extent, on temperature (Blundy and others, 2006). Viscosity can vary over many orders of magnitude, making it a difficult parameter to model in a context useful for interpreting the location of earthquakes (Goto, 1999). The lithostatic pressure, however, increased only slightly in the time period we describe. A decrease in the occurrence of earthquakes and multiplets after the October 1 explosion also suggests that the seismicity was dependent on pressure. We would therefore expect earthquake locations to remain fixed or to shallow slightly during the study period if the earthquakes were dependent on the lithostatic pressure, and the viscosity and velocity of the plug were fixed. The absolute depths of the multiplets were consistent with this observation and were also coincident with the depth of microlite crystallization of the rising magma (Cashman and others, this volume, chap. 19; Pallister and others, this volume, chap. 30). The depth of microlite crystallization is also thought to be a pressure-dependent phenomenon.

Not all earthquakes during the study period occurred as part of a multiplet. Indeed, the absolute locations show that earthquake hypocenters were spread across a wide range of depths, exceeding the depth range of the multiplets. The seismic energy declined after each explosion (Moran and others, this volume, chap. 6, their fig. 3), but for many of the explosions the multiplets persisted (fig. 8). This indicates that the earthquakes not associated with the multiplets declined in size and or number and therefore may also have been pressure dependent. Because the behavior of those earthquakes associated with multiplets and of those not associated with multiplets differs, we suggest that the cause of each phenomenon is distinct. In the case of the multiplets, the source is highly stable and nondestructive for long periods of time. In the case of earthquakes not associated with a multiplet, the source is nonrepeatable over short time scales.

Conclusions

Absolute and relative locations allowed us to characterize the possible source of earthquakes associated with renewed activity at Mount St. Helens beginning in September 2004. Absolute locations were improved with the use of a new velocity model. During periods of good depth constraint, absolute locations were found to be less than 1 km deep. A shallowing of earthquakes occurred between September 24 and 26, supported by changes in the difference of first-arrival picks at close-in stations (Moran and others, this volume, chap. 2). Absolute earthquake locations revealed a north-dipping structure which likely coincides with the shallow conduit that was formed during the initial vent-clearing phase.

Multiplets were prominent during the first months of the eruption. They included volcano-tectonic, hybrid, and low-

frequency events with a wide range of magnitudes. Multiplets varied in lifespan, but those of the vent-clearing phase had much shorter lifespans than multiplets occurring during dome extrusion. Multiplets also occurred in temporal clusters that were usually associated with large changes in the maximum RMS seismic-signal amplitude. Absolute locations derived from earthquake stacks show that the individual multiplets likely originated in nearly the same area. Relative locations showed source volumes with diameters on the order of 25 m before October 5 and larger, tabular source volumes oriented to the west-southwest thereafter, a change concurrent with the transition from vent clearing to dome building. In some cases, the cross-correlation coefficients of the first event compared to all subsequent events showed a steady decline, suggesting movement of the source location at a level within our uncertainty. The properties and locations of multiplets suggest that their occurrence was based on changes in pressure.

Acknowledgments

We wish to thank the staff at the Pacific Northwest Seismic Network for their meticulous work in collecting and archiving data and generating a consistent catalog throughout the volcanic sequence—notably Steve Malone, Tony Qamar, Amy Wright, Tom Yelin, Guy Medema, Karen Meagher, Bill Steele, Bob Norris, and Ruth Ludwin. We also wish to thank our reviewers, Seth Moran and Clifford Thurber, for insightful comments that significantly improved the final version of the manuscript, and Dave Ramsey for the map in figure 2.

References Cited

Aster, R.C., Borchers, B., and Thurber, C.H., 2005, Parameter estimation and inverse problems: Amsterdam, Elsevier Academic Press, 301 p.

Battaglia, J., Thurber, C.H., Got, J.-L., Rowe, C.A., and White, R.A., 2004, Precise relocation of earthquakes following the 15 June 1991 eruption of Mount Pinatubo (Philippines): Journal of Geophysical Research, v. 109, p. B07302, doi:10.1029/2003JB002959.

Blundy, J., Cashman, K., and Humphreys, M., 2006, Magma heating by decompression-driven crystallization beneath andesite volcanoes: Nature, v. 443, no. 7107, p. 76–80, doi:10.1038/nature05100.

Cashman, K.V., Thornber, C.R., and Pallister, J.S., 2008, From dome to dust; shallow crystallization and fragmentation of conduit magma during the 2004–2006 dome extrusion of Mount St. Helens, Washington, chap. 19 *of* Sherrod, D.R., Scott, W.E., and Stauffer, P.H., eds., A volcano rekindled; the renewed eruption of Mount St. Helens, 2004–2006: U.S. Geological Survey Professional Paper 1750 (this volume).

Dzurisin, D., Lisowski, M., Poland, M.P., Sherrod, D.R., and LaHusen, R.G., 2008, Constraints and conundrums resulting from ground-deformation measurements made during the 2004–2005 dome-building eruption of Mount St. Helens, Washington, chap. 14 *of* Sherrod, D.R., Scott, W.E., and Stauffer, P.H., eds., A volcano rekindled; the renewed eruption of Mount St. Helens, 2004–2006: U.S. Geological Survey Professional Paper 1750 (this volume).

Efron, B., and Gong G., 1983, A leisurely look at the bootstrap, the jackknife and cross-validation: American Statistician, v. 37, no. 1, p. 36–48.

Fréchet, J., 1985, Sismogenèse et doublets sismiques: Grenoble, France, Université Scientifique et Médicale de Grenoble, M.S. thesis, 206 p.

Frémont, M.J., and Malone, S.D., 1987, High precision relative locations of earthquakes at Mount St. Helens, Washington: Journal of Geophysical Research, v. 92, no. B10, p. 10223–10236.

Geller, R.J., and Mueller, C.S., 1980, Four similar earthquakes in central California: Geophysical Research Letters, v. 7, p. 821–824.

Got, J.-L., Fréchet J., and Klein, F.W., 1994, Deep fault plane geometry inferred from multiplet relative relocation beneath the south flank of Kilauea: Journal of Geophysical Research, v. 99, no. B8, p. 15375–15386.

Goto, A., 1999, A new model for volcanic earthquake at Unzen volcano; melt rupture model: Geophysical Research Letters, v. 26, no. 16, p. 2541–2544.

Green, D.N., and Neuberg, J., 2006, Waveform classification of volcanic low-frequency earthquake swarms and its implication at Soufrière Hills Volcano, Montserrat: Journal of Volcanology and Geothermal Research, v. 153, nos. 1–2, p. 51–63, doi: 10.1016/j.jvolgeores.2005.08.003.

Gret, A., Snieder, R., Aster, R.C., and Kyle, P.R., 2005, Monitoring rapid temporal change in a volcano with coda wave interferometry: Geophysical Research Letters, v. 32, L06304, doi: 10.1029/2004GL0211143.

Herrmann, R.B., 1979, FASTHYPO—a hypocenter location program: Earthquake Notes, v. 50, no. 2, p. 25–37.

Iverson, R.M., 2008, Dynamics of seismogenic volcanic extrusion resisted by a solid surface plug, Mount St. Helens, 2004–2005, chap. 21 *of* Sherrod, D.R., Scott, W.E., and Stauffer, P.H., eds., A volcano rekindled; the renewed eruption of Mount St. Helens, 2004–2006: U.S. Geological Survey Professional Paper 1750 (this volume).

Klein, F.W., 1989, HYPOINVERSE, a program for VAX computers to solve for earthquake locations and magnitudes: U.S. Geological Survey Open-File Report 89–314, 59 p.

Lahr, J.C., Chouet, B.A., Stephens, C.D., Power, J.A., and Page, R.A., 1994, Earthquake classification, location, and error analysis in a volcanic environment; implications for the magmatic system of the 1989–1990 eruptions at Redoubt Volcano, Alaska: Journal of Volcanology and Geothermal Research, v. 62, nos. 1–4, p. 137–151, doi:10.1016/0377-0273(94)90031-0.

Lees, J.M., and Crosson, R.S., 1989, Tomographic inversion for three-dimensional velocity structure at Mount St. Helens using earthquake data: Journal of Geophysical Research, v. 94, no. B5, p. 5716–5728.

Lisowski, M., Dzurisin, D., Denlinger, R.P., and Iwatsubo, E.Y., 2008, Analysis of GPS-measured deformation associated with the 2004–2006 dome-building eruption of Mount St. Helens, Washington, chap. 15 *of* Sherrod, D.R., Scott, W.E., and Stauffer, P.H., eds., A volcano rekindled; the renewed eruption of Mount St. Helens, 2004–2006: U.S. Geological Survey Professional Paper 1750 (this volume).

Malone, S.D., and Pavlis, G.L., 1983, Velocity structure and relocation of earthquakes at Mount St. Helens [abs.]: Eos (American Geophysical Union Transactions), v. 64, p. 895.

McChesney, P.J., Couchman, M.R., Moran, S.C., Lockhart, A.B., Swinford, K.J., and LaHusen, R.G., 2008, Seismic-monitoring changes and the remote deployment of seismic stations (seismic spider) at Mount St. Helens, 2004–2005, chap. 7 *of* Sherrod, D.R., Scott, W.E., and Stauffer, P.H., eds., A volcano rekindled; the renewed eruption of Mount St. Helens, 2004–2006: U.S. Geological Survey Professional Paper 1750 (this volume).

Michelini, A., and Lomax, A., 2004, The effect of velocity structure errors on double-difference earthquake location: Geophysical Research Letters, v. 31, L09602, doi:10.1029/2004GL019682.

Moran, S.C., Malone, S.D., Qamar, A.I., Thelen, W.A., Wright, A.K., and Caplan-Auerbach, J., 2008a, Seismicity associated with renewed dome building at Mount St. Helens, 2004–2005, chap. 2 *of* Sherrod, D.R., Scott, W.E., and Stauffer, P.H., eds., A volcano rekindled; the renewed eruption of Mount St. Helens, 2004–2006: U.S. Geological Survey Professional Paper 1750 (this volume).

Moran, S.C., McChesney, P.J., and Lockhart, A.B., 2008b, Seismicity and infrasound associated with explosions at Mount St. Helens, 2004–2005, chap. 6 *of* Sherrod, D.R., Scott, W.E., and Stauffer, P.H., eds., A volcano rekindled; the renewed eruption of Mount St. Helens, 2004–2006: U.S. Geological Survey Professional Paper 1750 (this volume).

Musumeci, C., Gresta, S., and Malone, S.D., 2002, Magma system recharge of Mount St. Helens from precise relative hypocenter location of microearthquakes: Journal of Geophysical Research, v. 107, no. B10, 2264, p. ESE 16-1–16-9, doi:10.1029/2001JB000629.

Neuberg, J.W., Tuffen, H., Collier, L., Green, D., Powell, T., and Dingwell, D., 2006, The trigger mechanism of low-frequency earthquakes on Montserrat: Journal of Volcanology and Geothermal Research, v. 153, nos. 1–2, p. 37–50, doi:10.1016/j.jvolgeores.2005.08.008.

Pallister, J.S., Thornber, C.R., Cashman, K.V., Clynne, M.A., Lowers, H.A., Mandeville, C.W., Brownfield, I.K., and Meeker, G.P., 2008, Petrology of the 2004–2006 Mount St. Helens lava dome—implications for magmatic plumbing and eruption triggering, chap. 30 *of* Sherrod, D.R., Scott, W.E., and Stauffer, P.H., eds., A volcano rekindled; the renewed eruption of Mount St. Helens, 2004–2006: U.S. Geological Survey Professional Paper 1750 (this volume).

Pearson, C.F., and Kienle, J., 1978, A seismic refraction study of Augustine volcano, Alaska [abs.]: Eos (American Geophysical Union Transactions), v. 59, no. 4, p. 311.

Petersen, T., Caplan-Auerbach, J., and McNutt, S.R., 2006, Sustained long-period seismicity at Shishaldin Volcano, Alaska: Journal of Volcanology and Geothermal Research, v. 151, p. 365–381.

Poupinet, G., Ellsworth, W.L., and Fréchet, J., 1984, Monitoring velocity variations in the crust using earthquake doublets; an application to the Calaveras Fault, California: Journal of Geophysical Research, v. 89, p. 5719–5731.

Pujol, J., 2000, Joint event location–the JHD technique and applications to data from local seismic networks, *in* Thurber, C.H., and Rabinowitz, N., eds., Advances in seismic event location: Dordrecht, Kluwer Academic Publishers, p. 163–204.

Qamar, A.I., Malone, S.D., Moran, S.C., Steele, W.P., and Thelen, W.A., 2008, Near-real-time information products for Mount St. Helens—tracking the ongoing eruption, chap. 3 *of* Sherrod, D.R., Scott, W.E., and Stauffer, P.H., eds., A volcano rekindled; the renewed eruption of Mount St. Helens, 2004–2006: U.S. Geological Survey Professional Paper 1750 (this volume).

Reeder, J.W., and Lahr, J.C., 1987, Seismological aspects of the 1976 eruption of Augustine Volcano, Alaska: U.S. Geological Survey Bulletin 1768, 32 p.

Rowe, C.A., Thurber, C.H., and White, R.A., 2004, Dome growth behavior at Soufriere Hills Volcano, Montserrat, revealed by relocation of volcanic event swarms, 1995–1996: Journal of Volcanology and Geothermal Research, v. 134, no. 3, p. 199–221.

Schaff, D.P., Bokelmann, G.H.R., Ellsworth, W.L., Zanzerkia, E., Waldhauser, F., and Beroza, G.C., 2004, Optimizing correlation techniques for improved earthquake location: Bulletin of the Seismological Society of America, v. 94, no. 2, p. 705–721.

Stephens, C.D., and Chouet, B.A., 2001, Evolution of the December 14, 1989 precursory long-period event swarm at Redoubt Volcano, Alaska: Journal of Volcanology and Geothermal Research, v. 109, p. 133–148.

Swanson, D.A., Casadevall, T.J., Dzurisin, D., Malone, S.D., Newhall, C.G., and Weaver, C.S., 1983, Predicting eruptions at Mount St. Helens, June 1980 through December 1982: Science, v. 221, no. 4618, p. 1369–1376.

Thelen, W.A., Malone, S.D., Qamar, A.I., and Pullammanappallil, S., 2006, Improvements to absolute locations from an updated velocity model at Mount St. Helens, Washington [abs.]: Seismological Research Letters, v. 77, no. 2, p. 238.

Ukawa, M., and Tsukahara, H., 1996, Earthquake swarms and dike intrusions off the east coast of Izu Peninsula, central Japan: Tectonophysics, v. 253, p. 285–303.

Vallance, J.W., Schneider, D.J., and Schilling, S.P., 2008, Growth of the 2004–2006 lava-dome complex at Mount St. Helens, Washington, chap. 9 *of* Sherrod, D.R., Scott, W.E., and Stauffer, P.H., eds., A volcano rekindled; the renewed eruption of Mount St. Helens, 2004–2006: U.S. Geological Survey Professional Paper 1750 (this volume).

Waite, G.P., and Moran, S.C., 2006, Crustal P-wave speed structure under Mount St. Helens from local earthquake tomography [abs.]: Eos (American Geophysical Union Transactions), v. 87, no. 52, Fall Meeting supplement, Abstract V11B-0578.

Waldhauser, F., 2001, HypoDD—a program to compute double-difference hypocenter locations (hypoDD version 1.0): United States Geologic Survey Open-File Report 01–113, 25 p.

Waldhauser, F., and Ellsworth, W.L., 2000, A double-difference earthquake location algorithm; method and application to the northern Hayward Fault, California: Bulletin of the Seismological Society of America, v. 90, p. 1353–1368.

Webb, S.L., and Dingwell, D.B., 1990, Non-Newtonian rheology of igneous melts at high stress and strain rates; experimental results for rhyolite, andesite, basalt, and nephelinite: Journal of Geophysical Research, v. 95, p. 15695–15701.

Williams, D.L., Abrams, G., Finn, C., Dzurisin, D., Johnson, D.J., and Denlinger, R., 1987, Evidence from gravity data for an intrusive complex beneath Mount St. Helens: Journal of Geophysical Research, v. 92, no. B10, p. 10207–10222.

Wolfe, C.J., 2002, On the mathematics of using difference operators to relocate earthquakes: Bulletin of the Seismological Society of America, v. 92, p. 2879–2892.

Appendix 1. Velocity Model

A velocity model serves an integral role in earthquake locations. Although many regions have three-dimensional velocity models available, computing power and speed requirements often mean that one-dimensional velocity models are used for routine locations. At Mount St. Helens, large static station corrections and earthquakes with locations above the velocity model datum (airquakes) were common during the beginning of the 2004 unrest and eruption, which demonstrated the need for a more accurate velocity model in the shallow part of the volcano. The velocity model used for routine locations by the Pacific Northwest Seismic Network (PNSN) was determined using nearby quarry blasts (Malone and Pavlis, 1983). That velocity model is regionally accurate, judging from the small station corrections on stations beyond the edifice of Mount St. Helens. The data used for the velocity model, however, had poor ray coverage through the shallow part of the edifice (<2 km). The result is a constant P-wave velocity of 4.6 km/s in the upper 2.2 km of the velocity model, far too fast for the pyroclastic deposits, thin lava flows, and fractured dacite lava domes found throughout the crater walls of the volcano. Exceedingly fast velocities resulted in large station corrections on edifice and crater stations used for routine processing (table 2). Three-dimensional P-wave velocity models exist for Mount St. Helens (Lees, 1989; Waite and Moran, 2006), but they also suffer from a lack of ray coverage and coarse resolution at the depths we are studying. Here we describe the method we used to develop a shallow (<2 km) one-dimensional P-wave velocity model to supplement the existing one-dimensional model (in use by the PNSN) for the Mount St. Helens area.

Table 2. Station corrections calculated for each velocity model with permanent Pacific Northwest Seismic Network (PNSN) stations used in routine earthquake locations between 2004 and 2006.

[See McChesney and others (this volume, chap. 7) for locations of seismic stations not shown in figure 2. Data shown here for each station are time residuals, in seconds, that result from the inadequacy of a one-dimensional model to represent the three-dimensional Earth. In theory, station residuals converge to zero as the computed velocity model converges toward the actual velocity structure between earthquake and station.]

PNSN Station	Existing PNSN Model[1] (s)	New Velocity Model[1] (s)	New Velocity Model[2] (s)
SEND	-0.087	0.000	-0.023
RAFT	-0.187	-0.083	0.063
MIBL	-0.218	-0.096	0.000
WESG	-0.179	-0.091	0.099
MIDE	-0.212	-0.190	0.000
SEP	-0.151	-0.102	0.071
BLIS	-0.393	-0.366	-0.170
NED	-0.050	0.000	0.131
SUG	0.200	0.000	0.064
YEL	0.024	0.000	0.078
EDM	0.179	0.059	0.033
HSR	0.192	0.070	0.088
SHW	0.108	0.042	-0.032
STD	0.070	0.057	0.000
SOS	0.017	0.039	0.000
JUN	-0.029	0.025	-0.034
FL2	-0.029	0.054	0.000
CDF	-0.043	0.134	0.062
ELK	-0.226	-0.177	-0.227
TDL	-0.163	-0.158	-0.223
LVP	-0.078	0.000	-0.060

[1]Datum is 1,700 m above sea level.

[2]Datum is 2,200 m above sea level.

Methods

In the summer of 2005, we deployed, at 100-m intervals, 39 RT-125 seismic recorders with alternating 4.5-Hz geophones and 1-Hz vertical seismometers (Thelen and others, 2006). The instruments were deployed for three days. The array began approximately 1 km north of the 2004–5 vent and extended northward 4 km onto the Pumice Plain (fig. 14).

We used an Occam's inversion scheme with second-order Tikhonov regularization to invert first-arrival data for a velocity model (Aster and others, 2005). The Occam's inversion scheme seeks a solution to $G(m) = d$ subject to the following constraints:

$$min \left\| Lm \right\|_2$$

$$\text{and} \left\| G(m) - d \right\|_2 \leq \delta ,$$

where $G(m)$ is a function of the model parameters that calculates the data, d, from the model. In this formulation, L is the roughening matrix (which is equal to the finite-difference approximation of the second derivative), and δ is the discrepancy parameter, $\sigma\sqrt{n}$, where n is the number of degrees of freedom and σ is the uncertainty of the time picks. Occam's inversion relies on an iteratively applied local linearization given by Taylor's theorem,

$$G(m^k + \Delta m) \approx G(m^k) + J(m^k)\Delta m \ ,$$

where m^k is a trial model and $J(m^k)$ is the Jacobian. Using a damped least-squares approach, the constraints above, combined with the Taylor approximation, give

$$\min \left\| G(m^k) + J(m^k)\Delta m - d \right\|_2^2 + \alpha^2 \left\| L(m^k + \Delta m) \right\|_2^2 \ ,$$

where the parameter α is adjusted after each iteration so that the solution will not exceed the allowable misfit. The inversion is terminated when $\delta^2 = \chi^2$, where

$$\chi^2 = \sum_{i=1}^{m} \frac{(d_i - (Gm_{L_2})_i)^2}{\sigma_i^2} .$$

Our "active sources" were earthquakes associated with dome building at Mount St. Helens. Twenty $M_d > 1.0$ earthquakes occurred within the crater from the surface to depths of 1 km while our instruments were recording. Of these, we chose the best earthquake (August 20, 2005, 21:28:37 PDT; $M_d = 2.6$) on the basis of its clarity of impulsive arrivals across the transect and the number of PNSN catalog picks used to routinely locate the earthquake. The epicenter of the earthquake is well constrained, owing to the excellent azimuthal coverage of seismometers around Mount St. Helens. The existing one-dimensional velocity model described above, however, allows for a tradeoff between the depth and the origin time within the upper 2.2 km of the velocity model. Thus, the depth is not as well constrained as the epicenter. With additional layers in the shallow part of the velocity model, this tradeoff is less important.

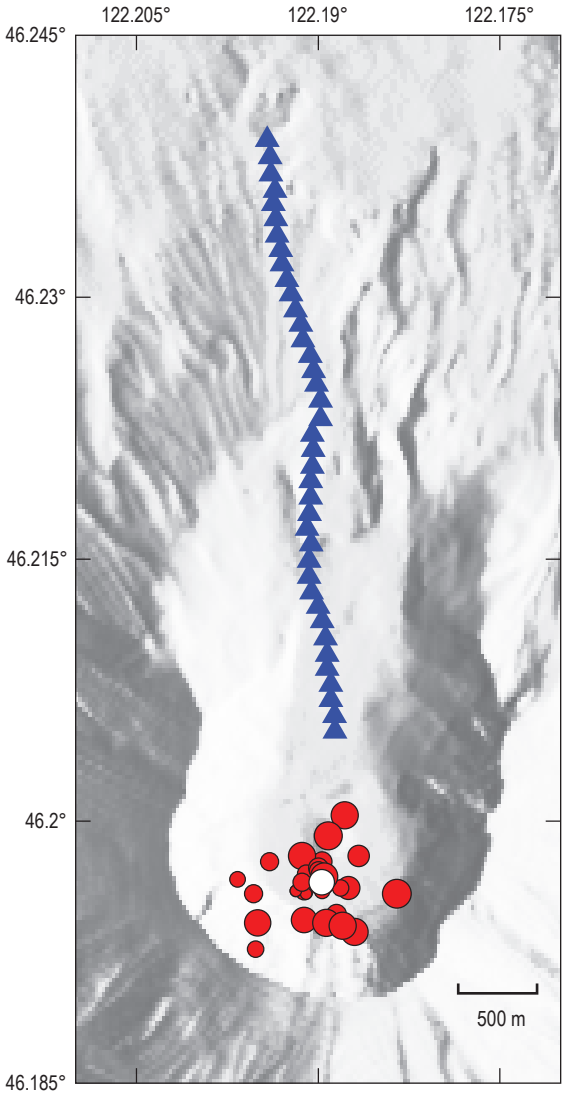

Figure 14. Instrument layout (blue triangles) with earthquake epicenters (red dots) used for P-wave inversion. Epicenter of primary earthquake used in inversion is shown by white dot.

Secondary arrivals were observed in the record section of the transect, but they were not easily picked across the array. We therefore used only the P-wave arrivals. Errors in picking first arrivals on the event used for the inversion were assumed to be constant and were estimated to be within five time samples (0.05 s) of the actual arrival. Our algorithm allows for the use of one earthquake at a time. We chose to use only one earthquake in our inversion for two reasons: (1) there was only one other earthquake (August 22, 2005, 03:32:45 PDT; $M_d = 1.4$) that possessed impulsive arrivals across the entire transect, and (2) that earthquake showed an identical pattern in first-arrival picks to the earthquake we used for the inversion. Using multiple earthquakes would not change or add to the information used in the inversion because the earthquakes that occurred during the deployment of the transect occurred in such a tight cluster. First arrivals from the other earthquakes that occurred during the deployment were picked only if they could be identified with a precision of better than 0.05 s. The time spread in picks at a given offset was used to define the standard deviation to ensure that the inversion did not overfit the data.

We used a one-dimensional travel-time calculator parameterized with constant velocity layers. The travel-time calculator allows for a three-dimensional geometry of stations and earthquake location. The setup of the inverse problem prescribes node depths and solves for the layer velocity between nodes. The node number and depths were based largely on constraints imparted by the program used for earthquake locations, SPONG. The first constraint is the use of a total of 10 layers in the velocity model. When combined with the existing PNSN velocity model, this only allowed for 4 layers. The second constraint is that different station altitudes can be used, but they must be included inside the top layer of the velocity model. Stations within 10 km of the crater, excluding the crater stations, span altitudes from 1,268 m to 1,700 m. We thus required a 500-m-thick top layer so that we could include the altitudes of these closest stations to the crater. Depths of the remaining three node-depths layers were found through a grid search with an increment of 100 m. The preferred model is the model that satisfies the condition above and has the smallest residual times ($t_{observed} - t_{calculated}$). Models with low-velocity inversions were poorly constrained using first-arrival data and thus were not considered.

The initial depth of the earthquake used in the inversion was 0.24 km (datum at 1,700 m above sea level). We iterated velocity-model solutions, each time updating the station corrections using a subset of PNSN catalog earthquakes with high-quality arrivals (see station correction discussion below) to get a new earthquake location and origin time. The new earthquake parameters were then used to update distance and time information of the transect, and the

velocity model inversion was run again. Iterations stopped when the change in depth between iterations was less than the calculated uncertainty of the solution. The final depth of the earthquake was calculated to be 0.13 km. By alternately recalculating the location and the velocity model, we minimize errors in the location of the earthquake and in the velocity inversion results.

Location uncertainties in our nonlinear velocity inversion were calculated using the diagonal of the covariance, a method that is appropriate in linear inverse problems. We adapted this technique to our problem by linearizing the solution through a central difference and then calculating the error as if it were a linear problem. This approach is often used, though not strictly correct, and may underestimate the uncertainties in the model (Aster and others, 2005).

Station corrections are static time corrections used in earthquake hypocenter inversions using one-dimensional velocity models. Station corrections, which compensate for the one-dimensional modeling of a truly three-dimensional velocity structure, can be minimized by finding the closest one-dimensional approximation of the three-dimensional velocity structure under the volcano (Pujol, 2000). We do not minimize the station corrections here; however, we do use decreases in station corrections as a proxy for the quality of our velocity model.

Station corrections were calculated using a subset of 29 PNSN catalog events that occurred between 2004 and 2006. These events were selected for their exceptionally sharp impulsive arrivals and were already in use for calibrating PNSN velocity models for Mount St. Helens (S. Malone, oral commun., 2006). The first arrivals of these events were picked on the PNSN stations only if the arrival was unambiguous to ±0.05 s. Locations were then calculated using the existing velocity model and station corrections. The new velocity model was then used with the existing, fixed location to calculate new residuals for each station for each event. The station residuals were then averaged across events to obtain the station correction. This approach is not without flaws. Earthquake locations using the old velocity model may have errors imparted by the velocity model itself, which would lead to a bias in the station corrections. Near-site effects may also introduce a bias in the station corrections. Despite these disadvantages, we find that comparing station corrections gives us the best measure of spatial quality between two velocity models.

Results

P-Wave Model

The final result of our P-wave velocity inversion is shown in figure 15. Disappointingly, our inversion did not constrain velocities deeper than 1.5-km depth. This is because of the lack of deep earthquakes during the deployment and the final length of the transect used. Our deepest velocity (5.12 km/s) agrees well with the shallowest velocity of the existing model that spans depths of 0 to 2.2 km. Inverting a subset of the 12 closest picks to the hypocenter resulted in shallow velocities as low as 2.4 km/s, instead of the 2.7 km/s that is calculated in the final model. Residuals of the model show trends imparted by the constant velocity layers used in the inversion. The 13 picks farthest from the hypocenter show apparent velocities that are abnormally high (7–8 km/s). In our inversion, we discarded points (seven in all) with the largest offsets until inverted velocities at depths of 1 to 1.5 km below the transect were reasonable with respect to the existing velocity model. Removing time picks from the most distant stations resulted in depth constraints that were not as deep as we had initially planned, but it was required in order to get reasonable results. The apparent high velocities in our time picks may be a result of three-dimensional variations in wave speed. An alternative explanation may be a large amount of scattering that is shifting the energy of the direct arrival later in the signal and masking the energy remaining in the actual first arrival buried in the noise. Three-dimensional effects are also seen near the 2.1-km offset (fig. 15*A*), where three picks are advanced with respect to surrounding picks.

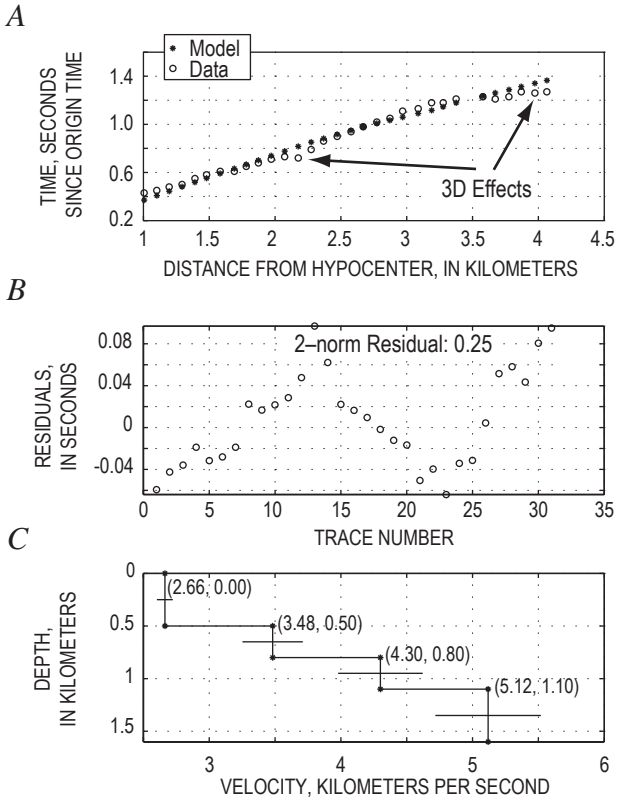

Figure 15. Results of final velocity inversion and grid search for P-wave model. *A*, Comparison of data (circles) and model (stars) for the final model. *B*, Plot of residuals. *C*, Velocity model plotted with 90-percent confidence intervals shown as horizontal lines.

Discussion

The results of our P-wave model show velocities of 2.4–2.7 km/s in the uppermost layer, approximately 1 km/s slower than found in the velocity model used at Mount St. Helens by Musumeci and others (2002). The discrepancy is due to different ray coverage within the crater. In our inversion, we had 39 instruments draping the crater floor and flank and recorded earthquakes less than 1 km deep. In the velocity model by Musumeci and others (2002), only three stations existed inside the crater and only earthquakes deeper than 2.5 km were recorded. The P waves used in our study thus better sampled the shallow structure of the volcano. Our shallowest velocities are similar to those measured at other volcanoes, including Augustine Volcano, Alaska (2.24–2.6 km/s; Pearson and Kienle, 1978), Redoubt Volcano, Alaska (2.9 km/s; Lahr and others, 1994), and Soufrière Hills, Montserrat (2.17 km/s; Rowe and others, 2004).

The new P-wave velocity model has relatively high velocities (4.3 km/s) at fairly shallow depths (0.8 km), considering the volcanic strata exposed within the crater. But such high velocities may be warranted, inasmuch as an intrusive suite at approximately 1-km depth has been interpreted from gravity data (Williams and others, 1987). Velocities of approximately 5.1 km/s have also been used in layered velocity models at Augustine Volcano at 0.9-km depth (Reeder and Lahr, 1987) and at Redoubt Volcano at 0.6-km depth (Lahr and others, 1994). Furthermore, the new P-wave model shows decreases in calculated station corrections at all stations on the volcano, suggesting that the new model is a closer approximation of the three-dimensional velocity structure under the edifice than the existing PNSN model (table 2).

By concatenating the existing S4 velocity model from the PNSN onto the bottom of the inverted velocity model, we are able to calculate improvements to station corrections resulting from the new model (table 2). The altitudes of our transect ranged between 1,100 m and 1,800 m above sea level. At best, our data only constrain the seismic velocities up to the maximum altitude of our transect. For consistency with the existing PNSN velocity model, we set our initial datum to 1,700 m. To allow for earthquake locations inside the new dome, we also considered a model identical to the final inverted velocity model, except with a datum at 2,200 m (datum-adjusted). The layer above the initial datum (1,700 m) has a constant velocity equal to the uppermost layer (2.66 km/s), and the layer depths are adjusted according to the new datum. Adjusting the datum to 2,200 m above sea level, the altitude of the highest seismic station, led to reduced station corrections. In particular, the station corrections on the dome are greatly reduced with respect to other velocity models we considered (table 2). The datum-adjusted model is preferred because it allows for earthquake locations within the new dome and results in lower station corrections for stations on the edifice and inside the crater. Admittedly, no dome material was present at 2,200-m altitude early in the study period, but in order to present the most consistent set of locations for the entire study period, a consistent velocity model should be used throughout the study period.

Appendix 2. Effect of Changing Station Configurations

We simulated the results of changing station configurations within the crater using PNSN catalog events from November 4 through November 20, 2004. During this time period, stations BLIS, YEL, and SEP were operational (McChesney and others, this volume, chap. 7), allowing an opportunity to understand the effect of particular stations on the geometry of the absolute locations. Absolute locations from September 23 until October 1 all lie along a north-dipping structure that descends beneath the 1980–86 dome. When good station coverage and impulsive arrivals were both present starting around November 4, 2004, a similar north-dipping structure emerged (fig. 16*A*). This north-dipping structure was found to be fairly robust analytically, persisting even when the two closest stations were excluded (figs. 16*B*, *C*). Only when station YEL is also excluded is there a breakdown in the shape of the cluster.

Generally, as we removed the close stations, the hypocentroid of the cluster moved deeper and the range of depths grew larger. For example, the original locations had a hypocentroidal depth of ~290 m. Upon removing station BLIS from calculation, the hypocentroid deepened to ~350 m. When both SEP and BLIS were removed, the hypocentroid was more than 400 m deep.

Appendix 3. Jackknife Tests

We show here the results of jackknife tests on the multiplet E7. The original relative locations show a tabular body with a surface projection spanning nearly 50 m. In depth the locations are restricted to a range of only about 20 m, outlining a cigar-shaped source region (figs. 10*B*, 17*A*). Multiplets D34 and F1 also show similar tabular bodies, so we are compelled to show the results of our jackknife tests to prove that the locations are not an artifact of station geometry or poor waveform alignment. In figure 17, we show the results of removing, one at a time, each of the four stations with the most observations. In almost all cases there is no change in the geometry of the source region. An exception is the source geometry when station YEL is removed (fig. 17*C*). In this test, the orientation of the source region is more southwest than in the original locations, and the relative hypocenters, viewed to the east, are elongate north-south.

We also tested the effect of a P-wave velocity model on the relative locations (fig. 17*F*). As mentioned previously, the velocity model that we chose lacks layer boundaries near the cluster centroid, so a change to higher velocities simply spreads the hypocenters out over a larger area without gross change in geometry.

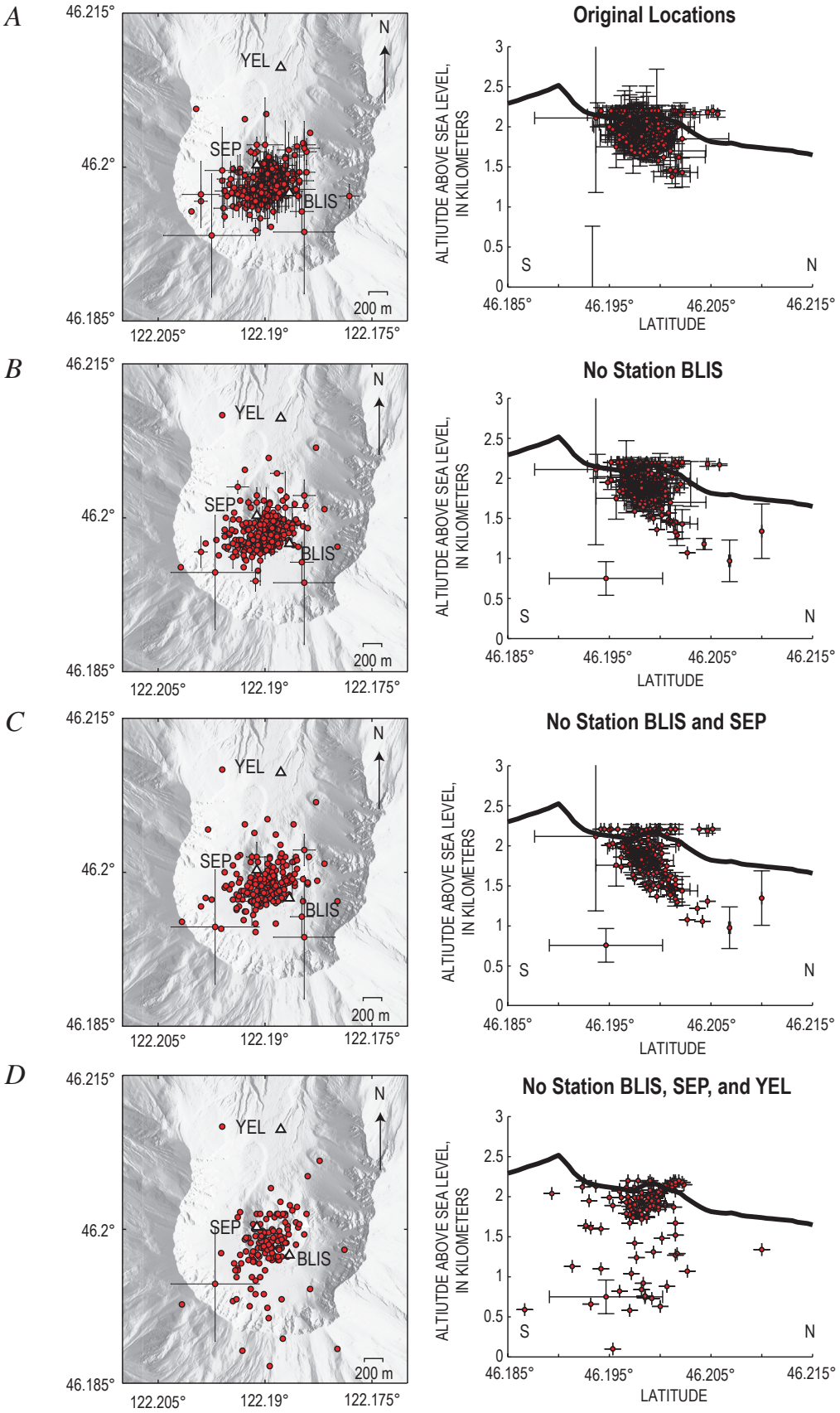

Figure 16. (*A–D*) Results of simulations of different station configurations using Pacific Northwest Seismic Network (PNSN) catalog earthquakes from November 4, 2004, to November 20, 2004.

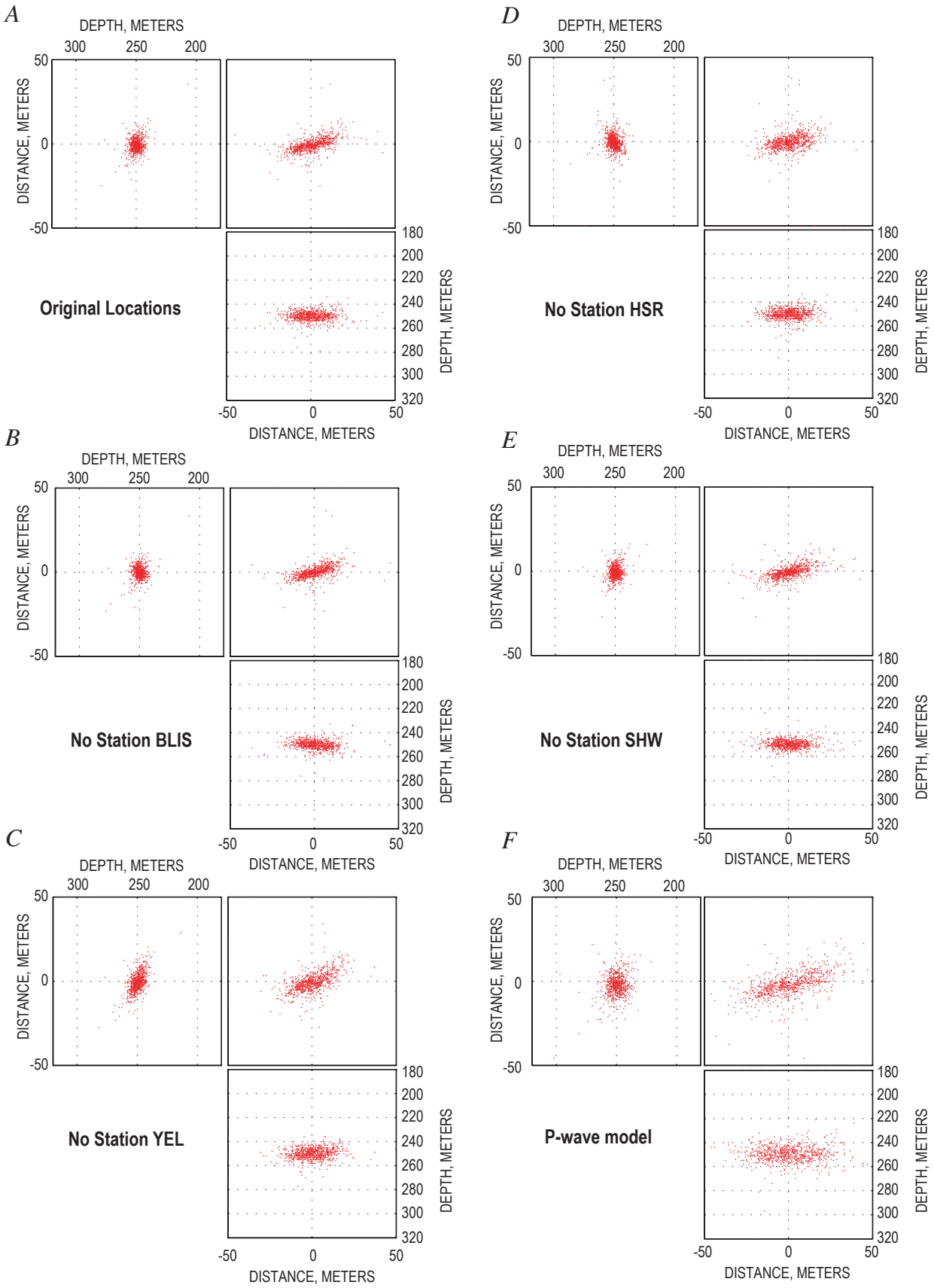

Figure 17. (*A–E*) Results of jackknife tests on multiplet E7. *F,* Results of the use of a P-wave model in the relative locations of multiplet E7.

This page intentionally left blank

A Volcano Rekindled: The Renewed Eruption of Mount St. Helens, 2004–2006
Edited by David R. Sherrod, William E. Scott, and Peter H. Stauffer
U.S. Geological Survey Professional Paper 1750, 2008

Chapter 5

Broadband Characteristics of Earthquakes Recorded During a Dome-Building Eruption at Mount St. Helens, Washington, Between October 2004 and May 2005

By Stephen P. Horton[1], Robert D. Norris[2], and Seth C. Moran[3]

Abstract

From October 2004 to May 2005, the Center for Earthquake Research and Information of the University of Memphis operated two to six broadband seismometers within 5 to 20 km of Mount St. Helens to help monitor recent seismic and volcanic activity. Approximately 57,000 earthquakes identified during the 7-month deployment had a normal magnitude distribution with a mean magnitude of 1.78 and a standard deviation of 0.24 magnitude units. Both the mode and range of earthquake magnitude and the rate of activity varied during the deployment. We examined the time domain and spectral characteristics of two classes of events seen during dome building. These include volcano-tectonic earthquakes and lower-frequency events. Lower-frequency events are further classified into hybrid earthquakes, low-frequency earthquakes, and long-duration volcanic tremor. Hybrid and low-frequency earthquakes showed a continuum of characteristics that varied systematically with time. A progressive loss of high-frequency seismic energy occurred in earthquakes as magma approached and eventually reached the surface. The spectral shape of large and small earthquakes occurring within days of each other did not vary with magnitude. Volcanic tremor events and lower-frequency earthquakes displayed consistent spectral peaks, although higher frequencies were more favorably excited during tremor than earthquakes.

Introduction

Two classes of earthquakes are commonly observed at volcanoes around the world. One class, termed volcano-tectonic (VT) earthquakes by Latter (1981), consists of high-frequency events with sharp, well-defined body-wave phases. Volcano-tectonic events are produced by shear failure in solid rock; their broadband seismic waveforms are indistinguishable from normal tectonic earthquakes (Chouet, 1996). The second class of earthquakes observed at volcanoes consists of lower-frequency events that are thought to originate from a boundary between a fluid, such as magma or gas, and the solid surrounding rock (see, for example, Neuberg and others, 2006).

In this study we follow the convention of Moran and others (this volume, chap. 2), dividing lower-frequency earthquakes into two groups, hybrid and low-frequency (LF) earthquakes. Low-frequency events have a weak high-frequency onset followed by a harmonic waveform with one to several dominant frequencies in the range of 0.5–5 Hz (Chouet, 1996). In LF events, the P wave is often emergent, and the S wave is often obscured. Hybrid events blend the characteristics of both the VT and LF events (Lahr and others, 1994). The onset of the hybrid earthquake shows more pronounced high-frequency energy than the LF event, whereas the coda of both types is dominated by a high-amplitude, low-frequency waveform (Chouet, 1996). First-motion polarities are often mixed for both VT and hybrid events, whereas LF events generally display the same polarity at all stations (Lahr and others, 1994).

A network of eight broadband seismometers was installed at Mount St. Helens in October 2004 (fig. 1) to record seismic activity associated with the dome-building eruption that began with seismic unrest on September 23. The Cascades Volcano Observatory (CVO) installed two broadband seismometers northwest of the Mount St. Helens crater in October 2004. The Center for Earthquake Research and Information (CERI) at

[1] Center for Earthquake Research and Information, University of Memphis, 3890 Central Avenue, Memphis, TN 38155

[2] U.S. Geological Survey, at Pacific Northwest Seismic Network, Department of Earth and Space Sciences, University of Washington, Box 351310, Seattle, WA 98195

[3] U.S. Geological Survey, 1300 SE Cardinal Court, Vancouver, WA 98683

the University of Memphis installed six temporary stations at complementary azimuths around the volcano to provide better coverage of the eruption at about the same time. The CERI stations were removed in May 2005, and a separate temporary broadband network, installed by the U.S. Geological Survey in May 2005, was operated until October 2005. This analysis covers only the time period of the first temporary deployment.

Moran and others (this volume, chap. 2) separated the seismic activity associated with the dome-building eruption at Mount St. Helens into two temporal phases. The first was the vent-clearing phase that began with a swarm of shallow VT earthquakes on September 23 and ended with an explosion on October 5. A gradual transition from the VT events to lower-frequency earthquakes occurred between September 25 and October 1. This transition from VT to lower-frequency earthquakes was not recorded with broadband seismometers, because the first broadband seismometer was installed by CVO at Johnston Ridge Observatory (JRO; fig. 1) on October 1, 2004, about 1600 PDT. After October 5, seismicity was dominated by lower-frequency earthquakes. Tens of thousands of lower-frequency earthquakes were recorded by the broadband network between then and May 2005, with just one high-frequency (VT) earthquake. A few episodes of volcanic tremor were also observed, mostly before the CERI component of the broadband network became operational (Moran and others, this volume, chap. 2).

Lower-frequency earthquakes at Mount St. Helens were observed in association with eruptions in the 1980s (see, for example, Endo and others, 1981; Malone, 1983; and Malone and others, 1983). Those events were recorded using short-period, vertical-component seismometers. Since the mid-1990s, broadband seismometers have been used to record earthquakes and volcanic tremor on numerous volcanoes around the world, but the broadband recordings discussed here were the first at Mount St. Helens.

Because hybrid and LF earthquakes form the bulk of the signals recorded during the CERI broadband deployment, our analysis focuses on those events. We examine aspects of the seismicity that can be addressed by continuous, broadband, and unclipped recordings of the earthquakes. Following a brief description of the temporary broadband seismic network at Mount St. Helens, we discuss our search of the dataset for very

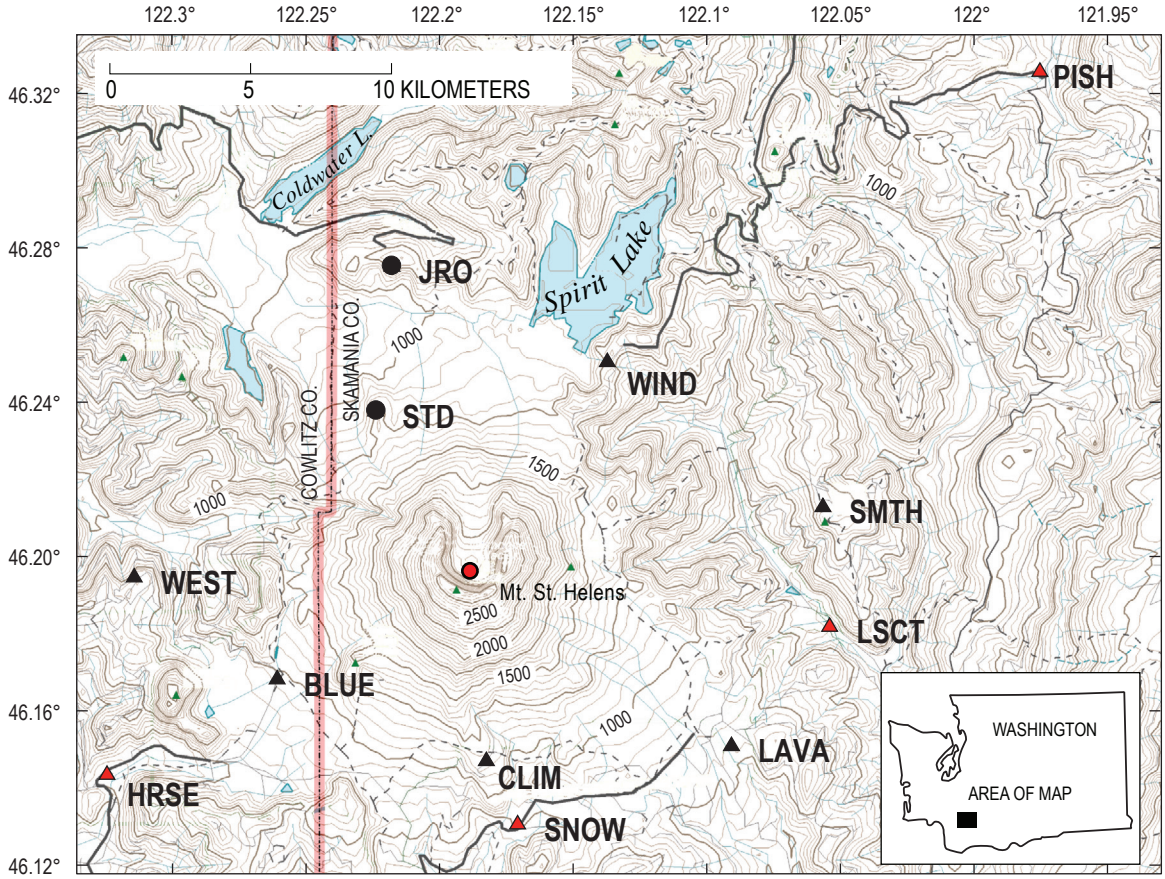

Figure 1. Broadband seismic stations at Mount St. Helens used in this study (from table 1). Black circles indicate location of CVO broadband seismometers. Black triangles indicate initial locations of CERI broadband seismometers. Red triangles show four CERI instruments redeployed to lower altitudes in early December 2004 to allow servicing throughout winter. Red circle indicates centroid of seismic activity. Roads shown in black; dashed lines are trails. Contours in meters, contour interval 50 m.

long period (VLP) pulses as described by Almendros and others (2002). We examine the variation in the rate and the magnitude distribution of the events identified by our trigger algorithm. We then look at the differences and similarities between hybrid and LF earthquakes and test a numerical measure of event character. Finally some issues are discussed related to wave propagation that make it difficult to determine focal mechanisms for these events through waveform modeling.

Broadband Network

Broadband seismic monitoring at Mount St. Helens began with CVO's installation of a Guralp CMG-6TD at JRO on October 1, 2004, approximately 1 week after the onset of increased seismic activity at the volcano (fig. 1). CVO installed a second instrument at Studebaker Ridge (STD) on October 5. Telemetry for both sites was established in late October, providing real-time broadband monitoring of Mount St. Helens seismicity (McChesney and others, this volume, chap. 7). On October 3, CERI, in cooperation with CVO and the Pacific Northwest Seismic Network (PNSN), began deploying broadband instruments with onsite recording capability. Station locations were chosen to provide the optimum azimuthal coverage, encircling the vent at the closest possible distance to Mount St. Helens. Budget, safety, and logistical considerations limited us to road-accessible sites. We deployed six Guralp CMG-6TD broadband seismometers within about 5 to 10 km of the seismic activity by October 5 (fig. 1). Four strong-motion instruments (Kinemetrics Altus K2 Recorder) were also deployed, although earthquakes in the sequence did not trigger the latter instruments.

A typical broadband station had a Guralp CMG-6TD sensor buried in a hole about 18 inches deep. Timing was provided by a GPS antenna. Power was provided by 12-V batteries recharged by a 30-W solar panel on a 1.2-m-tall stand. The broadband seismometers recorded three channels continuously at 50 samples per second and had a flat response to ground velocity between 0.033 and 25 Hz. Data were stored onsite using 2 GB of internal flash memory. With reasonable data compression, and a few sunny days for solar-power recharge, a service interval of 6 to 8 weeks was adequate to ensure no loss of data. In late October we started removing several temporary stations located in remote settings to avoid having them snowed under for the winter (table 1). By early November only two of the temporary stations, BLUE and LAVA, remained. Fortunately, these stations were southwest and southeast of the volcanic crater, so they, along with the two CVO stations, still provided reasonable azimuthal coverage. At the beginning of December, we moved stations to sites where the anticipated snow depth would not exceed 2.4 m. Three of these sites were winter recreational Sno-Parks maintained by the U.S. Forest Service, with plowed road access during normal snow years. The fourth site, LSCT, was sufficiently low in altitude to be accessible year-round.

Very Long Period Seismicity, October-November 2004

One of the principal reasons for our rapid deployment of broadband seismometers was to record any very long period (VLP) seismicity associated with the eruption that would otherwise have been missed by the PNSN short-period stations. We looked for evidence of VLP signals as described by Almendros and others (2002) in the period range 5–30 s. A moving root-mean-squared (RMS) average applied to bandpass-filtered seismograms was helpful in identifying trends and potential pulses. We checked peaks and trends observed in the moving average by visual inspection of the time series. For example, a moving RMS average was computed from seismograms recorded from October 5 through October 8 (fig. 2*A*). The two large peaks observed at station WIND in figure 2*A* at about 1600 (PDT) on October 6 and 0200 on October 8 can be correlated with spikes at other stations in the network. The first peak was produced by surface waves following a shallow M_w 6.2 earthquake that occurred in Indonesia at 1531 (PDT) on October 6. The second large peak was produced by body and surface waves following a shallow M_w 6.8 earthquake that occurred in the Solomon Islands at 0127 on October 8.

Two broad increases in RMS levels occurred between October 7 and 9. These trends were too broad to be teleseismic arrivals or VLP pulses but could have been caused by very long duration resonance of the volcano's magmatic-hydrologic system. We computed the RMS average at station LON, approximately 68 km north of Mount St. Helens and found that the broad trend increases observed at WIND, only 7.15 km from the vent, were matched by concurrent increases at LON, which suggests the source of the increase may be regional. Seismic waves that emanated from a local source below the Mount St. Helens crater should have attenuated with distance. To investigate amplitude as a function of distance from the crater, we plotted seismograms from October 7 to 9 arranged by the station distance from the crater (fig. 2*B*). The peak amplitudes and general character of the waveforms were similar at all stations, including LON. Because attenuation was not evident, we concluded that the broad energy increases did not result from a local source below the Mount St. Helens crater, but rather from a regional source. The increased long-period energy is best explained as seismic noise (microseisms) generated by a low-pressure weather system that approached the Pacific Northwest coast on October 7 and remained in the coastal area during the following 3 days. Microseisms, a nearly harmonic modulated waveform with periods around 6 s, have long been associated with storms over water, including normal low-pressure systems. Longuet-Higgins (1950) showed that the interaction of water waves with similar periods and different directions generates pressure waves that efficiently couple with the solid earth to produce seismic surface waves. These surface waves can propagate with gradual loss of energy over broad areas of the continent.

Table 1. Broadband station locations and dates of operation.

[Stations JRO and STD operated by Cascades Volcanic Observatory; others installed by Center for Earthquake Research and Information as part of this report. Datum is WGS84. Altitude is orthometric, interpolated from topographic maps after plotting locations. Distance is measured from centroid of seismic activity, the surface trace of which approximates the position of the vent.]

Station	Latitude (N)	Longitude (W)	Altitude (m)	Distance from vent (km)	Dates of operation
JRO	46.2751	122.2178	1,290	8.98	10/01/04–08/10/06
STD	46.2376	122.2240	1,250	5.28	10/25/04–present [1]
WIND	46.2504	122.1372	1,230	7.15	10/03/04–10/31/04
LAVA	46.1509	122.0908	850	9.13	10/03/04–12/02/04
BLUE	46.1682	122.2608	980	6.41	10/03/04–12/02/04
WEST	46.1946	122.3143	1,120	9.66	10/04/04–11/01/04
CLIM	46.1470	122.1825	1,140	5.58	10/04/04–11/01/04
SMTH	46.2128	122.0566	1,090	10.34	10/05/04–10/27/04
LSCT	46.1818	122.0540	500	10.52	12/03/04–05/07/05
SNOW	46.1306	122.1708	810	7.51	12/04/04–05/07/05
HRSE	46.1434	122.3244	620	12.02	12/05/04–05/06/05
PISH	46.3256	121.9754	860	21.77	12/07/04–05/08/05

[1] As of March 17, 2008.

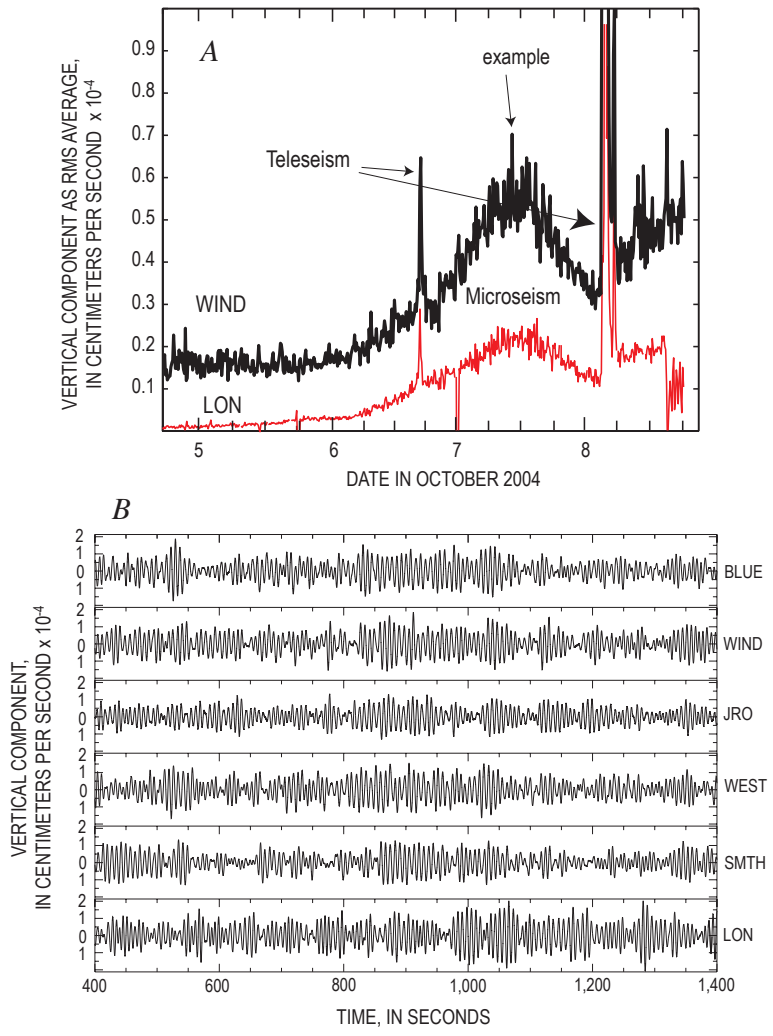

Figure 2. Ground motion recorded at Mount St. Helens, October 5–8, 2004. *A*, Moving RMS average (over consecutive 600-s window) of filtered (5–30 s) vertical component data at station WIND (black) and Pacific Northwest Seismic Network broadband station LON (red). Data from LON plotted in counts but scaled for visual comparison with velocity data from WIND. Date on x axis marks start of each day, PDT. Concurrent large sharp peaks at both stations are teleseismic arrivals. Broad increase that peaks about midday October 7 was most likely due to weather system impinging on region. Arrow labeled "example" shows approximate time displayed in bottom figure. *B*, Vertical component seismograms, all scaled to same absolute amplitude, for ~16-minute interval of intense low-frequency energy as recorded at six stations (listed at right edge).

Visual inspections of all moving RMS average peaks occurring in October and November 2004 revealed no VLP signals that originated below the Mount St. Helens crater. The absence of observed VLP signals could have been due in part to the distance of our stations from the source. Rapid decay of signal amplitude with distance is considered characteristic of VLP signals (Almendros and Chouet, 2003). VLP signals have been observed at other volcanoes at distances of less than 5 km (for example, Almendros and others, 2002; Aster and others, 2003). The closest broadband stations recording during the first deployment were STD and CLIM, about 5.28 km and 5.58 km respectively from the centroid of seismicity (fig. 1). Thus we cannot definitively rule out the occurrence of VLP signals at Mount St. Helens during this time period.

October 2004–May 2005 Seismicity Recorded by the Broadband Network

Event Magnitudes and Rates

Thousands of earthquakes were recorded during the 7-month broadband network deployment at Mount St. Helens. Because our data were not recorded in trigger mode, we developed a trigger algorithm based on the ratio of short-term (0.2 s) and long-term (320 s) averages to isolate individual events from the continuous records. We first applied a 0.5–3-Hz bandpass filter to the data and then used a short-term to long-term trigger ratio of 6 to identify 57,635 events. We assigned a magnitude for each event on the basis of the peak velocity (*pv*) measured on the vertical component at each CERI station. The body-wave arrivals of both hybrid and LF events were of smaller amplitude than the low-frequency waveforms that followed, so we assumed *pv* to be a surface-wave amplitude. We therefore adjusted the measured *pv* by the square root of the distance from the centroid of seismicity to the station (table 1) to account for geometrical spreading. The centroid location, 46.1964ºN and 122.18882ºW, was calculated from the PNSN catalog for events with $M_d \geq 2.5$ during this time period. The magnitude was given by $M_S = \log_{10}(pv) + 5.78$, where the distance-adjusted *pv* was averaged over all CERI stations and the constant (5.78) was calculated so that the largest event had M_S 3.4, equal to the PNSN duration-magnitude estimate for that event. Our magnitude estimates were reasonably consistent with PNSN magnitudes for events above M_d 2.6.

Figure 3*A* shows the distribution of event magnitudes selected by our trigger algorithm for the entire period of the network deployment. These have a normal distribution, with mean magnitude (M_S) of 1.78 and a standard deviation of 0.24 magnitude units. When comparing event triggers to the continuous seismograms, we observed that small earthquakes occurring in the coda of larger events were not likely to be selected by our trigger algorithm. Therefore, the distribution of smaller earthquakes in the sequence is probably not well characterized. The distribution of larger events, however, is probably well characterized. The distribution of earthquake size and the rate of activity varied with time, with larger earthquakes occurring irregularly throughout the sequence. To help discern patterns, we divided the entire dataset into 24-hour segments, calculated the magnitude distribution of each time interval as in figure 3*A*, and contoured the resulting magnitude distributions over time (fig. 3*B*). Most of the events with $M_S \geq 3$ occurred before October 5 and were associated with the closing days of the vent-clearing phase (Moran and others, this volume, chap. 2). The rate of seismic activity was quite high at that time, and the distribution of earthquake sizes was bimodal, with peaks around M_S 2.5 and M_S 2 and a range slightly greater than 2 magnitude units.

After October 5 the rate of seismic activity slowed drastically and the modal event size decreased to M_S 1.7 (fig. 3*B*). The minimum event size also increased to about M_S 1.5 from a minimum M_S of ~1.0 during the more active vent-clearing

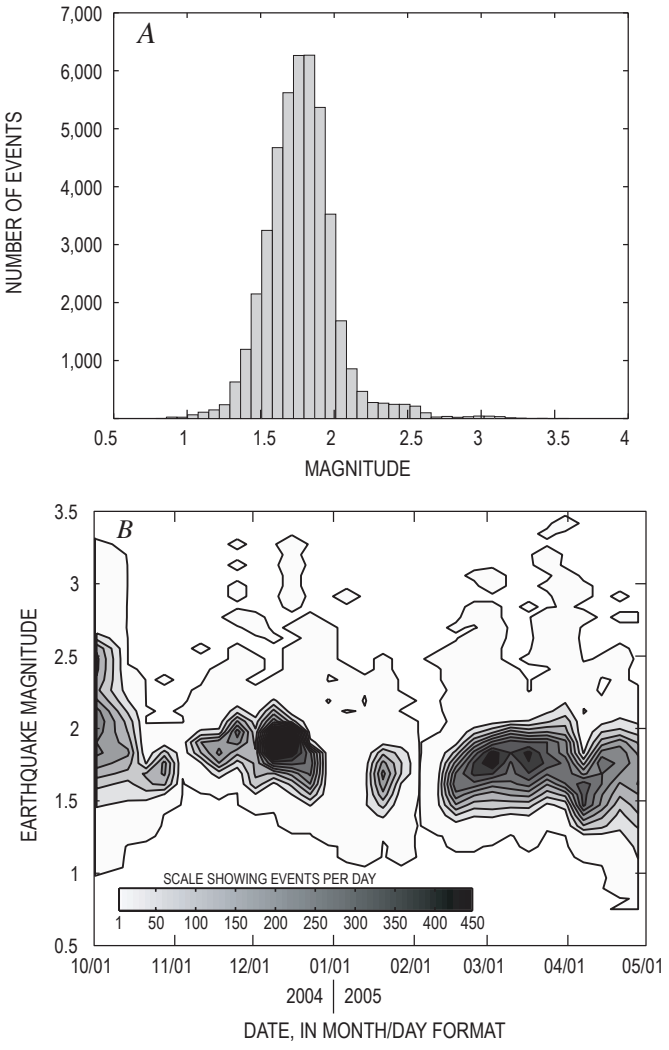

Figure 3. Event-magnitude occurrence for the more than 57,000 earthquakes identified during this deployment. Magnitudes are binned in 0.072-magnitude intervals. *A,* Histogram showing magnitude distribution. *B,* Time-series plot showing magnitude distribution. Contour interval is 50 events per day.

period. Because the trigger algorithm should have been more sensitive to small events when the rate of larger events was low, this increase of minimum event size during a period of reduced seismic activity suggests that the observed distribution for small events was not entirely due to lack of detection. Instead, small events were simply not plentiful during some time intervals.

Both the range and mode of earthquake size and the rate of seismic activity increased through the latter part of November 2004. These increases coincided with the approach and collision of spine 3 with the south crater wall (Schilling and others, this volume, chap. 8; Vallance and others, this volume, chap. 9). The seismic activity continued at a high rate through the middle of December, when 10 events with $M_S \geq 3.0$ occurred between December 17 and 19. Subsequently, both the rate of seismic activity and the modal size of events began to decrease. This trend continued through the middle of January, as spine 3 was disintegrating and being shoved aside by spine 4, and a large explosion occurred on January 16, 2005 (Moran and others, this volume, chap. 6). The seismicity rate increased through the latter part of January 2005. The small number of events between January 29 and February 6 was artificial, reflecting a loss of network data during that time interval. The seismicity rate remained high in March and April, when 14 $M_S \geq 3.0$ events occurred. It appears that the sporadic occurrence of events of $M_S \geq 3.0$ coincided with intervals of high seismicity rates.

Characteristics of Lower-Frequency Earthquakes at Mount St. Helens

Since the mid-1990s, broadband seismometers have been used to record earthquakes and tremor on numerous volcanoes around the world. Because our data were the first broadband recordings at Mount St. Helens, we looked with special care at the broadband character of the events recorded on our network. We recorded one high-frequency tectonic earthquake, two episodes of volcanic tremor, and thousands of lower-frequency earthquakes during the deployment. In this section we describe the characteristics of the lower-frequency events and compare our observations to the reported features of earthquakes observed at other volcanoes.

The first step was to compare a lower-frequency event to the high-frequency tectonic earthquake, because these form the two main types of earthquakes recorded at volcanoes (see, for example, Latter, 1981). We did not record volcano-tectonic events associated with the vent-clearing phase, because the broadband seismometers were only installed at the close of that phase. However, a small local tectonic event was recorded on November 22, 2004, at 0853 PST. Figure 4 shows seismograms and their associated spectra for that tectonic earthquake and an example LF earthquake, M_S 3.3, recorded on November 27, 2004, at 0601 PST. The tectonic event was not located by PNSN. However, a local hypocenter is required by the short S-P arrival-time differences at stations LAVA (1.5 s) and BLUE (2 s). We consider the event to be tectonic because it had sharp and well-defined P and S phases followed by a short high-frequency coda. Peak energy for this event was between 5 and 12 Hz, with very low spectral levels at frequencies less than 5 Hz. By contrast, the LF event had a low-amplitude onset, with frequencies as high as about 10 Hz, followed by a strong, long-duration, and lower-frequency waveform. The spectrum had significant energy between 0.3 and 5 Hz, with multiple spectral peaks suggestive of harmonic motion as observed for lower-frequency earthquakes at other volcanoes (for example, Chouet, 1996; Neuberg and others, 2006).

Next we compare the hybrid and LF earthquakes that form the two types of lower-frequency earthquakes recorded during the first year of renewed eruption at Mount St. Helens (Moran and others, this volume, chap. 2). For example, figure 5*A* shows the broadband seismograms for a M_S 3.13 hybrid earthquake recorded on October 3, 2004, at 1812 (PDT) and a M_S 3.2 LF earthquake recorded on November 28, 2004, at 1807 (PST). Figure 5*B* shows the same seismograms after 7-Hz highpass filters were applied, and figure 5*C* shows the Fourier displacement spectra for both events. The broadband waveforms of both events are dominated by the lower-

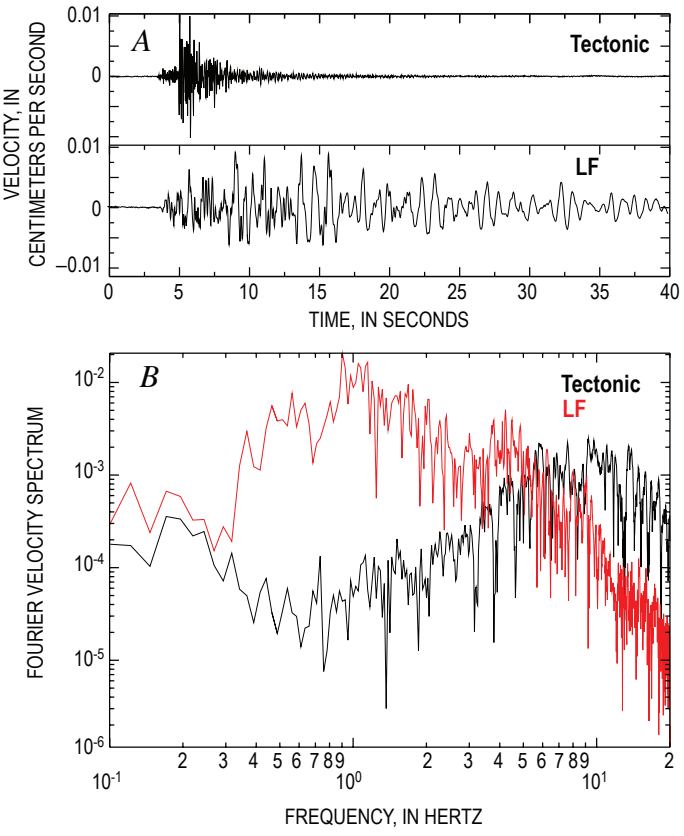

Figure 4. Seismograms and spectral characteristics for tectonic earthquake recorded November 22, 2004, and a low-frequency earthquake recorded November 27, 2004. *A*, Comparison of seismograms from station LAVA, plotted at same absolute scale. *B*, Fourier velocity spectra of associated seismograms. Tectonic earthquake is black trace; low-frequency event is red trace.

frequency (from 0.3 to about 5 Hz), nondispersive waves that give rise to the name of this class of earthquake. At frequencies between 0.3 and 2.0 Hz, the spectral amplitudes of the LF event slightly exceed those of the hybrid event (consistent with the slightly larger magnitude estimate), whereas at frequencies above 3.0 Hz, the spectral amplitudes of the hybrid event exceed the LF spectral amplitudes. This difference in high-frequency energy is also apparent in the time series, where the hybrid earthquake has a much more pronounced high-frequency onset (fig. 5*A*).

This difference in high-frequency energy is the primary difference between hybrid and LF earthquakes. It may result from a difference in the earthquake source process or a difference in the rock along the path from source to receiver that affects wave propagation (an increase in attenuation related to a reduction in source depth, for example). To investigate these possibilities, we filtered the lower-frequency energy from the signal. The filtered records (fig. 5*B*) show that both events actually have a high-frequency onset, although the amplitude is about five times larger for the hybrid event. Further, the high-frequency component of both events is similar in form and of comparable duration, extending well into the low-frequency waveform. This similarity in form and duration indicates that attenuation near the earthquake sources and along the paths to the receiver did not differ significantly. Rather, more high-frequency energy was generated at the source for the hybrid than for the LF earthquake. This is consistent with a larger component of shear faulting during the hybrid earthquake.

We explored the similarity in spectra between small and larger events in figure 6, where the velocity spectrum of the M_S 3.1 hybrid event (October 3, 2004) was compared to a randomly chosen M_S 1.7 event that occurred on October 11, 2004. The spectrum of the M_S 1.7 event was multiplied by a factor of 20 in order to compare the shape of the spectra of both events. The spectrum of the smaller event disappears into the background noise and is undetectable above 10 Hz and below 0.5 Hz. Between 0.5 and 10 Hz, the spectra of the large and small events were quite similar in shape and amplitude. The similarity in spectral shape suggests that both the source and path were similar for the two events. For tectonic earthquakes, the peak in the velocity spectrum would be expected to shift to lower frequencies as rupture zone size increased for larger earthquakes (Brune, 1970). The consistency in the frequency range of the peak of spectral energy for different-size earthquakes favors models such as that of Chouet (1996), in which a pressure transient resonates in a crack of constant dimension (a few centimeters in width), or that of Neuberg and others (2006), in which brittle failure of magma provides seismic energy that resonates in a conduit section of constant dimension (~30 m wide and several hundred meters long). In both cases the amplitude of the resonance would be determined by the strength of the pressure transient or size of the brittle failure, whereas the shape of the spectrum would be constrained by the size and properties of the resonator.

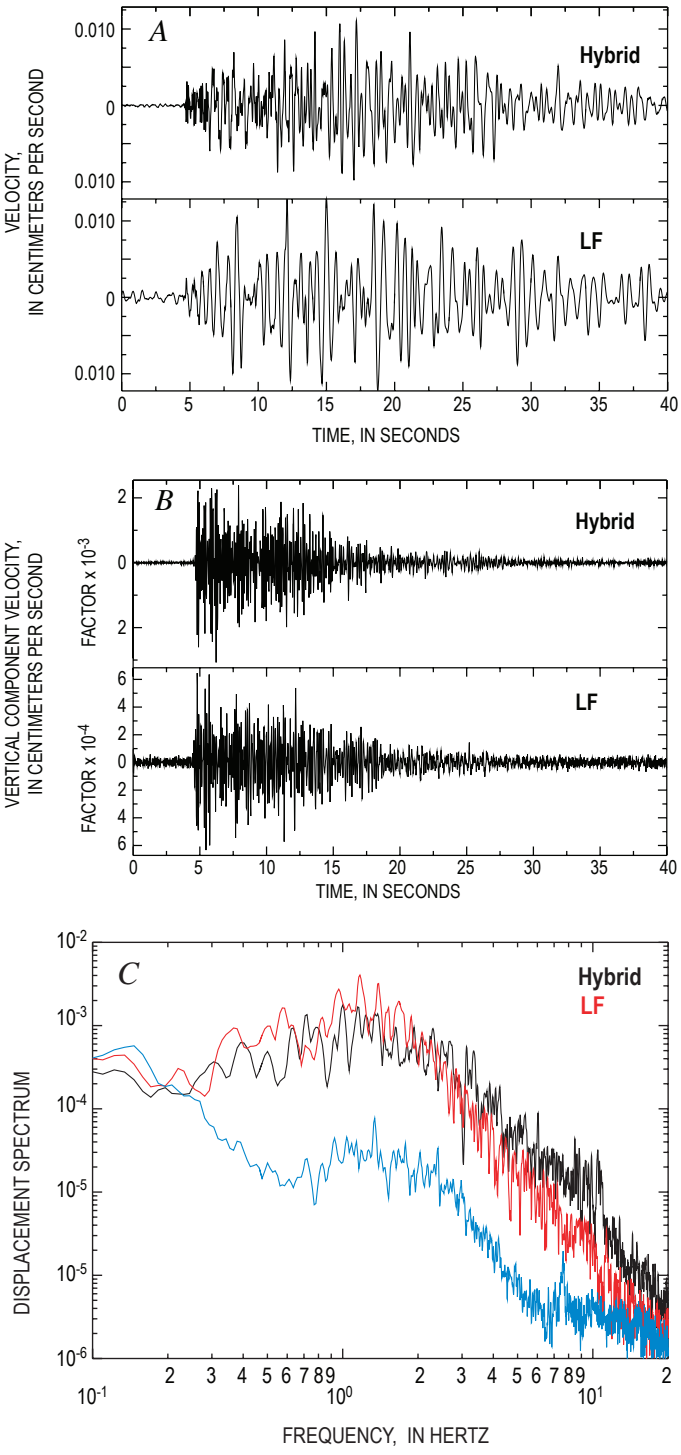

Figure 5. Comparison of seismic data from station BLUE for hybrid and low-frequency (LF) earthquakes. *A*, Vertical-component seismograms, plotted at same absolute scale. *B*, Corresponding 7-Hz highpass-filtered seismograms; note different scales. Decay of the waveforms is remarkably similar. *C*, Fourier displacement spectra of the original hybrid (black) and LF (red) seismograms. Spectrum of a 60-s interval from a "quiet" period on November 1, 2004, shows representative background noise level (blue). (This interval chosen because time intervals just before the two earthquakes contain the coda of other earthquakes.)

Resonance in a crack or conduit of constant dimensions produces amplitude spectra with strong peaks resulting from the summation of waves propagating between the boundaries of the structure. The specific frequencies of resonance are determined by the dimensions of the structure and the properties of the material within the conduit or crack. Identifying the frequencies of resonance would therefore place useful constraints on the volcanic process. Any given station can have a variety of peaks derived from its own particular source-receiver path and local site conditions, but the resonance peaks associated with a symmetric conduit or crack should be common to spectra observed at all stations independent of azimuth and distance. By comparing spectra at all stations, it should simply be a matter of identifying the common peaks.

A feature of the seismicity associated with this eruption of Mount St. Helens was the prominence of earthquake multiplets having highly similar waveforms (Thelen and others, this volume, chap. 4). Figure 7 shows the Fourier velocity spectra at six stations for a multiplet of 29 lower-frequency events ($2.1 \leq M_S \leq 2.2$) that occurred on October 16, 2004. The velocity spectra were normalized and overlaid for each station so that peaks that are consistent from event to event tend to stand out. Each station exhibits several consistent peaks in the range 0.4–2 Hz, but no peak appears consistently at all stations to indicate a specific frequency of source resonance. This lack of identifiable frequencies of source resonance is inconsistent with the resonance of a structure with simple geometry such as the rectangular crack of the Chouet (1996) model and the rectangular conduit of the Neuberg and others (2000) model. It suggests instead that wave propagation dominated the response at a given station and that source harmonics played a minor role. Alternatively, one can appeal to the excitation of a more complex, perhaps asymmetric, structure, where the harmonic response observed at a given station depends upon its location relative to the orientation of the source structure.

Fehler (1983) analyzed short-period records of tremor at Mount St. Helens that accompanied eruptions on August 7 and October 16–18, 1980. He found that the spectra of lower-frequency earthquakes were very similar to volcanic tremor, and he suggested that tremor was composed of many lower-frequency events inseparable in time. Neuberg and others (2000) observed that many episodes of volcanic tremor at Soufrière Hills volcano in Montserrat, West Indies, followed swarms of lower-frequency earthquakes in which the rate of earthquake occurrence continually increased until they merged into tremor. Figure 8*A* shows a seismogram with lower-frequency earthquakes followed by 58 minutes of volcanic tremor at Mount St. Helens on October 2, 2004. In this case, the lower-frequency earthquakes appeared to be distinct events occurring before and again after the volcanic tremor. There is no evidence to suggest that individual earthquakes merged to generate the volcanic tremor. Figure 8*B* shows the normalized velocity spectrum of one lower-frequency event and a 60-s window from the volcanic tremor. Neither spectrum displayed harmonic peaks at whole-number multiples of fundamental

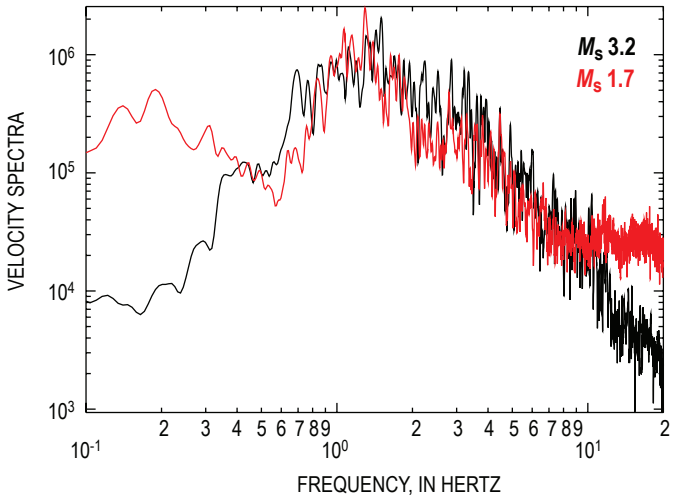

Figure 6. Spectral shapes of large and small events. Vertical-component Fourier velocity spectra recorded at station BLUE are shown for a M_S 3.2 hybrid event (black) and a randomly chosen M_S 1.7 event (red) occurring close together in time. Spectra of the small event (scaled up by a factor of 20) and large event are similar in shape between 0.5 and 10 Hz.

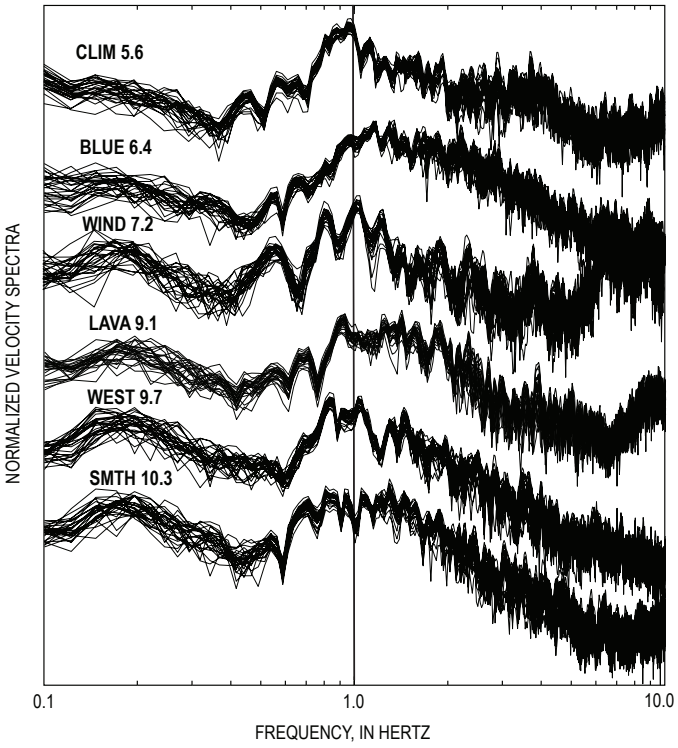

Figure 7. Comparison of spectra from six stations to identify source peaks. Fourier velocity spectra are plotted for a multiplet of 29 lower-frequency events ($2.1 \leq M_S \leq 2.2$) that occurred October 16, 2004. Velocity spectra are normalized and overlaid for each station so that peaks consistent from event to event become prominent. The distance to vent (see table 1) is to right of each station name.

frequencies. Both spectra had distinct peaks in common (for example, 0.8 and 1.1 Hz), consistent with Fehler's (1983) observations. However, the lower-frequency earthquake spectrum had a prominent peak at 0.6 Hz that was not observed in the spectrum of the volcanic tremor. This lower-frequency peak would be consistent with resonance of a structure having a larger dimension or with favorable excitation of the longer dimension of the same structure.

The progression from primarily volcano-tectonic events at the beginning of the 2004 eruption to combined hybrid and low-frequency (LF) events, then to dominantly LF events, reported by Moran and others (this volume, chap. 2), suggests a progressive loss of high-frequency seismic energy as magma moved toward and eventually onto the surface. Malone and collaborators have pointed out that gradual changes in event character were observed in many precursory swarms preceding dome-building eruptions at Mount St. Helens in the 1980s (Malone, 1983; Malone and others, 1983). During the 1980–86 dome-building eruptions, this transition became a diagnostic tool to predict eruption onset time (Malone and others, 1983; Swanson and others, 1983; Swanson and others, 1985). The high-frequency spectral difference between hybrid and LF events observed in figure 5*C* suggests that the slope of the high-frequency falloff could provide a measure to track the loss of high-frequency energy through time. To investigate this, the power spectra of an example hybrid and example LF event are compared in figure 9. Lines were fit by least squares to the high-frequency spectral amplitudes in the range 1–10 Hz. The slope of each line quantifies the rate of spectral amplitude decay with frequency or the high-frequency falloff of the velocity spectrum. The slope of the fitted line was −2.6 for the hybrid event and −4.9 for the LF event, indicating that this slope is a useful measure to quantify the high-frequency earthquake character.

We computed the high-frequency falloff for all events between October 4 and December 1, 2004 (CERI network station locations changed after December 1). Figure 10*A* shows earthquake magnitude versus time. Those events with magnitude in the range 1.5–2.0 are plotted in black, and other magnitudes are plotted in red. Because the high-frequency falloff could have a magnitude bias, the high-frequency falloff is plotted versus time (fig. 10*B*) with this same color convention. The slope of the high-frequency falloff ranged from approximately −1.75 to −5, defining a continuum between the ideal hybrid and LF events such as observed at Montserrat by Neuberg and others (2000). In early October, the slope values ranged from about −1.75 to −3.5, regardless of magnitude. The range was somewhat narrower for events with magnitude 1.5–2.0. Over time the slope values

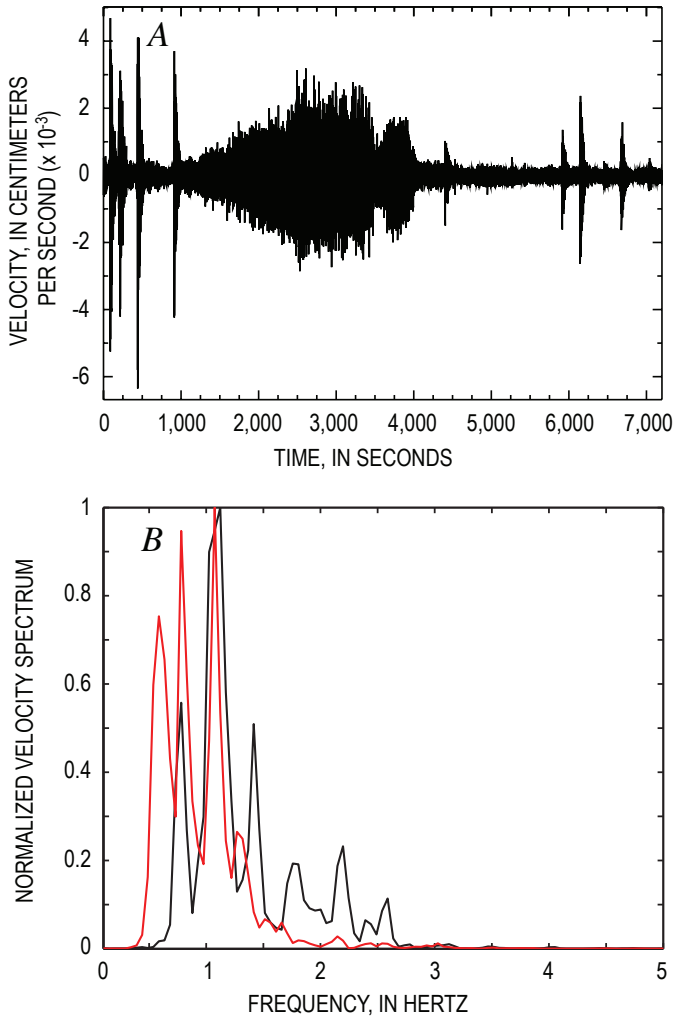

Figure 8. Seismic data showing 2-hour sequence of tremor recorded October 2, 2004, at JRO broadband station. *A*, Seismogram showing north component. Record of tremor is punctuated by impulsive earthquakes of lower-frequency type. *B*, Normalized velocity spectra for a lower-frequency earthquake (red) and the volcanic tremor (black) of October 2.

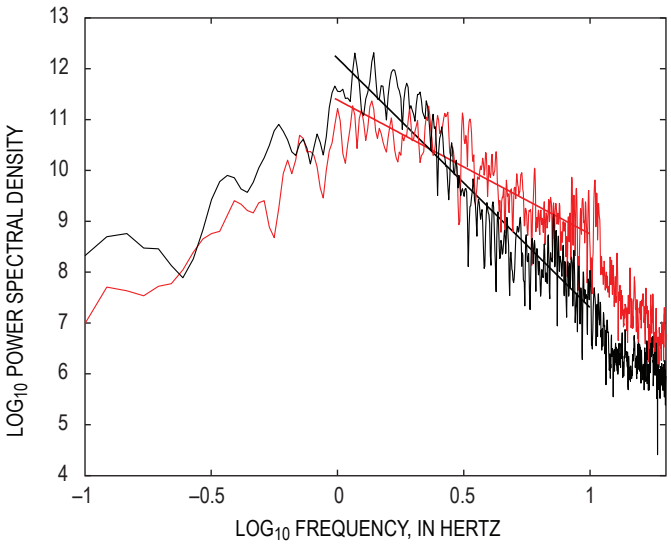

Figure 9. Power spectra of the vertical velocity components of a hybrid event (red) and a low-frequency event (black). Lines are least-squares fit to spectral amplitudes between 1 and 10 Hz; slopes are –2.6 for hybrid event and –4.9 for the LF event.

decreased to between about −3 and −4 at the end of October. The slope values continued at this level or decreased slightly until the end of November. If we arbitrarily declared a slope of −3.0 as the dividing line between hybrid and LF, then this figure would suggest about a 4:1 ratio of hybrid to LF events occurred between October 4 and October 5, decreasing smoothly to a 1:1 ratio by October 10, and decreasing to a 1:4 ratio by October 17. Other than a small increase around October 20, the slope continued to decrease so that by October 24, around 95 percent of the events were low frequency.

The gradual decrease in the slope of the high-frequency falloff over time reflects a progressive loss of high-frequency seismic energy. The loss of high-frequency seismic energy coincides with magma approaching and reaching the surface on October 11 (Scott and others, this volume, chap. 1). This lessening of high-frequency energy could be related to a decrease in earthquake source depth, with near-surface heterogeneity and anelasticity serving to filter out the higher-frequency parts of the seismograms. Alternatively, it may be related to a decrease in the static stress drop accompanying frictional slip as the magma plug, which initially needed to force its way through overlying rock, met with less resistance after the path to the surface was cleared.

Waveform Modeling

The record section in figure 11*A* shows bandpass-filtered (0.1–1 Hz) seismograms for a *M*s 2.9 LF earthquake that occurred on March 1, 2005, at 0928 PST. For this event, the acceleration record at station SEP in the crater was available. The SEP record was substantially clipped, but the filtered record should still illustrate the general character of ground acceleration in this passband. This earthquake was assigned a depth of 0.4 km by the PNSN. The seismograms all exhibited a low-amplitude onset followed by a long-duration, low-frequency waveform even at the closest station (SEP) recording acceleration. Signal duration increased with distance, from 15–20 s at less than 1 km epicentral distance from the source to ~50 s at 20 km distance. The first onset of larger-amplitude arrivals propagated at roughly 2 km/s. To investigate particle motion we chose a 6-s window having

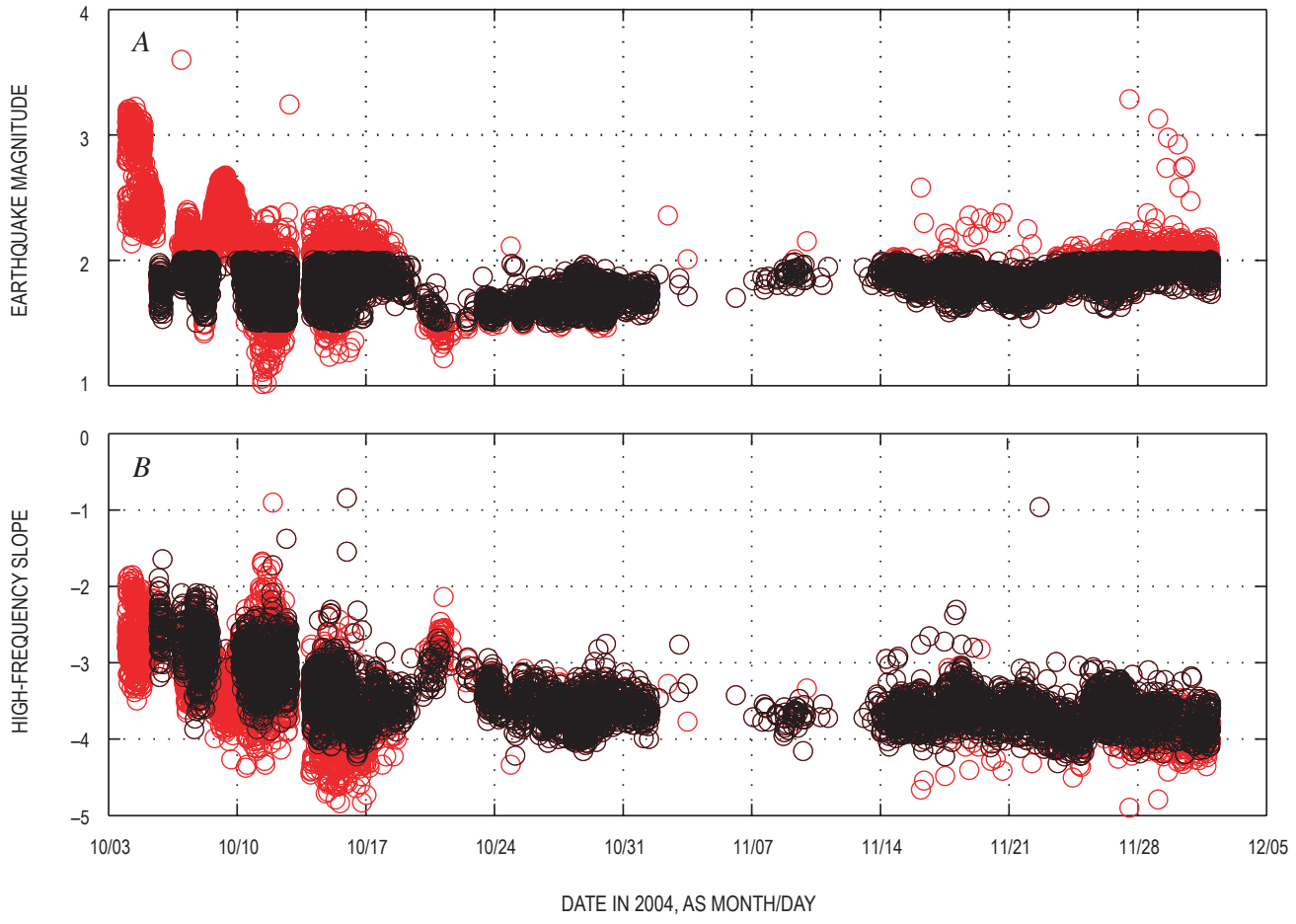

Figure 10. Time series showing seismic data from station BLUE. *A*, Magnitude versus time. Black circles show events in the range $1.5 \leq M_s \leq 2.0$; red circles are all other events. *B*, Plot of high-frequency slope versus time. Symbol color is determined by magnitude as in *A* (black circles, $1.5 \leq M_s \leq 2.0$).

a group velocity of 2 km/s for each station. At station PISH the particle motion in the vertical-radial plane was retrograde elliptical motion, characteristic of Rayleigh waves. However, the transverse component also had significant energy in this window, indicative either of Love waves or of multipathing. For the closer stations, the particle motion in the vertical-radial plane was more complex, suggesting interaction of body and surface waves in this window.

We used a reflection matrix method (Randall and others, 1995) to compute synthetic seismograms for a one-dimensional (1D) velocity model. The velocity model (table 2) was modified from the P-wave velocity model of Lees and Crosson (1989). The S-wave velocity in each layer was calculated from the P-wave velocity using a ratio of 1.7, based on the work of Sudo and Kong (2001), who found an average V_P / V_S ratio of 1.704 fit observed P- and S-wave travel times at all stations for a large number of well-recorded earthquakes at Aso volcano, Kyushu, Japan. A low-velocity surface layer with Swave velocity of 2 km/s was required to have the synthetic surface waves propagate at a velocity near 2 km/s. Moderate Q values were assumed (see table 2). We assumed an implosive source with −1 on the diagonal elements of the moment tensor and 0 on the off-diagonal elements. The synthetics were convolved with a triangular source pulse of 1-s duration and then lowpass filtered at 1 Hz.

The synthetic waveforms in figure 11*B* did a reasonable job of predicting the character of the initial arrivals and the beginning of the surface wave train. The synthetic P wave had a down first motion and was emergent at all azimuths. The synthetics do not have the long duration of the observed surface waves but rather a slightly dispersed surface wave traveling at approximately 2 km/s. We also tested other reasonable permutations of the layer velocities within a vertically stratified velocity model without producing the low-frequency coda. From this exercise we concluded that the low-frequency coda observed in figure 11*A* was not produced by a slow surface layer in a 1D velocity model. Scattering of low-frequency surface waves by the extreme local topography of the volcano would be a likely source of some of the coda. The resonance of a source structure (for example, Chouet, 1996, or Neuberg and others, 2006) could also contribute. Examination of surface-wave propagation in a 3D velocity model was beyond the scope of the current study. Unfortunately, we concluded that our simple 1D velocity model was inadequate for modeling waveforms for the purpose of determining the source time function and focal mechanism for these events, because the coda would map into the source.

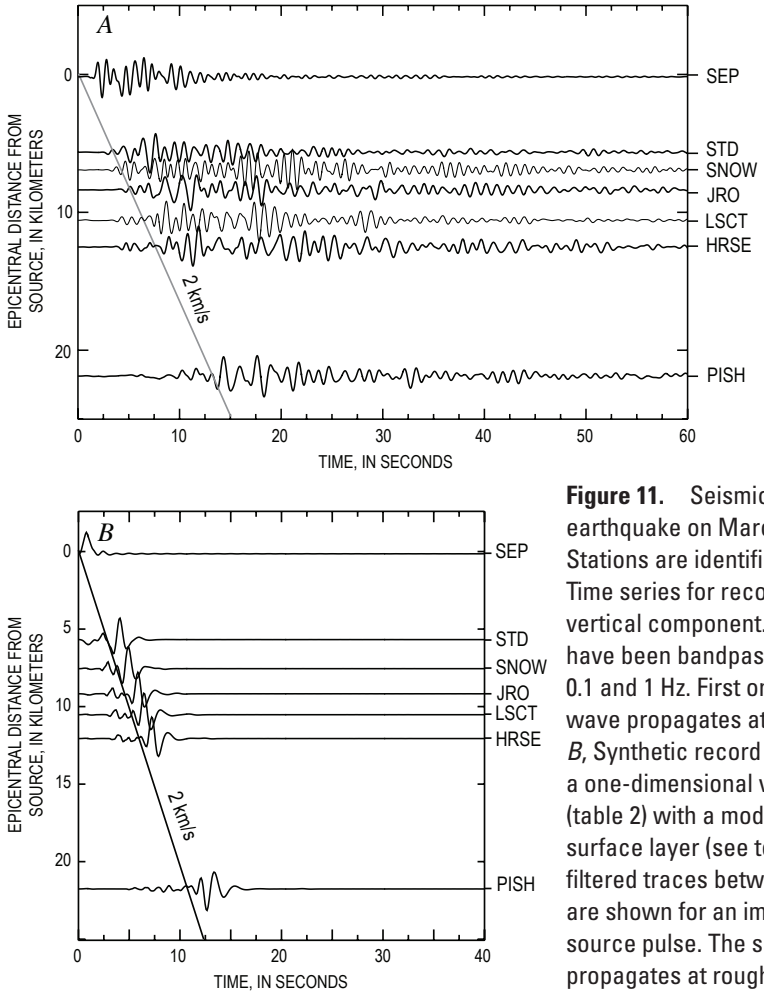

Figure 11. Seismic data for earthquake on March 1, 2005. Stations are identified at right. *A*, Time series for record section from vertical component. Vertical traces have been bandpass filtered between 0.1 and 1 Hz. First onset of the surface wave propagates at roughly 2 km/s. *B*, Synthetic record section assuming a one-dimensional velocity model (table 2) with a moderately slow surface layer (see text). Bandpass-filtered traces between 0.1 and 1 Hz are shown for an implosive, triangular source pulse. The surface wave propagates at roughly 2 km/s.

Table 2. Velocity structure of Mount St. Helens used in this study.

[For a material cycled in stress, Q is the inverse ratio of the energy lost each cycle to the peak strain energy. Q_P and Q_S specify the anelasticity of a material to P- and S-wave motion, respectively.]

Layer	Depth to top of layer (km)	S-wave velocity (km/s)	P-wave velocity (km/s)	Density (g/cm^3)	Q_S	Q_P
1	0	2.0	3.4	2.1	100	200
2	2	3.18	5.4	2.2	100	200
3	4	3.75	6.38	2.2	100	200
4	9	3.88	6.59	2.3	100	200
5	16	3.96	6.73	2.8	250	500
6	20	4.04	6.86	2.8	250	500
7	25	4.09	6.95	2.8	250	500
8	32	4.06	6.90	2.8	250	500
9	41	4.59	7.85	3.3	300	600

Summary

A network of broadband seismometers was rapidly deployed at Mount St. Helens when it became restless in September 2004 and maintained through the winter of 2004–5 without a significant loss of data. A principal reason for deploying broadband seismometers was to record any very long period (VLP) seismicity (5–30 s) associated with the eruption that would otherwise have been missed by the PNSN short-period stations. We found no evidence of VLP pulses at our stations in the first 2 months of recording. Our closest stations were more than 5 km distant from the centroid of seismic activity, and these pulses may attenuate too quickly to be observed at that distance.

More than 57,000 earthquakes were recorded during the 7-month deployment. They had a normal magnitude distribution, with a mean magnitude of 1.78 and a standard deviation of 0.24 magnitude units. Both the mode and range of earthquake size and the rate of activity varied during the 7-month period. Some cases of this variation can be associated with spine growth and breakup. In general, larger earthquakes tended to occur when the earthquake rate was high.

The dataset consisted largely of hybrid and low frequency (LF) earthquakes. These lower-frequency events typically had a low amplitude onset with frequencies up to about 10 or 20 Hz, followed by a strong, long-duration, and lower-frequency waveform. The shape of the Fourier spectrum at the low-frequency end was similar for both types of events, having significant energy between 0.3 and 5 Hz with multiple spectral peaks. Hybrid events exhibited more energetic high-frequency onsets than LF events, but the rate of high-frequency decay with time was similar for both types. The difference in high-frequency energy was more likely related to the source than to attenuation near the source or along the path, inasmuch as the high-frequency decay rate was the same for both events.

The spectra of large and small events that occurred close in time were quite similar in shape between 0.5 and 10 Hz. The similarity in spectral shape suggested that both the source and path were similar for the larger and smaller events. As opposed to the ideal tectonic earthquake spectra, in which the peak in the velocity spectrum changes to lower frequency as rupture zone area increases for larger earthquakes, the frequency range of the peak of spectral energy remained constant for different-size, lower-frequency earthquakes. This relative constancy is consistent with a resonating source, whereby the shape of the spectrum is constrained by the size and properties of the resonator. However, a search of spectra of the same events observed at multiple stations revealed no specific frequencies of source resonance, and so the spectra may reflect a complex, perhaps asymmetric, resonating structure.

The spectra of a lower-frequency earthquake and an episode of volcanic tremor had distinct peaks in common. However, the lower-frequency earthquake spectrum had a prominent peak at 0.6 Hz that was not observed in the spectrum of the volcanic tremor, and higher frequencies were more favorably excited during the tremor. This lower-frequency peak would be consistent with resonance of a larger structure during the earthquake or a change in the source such that excitation of the longer dimension of the same structure was favorable.

The high-frequency spectral difference between hybrid and LF events was quantified using the slope of the high-frequency falloff. The slope computed for several thousand lower-frequency earthquakes between October 4 and December 1, 2004, defined a continuum between the ideal hybrid and ideal LF events. The slope started relatively high on October 4 and transitioned smoothly to lower values until around October 14. The gradual decrease in the slope of the high-frequency falloff over time reflected a progressive loss of high-frequency seismic energy as magma approached and eventually reached the surface.

The first onset of the surface-wave train produced by low-frequency earthquakes propagated at roughly 2 km/s. This propagation velocity favors an areally extensive surface layer with an average S-wave velocity of about 2 km/s. A window of the vertical and radial components for a 2 km/s group velocity has retrograde elliptical particle motion when observed at 20 km distance. Signal duration ranges from 15 to 50 s. A one-dimensional velocity model was unsuitable for waveform modeling to determine the source time function and focal mechanism of the lower-frequency earthquakes.

Acknowledgments

Deployment and maintenance of the seismic network was facilitated by numerous individuals at the U.S. Forest Service, the Cascades Volcano Observatory, and the Pacific Northwest Seismic Network of the University of Washington. Federal Express shipped our equipment to Portland, Oregon, without cost. We are grateful to Thomas Brackman, Chris Watson,

and Gary Patterson of the Center for Earthquake Research and Information (CERI) at the University of Memphis for taking time to assist in the field. We obtained seismic data for stations LON, JRO, and STD from the Incorporated Research Institutions for Seismology Data Management Center. Greg Waite and Charles Langston provided thoughtful and helpful reviews of this paper. This is CERI contribution 511.

References Cited

Almendros, J., and Chouet, B., 2003, Performance of the radial semblance method for the location of very long period volcanic signals: Seismological Society of America Bulletin, v. 93, p. 1890–1903.

Almendros, J., Chouet, B., Dawson, P., and Bond, T., 2002, Identifying elements of the plumbing system beneath Kilauea Volcano, Hawaii, from the source locations of very-long-period signals: Geophysical Journal International, v. 148, p. 303–312.

Aster, R., Mah, S., Kyle, P., McIntosh, W., Dunbar, N., Johnson, J., Ruiz, M., and McNamara, S., 2003, Very long period oscillations of Mount Erebus Volcano: Journal of Geophysical Research, v. 108, no. B11, 2522, doi:10.1029/2002JB002101.

Brune, J.N., 1970, Tectonic stress and the spectra of seismic shear waves from earthquakes: Journal of Geophysical Research, v. 75, no. 23, p. 4997–5009.

Chouet, B.A., 1996, Long-period volcano seismicity; its source and use in eruption forecasting: Nature, v. 380, p. 309–316.

Endo, E.T., Malone, S.D., Noson, L.L., and Weaver, C.S., 1981, Locations, magnitudes, and statistics of the March 20–May 18 earthquake sequence, *in* Lipman, P.W., and Mullineaux, D.R., eds., The 1980 eruptions of Mount St. Helens, Washington: U.S. Geological Survey Professional Paper 1250, p. 93–107.

Fehler, M., 1983, Observations of volcanic tremor at Mount St. Helens Volcano: Journal of Geophysical Research: v. 88, p. 3476–3484.

Lahr, J.C., Chouet, B.A., Stephens, C.D., Power, J.A., and Page, R.A., 1994, Earthquake classification, location, and tremor analysis in a volcanic environment; implications for the magmatic system of the 1989–1990 eruptions at Redoubt Volcano, Alaska: Journal of Volcanology and Geothermal Research, v. 62, nos. 1–4, p. 137–151, doi:10.1016/0377-0273(94)90031-0.

Latter, J.H., 1981, Volcanic earthquakes, and their relationship to eruptions at Ruapehu and Ngauruhoe volcanoes: Journal of Volcanology and Geothermal Research, v. 9, p. 293–309.

Lees, J.M., and Crosson, R.S., 1989, Tomographic inversion for three-dimensional velocity structure at Mount St. Helens using earthquake data: Journal of Geophysical Research, v. 94, no. B5, p. 5716–5728.

Longuet-Higgins, M.S., 1950, A theory of the origin of microseisms: Philosophical Transactions of the Royal Society of London, series A, v. 243, p. 1–35.

Malone, S.D., 1983, Volcanic earthquakes; examples from Mount St. Helens, *in* Earthquakes; observations, theory and interpretation: Bologna, Italy, Società Italiana di Fisica, p. 436–455.

Malone, S.D., Boyko, C., and Weaver, C.S., 1983, Seismic precursors to the Mount St. Helens eruptions in 1981 and 1982: Science, v. 221, p. 1376–1378.

McChesney, P.J., Couchman, M.R., Moran, S.C., Lockhart, A.B., Swinford, K.J., and LaHusen, R.G., 2008, Seismic-monitoring changes and the remote deployment of seismic stations (seismic spider) at Mount St. Helens, 2004–2005, chap. 7 *of* Sherrod, D.R., Scott, W.E., and Stauffer, P.H., eds., A volcano rekindled; the renewed eruption of Mount St. Helens, 2004–2006: U.S. Geological Survey Professional Paper 1750 (this volume).

Moran, S.C., Malone, S.D., Qamar, A.I., Thelen, W.A., Wright, A.K., and Caplan-Auerbach, J., 2008a, Seismicity associated with renewed dome building at Mount St. Helens, 2004–2005, chap. 2 *of* Sherrod, D.R., Scott, W.E., and Stauffer, P.H., eds., A volcano rekindled; the renewed eruption of Mount St. Helens, 2004–2006: U.S. Geological Survey Professional Paper 1750 (this volume).

Moran, S.C., McChesney, P.J., and Lockhart, A.B., 2008b, Seismicity and infrasound associated with explosions at Mount St. Helens, 2004–2005, chap. 6 *of* Sherrod, D.R., Scott, W.E., and Stauffer, P.H., eds., A volcano rekindled; the renewed eruption of Mount St. Helens, 2004–2006: U.S. Geological Survey Professional Paper 1750 (this volume).

Neuberg, J., Luckett, R., Baptie, B., and Olsen, K., 2000, Models of tremor and low-frequency earthquake swarms on Montserrat: Journal of Volcanology and Geothermal Research, v. 101, p. 83–104.

Neuberg, J.W., Tuffen, H., Collier, L., Green, D., Powell, T., and Dingwell, D., 2006, The trigger mechanism of low-frequency earthquakes on Montserrat: Journal of Volcanology and Geothermal Research, v. 153, nos. 1–2, p. 37–50, doi:10.1016/j.jvolgeores.2005.08.008.

Randall, G.R., Ammon, C.J., and Owens, T.J., 1995, Moment-tensor estimation using regional seismograms from a Tibetan Plateau portable network deployment: Geophysical Research Letters, v. 22, p. 1665–1668.

Schilling, S.P., Thompson, R.A., Messerich, J.A., and Iwatsubo, E.Y., 2008, Use of digital aerophotogrammetry to

determine rates of lava dome growth, Mount St. Helens, Washington, 2004–2005, chap. 8 *of* Sherrod, D.R., Scott, W.E., and Stauffer, P.H., eds., A volcano rekindled; the renewed eruption of Mount St. Helens, 2004–2006: U.S. Geological Survey Professional Paper 1750 (this volume).

Scott, W.E., Sherrod, D.R., and Gardner, C.A., 2008, Overview of 2004 to 2006, and continuing, eruption of Mount St. Helens, Washington, chap. 1 *of* Sherrod, D.R., Scott, W.E., and Stauffer, P.H., eds., A volcano rekindled; the renewed eruption of Mount St. Helens, 2004–2006: U.S. Geological Survey Professional Paper 1750 (this volume).

Sudo, Y., and Kong, L.S.L., 2001, Three-dimensional seismic velocity structure beneath Aso Volcano, Kyushu, Japan: Bulletin of Volcanology, v. 63, p. 326–344.

Swanson, D.A., Casadevall, T.J., Dzurisin, D., Malone, S.D., Newhall, C.G., and Weaver, C.S., 1983, Predicting eruptions at Mount St. Helens, June 1980 through December 1982: Science, v. 221, no. 4618, p. 1369–1376.

Swanson, D.A., Casadevall, T.J., Dzurisin, D., Malone, S.D., Holcomb, R.T., Newhall, C.G., and Weaver, C.S., 1985, Forecasts and predictions of eruptive activity at Mount St. Helens, USA: 1975–1984: Journal of Geodynamics, v. 3, p. 397–423.

Thelen, W.A., Crosson, R.S., and Creager, K.C., 2008, Absolute and relative locations of earthquakes at Mount St. Helens, Washington, using continuous data; implications for magmatic processes, chap. 4 *of* Sherrod, D.R., Scott, W.E., and Stauffer, P.H., eds., A volcano rekindled; the renewed eruption of Mount St. Helens, 2004–2006: U.S. Geological Survey Professional Paper 1750 (this volume).

Vallance, J.W., Schneider, D.J., and Schilling, S.P., 2008, Growth of the 2004–2006 lava-dome complex at Mount St. Helens, Washington, chap. 9 *of* Sherrod, D.R., Scott, W.E., and Stauffer, P.H., eds., A volcano rekindled; the renewed eruption of Mount St. Helens, 2004–2006: U.S. Geological Survey Professional Paper 1750 (this volume).

A Volcano Rekindled: The Renewed Eruption of Mount St. Helens, 2004–2006
Edited by David R. Sherrod, William E. Scott, and Peter H. Stauffer
U.S. Geological Survey Professional Paper 1750, 2008

Chapter 6

Seismicity and Infrasound Associated with Explosions at Mount St. Helens, 2004–2005

By Seth C. Moran[1], Patrick J. McChesney[2], and Andrew B. Lockhart[1]

Abstract

Six explosions occurred during 2004–5 in association with renewed eruptive activity at Mount St. Helens, Washington. Of four explosions in October 2004, none had precursory seismicity and two had explosion-related seismic tremor that marked the end of the explosion. However, seismicity levels dropped following each of the October explosions, providing the primary instrumental means for explosion detection during the initial vent-clearing phase. In contrast, explosions on January 16 and March 8, 2005, produced noticeable seismicity in the form of explosion-related tremor, infrasonic signals, and, in the case of the March 8 explosion, an increase in event size ~2 hours before the explosion. In both 2005 cases seismic tremor appeared before any infrasonic signals and was best recorded on stations located within the crater. These explosions demonstrated that reliable explosion detection at volcanoes like Mount St. Helens requires seismic stations within 1–2 km of the vent and stations with multiple acoustic sensors.

Introduction

On September 23, 2004, a swarm of volcano-tectonic earthquakes heralded the reawakening of Mount St. Helens after 18 years of quiescence (Moran and others, this volume, chap. 2). On October 1 the first small explosion occurred, with three others following over the next four days (table 1). Several of these happened during daylight hours and were broadcast on live television across the United States, perhaps creating an impression that Mount St. Helens was building towards a larger explosive eruption. Instead, these explosions were followed by the steady-state extrusion of a new dome in the southern part of the 1980 crater. The relatively steady-state extrusion was punctuated by just two explosions, one on January 16, 2005, and the other on March 8, 2005 (table 1). All six explosions were phreatic, with no evidence, such as fresh pumice, of any significant magmatic component (Scott and others, this volume, chap. 1; Rowe and others, this volume, chap. 29). Overall, the eruption in 2004–5 featured very little explosive activity, a result of the gas-poor nature of the erupted magma (Gerlach and others, this volume, chap. 26).

We use the term "explosion" in this paper to refer to an impulsive, sudden yet sustained emission of volcanic gas and pyroclasts. Rapid detection of ash-producing explosions is of paramount importance because of the demonstrated dangers posed to aircraft by airborne ash particles (for example, Neal and others, 1997). Despite the paucity of explosions, seismic and acoustic recordings of the six explosions at Mount St. Helens have yielded several important insights into the utility and placement of seismic and acoustic sensors for improved explosion-detection capabilities, as well as insights into the nature of minor explosive activity during dome-building eruptions. In this paper we present a chronology of observations and recordings of explosions from 2004–5, focusing on our ability to detect the onset and termination of each explosion and on insights gained from seismic and acoustic data into the evolution of individual explosions.

Explosions During the Vent-Clearing Phase, October 1–October 5, 2004

Explosion 1: October 1, 1202 PDT

The first explosion occurred without warning at 1202 PDT on October 1 (fig. 1*A*, table 1), 8.5 days after the start of seismic unrest (Moran and others, this volume, chap. 2). The explosion was well documented, as it took place on a clear day

[1] U.S. Geological Survey, 1300 SE Cardinal Court, Vancouver, WA 98683

[2] Pacific Northwest Seismic Network, Department of Earth and Space Sciences, University of Washington, Box 351310, Seattle, WA 98195

Table 1. Summary of eruption parameters and seismic and acoustic observations of the six explosions occurring at Mount St. Helens, Washington, during 2004–5.

[PDT, Pacific daylight (saving) time; PST, Pacific standard time.]

Explosion number, date, and time	Duration (minutes)	Seismicity before, during, and after	Infrasound detected?	Plume height (approximate, m above vent)	Eruption phase
Explosion 1: 10/01/04, 1202 PDT	19	No precursors; earthquakes stopped following onset; tremor associated with end of explosion; almost no earthquakes for several hours afterwards	N/A (no sensors)	2,400	Vent clearing
Explosion 2: 10/03/04, 2240 PDT	~25	No precursors; earthquake rates decreased after onset (drop not as pronounced as explosion 1); tremor associated with end of explosion; seismicity low following explosion	Possible, but could also be coseismic shaking	400	Vent clearing
Explosion 3: 10/04/04, 0943 PDT	~32	No precursors; earthquake rates gradually declined after onset (drop not as pronounced as explosion 2); no tremor associated with end of explosion	No	1,500	Vent clearing
Explosion 4: 10/05/04, 0905 PDT	70	No precursors; gradual but significant decline in earthquake rate and size after onset; no tremor associated with end of explosion	No	2,400	Vent clearing
Explosion 5: 01/16/05, 0312 PST	~33	No precursors; tremor occurred during entire event; no change in earthquake rate observed after explosion	Yes	Unknown	Dome building
Explosion 6: 03/08/05, 1725 PST	~20	Earthquake magnitudes increased ~2 hours before onset; tremor associated with entire event; short-lived increase in earthquake rate after explosion, rate returned to normal within 1–2 hours	Yes	9,000	Dome building

with a U.S. Geological Survey (USGS) crew flying over the crater at the start of the explosion (Schneider and others, this volume, chap. 17), and many television cameras were transmitting images live from a site near Johnston Ridge Observatory (JRO) (fig. 2) to a nationwide audience (Driedger and others, this volume, chap. 24). Infrared recordings of the base of the eruption column showed peak temperatures around 160°C, consistent with visual observations that the explosion was phreatic (Schneider and others, this volume, chap. 17). Eruption cloud tops reached ~4,500 m above sea level (asl), or 2,400 m above the vent.

As described by Moran and others (this volume, chap. 2), seismicity had intensified in a series of steps through the first several days of the crisis that began on September 23, 2004 (fig. 3). By September 29, earthquakes of magnitude 2 and greater were occurring at a rate of ~1 per minute. Although seismicity intensified gradually between 0800 and 1100 PDT on October 1, several more-rapid intensifications had occurred in the previous two days, and so this intensification was not recognized as a short-term warning sign. Because preexplosion seismicity was so intense, it was difficult to see any obvious seismicity associated with the explosion in the first several minutes after 1202 PDT (fig. 1*A*). The most obvious seismic signal was the sudden cessation of earthquakes ~1 minute after the explosion began. After the earthquakes stopped, explosion-related tremor (defined here as seismic tremor accompanying

an explosion) with frequencies of 1–3 Hz and a peak reduced displacement, or D_R (Aki and Koyanagi, 1981), of ~6 cm^2 could clearly be seen on many nearby stations (fig. 1*A*; see fig. 2 for station locations). Tremor began increasing in amplitude at 1216, then abruptly stopped at 1221, when the explosion also stopped. Weak tremor occurred again starting at 1240, but earthquakes did not occur again until ~3 hours later (Moran and others, this volume, chap. 2).

If the earthquakes had not ceased when the explosion started and the explosion had not occurred during daylight hours in clear conditions, it is possible that staff at the Cascades Volcano Observatory (CVO) and the Pacific Northwest Seismic Network (PNSN) might not have realized that an explosion had occurred. The intense earthquake activity at the time was continuously saturating nearby seismic stations, all of which had short-period vertical-component seismometers, and the explosion-related tremor would have been almost impossible to distinguish had the earthquakes not ceased. In an attempt to improve our explosion detection capability, 1-Hz infrasound-sensitive acoustic sensors (see appendix 1) were

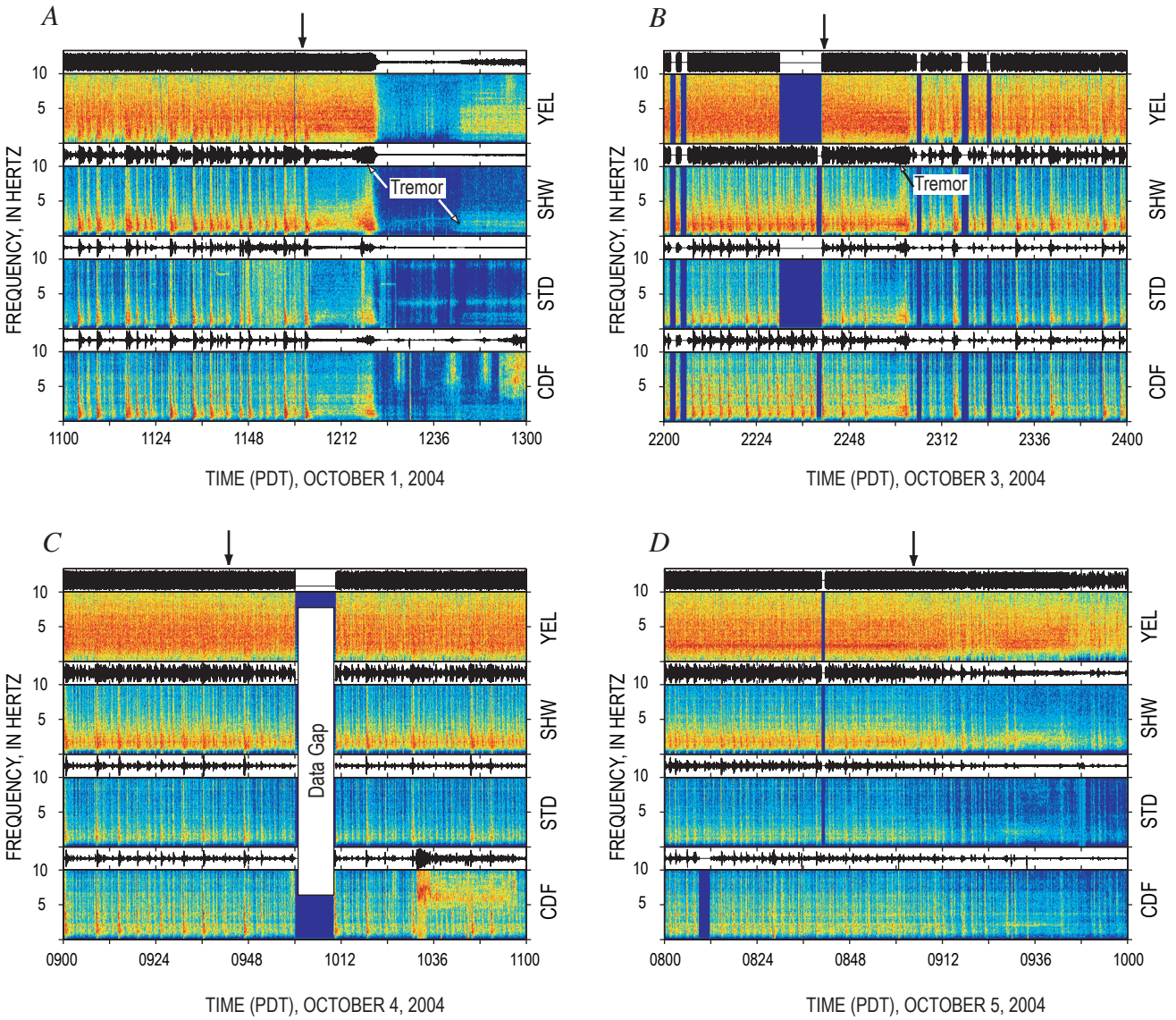

Figure 1. Multistation 2-hour-long spectrograms for explosions 1–4 at Mount St. Helens, Washington, October 2004. Time series (top) and frequency spectrogram (bottom) are shown for each of four seismic stations (see fig. 2 for station locations). Stations are shown in order of distance from vent, with closest station at top of the plot. Each time series is normalized to the maximum amplitude in each 2-hour window. Frequency spectrograms show spectral amplitudes for frequencies ranging from 0 to 10 Hz using a rainbow color palette, with dark blue corresponding to low spectral amplitudes (< 30 dB) and red to high amplitudes (>100 dB). Explosion onset time indicated by an arrow at top of each spectrogram. *A*, October 1, 2004, 1100–1300 PDT (explosion at 1202). *B*, October 3, 2004, 2200–2400 PDT (explosion at ~2240). *C*, October 4, 2004, 0900–1100 PDT (explosion at 0943). *D*, October 5, 2004, 0800–1000 PDT (explosion at 0905).

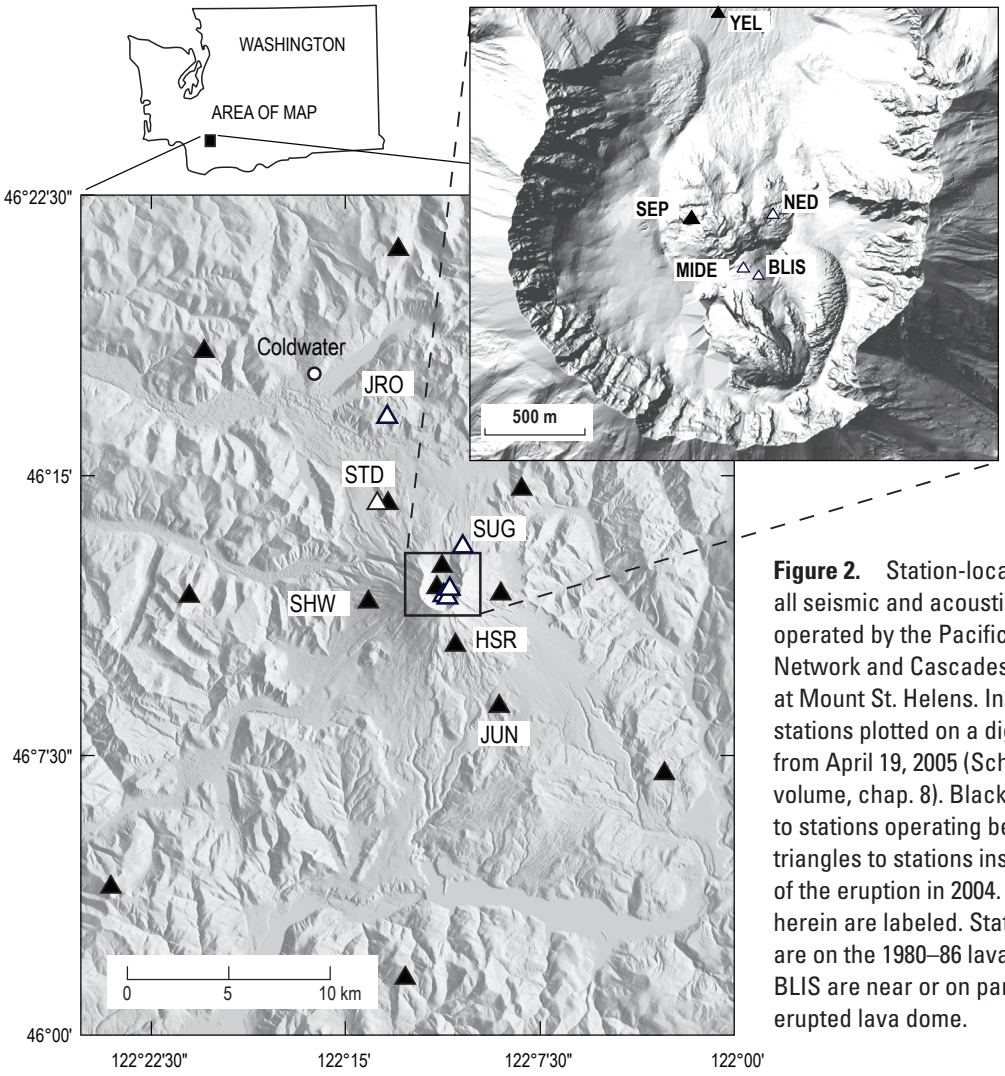

Figure 2. Station-location map showing all seismic and acoustic sensors jointly operated by the Pacific Northwest Seismic Network and Cascades Volcano Observatory at Mount St. Helens. Inset map shows stations plotted on a digital elevation model from April 19, 2005 (Schilling and others, this volume, chap. 8). Black triangles correspond to stations operating before 2004, white triangles to stations installed after the start of the eruption in 2004. All stations discussed herein are labeled. Stations SEP and NED are on the 1980–86 lava dome, MIDE and BLIS are near or on parts of the newly erupted lava dome.

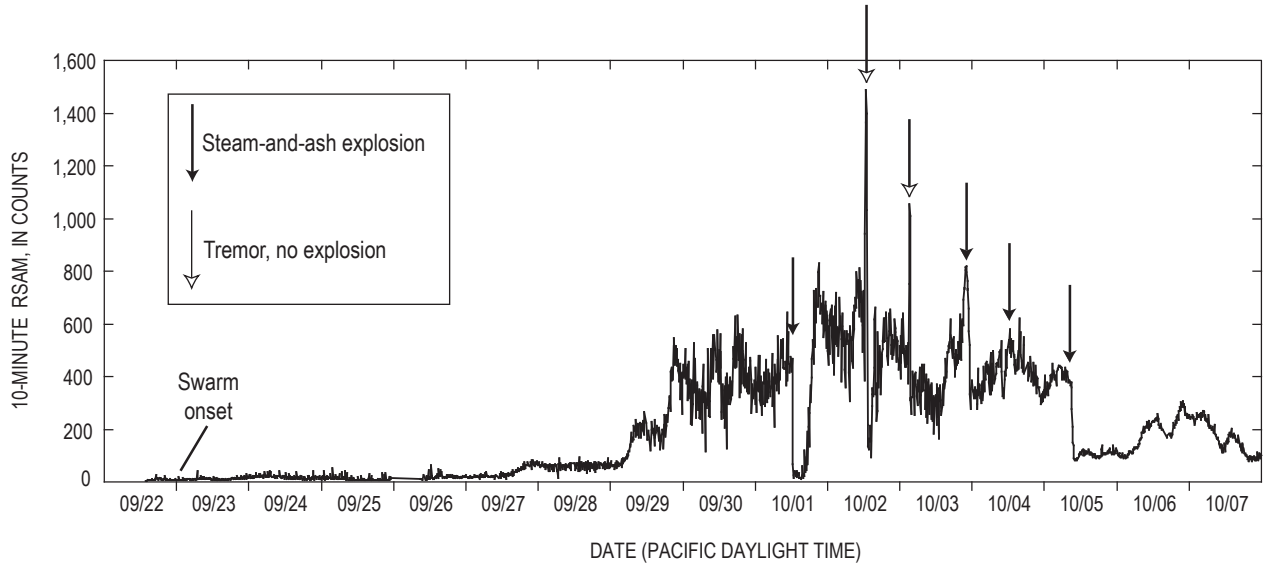

Figure 3. Plot of 10-minute RSAM values (Endo and Murray, 1991) for station SHW (see fig. 2) from September 22 to October 8, 2004. Black arrows indicate timing of individual explosions; white arrows, timing of two tremor episodes that did not correspond to any explosions (the only two such cases during entire eruption; Moran and others, this volume, chap. 2).

installed at the Studebaker Ridge station (STD) on October 2 and at Sugar Bowl (SUG) on October 3 (McChesney and others, this volume, chap. 7; see fig. 2 for station locations).

Explosion 2: October 3, ~2240 PDT

The second explosion occurred at ~2240 PDT on October 3 (fig. 1*B*). Although this explosion occurred at night, the weather was clear and U.S. Forest Service observers stationed 13 km north-northwest of the crater at the Coldwater Ridge Visitor Center reported seeing an ash cloud that barely reached the crater rim (~2,500 m asl, or 400 m above the vent) starting at ~2240 PDT (M. Guffanti, written commun., 2004). Earthquake rates and real-time seismic amplitude measurement (RSAM; Endo and Murray, 1991) levels had increased several hours before the explosion (fig. 3), and by 2100 PDT events were occurring so close together that they were difficult to distinguish, forming a spasmodic, tremorlike signal (Moran and others, this volume, chap. 2). Because there had been much more energetic tremor earlier on October 2 and October 3 with no associated explosions, the spasmodic tremor was not regarded as a short-term warning sign. As with the October 1 explosion, earthquake rates dropped significantly at ~2305 PDT following a ~3-minute-long tremor episode (peak D_R ~3 cm^2) that presumably marked the end of the explosion (fig. 1*B*). A weak, continuous acoustic signal appeared on the newly deployed microphone at STD. However, with just that single sensor, we cannot distinguish between mechanical shaking of the microphone by passing seismic waves and explosion-related infrasound. The STD microphone did record many small (~0.5 Pa) infrasonic pulses associated with M >2 earthquakes, indicating that it was sufficiently close to record weak infrasonic signals from the crater.

Explosion 3: October 4, 0943 PDT

Earthquake rates gradually increased on the morning of October 4 until the third explosion occurred at 0943 PDT (maximum plume height ~3,650 m asl, or about 1,500 m above the vent), lasting until 1015 (fig. 1*C*). The explosion was recorded by a U.S. Forest Service Web camera at the JRO and was also noted by many observers. Earthquake rates decreased following the explosion (fig. 3), although not as markedly as either of the decreases following the previous two explosions. In contrast to the October 3 explosion, no obvious signal was apparent on the acoustic sensors and no explosion-related tremor was recorded on the nearby seismic stations (fig. 1*C*). The decline in seismicity was gradual and, unlike that accompanying the October 1 explosion, did not correspond in any direct way to the onset or termination of the explosion. Given the lack of obvious associated seismic signals, it is likely that the explosion would not have been detected had it occurred during bad weather.

Dzurisin and others (2005) show in their figure 1 a second steam-and-ash explosion on October 4 at ~1400 PDT. This was based on a report of anomalous steaming in the crater at that time (M. Guffanti, written commun., 2004), a report that coincided with a small drop in RSAM values. However, subsequent review of images from the JRO Web camera (taken every five minutes; Poland and others, this volume, chap. 11) showed no obvious steam or ash plume at that time, in contrast to the 0943 explosion. Given the absence of visible ash, we consider the 1400 event, if there was an event at all, to be at most a small steam explosion that is not comparable to the confirmed explosions, and we do not consider it further in this paper.

Explosion 4: October 5, 0905 PDT

The fourth and final explosion of the vent-clearing phase occurred at 0905 PDT on October 5 and lasted until 1015 (fig. 1*D*). This was the most vigorous and long-lasting explosion of the sequence, with the ash plume reaching ~4,500 m asl (2,400 m above the vent) and depositing trace amounts of ash ~100 km from the volcano (Scott and others, this volume, chap. 1). Before the explosion, RSAM levels had increased over a 6-hour period, reaching a peak level at 0600 that was maintained until the explosion (fig. 3). Earthquake sizes and rates began declining ~15 minutes after the explosion began (fig. 1*D*), with RSAM levels falling below post-September 29 levels by the end of the explosion (fig. 3). As with the October 4 explosion, no obvious explosion-related signals were apparent either on seismic or acoustic sensors (fig. 1*D*). However, the decline in seismicity was significant enough that an explosion could have been inferred if weather conditions had prohibited observation of the explosion. A delayed indicator of the explosion was the loss of the radio signal from station YEL from 1045 to 1238 following the explosion as a result of attenuation of its radio signal by the ash cloud.

Discussion

Because there was no attempt to maintain a full-time official observer near the volcano, there is a remote possibility that other small explosions occurred between October 1 and 5 that were not detected. We feel confident that no undetected explosions occurred during daylight hours, as clear weather provided excellent viewing conditions for the mass of people and media watching the volcano from various vantage points (Driedger and others, this volume, chap. 24). During nighttime hours clear viewing conditions still existed, aided by moonlight from an almost-full moon, and, as a result, members of the public and U.S. Forest Service staff were able to see one nighttime explosion (October 3). Nevertheless, we cannot rule out the possibility that other explosions occurred at night when the volcano was not watched.

Short-term declines in seismic energy following all four explosions were perhaps the most reliable indicator that an explosion had occurred. Seismicity declines following the explosions on October 1, 3, and 5 were particularly significant (fig. 3). However, similarly significant declines followed tremor episodes on October 2 and 3, which were not associ-

ated with explosions (Moran and others, this volume, chap. 2). In addition, smaller declines similar to that following the October 4 explosion (including several on October 4) did not correspond to known explosions. Thus short-term declines in seismic energy were not, by themselves, a reliable indicator that an explosion had occurred.

Explosions During the Dome-Building Phase

Several days after the October 5, 2004, explosion, a lava spine emerged from the vent (Vallance and others, this volume, chap. 9). The rest of 2004 was dominated by lava dome construction accompanied by low gas levels (Gerlach and others, this volume, chap. 26) and regularly spaced earthquakes (Moran and others, this volume, chap. 2). During October, November, and December of 2004 we installed several seismic stations within 500 m of the vent (fig. 2) and disabled the microphone at STD, because we needed the radio telemetry channel for data from another station (McChesney and others, this volume, chap. 7). One of the new stations on the 1980–86 lava dome (SEP) had a 2-Hz three-component velocity sensor and two 1-Hz acoustic sensors spaced ~15 m apart in a north-south alignment (appendix 1), roughly radial to the vent. With two microphones we hoped to be able to use relative arrival times of signals between the two sensors to distinguish between wind gusts (which would not necessarily produce similar waveforms, but any similar waveforms would have separations of as much as several seconds between the two sensors), coseismic signals due to shaking of the microphones by passing seismic waves (which would vary depending on the coupling of each microphone to the ground), and infrasonic signals (which would produce very similar waveforms with no more than ~0.05 s difference between the two sensors).

Explosion 5: January 16, 2005, ~0312 PST

The dome-building eruption was punctuated by a relatively short-lived explosion at ~03:12:50 PST on January 16, 2005. The explosion occurred at night during poor weather and was not visually observed. It was instead signaled by the sudden onset of a continuous broadband (1–10 Hz) tremor signal (fig. 4) accompanied by several larger-than-average low-frequency (dominant frequency <5 Hz) seismic events. The explosion-related tremor was relatively small (peak D_R of ~0.5 cm^2) and did not show up well on stations outside the crater (fig. 4). As a result, preestablished amplitude-based thresholds for generating automated alarms were not exceeded (Qamar and others, this volume, chap. 3) and the explosion was not detected by CVO and PNSN staff until more than an hour later during a routine scan of seismic records.

The explosion signal initially was most obvious on station BLIS (fig. 5), located ~250 m east of the vent (fig. 2). The estimated start time for the explosion is based on the onset of tremor at BLIS. Tremor did not become obvious on other stations, including two stations located ~500 m from the vent, until it increased in amplitude starting at ~0318 (figs. 4, 5). As BLIS was close to the actively growing spine 4, the tremor signal could conceivably have been caused by rockfalls coming off the spine. Rockfalls at Mount St. Helens commonly produce spindle-shaped signals 1–2 minutes long that often only appear on nearby stations. The tremor signal on BLIS was continuous between 0312 and 0318, however, indicating that the signal was the result of a longer duration process. We speculate that this signal could have been caused by relatively weak jetting before the more significant explosion that presumably occurred in association with the increase in tremor amplitudes starting at 0318.

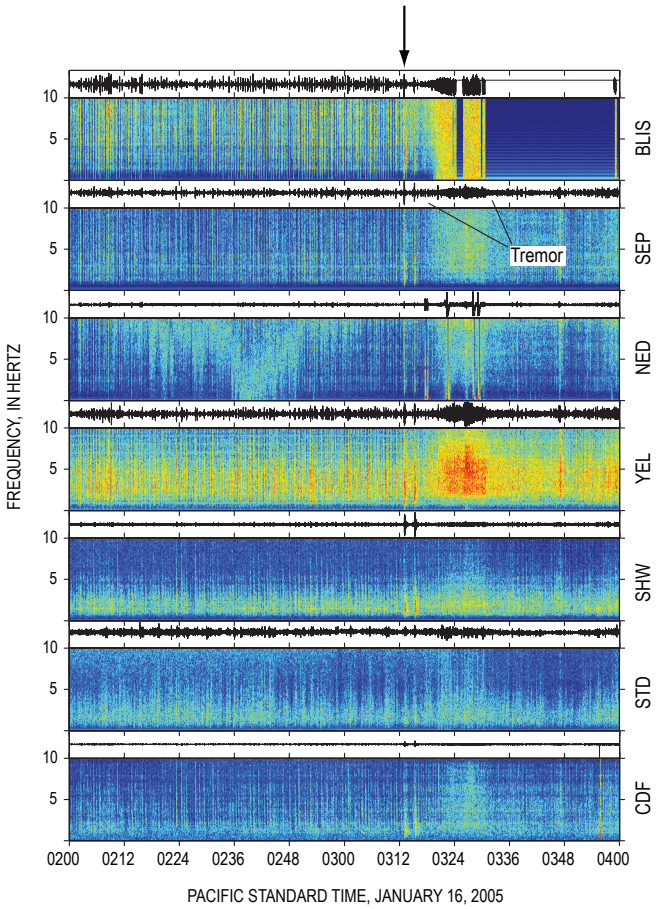

Figure 4. Multistation 2-hour-long spectrogram from 0200 to 0400 PST on January 16, 2005. See figure 2 for station locations and caption to figure 1 for description of spectrograms. Black-tipped arrow indicates estimated start time of explosion at 0312 PST; duration of tremor as seen on station SEP is indicated. Note that stations BLIS and NED had accelerometer sensors, SEP had a 2-Hz velocity sensor, and all other stations had 1-Hz velocity sensors. For more details on configuration of seismic stations, see McChesney and others (this volume, chap. 7).

Tremor rapidly intensified between 0318 and 0320. At ~0320 an emergent continuous signal became apparent on the SEP and SUG microphones (fig. 5). Given that these signals appeared in association with the seismic tremor, it is possible that some, if not most, of this signal reflects mechanical shaking of the microphones by seismic waves. We have no means of assessing this at the SUG site because it had just a single microphone and no collocated seismometer, but the near-simultaneous onset of acoustic signals at SEP and SUG suggest that at least a component of the SUG signal was due to shaking of the microphone housing. At 03:20:30, however, the two acoustic sensors at SEP began recording small-amplitude individual phases within the acoustic signals that were coherent between the two microphones and consistent with a source located at the vent. No correlative signals were apparent on the SUG acoustic sensor ~5 s later (the traveltime difference between SEP and SUG for acoustic waves traveling at 340 m/s). However, this is not surprising, given the fact that SUG is located on a ridgetop that was being buffeted by high winds from an oncoming storm system at the time. We infer that the coherent signals on the two acoustic sensors at SEP reflect the onset of explosion-related infrasound. Although the microphone recordings were still mostly incoherent at the onset of the continuous acoustic signal (fig. 5), individual phases in the signal became progressively more coherent with time. By ~0326, most of the signal was coherent and thus likely due to explosion-related infrasound (as opposed to explosion-related air currents or mechanical shaking of the sensors). The continuous acoustic signal peaked at ~0327 with maximum peak-to-peak amplitudes of 2–4 Pa (see appendix 1 for discussion of microphone calibration uncertainties) and faded to background levels by ~0331. The timing, size, duration, and character of the SEP infrasonic signals are consistent with an emergent infrasonic signal starting at 03:21:22 recorded on a microbarometer array located 13 km northwest of

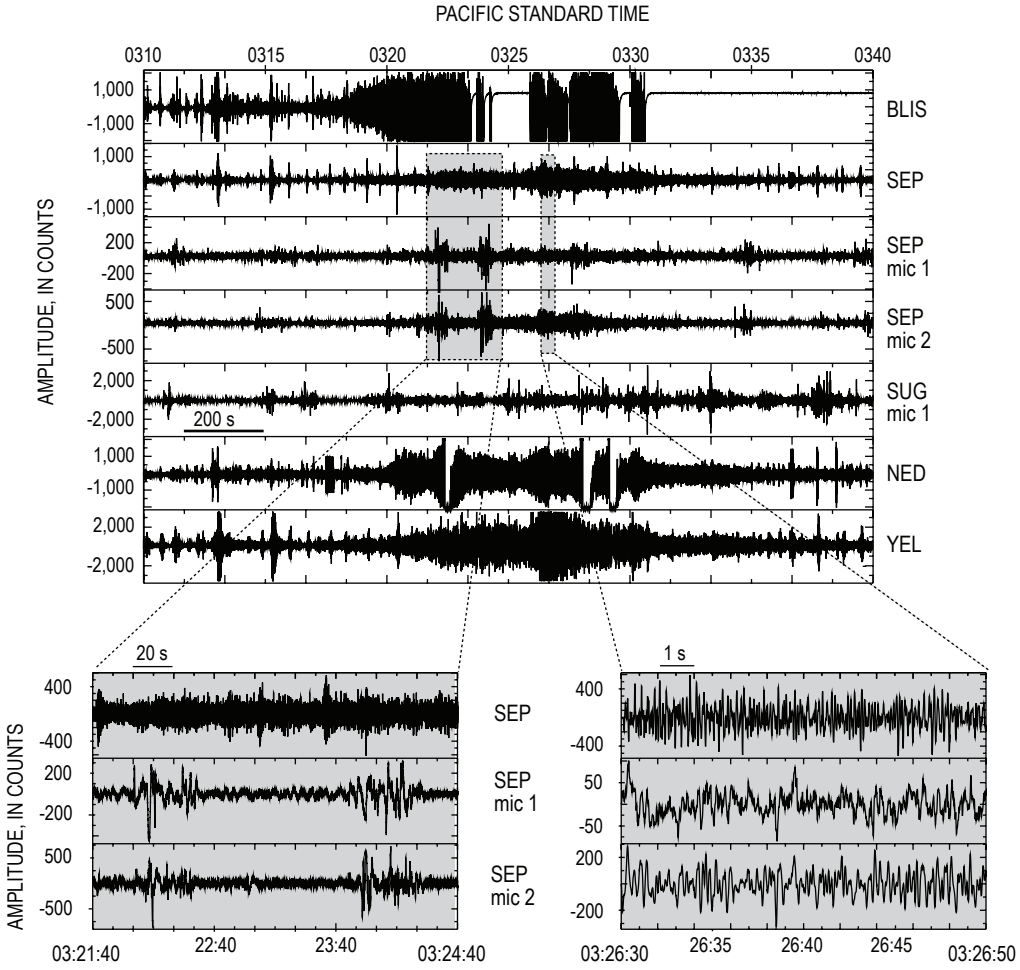

Figure 5. Multistation 30-minute plot showing unfiltered time-series data from 0310 to 0340 PST on January 16, 2005. See figure 2 for station locations. Insets at bottom of plot show 3 minutes (left) and 20 s (right) of data from vertical component of SEP seismometer (top) and two acoustic sensors (microphone 1, middle, and microphone 2, bottom), bandpass filtered with corner frequencies of 0.1 and 15 Hz. Left inset shows two events, recorded by acoustic sensors at ~03:22:00 and ~03:23:50, that we infer to be wind gusts associated with the explosion. Right inset shows mostly coherent signals between the two microphones, indicating that signals are mostly infrasonic energy produced by the explosion.

the vent near the U.S. Forest Service's Coldwater Ridge Visitor Center (Matoza and others, 2007).

Superimposed on the continuous infrasonic signal at SEP were several larger ~1 Hz pulses at 03:20:00, 03:22:05, and 03:23:50 (fig. 5). Although these pulses were broadly coherent between the two microphones, in detail the waveforms have significant variability. In addition, the time separation between relative peaks (as much as 2 s) is too large for an infrasonic signal, given the 15-m spacing of the microphones. The variability and large time differences between these pulses on the two microphones indicate that they were not traveling at sound velocities (~340 m/s) and are thus not infrasound. Other such signals were recorded in the hours before and after the explosion on both the SEP and SUG acoustic sensors, as well as at other times during stormy weather. Because a storm system was moving into the area at the time of the explosion, these pulses are likely wind gusts unrelated to the explosion. The 03:22:05 and 03:23:50 pulses, however, had larger-than-average amplitudes and broadly similar waveforms (fig. 5). On the basis of the admittedly subtle contrasts to other wind gust-related signals, we speculate that these pulses may have been caused by air flow from the explosion that swept across the SEP site at speeds of ~20 m/s.

Evidence that ash was moving across the 1980–86 lava dome shortly after the tremor-amplitude increase at 0318 comes from a several-second-long loss (or "dropout") of the radio signal from NED at 03:22:20 (fig. 5; see fig. 2 for site location). The radio signal from NED was known to be very strong. At the radio receiver for NED we measured a 30 dB fade margin—a quality determined by adding impedance at the receiver until it stops receiving the radio signal from the transmitter. The NED signal had never before been lost, even during stormy weather. The most likely explanation for the NED dropout is that the radio signal was temporarily blocked by ash. Radio telemetry was lost ~60 s later at BLIS, which had a much weaker radio signal (~10 dB fade margin at the receive site) and commonly dropped out during winter storms. Signals from both stations returned in time to record the peak of the tremor signal at 0327 (fig. 5). Shortly after this peak there were two more short-lived radio dropouts at 0328 and 0329 from station NED, followed by a dropout of several hours at station BLIS. The long duration of the BLIS dropout is consistent with a diffuse ash cloud lingering in the vent area following the explosion. Given that no dropouts occurred at SEP and that the first NED dropout occurred before the first BLIS dropout (despite BLIS being located much closer to the vent), we infer that ash was initially blown northeastwards across the dome towards NED.

Explosion-related seismic tremor gradually subsided after 0327, eventually fading to background levels at ~0345 PST on the crater stations. The tremor signal lasted for roughly 32 minutes, similar to the duration of the October 1, 2004, explosion. Subsequent geological reconnaissance on January 19 (3 days later but the first day of clear weather after the explosion) confirmed that an explosion had occurred (Scott and others, this volume, chap. 1), with the primary axis of ash deposition extending east-northeast from the vent toward both NED and BLIS (fig. 2). A field of impact craters as large as 1 m in diameter extended several hundred meters eastwards from the vent towards and beyond BLIS. Station BLIS survived in large part because it was mostly buried in snow. The distribution and thickness of deposits were similar in scope and size to those from the October 1, 2004, explosion (Scott and others, this volume, chap. 1), and it is reasonable to assume that the plume reached heights similar to the October 1 plume (~3,500–4,500 m asl).

In contrast to the October 1 explosion, nearby seismic stations were not saturated by large earthquakes before the January 16 explosion; as a result, the explosion-related tremor could clearly be seen on stations within the crater. Seismic signals from the explosion showed up poorly on stations outside the crater, however (fig. 4). If there had been no seismic stations inside the crater at the time of the explosion, it is conceivable that CVO and PNSN staff would not have known that an explosion had occurred until the next observation flight in the crater. This highlights the importance of having stations close to the vent for accurate and timely detection of explosions. In particular, the loss of telemetry on several crater stations, coupled with the tremor signal, made it clear that an ash-producing explosion had occurred.

As described above, the explosion produced infrasound that was recorded at SEP and at the Coldwater microbarometer array (Matoza and others, 2007). Had there been no crater stations, the Coldwater array might have provided the only definitive instrumental evidence that an explosion had occurred. The infrasonic signal was relatively subtle at both sites, however, and required multiple collocated acoustic sensors to distinguish between explosion-related infrasonic signals, wind noise, coseismic shaking of the acoustic sensors, and other acoustic noise sources. The subtlety of the infrasonic signals illustrates the important role that arrays of acoustic sensors can play in detecting explosions at volcanoes. Given the relatively small infrasonic signals, this explosion may represent an example of the type of ash-rich explosion that elsewhere has been found to be relatively inefficient at producing infrasound (Woulff and McGetchin, 1976; Johnson and Aster, 2005).

Explosion 6: March 8, 2005, 1725 PST

The dome-building eruption was not at all disturbed by the January 16 explosion, with earthquakes and steady-state lava-dome extrusion continuing unabated for the next seven weeks. The steady-state lava-dome extrusion was again punctuated by an explosion at ~17:25:20 PST on March 8, 2005. This was the largest of the six 2004–5 explosions; it was also the best documented and recorded of the six, as it occurred in the early evening of a cloudless day and as a result could be seen from the Portland, Oregon, metropolitan area, 85 km to the south. Tremor associated with the explosion was visible on all stations within 15 km (fig. 6), and CVO personnel who had seen the signal on seismic displays began contacting Federal, airline, and emergency officials within a minute of the start of

the explosion. Explosion-related tremor appeared simultaneously at stations inside and outside the crater and achieved maximum amplitudes (peak D_R ~1 cm^2) within the first minute, indicating that the explosion rapidly reached maximum intensity, in contrast to the January 16 explosion. Visual observations confirmed the rapid intensification, with the resultant ash plume reaching heights of about 11,000 m (9,000 m above the vent) within 5 minutes (Scott and others, this volume, chap. 1). Explosion-related tremor began declining after ~8 minutes and became indistinct from normal seismic background levels within 20 minutes. All three stations within 500 m of the vent were destroyed by the explosion (fig. 7).

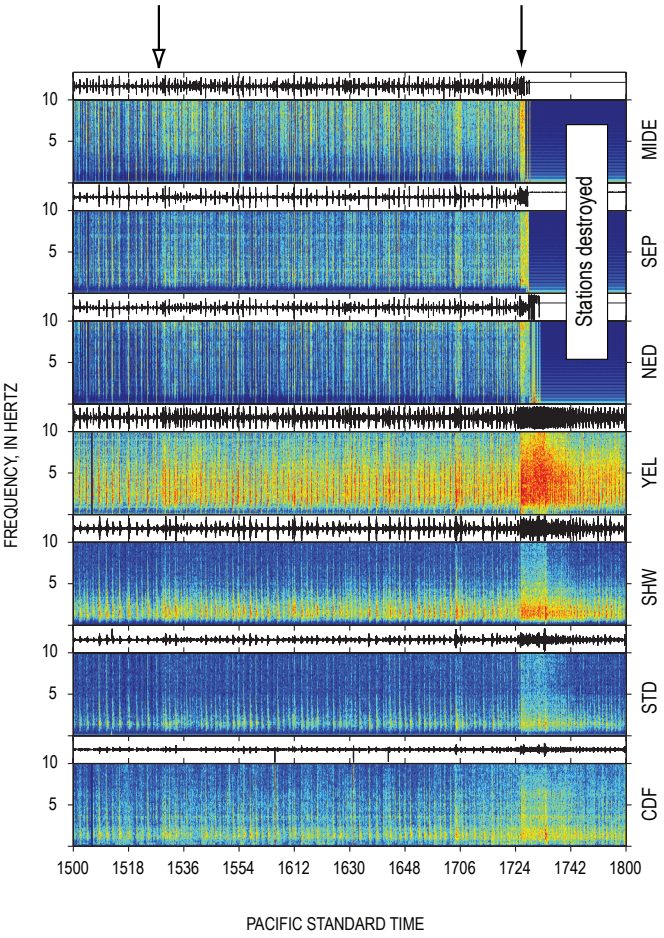

Figure 6. Multistation 3-hour-long spectrogram from March 8, 2005, between 1500 and 1800 PST. See figure 2 for station locations and caption to figure 1 for description of spectrograms. White-tipped arrow indicates start of an increase in number of larger events ~2 hour before the March 8 explosion; black-tipped arrow indicates start of explosion at 1725 PST. Note that stations MIDE and NED had accelerometer sensors, SEP had a 2-Hz velocity sensor, and all other stations had 1-Hz velocity sensors. For more details on configuration of seismic stations, see McChesney and others (this volume, chap. 7).

RSAM Increase

Roughly 2 hours before the March 8 explosion, RSAM levels began increasing at stations as far as 6 km from the vent (fig. 8). Although the increase was relatively small, particularly in comparison to increases seen in the first week of the eruption (Moran and others, this volume, chap. 2), the synchronous rise in RSAM at stations within and outside of the crater was unusual enough for CVO and PNSN staff to take notice roughly an hour before the explosion. This increase was one of the factors that contributed to the timely detection of the explosion, and it may be a relatively rare example of a short-term seismic precursor to an explosion. The RSAM increase was caused by an increase in the percentage of larger (M_d >1.5) earthquakes (fig. 9). Events in this magnitude range had been occurring at a rate of one every 3–4 minutes before the explosion. Starting at ~1529 the rate of larger events increased to one every 1–2 minutes, with the rate increasing through to the start of the explosion. No other attributes of the seismicity, including the total number of earthquakes per unit time (fig. 9), event frequency, event type, event location, and degree of similarity of waveforms between events, changed at this time.

Similar increases in event size occurred over short time intervals during the first week of seismic unrest in 2004. The fact that seismic energy levels dropped following the four explosions (particularly the October 1 and October 5, 2004, explosions) and two noneruptive tremor episodes indicates that the preexplosion elevated seismicity was a result of increased pressures in the shallow (<1 km) conduit system (Moran and others, this volume, chap. 2). We infer that the increase in seismic energy ~2 hours before the March 8 explosion similarly reflected an increase in pressure within the conduit. Given that an explosion occurred 2 hours after this increase, it is reasonable to assume that a pocket of steam and/or magmatic gas had accumulated within the conduit or along its margins at shallow depths shortly before the explosion, and that the gas pocket locally increased pressures. Given that there were no other significant changes in earthquakes before the explosion, we infer that the pressure increase merely perturbed the regular seismogenic process. Certainly, the increase in event size could reflect an increased pressurization in gas- or fluid-filled cracks (for example, Chouet, 1996). However, other factors, such as the ~1-m-thick layer of fault gouge found on most spines (Pallister and others, 2005; Cashman and others, this volume, chap. 19; Moore and others, this volume, chap. 20); the geologic evidence found for shearing within the extruded lava domes (Pallister and others, 2006); the low gas content (Gerlach and others, this volume, chap. 26); and the correlation of changes in earthquake character with changes in extrusive style at the surface (Moran and others, this volume, chap. 2), all combine to suggest that the regular earthquakes may have been a result of stick-slip motion (Iverson and others, 2006). If the earthquakes were the result of a stick-slip process, the pressure increase could have caused a seismic energy increase through (1) an increase in pressure at the base

of the plug (Iverson and others, 2006); (2) a localized increase in applied shear stress along the conduit margins; (3) a change in fault properties in the seismogenic region; or (4) some combination of these factors. Because there are no constraints on the rate of motion of the active spine or the location of the gas pocket in the hours before the explosion, there is no basis for favoring or discarding any of these explanations. Nevertheless, the increase in RSAM values shortly before the March 8 explosion represents a relatively rare instance of a seismic precursor to a volcanic explosion and provides an example of a signal that could enable future short-term forecasts of explosive events during eruptions similar to the dome-building eruption at Mount St. Helens during 2004–5.

Acoustic Recordings

In contrast to the January 16 explosion, the March 8 explosion produced significant infrasonic signals that were well recorded on the two SEP microphones (the SUG microphone had stopped working before the March 8 explosion) as well as on the Coldwater infrasound array (Matoza and others, 2007). No infrasonic signals were recorded, however, until a discrete low-frequency (1–2 Hz) pulse at 17:26:20, ~60 s after the explosion signal first appeared on seismic stations (fig. 7). We note that the delay between seismic and infrasonic signals is similar to seismicity and infrasonic observations reported by Johnson and others (2003) in association with explosions at Guagua Pichnicha volcano, Ecuador, in 1998–99. These first infrasonic pulses were low frequency (1–2 Hz) and appeared on the SEP acoustic sensors ~2 s after a seismic event was recorded on the SEP seismometer (fig. 7), consistent with the time lapse expected between seismic and acoustic waves for a source ~500 m away. Matoza and others (2007) report seeing similar infrasonic signals at their Coldwater array starting at 17:26:55, 35 s after they appeared on the SEP acoustic sensors (35 s is the expected time difference, given the 12.5-km separation between the two sites). Several similar pulses occurred over the next 20 s, followed by much larger infrasonic signals

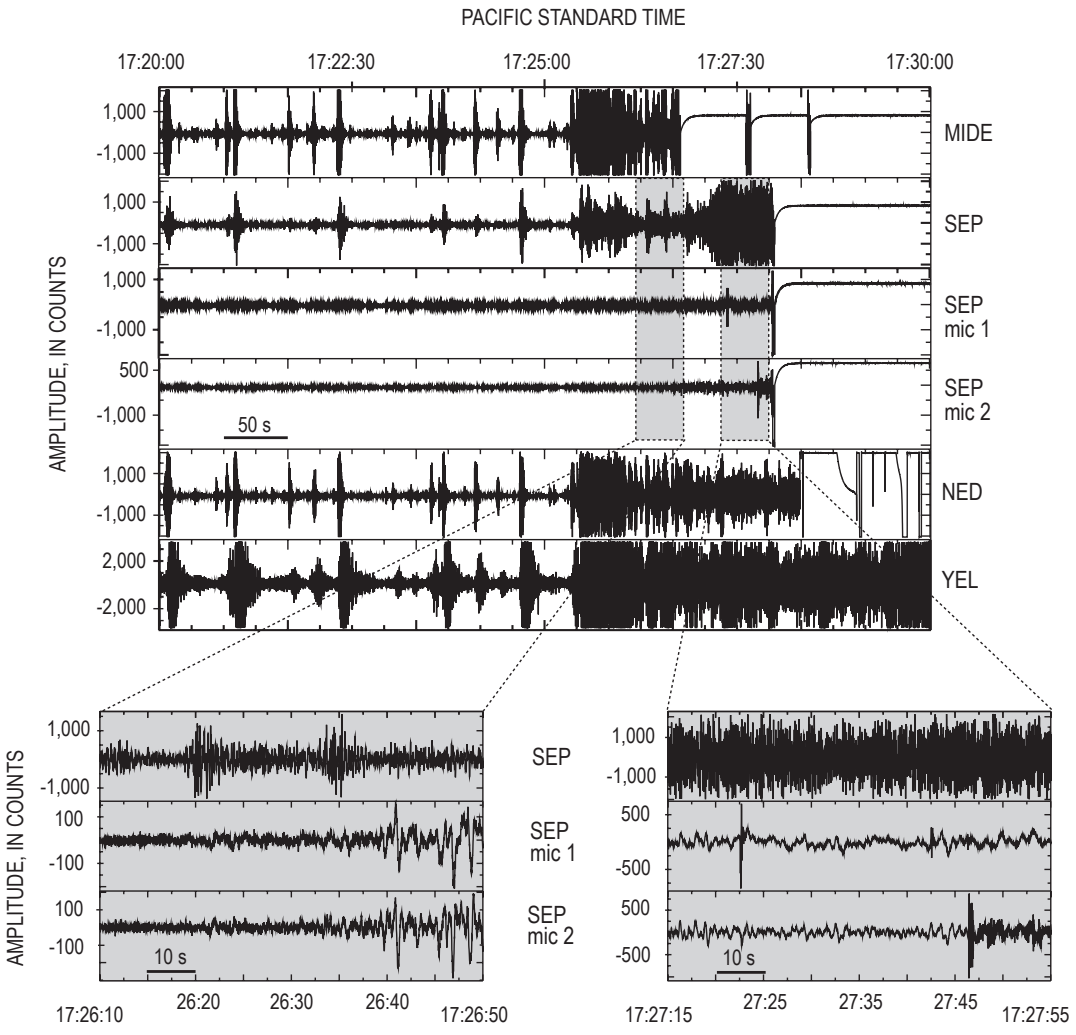

Figure 7. Multistation 10-minute plot showing time-series data from 1720 to 1730 PST on March 8, 2005. See figure 2 for station locations. Insets at bottom of plot show two 40-s windows of unfiltered data from the vertical component of the SEP seismometer (top) and two acoustic sensors (microphone 1, middle, and microphone 2, bottom). The left inset shows the onset of infrasonic signals at ~17:26:20, with amplitudes increasing significantly at ~17:26:40. Right inset shows several sharp spikes on acoustic sensors, which we infer to be caused by ballistic fragments landing close to each sensor. Conversion factor for counts to Pascals is nominally 44.5 counts/Pa for microphones at SEP (see appendix 1).

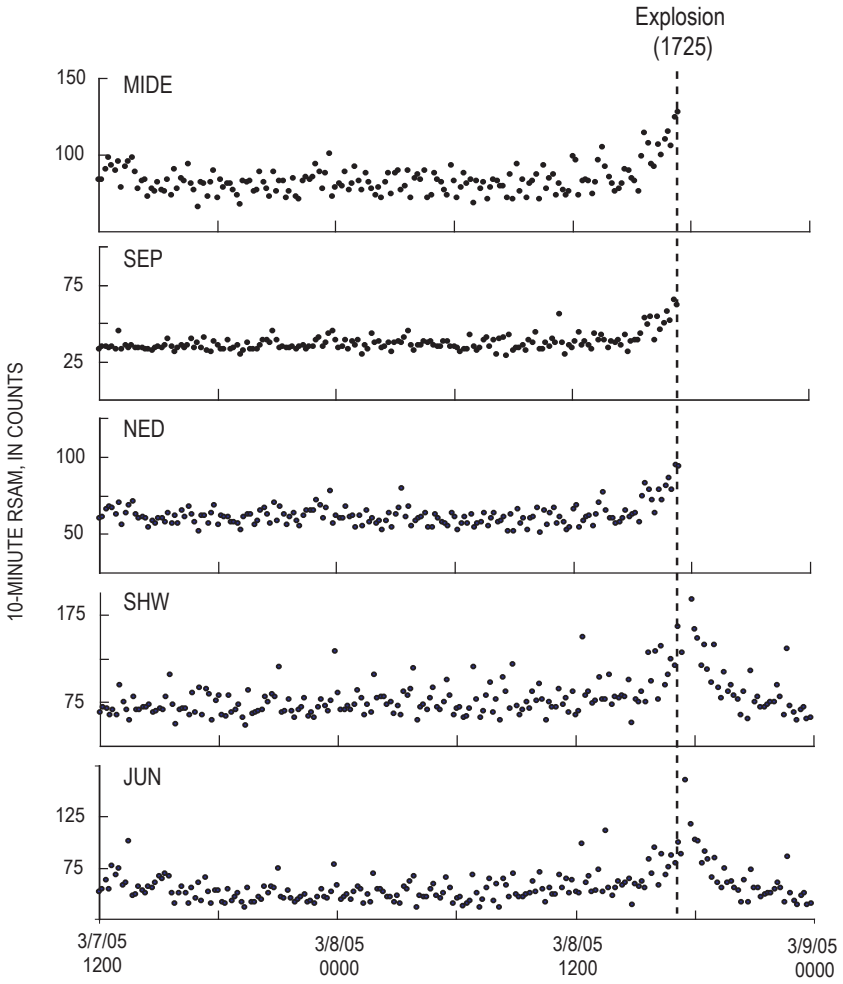

Figure 8. Plot of 10-minute RSAM values (Endo and Murray, 1991) on five stations over 36-hour time window extending from March 7 to March 9, 2005. Stations are ordered by distance from vent, nearest (MIDE, 0.25 km) to farthest (JUN, ~6.5 km). Vertical dashed line indicates start time for March 8 explosion.

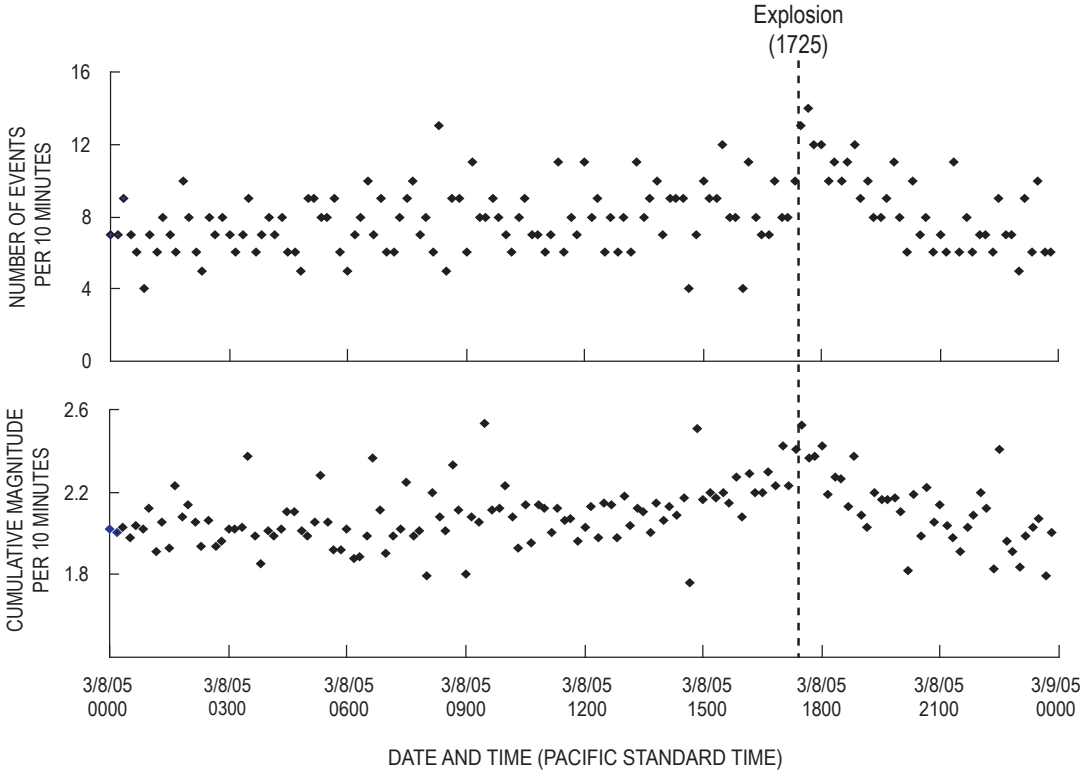

Figure 9. Plot showing number of events detected every 10 minutes at station HSR (top) and 10-minute cumulative event magnitude (bottom). Event detection is done using a standard STA/LTA trigger algorithm; for details see Moran and others (this volume, chap. 2). Event magnitudes determined using peak amplitudes at station HSR and a local magnitude relation calibrated to match the Pacific Northwest Seismic Network's coda-duration magnitude scale. Note that magnitudes began increasing slightly after 1500 PST, whereas number of events stayed constant until after explosion.

starting at 17:26:40. These larger signals were highly correlative between the two SEP acoustic sensors and did not correspond to seismic events on the SEP seismometer (fig. 7). Thus over the space of ~80 s the first phase of the explosion transitioned from producing mostly seismic signals in the first 60 s to producing both acoustic and seismic signals, and finally, 20 s later, to producing mostly acoustic signals.

Such variability in the production of acoustic and seismic energy during explosions has been documented at other volcanoes (Mori and others, 1989; Garcés and others, 1998; Johnson and others, 2003; Johnson and others, 2005; Johnson and Aster, 2005). Johnston and Aster (2005) demonstrated that this variability can be attributed to a variety of factors, including plume density, with dense plumes resulting in reduced acceleration of the atmosphere and reduced infrasonic amplitudes; magma/wall rock impedance contrast, with low impedances resulting in reduced seismic amplitudes; viscous flow in the conduit, with long and narrow conduits acting to reduce seismic and enhance infrasonic amplitudes; and source dimension, with large source regions yielding reduced infrasonic amplitudes. For the March 8 explosion, we favor an ash-rich plume as the primary reason for the apparent absence of acoustic signals in the first 60 s. Given that no open vent existed before the explosion, the initial explosion must have contained substantial amounts of ash and fractured rock mixed with steam and/or magmatic gas during the initial vent clearing. Evidence for this comes from a picture taken at 17:27:42 from a remote camera located 2.5 km northeast of the vent at SUG (fig. 10, lower photo; see fig. 2 for site location). That photograph shows a dark ash-rich cloud to the left (south) of the vent, a convecting lighter-colored plume to the right (north) that is relatively close to the SEP site, and impact craters (white patches) in snowfields on the northern side of the 1980–86 lava dome. The extent of the dark ash cloud, which enveloped most of the southern half of the crater just 140 s after the initial explosion signal (fig. 10), suggests that the initial plume contained a substantial amount of ash. The appearance of acoustic signals after 60 s could correspond to reduced ash content in the plume (and more efficient acoustic energy production) following vent clearing, with the subsequent increase in acoustic-to-seismic energy ratios over the next 20 s corresponding to progressively reduced amounts of ash entrained in the plume.

At 17:27:00 a high-frequency (>5 Hz) tremor signal that rapidly increased in amplitude appeared on the SEP seismometer (fig. 6), clipping the seismometer after 20 s. This increase was also registered at other stations within 15 km, although relative amplitude increases were much smaller, indicating that the source was close to the SEP seismometer and was likely shallow. There was no associated change in the nature or amplitude of the infrasonic signals recorded on the SEP microphones. We infer that this signal represents the generation of a second and perhaps more vigorous ash-rich plume. Although the explosion chronology is poorly detailed, photographs taken from Camas, Washington, (75 km south of Mount St. Helens), show a second plume starting to rise above the crater rim at 1727; by 1729 it had risen to the first plume's altitude at 1727 (fig. 11). The appearance of this second plume matches well with the timing of the onset of the more energetic tremor.

Further evidence for a second, more vigorous explosive phase comes from ballistic impacts. Most evidence comes from events that occurred after the tremor increase at 1727. At 17:27:22 the first of several sharp high-frequency signals appeared on the SEP microphones (fig. 7). Most of these signals appeared only on a single microphone, indicating that the source was small and very close to the sensors. We infer these to be caused by small ballistic fragments landing near individual microphones. This inference is supported by the appearance of impact craters in snow fields on the 1980–86 dome in a photo from the Sugar Bowl camera taken at 17:27:40 (fig. 10), indicating that ballistic fragments were falling at the time of the high-frequency spikes. Furthermore, the downward first-motion of the spikes (fig. 7) is inconsistent with an explosive source. We speculate that the downward first-motions might have been related to a pressure drop associated with nearby ballistic impacts. At 17:27:46, 12 s before SEP was destroyed, a low-amplitude, high-frequency signal appeared superimposed on the lower frequency infrasonic signals on both SEP microphones. On the basis of the high frequency content and small amplitude, we infer that this signal was caused by a rain of many small ballistic fragments across the SEP site. Finally, SEP and NED were both destroyed by hot ballistic fragments at 17:27:58 and 17:28:18, respectively, as indicated by multiple sharp punctures in enclosures, melted nylon ropes, and melted circuit-board solder found in equipment that was later retrieved from each site. The evidence for the bulk of ballistic impacts occurring after the tremor increase at 1727, coupled with the photographic evidence for a second plume starting at 1727, leads us to conclude that the 1727 tremor increase heralded the onset of the second and most energetic phase of the March 8 explosion.

Discussion

The explosions of 2004–5 at Mount St. Helens, although few in number and small in size, yielded a number of important insights regarding the use of acoustic and seismic instruments for reliable explosion detection, in particular for small explosions. One such insight comes from the observation that the most reliable seismic indicator for each of the four explosions occurring during the vent-clearing phase of October 1–5, 2004, was the seismicity decline following each explosion (table 1). None of the explosions had an obvious seismic precursor, and no seismic signals were recorded that heralded the start of any of the October 1–5 explosions. The lack of such obvious seismic signals may in part have been due to the intense seismicity associated with the vent-clearing phase, which would have obscured any moderate-amplitude seismic signals associated with the explosions. Despite the fact that seismicity declines followed each explosion, however,

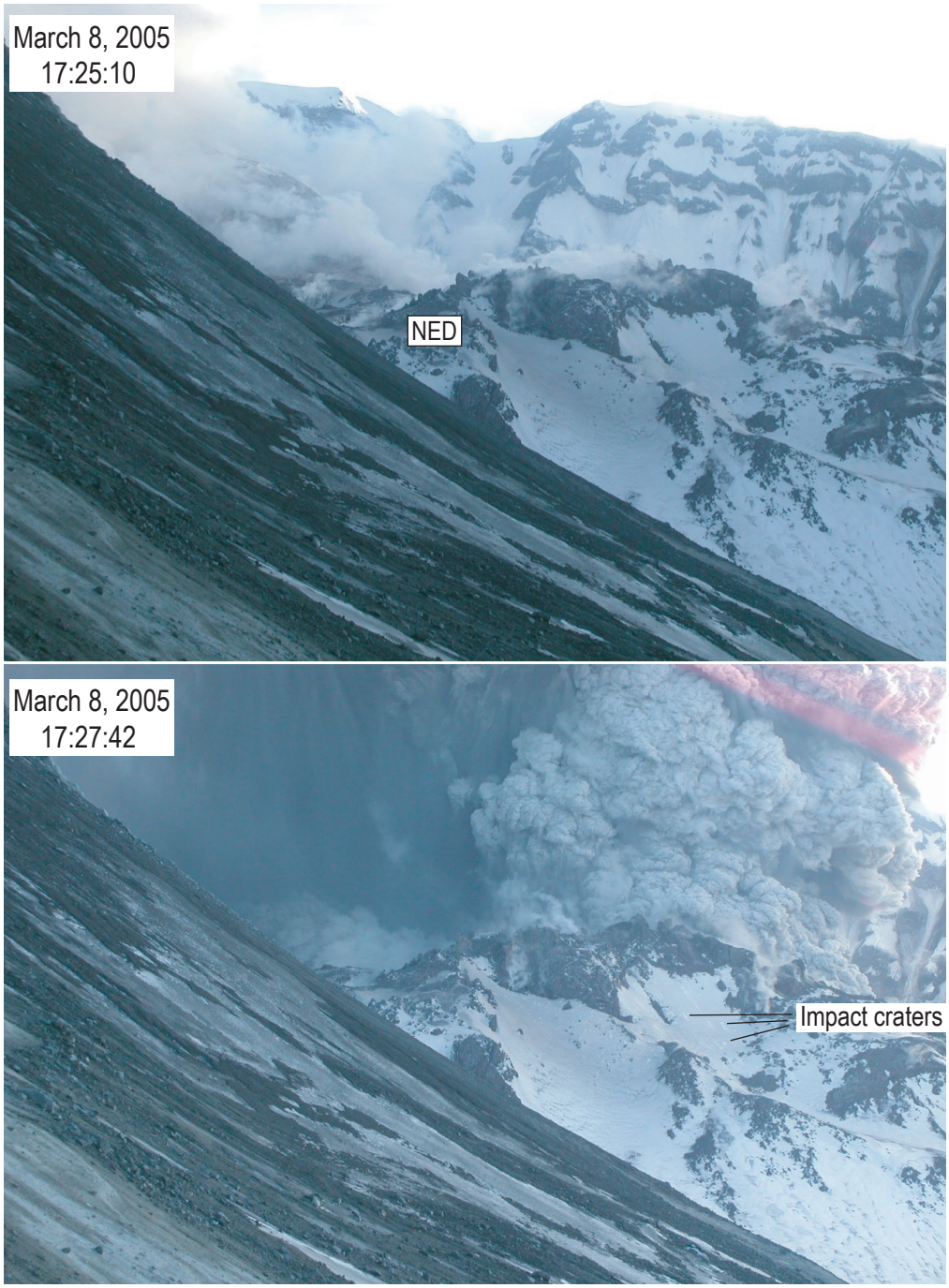

Figure 10. Photographs of the crater of Mount St. Helens taken by a remote camera installed by the Cascades Volcano Observatory at SUG (2 km northeast of vent; see fig. 2) 10 s before (top) and ~140 s after (bottom) the start of the March 8 explosion at 17:25:20 PST. Times for each photo are accurate to nearest second, because time stamps were based on a clock periodically synchronized to Internet time server. View is to south; the south crater rim is in background and the northeast crater wall in foreground. The new lava dome is mostly shrouded by steam in upper image and completely obscured by ash clouds in lower image. The 1980–86 lava dome is in the center of each image (station NED is located on northeast side of that dome). Small white circles in the snow, visible in center of lower image, formed as impact craters from ballistic fragments that fell on all sides of the 1980–86 lava dome during explosion. (Pink diagonal lines in upper right corner of lower image result from damage to the camera in previous months when sun at low zenith shone directly into lens.)

seismicity declines also occurred during this phase that did not correspond to explosions. Clearly, real-time explosion detection cannot be based on seismic instruments alone.

Another insight comes from the fact that there were no obvious acoustic signals associated with the October 3–5 explosions that occurred after two single-sensor acoustic sites were established. The lack of acoustic signals in part indicates that the explosions were not large. However, because each site had only a single acoustic sensor, it is impossible to use methods such as those employed by Matoza and others (2007) on arrays of collocated acoustic sensors to significantly reduce noise levels. As illustrated by the subsequent explosion signals recorded at SEP in 2005, multiple acoustic sensors make it much easier to distinguish between explosion-related infrasonic signals and noninfrasonic noise sources such as wind and coseismic shaking of the microphone from passing seismic waves, especially if the explosion-related signals are weak.

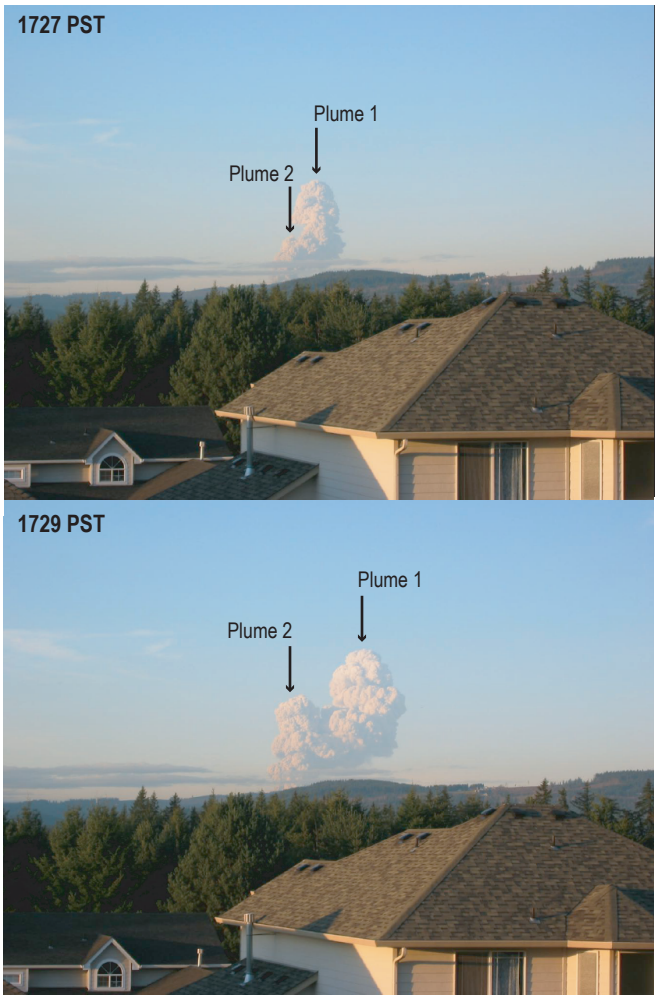

Figure 11. Views of March 8, 2005, ash cloud at 1727 and 1729 PST as seen from Camas, Washington, 75 km south of Mount St. Helens. Time for each photo is precise to nearest minute (resolution of internal clock in camera used to take these photos). Two plumes are seen clearly in lower photograph, with second plume likely corresponding to intensification in tremor seen on SEP and other seismic stations starting at 17:27:00 (see fig. 7). Given that second plume can also be seen in the 1727 photo, we estimate that the photo was taken several tens of seconds after 17:27:00. Photographs by Elisa Wells, used with permission.

The intense seismicity during the first two weeks at Mount St. Helens highlighted an additional underappreciated attribute of acoustic sensors; because they are isolated from the ground, acoustic sensors are not nearly as susceptible as seismometers to saturation by energetic seismicity and thus may record explosion-related infrasound when seismic waves from frequent large earthquakes mask any explosion-related seismicity. Although acoustic sensors deployed 3–5 km from the vent did not record obvious infrasound associated with the October 3–5 explosions, at the same time the acoustic sensors were not overwhelmed by ground waves from the continuous large earthquakes and thus were more capable of detecting explosion-related signals than the seismic network. Because vigorous precursory seismicity can happen at any volcano, acoustic sensors with real-time telemetry, in particular arrays of sensors such as those deployed at SEP and Coldwater (Matoza and others, 2007), should be installed as soon as possible after the onset of volcanic unrest to improve explosion-detection capabilities. The destruction of SEP by the March 8 explosion (and the resultant loss of acoustic information about the evolution of the explosion) also demonstrates the value in placing some acoustic arrays at safe distances, despite the greater complexity of path effects, the higher signal attenuation, and the increased time delay in explosion detection inherent in recording explosion-related signals at more distant sites.

The January 16 and March 8, 2005, explosions also demonstrated the importance of having seismic stations within 1–2 km of a vent for reliable explosion detection. Explosion-related tremor from the January 16 explosion first appeared only on a station located ~250 m from the vent and only became apparent (albeit marginally) on stations outside the crater ~8 minutes later, when infrasonic signals also became apparent on acoustic sensors. Without seismic stations operating within 1–2 km of the vent, the explosion might have gone unnoticed until later field work by CVO staff. The March 8 explosion was also recorded first by the seismic network, with infrasound signals appearing ~60 s after the start of the explosion. Given the aviation sector's stated need to be alerted within 5 minutes of the start of an eruption (Ewert and others, 2005), such delays are potentially problematic. Seismic signals were large enough to be seen on stations within 15 km of the vent, but the explosion-related tremor was most clearly recorded on crater stations. An additional benefit of having stations in the crater came from the loss of telemetry experienced at one or more crater stations during the October 1, October 5, January 16, and March 8 explosions. These dropouts provided independent confirmation that ash was in the air, and for this reason the loss of telemetry from individual sta-

tions has since become a key element in the automated alarm system employed by CVO and PNSN (Qamar and others, this volume, chap. 3). Thus, installation of real-time seismic stations within 1–2 km of a volcanic vent is vital for improving explosion-detection capabilities at erupting volcanoes.

Acknowledgments

We are indebted to Marvin Couchman for his contributions in assembling, testing, and deploying the acoustic sensors at BLIS and SEP. We also wish to acknowledge Jeff Johnson for his advice on deploying multiple acoustic sensors at SEP; Robin Matoza and Michael Hedlin for generously sharing data and interpretations of acoustic signals recorded at their Coldwater infrasonic site; Mike Poland for having the foresight to install the Sugar Bowl camera in October 2004; Rick LaHusen, for maintaining the camera and associated telemetry system in the months after Mike's move to the Hawaiian Volcano Observatory; and Elisa Wells (wife of S. Moran) for having the presence of mind to start taking photos of the March 8, 2005, explosion cloud and for allowing us to publish them. Finally, we gratefully acknowledge Jackie Caplan-Auerbach and Jeff Johnson for their thoughtful and helpful reviews of this paper.

References Cited

Aki, K., and Koyanagi, R.Y., 1981, Deep volcanic tremor and magma ascent mechanism under Kilauea, Hawaii: Journal of Geophysical Research, v. 86, p. 7095–7110.

Cashman, K.V., Thornber, C.R., and Pallister, J.S., 2008, From dome to dust; shallow crystallization and fragmentation of conduit magma during the 2004–2006 dome extrusion of Mount St. Helens, Washington, chap. 19 *of* Sherrod, D.R., Scott, W.E., and Stauffer, P.H., eds., A volcano rekindled; the renewed eruption of Mount St. Helens, 2004–2006: U.S. Geological Survey Professional Paper 1750 (this volume).

Chouet, B.A., 1996, Long-period volcano seismicity; its source and use in eruption forecasting: Nature, v. 380, p. 309–316.

Driedger, C.L., Neal, C.A., Knappenberger, T.H., Needham, D.H., Harper, R.B., and Steele, W.P., 2008, Hazard information management during the autumn 2004 reawakening of Mount St. Helens volcano, Washington, chap. 24 *of* Sherrod, D.R., Scott, W.E., and Stauffer, P.H., eds., A volcano rekindled; the renewed eruption of Mount St. Helens, 2004–2006: U.S. Geological Survey Professional Paper 1750 (this volume).

Dzurisin, D., Vallance, J.W., Gerlach, T.M., Moran, S.C., and Malone, S.D., 2005, Mount St. Helens reawakens: Eos (American Geophysical Union Transactions), v. 86, no. 3, p. 25, 29.

Endo, E.T., and Murray, T., 1991, Real-time seismic amplitude measurement (RSAM); a volcano monitoring and prediction tool: Bulletin of Volcanology, v. 53, no. 7, p. 533–545.

Ewert, J.W., Guffanti, M., and Murray, T.L., 2005, An assessment of volcanic threat and monitoring capabilities in the United States; framework for a National Volcano Early Warning System: U.S. Geological Survey Open-File Report 2005–1164, 62 p.

Garcés, M.A., Hagerty, M.T., and Schwartz, S.Y., 1998, Magma acoustics and time-varying melt properties at Arenal Volcano, Costa Rica: Geophysical Research Letters, v. 25, p. 2293–2296.

Gerlach, T.M., McGee, K.A., and Doukas, M.P., 2008, Emission rates of CO_2, SO_2, and H_2S, scrubbing, and preeruption excess volatiles at Mount St. Helens, 2004–2005, chap. 26 *of* Sherrod, D.R., Scott, W.E., and Stauffer, P.H., eds., A volcano rekindled; the renewed eruption of Mount St. Helens, 2004–2006: U.S. Geological Survey Professional Paper 1750 (this volume).

Iverson, R.M., Dzurisin, D., Gardner, C.A., Gerlach, T.M., LaHusen, R.G., Lisowski, M., Major, J.J., Malone, S.D., Messerich, J.A., Moran, S.C., Pallister, J.S., Qamar, A.I., Schilling, S.P., and Vallance, J.W., 2006, Dynamics of seismogenic volcanic extrusion at Mount St. Helens in 2004–05: Nature, v. 444, no. 7118, p. 439–443, doi:10.1038/nature05322.

Johnson, J.B., and Aster, R.C., 2005, Relative partitioning of acoustic and seismic energy during Strombolian eruptions: Journal of Volcanology and Geothermal Research, v. 148, p. 334–354.

Johnson, J.B., Aster, R.C., Ruiz, M.C., Malone, S.D., McChesney, P.J., Lees, J.M., and Kyle, P.R., 2003, Interpretation and utility of infrasonic records from erupting volcanoes: Journal of Volcanology and Geothermal Research, v. 121, p. 15–63.

Johnson, J.B., Ruiz, M.C., Lees, J.M., and Ramon, P., 2005, Poor scaling between elastic energy release and eruption intensity at Tungurahua Volcano, Ecuador: Geophysical Research Letters, v. 32, L15304, 5 p., doi:10.1029/2005GL022847.

Matoza, R.S., Hedlin, M.A.H., and Garcés, M.A., 2007, An infrasound array study of Mount St. Helens: Journal of Volcanology and Geothermal Research, v. 160, p. 249–262, doi:10.1016/j.jvolgeores.2006.10.006.

McChesney, P.J., 1999, McVCO handbook 1999: U.S. Geological Survey Open-File Report 99–361, 48 p. [http://wrgis.wr.usgs.gov/open-file/of99-361.]

McChesney, P.J., Couchman, M.R., Moran, S.C., Lockhart, A.B., Swinford, K.J., and LaHusen, R.G., 2008, Seismic-monitoring changes and the remote deployment of seismic stations (seismic spider) at Mount St. Helens, 2004–2005, chap. 7 *of* Sherrod, D.R., Scott, W.E., and Stauffer, P.H., eds., A volcano rekindled; the renewed eruption of Mount St. Helens, 2004–2006: U.S. Geological Survey Professional Paper 1750 (this volume).

Moore, P.L., Iverson, N.R., and Iverson, R.M., 2008, Frictional properties of the Mount St. Helens gouge, chap. 20 *of* Sherrod, D.R., Scott, W.E., and Stauffer, P.H., eds., A volcano rekindled; the renewed eruption of Mount St. Helens, 2004–2006: U.S. Geological Survey Professional Paper 1750 (this volume).

Mori, J., Patia, H., McKee, C., Itikarai, I., Lowenstein, P., De Saint Ours, P., and Talai, B., 1989, Seismicity associated with eruptive activity at Langila Volcano, Papua New Guinea: Journal of Volcanology and Geothermal Research, v. 38, p. 243–255.

Moran, S.C., Malone, S.D., Qamar, A.I., Thelen, W.A., Wright, A.K., and Caplan-Auerbach, J., 2008, Seismicity associated with renewed dome building at Mount St. Helens, 2004–2005, chap. 2 *of* Sherrod, D.R., Scott, W.E., and Stauffer, P.H., eds., A volcano rekindled; the renewed eruption of Mount St. Helens, 2004–2006: U.S. Geological Survey Professional Paper 1750 (this volume).

Neal, C.A., Casadevall, T.J., Miller, T.P., Hendley, J.W., II, and Stauffer, P.H., 1997, Volcanic ash—danger to aircraft in the North Pacific: U.S. Geological Survey Fact Sheet 030–97, 2 p.

Pallister, J.S., Reagan, M., and Cashman, K., 2005, A new eruptive cycle at Mount St. Helens?: Eos (American Geophysical Union Transactions), v. 87, no. 48, p. 499–500, doi:10.1029/2005EO480006.

Pallister, J.S., Hoblitt, R., Denlinger, R., Sherrod, D., Cashman, K., Thornber, C., and Moran, S., 2006, Structural geology of the Mount St. Helens fault-gouge-zone field relations along the volcanic conduit-wallrock interface [abs.]: Eos (American Geophysical Union Transactions), v. 87, no. 52, Fall Meeting supplement, Abstract V41A-1703.

Poland, M.P., Dzurisin, D., LaHusen, R.G., Major, J.J., Lapcewich, D., Endo, E.T., Gooding, D.J., Schilling, S.P., and Janda, C.G., 2008, Remote camera observations of lava dome growth at Mount St. Helens, Washington, October 2004 to February 2006, chap. 11 *of* Sherrod, D.R., Scott, W.E., and Stauffer, P.H., eds., A volcano rekindled; the renewed eruption of Mount St. Helens, 2004–2006: U.S. Geological Survey Professional Paper 1750 (this volume).

Qamar, A.I., Malone, S.D., Moran, S.C., Steele, W.P., and Thelen, W.A., 2008, Near-real-time information products for Mount St. Helens—tracking the ongoing eruption, chap. 3 *of* Sherrod, D.R., Scott, W.E., and Stauffer, P.H., eds., A volcano rekindled; the renewed eruption of Mount St. Helens, 2004–2006: U.S. Geological Survey Professional Paper 1750 (this volume).

Rowe, M.C., Thornber, C.R., and Kent, A.J.R., 2008, Identification and evolution of the juvenile component in 2004–2005 Mount St. Helens ash, chap. 29 *of* Sherrod, D.R., Scott, W.E., and Stauffer, P.H., eds., A volcano rekindled; the renewed eruption of Mount St. Helens, 2004–2006: U.S. Geological Survey Professional Paper 1750 (this volume).

Schilling, S.P., Thompson, R.A., Messerich, J.A., and Iwatsubo, E.Y., 2008, Use of digital aerophotogrammetry to determine rates of lava dome growth, Mount St. Helens, Washington, 2004–2005, chap. 8 *of* Sherrod, D.R., Scott, W.E., and Stauffer, P.H., eds., A volcano rekindled; the renewed eruption of Mount St. Helens, 2004–2006: U.S. Geological Survey Professional Paper 1750 (this volume).

Schneider, D.J., Vallance, J.W., Wessels, R.L., Logan, M., and Ramsey, M.S., 2008, Use of thermal infrared imaging for monitoring renewed dome growth at Mount St. Helens, 2004, chap. 17 *of* Sherrod, D.R., Scott, W.E., and Stauffer, P.H., eds., A volcano rekindled; the renewed eruption of Mount St. Helens, 2004–2006: U.S. Geological Survey Professional Paper 1750 (this volume).

Scott, W.E., Sherrod, D.R., and Gardner, C.A., 2008, Overview of the 2004 to 2006, and continuing, eruption of Mount St. Helens, Washington, chap. 1 *of* Sherrod, D.R., Scott, W.E., and Stauffer, P.H., eds., A volcano rekindled; the renewed eruption of Mount St. Helens, 2004–2006: U.S. Geological Survey Professional Paper 1750 (this volume).

Vallance, J.W., Schneider, D.J., and Schilling, S.P., 2008, Growth of the 2004–2006 lava-dome complex at Mount St. Helens, Washington, chap. 9 *of* Sherrod, D.R., Scott, W.E., and Stauffer, P.H., eds., A volcano rekindled; the renewed eruption of Mount St. Helens, 2004–2006: U.S. Geological Survey Professional Paper 1750 (this volume).

Woulff, G., and McGetchin, T.R., 1976, Acoustic noise from volcanoes; theory and experiment: Geophysical Journal of the Royal Astronomic Society, v. 45, p. 601–616.

Appendix 1. Acoustic Sensors Used at Mount St. Helens

The acoustic sensors installed by CVO and PNSN at Mount St. Helens were previously designed as additions to the McVCO voltage-controlled oscillator (McChesney, 1999) that is in wide use by the PNSN and the USGS in the Cascades and elsewhere. The sensor consists of either 9 or 18 electret microphones with a 1-Hz frequency response, the signals from all microphones being summed to reduce electronic noise. Including the responses of other components in the recording system (for example, radio, digitizers, system gain), each 9-element microphone has a nominal response of 22.7 counts/Pascal (44.5 counts/Pascal for an 18-element microphone). The acoustic sensors installed at stations SEP and SUG had 18-element microphones, and the STD sensor had a 9-element microphone. An important caveat to the acoustic response of these sensors is that individual sensors were not calibrated before installation. Given that the sensitivity of individual electret sensors varies by ±3 dB and that their sensitivity is known to decline with time after installation (depending on environmental conditions), we estimate that the true response could vary by 30 percent or more for each nine-element microphone. For this reason we only give a range of possible pressure values in this paper.

The circuit board with electret sensors is typically placed in a PVC plastic tube with end caps and a hose connection on one end. The PVC tubing reduces bellows-type motion caused by wind or ground shaking. A soaker hose of variable length is attached to the hose connection to further reduce wind noise. At SUG and STD the sensors were placed inside an enclosure with the soaker hose strung in a line away from the enclosure. At SEP the two sensors were placed on the ground ~15 m apart, with rocks piled around the PVC tube to prevent movement and the soaker hose coiled next to each sensor.

This page intentionally left blank

A Volcano Rekindled: The Renewed Eruption of Mount St. Helens, 2004–2006
Edited by David R. Sherrod, William E. Scott, and Peter H. Stauffer
U.S. Geological Survey Professional Paper 1750, 2008

Chapter 7

Seismic-Monitoring Changes and the Remote Deployment of Seismic Stations (Seismic Spider) at Mount St. Helens, 2004–2005

By Patrick J. McChesney[1], Marvin R. Couchman[2], Seth C. Moran[2], Andrew B. Lockhart[2], Kelly J. Swinford[2], and Richard G. LaHusen[2]

Abstract

The instruments in place at the start of volcanic unrest at Mount St. Helens in 2004 were inadequate to record the large earthquakes and monitor the explosions that occurred as the eruption developed. To remedy this, new instruments were deployed and the short-period seismic network was modified. A new method of establishing near-field seismic monitoring was developed, using remote deployment by helicopter. The remotely deployed seismic sensor was a piezoelectric accelerometer mounted on a surface-coupled platform. Remote deployment enabled placement of stations within 250 m of the active vent.

Introduction

The earthquake swarm that signaled the start of the eruption at Mount St. Helens on September 23, 2004 (Scott and others, this volume, chap. 1), was recorded by a dense network of short-period stations operated jointly by the Pacific Northwest Seismic Network (PNSN), based at the University of Washington, and the U.S. Geological Survey (USGS) Cascades Volcano Observatory (CVO). The network consisted of 13 stations within 20 km of the volcano; 6 of these were within 5 km (fig. 1). Many stations had been in place since the early 1980s. Although the established monitoring was sufficient to detect the onset of the unrest, it proved inadequate to record and monitor the intense seismicity of the developing 2004–2005 eruption.

This paper recounts the changes made to the Mount St. Helens seismic network during the first year of the eruption. These include changes to the existing short-period network, the first installations of telemetered broadband seismometers, the addition of infrasonic microphones, and the remote deployment of piezoelectric accelerometers. The method of remote deployment is new—it relies on an innovative instrument package, called a "spider," that was developed during the first month of the eruption (LaHusen and others, this volume, chap. 16). The package enabled us to safely deploy fully functional seismic stations, by helicopter, to sites within a few hundred meters of the active vent without setting a foot on the crater floor (fig. 2). Seismic spider development occurred during the response to volcanic unrest, and the following chronological sections complement the technical discussion by showing how the seismic spiders were used and how our field experiences drove the design process. Because the seismic spider uses both an uncommon sensor and unconventional deployment, we describe it at length in a subsequent section, "Technical Description of the Seismic Spiders."

Deployment Chronology

The deployment chronology is divided into two sections. During the initial response we modified the existing short-period network and made new installations using traditional methods. Later, our focus was seismic spider deployment. To provide an overview, a summary of changes to the seismic monitoring system through 2005 is given in table 1. The instrument parameters for the spider deployments are described in a later section. The infrasonic microphones are described elsewhere (Moran and others, this volume, chap. 6).

[1] Pacific Northwest Seismic Network, Department of Earth and Space Sciences, University of Washington, Box 351310, Seattle, WA 98195

[2] U.S. Geological Survey, 1300 SE Cardinal Court, Vancouver, WA 98683

Initial Response to Seismic Unrest

Because Mount St. Helens was regarded as adequately monitored (Moran, 2004; Ewert and others, 2005), there was little urgency to install new instruments during the first several days of the seismic swarm that began on September 23, 2004. However, after seismicity intensified on September 26, the existing network proved inadequate in four ways (Moran and others, this volume, chap. 2): (1) The short-period network lacked dynamic range and repeatedly clipped on larger events. (2) There were no three-component instruments. (3) The network lacked the ability to record low-frequency signals. (4) There were no infrasonic sensors to record explosive activity. Consequently, CVO and the PNSN began mobilizing to put new stations in the field. Our priorities were the installation of broadband three-component seismometers and deployment of infrasonic microphones to complement the dense short-period network.

At the same time, other cooperating groups were mobilizing to deploy broadband and strong-motion sensors with onsite recording around the volcano (Horton and others, this volume, chap. 5). However, to overcome the limited dynamic range and frequency response of the short-period network, we felt it essential to have real-time data from several broadband stations transmitted to CVO and PNSN. Because of the added complication of providing telemetry, it took several days to organize the deployment.

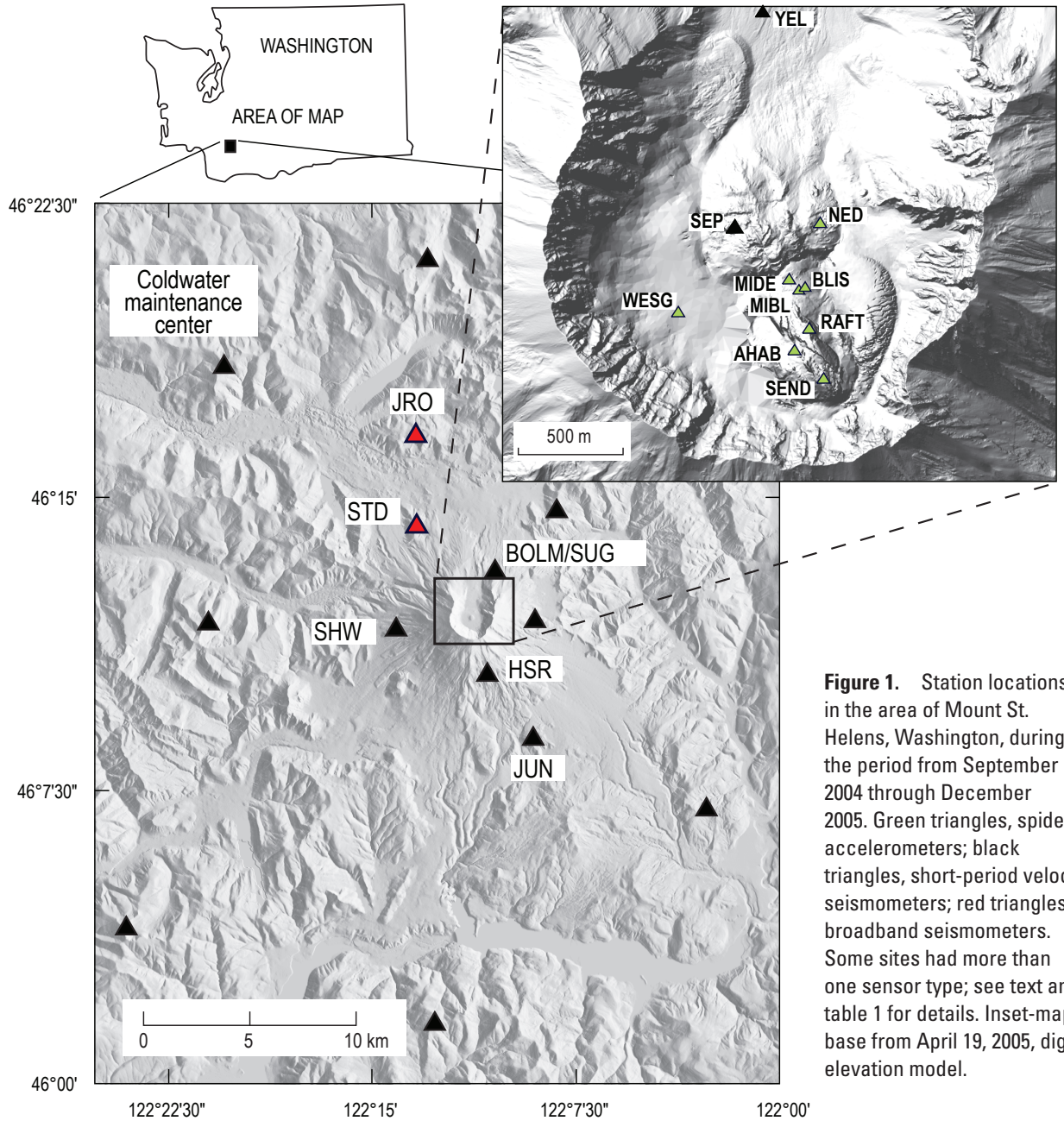

Figure 1. Station locations in the area of Mount St. Helens, Washington, during the period from September 2004 through December 2005. Green triangles, spider accelerometers; black triangles, short-period velocity seismometers; red triangles, broadband seismometers. Some sites had more than one sensor type; see text and table 1 for details. Inset-map base from April 19, 2005, digital elevation model.

On October 1, 2004, we made our first attempt to install a broadband seismometer and an infrasonic microphone at Studebaker Ridge, the site of an existing short-period station (STD; fig. 1). Work at the site, about 5 km from the vent, stopped when the first explosion of the eruption (at 1202 PDT) triggered a mandatory evacuation. As an alternative, we installed a broadband seismometer at the Johnston Ridge Observatory (JRO; fig. 1), 9 km north-northwest of the crater. Later, a broadband seismometer was successfully installed at Studebaker Ridge on October 5. Both seismometers were Guralp CMG-6TDs. These three-component instruments have a response of 30 s and were configured to measure each channel at 50 samples per second. Telemetry was not yet complete, so data were recorded initially in each instrument's 2-GB flash memory and collected later with a portable hard drive.

The interrupted installation of an infrasonic microphone at Studebaker Ridge (STDM) was completed on October 2, 2004, and another microphone (BOLM) was deployed at Sugar Bowl (fig. 1) on October 3 (Moran and others, this volume, chap. 6). The short-period seismic network was modified to provide telemetry for the microphone signals. Other changes to short-period stations were necessary in the first weeks of the eruption because signals were clipped for many earthquakes. To improve the dynamic range, a low-gain channel was added at several stations. Stations SHW and HSR were converted to dual gain on October 4 and JUN on October 7 (fig. 1). The sensitivity on the high-gain channel from HSR was also reduced, because signals from even relatively small earthquakes were severely clipped.

Figure 2. Overhead view of seismic spider deployed at station RAFT. Sensor platform (Marv lander) is at upper left. Instrument box on spider is 70 cm long. USGS photo by S.C. Moran, June 20, 2006.

Ideally the broadband instruments and microphones would have been located closer to the vent. Experience elsewhere has shown that very long period (VLP) earthquakes are best recorded on broadband instruments located within 4 km of the source region (B.A. Chouet, oral commun., 2004). By October 1, however, conditions inside the crater and on the crater rim were considered too dangerous for extended field work, so the instruments were installed more than 4 km from the source region. We will never know if VLP events occurred during the first several months of the eruption, a shortcoming that shows the importance of having at least one broadband instrument installed within 1–3 km of a potentially active vent before the beginning of unrest. None of the three explosions that occurred in the days after the October 1 event created an obvious signal on the microphones placed outside the crater (Moran and others, this volume, chap 6).

On October 20, an Earthworm data-processing node was established at the Gifford Pinchot National Forest's Coldwater Ridge maintenance facility, ~13 km northwest of the crater (fig. 1). This achievement marked a turning point in our response to the eruption by allowing Coldwater to function as a radio-telemetry terminus near the volcano. Links for the data from JRO and STD broadband seismometers were made to Coldwater with Freewave spread-spectrum digital radios (2.4 GHz). The presence of an Earthworm digitizer vastly expanded our analog channel capacity and allowed further seismic deployments to occur without long and difficult radio paths to CVO. Internet connectivity at Coldwater was through VSAT (very small aperture terminal) linked to a commercial communications network by microwave radio and satellite.

The explosion on October 1, 2004, destroyed the short-period seismic station at September lobe on the 1980–86 lava dome (SEP; fig. 1). Positioned ~500 m from the vent, SEP was the closest station to the earthquake sources. Losing this station greatly hampered earthquake location quality (Moran and others, this volume, chap. 2). The only remaining station within 3 km of the vent was the short-period station YEL (fig. 1) on the crater floor. However, the signal from YEL was clipped on many events until the gain was reduced by 12 dB during a quick visit on October 21.

Chronology of Seismic Spider Deployment

The need to reestablish near-field seismometers in the still-hazardous working conditions in the crater turned our attention to the development of a seismic station that could be deployed remotely. Available to us was the spider instrument package, originally developed for GPS deformation instruments and telemetry (LaHusen and others, this volume, chap. 16). We adapted this platform to carry an accelerometer (described in the next section) and an infrasonic microphone. The first seismic spider (BLIS, fig. 1) was deployed on October 12, 2004, at a location ~250 m east of the vent. The spider was

Table 1. Summary of changes to preeruption seismic network at Mount St. Helens, Washington, through 2005, including infrasonic microphones.

Station	Date	Change
SEP	10/1/04	Destroyed by explosion (L4-C seismometer)
JRO	10/1/04	Guralp CMG-6TD broadband installed
STDM	10/2/04	Nine-element infrasonic microphone installed
BOLM	10/3/04	Eighteen-element infrasonic microphone installed
SHW	10/4/04	Low gain added. High gain = 60 dB, low gain = 36.5 dB (L4-C seis.)
HSR	10/4/04	Dual gain. High gain = 28 dB, low gain = -1.32 dB (S-13 seis.)
STD	10/5/04	Guralp CMG-6TD broadband installed
JUN	10/7/04	Low gain added. High gain = 60 dB, Low gain = 36.5 dB (L4-C seis.)
STDM	10/12/04	Disconnected microphone telemetry for use at station BLIS
BLIS	10/12/04	Spider with accelerometer and 18-element infrasonic microphone
YEL	10/21/04	Gain reduced by 12 dB to 54 dB (L4-C seismometer)
SEP	11/4/04	Installed L22-3D and a pair of 18-element infrasonic microphones
NED	11/20/04	Spider with accelerometer
NED	12/20/04	Spider with accelerometer on separate platform (first Marv lander)
AHAB	2/8/05	Temporary spider deployment, accelerometer, and GPS
MIDE	2/16/05	Spider with accelerometer
SEP	3/8/05	Destroyed by explosion
NED	3/8/05	Destroyed by explosion
MIDE	3/8/05	Destroyed by explosion
SUG	3/9/05	L4-C seismometer at 42 dB added to station BOLM
SEP	3/14/05	Spider with accelerometer and two 18-element infrasonic microphones
YEL	3/15/05	Gain reduced by 6 dB to 48 dB
NED	4/6/05	Reinstalled spider with accelerometer
MIDE	4/6/05	Reinstalled spider with accelerometer, reinstalled again 04/14/05
SEND	6/30/05	Spider with accelerometer
WESG	7/12/05	Temporary spider deployment, accelerometer; removed 09/14/05
MIDE	7/19/05	Destroyed by rockfall
RAFT	7/28/05	Spider with accelerometer
MIBL	11/17/05	Spider with accelerometer

remarkably successful, despite noise spikes in the seismic signal caused by radio transmissions from the co-housed GPS system. These noise spikes were eliminated by remotely turning off the GPS instrument, which had been damaged during deployment.

Volcanic and seismic activity declined substantially after October 5, 2004 (Moran and others, this volume, chap. 2). After several weeks of reduced activity, we decided it was safe to work at SEP for a short time to replace the destroyed station with a three-component seismometer and a pair of infrasonic microphones. Usually such installations take hours, but by using the spider package we thought the visit would require less than one hour. On November 4, a spider was deployed in advance of the crew. Everything required for the station was preassembled and housed in the spider except the seismometer and microphones. It took only 45 minutes to install the Sercel L22-3D three-component seismometer and two infrasonic microphones. Even so, the helicopter was forced to depart hurriedly when an ash cloud advanced on the site, just as the crew was loading the ship to leave.

The success of the spider at BLIS led to another spider deployment at the northeast corner of the old dome (NED; fig. 1) on November 20, 2004. This site was selected because it improved the geometry of stations in the crater and included a patch of warm ground that was free of snow. Data became available on November 22, after an expansion of the analog telemetry channels at the Coldwater Earthworm node.

The first NED spider worked poorly. Unlike BLIS, the seismic signal from NED was often obscured by noise. At both stations the accelerometers were mounted in a leg of the spider platform. However, NED used a heavy radome antenna mounted on a mast, whereas BLIS had used a low-mass whip antenna. Wind or ground motion shook NED's antenna and sent vibrations through the spider to the sensor. We considered using whip antennas in the future, instead of radomes, but the heavier antenna had two advantages—increased signal strength and protection from icing. In addition, we could not be certain that the antenna was the only noise source. Consequently we decided to isolate the sensor from spider vibrations

by mounting it in a separate platform, which we dubbed the "Marv lander" (see technical description in the next section). On December 23, 2004, a new spider equipped with a Marv lander was exchanged for the old one, solving the noise problem at NED.

On February 8, 2005, the spider AHAB was deployed atop the actively moving spine 4 (fig. 1). The location on the spine was chosen because it appeared stable and its slope of ~20º was not too steep for the spider. The objective of this short-term experiment was to record spine motion using GPS and to look for a correlation between "drumbeat" seismic events (Moran and others, this volume, chap. 2) and discrete movements of the spine. The spider housed an L-1 GPS receiver with an accelerometer and electronic thermometer mounted on a Marv lander. After 8 days of successful operation, AHAB was retrieved before the spine's process of growth and collapse could destroy it.

By the end of January 2005, following a period of intermittent operation, the BLIS spider stopped operating. We were unable to find the spider because it was buried in snow. Consequently, when AHAB was removed from spine 4, it was modified in the field to become a replacement for BLIS. The new location, MIDE, was a snowfree warm spot near the BLIS site (fig. 1). Station MIDE began operation on February 16, 2005.

A small but destructive explosion occurred on March 8, 2005 (Scott and others, this volume, chap 1; Moran and others, this volume, chap. 6). Ballistic fragments from the explosion destroyed MIDE, SEP, and NED. The MIDE equipment was never found. Scattered parts of SEP were barely visible under a blanket of ash. Although NED was recovered, little could be salvaged—even the apparently undamaged accelerometer no longer functioned. The loss of these three stations severely reduced our ability to record and locate earthquakes, and the loss of the close-in microphones at SEP eliminated our ability to detect small explosions.

The first step in restoring lost monitoring capacity was the installation of a short-period seismometer just north of the crater at SUG (fig. 1) on March 9. We chose this site because of its relative safety and the fact that the Sercel L4-C seismometer could be easily connected to the existing infrasonic microphone (BOLM) telemetry. A new seismic spider, including two 1-Hz microphones, was rapidly constructed and deployed at SEP on March 14. The crater station YEL was visited on March 15 and the gain lowered by another 6 dB because of continuing clipping problems.

The weather then took a turn for the worse, delaying replacement of spiders at MIDE and NED until April 6, 2005. The NED deployment went smoothly, but the MIDE spider toppled when released by the helicopter. We retrieved and inspected it and, finding no obvious problems, returned the spider to MIDE. However, it failed several days later and was retrieved again on April 10. Several of the power system's primary cell casings had melted, likely a result of internal damage caused by the spider's tumble on April 6. After replacing the cells, the spider was returned to MIDE on April 14.

With the arrival of summer, more sites were free of snow and available for seismic spider deployment. On June 30, 2005, in an effort to surround the source of the drumbeat earthquakes, a spider was placed at SEND, southeast of the former AHAB installation at the southeast end of spine 4, which by then was disintegrating (fig. 1). Another installation followed at WESG (western arm of the Crater Glacier) on July 12 (fig. 1). Unfortunately, the sensitivity of WESG was poor. We suspected bad ice-rock coupling or an electronic fault. Examination after the station was retrieved showed an intermittent problem with the accelerometer interface circuit. On July 19, MIDE was destroyed by a rock fall. On July 28, 2005, a replacement spider was deployed at RAFT, the only available patch of stable ground close to the vent (figs. 1, 2).

Finally, with the approach of winter we took several steps to improve the robustness of the crater spiders. WESG was removed on September 14, 2005, before it could be buried by snow. We also retrieved all spiders except RAFT to replace batteries and, if necessary, to add directional antennas. Subsequently, ice accumulation from an early winter storm damaged the coaxial cable for the radio transmitter at SEND. The SEND spider was retrieved and repaired on November 17. Because earthquakes had become much smaller, we relocated this spider to a new site, MIBL, closer to the vent (fig. 1). The MIBL site was warm and free of snow and near the previous MIDE and BLIS sites.

By the end of 2005, the CVO and PNSN real-time seismic network at Mount St. Helens consisted of 2 broadband seismometers, 13 conventional short-period instruments (3 with dual-gain channels), 4 seismic spiders, and 2 infrasonic microphones, all within 20 km of the volcano (table 1).

Technical Description of the Seismic Spiders

The loss of SEP during the explosion of October 1, 2004, forced us to improvise new techniques in order to restore seismic monitoring near the vent. Particularly for the first installations, we hurried to get something in the field, and each deployment was an experiment that led to changes in design. The evolving design complicates the description of the spider, because it is necessary to include the changes that were made. We trust that this section gives sufficient detail to satisfy both those who need to know the response parameters for a spider installation and those who are considering the design of remotely deployed seismic instruments.

Seismic Spider Overview

We designed the seismic spider for remote deployment close to an active volcanic vent where seismic signals were strong. Remote deployment ruled out the use of traditional seismic sensors, which require leveling by hand during instal-

lation. We knew of a sensor, used for measuring seismic activity of lava flowing through tubes in Hawai‘i (R. Hoblitt, oral commun., 2004), that did not require leveling, could measure strong signals, and could survive the rigors of remote deployment. This sensor, a piezoelectric accelerometer, made the seismic spider possible.

Analog telemetry was used for a variety of reasons. Given strong signals, the contribution of some noise by the analog telemetry system did not detract much from the overall signal-to-noise ratio. The limited dynamic range of the telemetry system was overcome by using high- and low-gain channels. Analog telemetry allowed the use of lower frequency analog radios that, unlike digital spread-spectrum radios, do not require line-of-sight transmission paths and use much less power. The radios operated on the 406 to 420 MHz band, where antennas are fairly compact and their 100-mW transmissions can cover tens of kilometers. Several antennas were tried, but high-gain directional antennas were preferred because the radio path was often obstructed by terrain or snow. To prevent breakage from snow and ice loading, radome-protected antennas were favored.

Power was supplied by Air-Alkaline primary cells (Celair Corp.). Nine series-connected cells provided 12.6 V at 1,200 Ah. Total current drain was 110 mA, so 450 days of continuous operation were possible, but we planned for no more than a year because of capacity loss in cold weather.

The spider instrument package, developed early in this eruption to remotely deploy GPS instruments (LaHusen and others, this volume, chap. 16), provides an instrument compartment (~70×40×40 cm) optimized for helicopter transport and placement (fig. 3). We used the spider to house the power and telemetry systems and, initially, the sensor. Because of noise problems with the first two deployments, the sensor was moved to a separate platform, the Marv lander (described below).

Figure 3. Seismic spider slung by helicopter from staging area on March 14, 2005, for deployment at SEP. Included are two infrasonic microphones, one suspended immediately beneath the spider and another below it on the lander sensor platform (Marv lander), last item in the string. PNSN photo by P.J. McChesney, March 14, 2005.

Piezoelectric Accelerometer

Long used by industry for machine vibration measurement, piezoelectric accelerometers do not require leveling because they operate in any orientation. These devices convert dynamic forces to electrical energy through charge separation in a piezoelectric material. Acceleration (a) along the axis of the transducer acts on the seismic mass (M) to apply a force to the piezoelectric element. The force on the element produces a charge (q) such that $q = dMa$, where d is the piezoelectric constant. The stressed piezoelectric material acts as a capacitor (C), producing an open-circuit voltage (V) where $V = q/C$. Consequently the sensitivity of the accelerometer is V/g, where g is the unit of acceleration (Allocca and Stuart, 1984, p. 122).

Piezoelectric accelerometers respond to dynamic forces—to vibrations. The circuit model is a current generator in parallel with a capacitor, or its equivalent circuit, a voltage generator in series with a capacitor (Allocca and Stuart, 1984, p. 122–123). The model shows that there is an inherent low-frequency limit to a piezoelectric accelerometer. In addition, low-frequency vibrations produce weak acceleration signals, so piezoelectric accelerometers operating at low frequencies must use charge amplifiers to boost signal levels. The low-noise design of this amplifier is critical for low-frequency measurements because noise from the high input resistance of the charge amplifier increases with decreasing frequency (Schloss, 1993, p. 2). Consequently, poor signal-to-noise ratios at low frequency set the practical limit of piezoelectric response.

Sensor Parameters

We chose the Wilcoxon Model 731-207 Ultra Low Frequency Seismic Accelerometer for this application because of its relatively good low-frequency performance (see abbreviated specifications in table 2). There are other piezoelectric accelerometers with better low-frequency specifications than this model, but there is a tradeoff between increased low-

frequency response and increased fragility. Because the sensors are subject to significant forces during deployment, the 250 *g* shock limit of the Model 731-207 was attractive. All units survived our handling and the helicopter deployment. However, one unit from NED, recovered after the explosion of March 8, 2005, was irreparably damaged, probably from ballistic impact.

The peak acceleration range of this model is more than sufficient for close-in monitoring. The low-gain telemetry channel was set for a maximum measurement of 0.1 *g*, a limit that was never exceeded despite recording M_L 3.4 earthquakes within 250 m of the source. The high sensitivity of the device permitted conservative seismic amplifier gain settings. Two telemetry channels were used for high- and low-gain recordings of the signal, with the low-gain channel set at 2.5 V/V. The high-gain channel was initially set at 83.17 V/V but was reduced to 41.75 V/V for later deployments. In the absence of noise, these gain settings achieve 16-bit dynamic range using two analog telemetry channels digitized at 12 bits each.

Response information for individual sensors is unavailable from the manufacturer. The nominal frequency response at 0.2 Hz is a worst-case limit. The design value for the low-frequency cutoff (−3 dB) is 0.1 Hz. This high-pass response has a pole at (−0.628319, 0) and a zero at (0, 0) set by charge amplifier components. Actual response is determined by component variation, and any particular unit may have a pole frequency from 0.1 to 0.15 Hz (Ron Denton, Application Engineer, Wilcoxon Research, written commun., 2006).

We attempted continuous electronic integration of the accelerometer output to produce a velocity response. Even though integration in the field was not satisfactory, it demonstrated the noise characteristics of the sensor. The data sheet for the Model 731-207 states that spectral noise, a 1-Hz bandwidth noise-density measurement at a particular frequency (Schloss, 1998, p. 1), increases as frequency decreases. At 2 Hz the noise density is 0.28 *g*/Hz. However, integration provides gain relative to the acceleration response; gain increases by a factor of two each time frequency is halved. In addition, below 2 Hz, sensor noise increases as 1/*f* (Ron Denton, Application Engineer, Wilcoxon Research, written commun., 2005). The combination of decreasing signal-to-noise ratio and increasing gain causes low-frequency noise to be prominent in the integrated response. Analog filtering of the low-frequency noise interfered with the integrator phase response. On the other hand, the acceleration response of the sensor has very good noise performance. Consequently the acceleration response was telemetered because we felt that digital postprocessing could do a better job if the velocity response was desired.

Table 2. Abbreviated specifications for the Wilcoxon Model 731-207 piezoelectric accelerometer.

[Additional information online at www.wilcoxon.com.]

Accelerometer Specifications	
Sensitivity	10 V/*g*, ±10 %, 25ºC
Acceleration Range	±0.5 *g*
Frequency Response	0.2–1300 Hz, −3 dB
Resonance Frequency	2,400 Hz
Temperature Response	−18% at 0ºC, +8% at 80ºC
Broadband Noise	2 µ*g*, 2.5 Hz to 25 kHz
Input Voltage Range	18–30 VDC, in series with a 2–10 mA current source diode
Shock Limit	250 *g*

Piezoelectric Accelerometer Interfacing

The charge amplifier in the accelerometer can produce high-amplitude signals (5 V) and requires a power source. The voltage-controlled oscillators (VCOs) used to telemeter seismic signals are usually connected to passive seismometers that produce small-amplitude signals in the millivolt range. This mismatch required an interface circuit and VCO gain adjustments. We used McVCO, a microcontroller-based mimic of an analog VCO (McChesney, 1999). The interfacing problems are similar for other VCOs, but the details are best appreciated if the McVCO documentation is at hand.

The Model 731-207 accelerometer is a two-wire device. There is a ground connection and a combined signal and power connection. Power is provided through a current-source diode in series with a DC supply of 18–30 V. The signal rides on a 10-V bias. The most straightforward way to connect the accelerometer to the VCO is to raise the impedance of one VCO input and make a single-ended connection through a coupling capacitor. The nominal 24-V power required by the accelerometer can be generated from the 12-V telemetry power system with a voltage-doubler circuit.

This approach was used for the first deployments at BLIS and NED. The coupling capacitor at the VCO input produced a high-pass pole at 0.047 Hz, well below the nominal 0.2-Hz charge amplifier pole in the accelerometer. To achieve this low frequency, tantalum electrolytic capacitors were used. However, investigation of noise problems with the first NED deployment indicated that some sudden baseline shifts were due to the capacitor. The second deployment at NED used a polypropylene capacitor and higher input resistance to produce a pole at 0.04 Hz.

The polypropylene capacitor appeared to reduce some noise problems, but the design was still bothered by the spikes that occurred when GPS and seismic instruments cohabited the same spider. This and an interest in electronic integration of the accelerometer signal provoked the development of a different interface (fig. 4). The new interface used an input buffer to raise the impedance and a differential output stage that allowed connection directly to an unmodified VCO input. Rather than use a 24-V supply, the sensor ground was operated at −12 V, putting the output offset at −2 V and eliminating the need for a coupling capacitor at the sensor output. An optional integration stage was provided.

A high-pass pole (R4, C16) is included in the interface after the buffer stage. This was initially set to 0.017 Hz, making the charge amplifier pole dominant at low frequencies and reducing interaction with the optional integrator. This was later raised to 0.17 Hz when some low-frequency noise problems were seen in the accelerometer response. It has not been possible to duplicate this noise; it may have been unique, but for the sake of uniformity the pole continues to be set at 0.17 Hz. Table 3 lists deployment interface response characteristics and gains. Poles and zeros are from circuit simulation. All responses more than ten times the 30-Hz VCO low-pass filter are ignored.

This interface has been used for all our piezoelectric accelerometer deployments starting with the deployment of AHAB on February 8, 2005, and continuing through 2005, but it could be improved. Cohabitation with GPS still produces small glitches in the seismic signal when the GPS data transmission occurs. We expect that GPS noise could be reduced further by locating the interface on the sensor platform (fig. 3). This would change the connection in the long cable between the lander and the spider from a high impedance single-ended connection to a lower impedance differential connection. Better supply regulation might also help eliminate noise.

Gain Setting

The gain model for the dual-gain mode we used for all seismic spiders is shown in figure 5. Maximum acceleration of the Model 731-207 produces a maximum signal level of 5 V. This is greater than the input range of the McVCO, so the signal is reduced by half in all versions of the interface. The gain of two, created by the differential connection of the

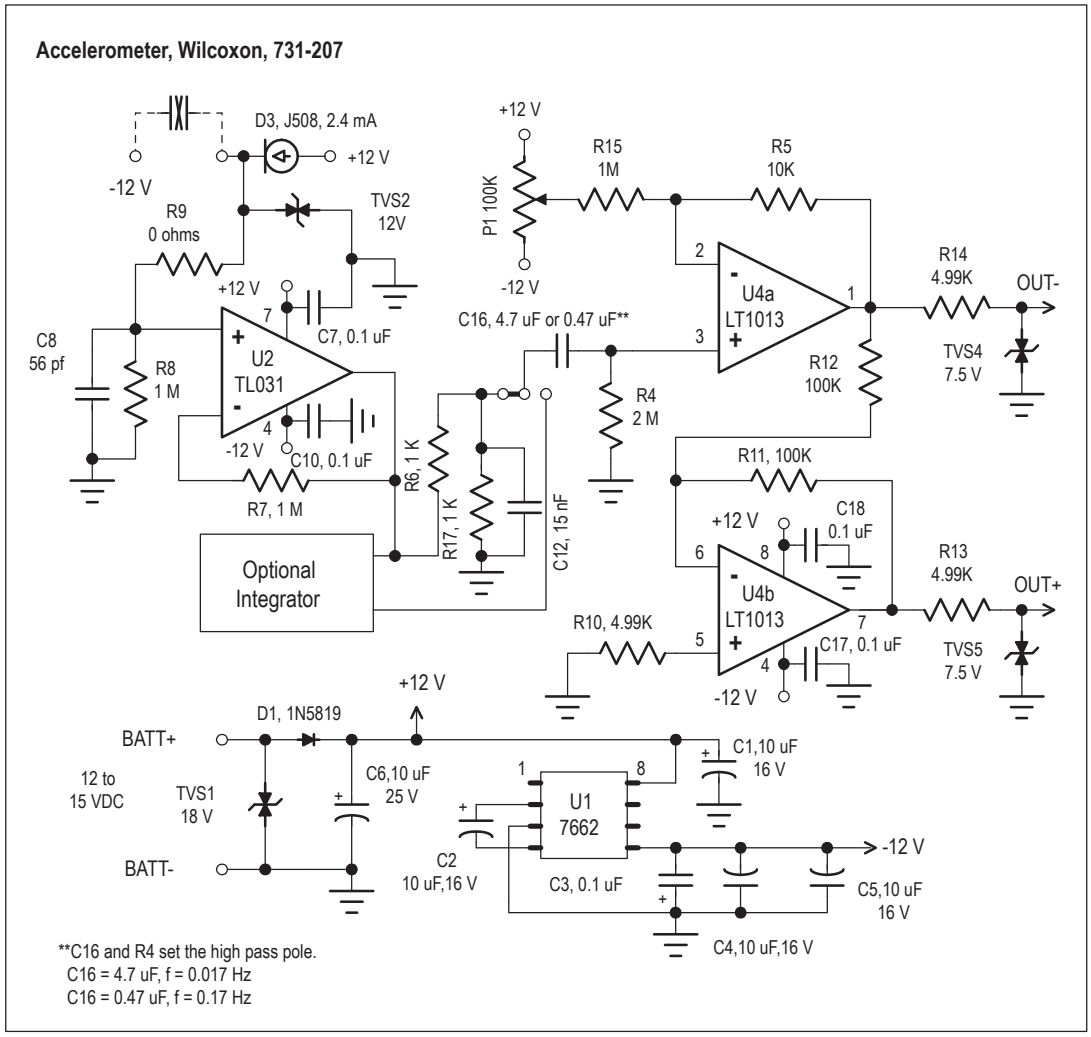

Figure 4. Piezoelectric accelerometer interface used from February 8, 2005, onward. Low-frequency response controlled by C16 and R4.

Table 3. Piezoelectric accelerometer channel gains and interface frequency responses.

[Different deployments to the same location are indicated by numerals in parentheses in station column. Last date for each station entry indicates modification or end of operation. nc, no change.]

Station	Date	High gain V/V	Low gain V/V	Interface response (poles), (zeros)
BLIS	10/12/04	83.17	2.5	(–0.294685, 0), (0, 0)
lost	01/31/05	--	--	--
NED(1)	11/20/04	83.17	2.5	(–0.294685, 0), (0, 0)
exchanged	12/20/04	--	--	--
NED(2)	12/20/04	83.17	2.5	(–0.249969, 0), (0, 0)
destroyed	03/08/05	--	--	--
AHAB	02/08/05	41.75	2.5	(–0.106357, 0), (0, 0)
removed	02/16/05	--	--	--
MIDE(1)	02/16/05	41.75	2.5	(–0.106357, 0), (0, 0)
destroyed	03/08/05	--	--	--
SEP	03/14/05	41.75	2.5	(–0.106357, 0), (0, 0)
modified	10/18/05	nc	nc	(1.06357, 0), (0, 0)
NED(3) modified	04/06/05	41.75	2.5	(–0.106357, 0), (0, 0)
	10/18/05	nc	nc	(–1.06357, 0), (0, 0)
MIDE(2)	04/06/05	41.75	2.5	(–0.106357, 0), (0, 0)
destroyed	07/19/05	--	--	--
SEND	06/30/05	41.75	2.5	(–1.06357, 0), (0, 0)
removed	11/17/05	--	--	--
WESG	07/12/05	41.75	2.5	(–1.06357, 0), (0, 0)
removed	09/14/05	--	--	--
RAFT	07/28/05	41.75	2.5	(–1.06357, 0), (0, 0)
MIBL	11/17/05	41.75	2.5	(–1.06357, 0), (0, 0)

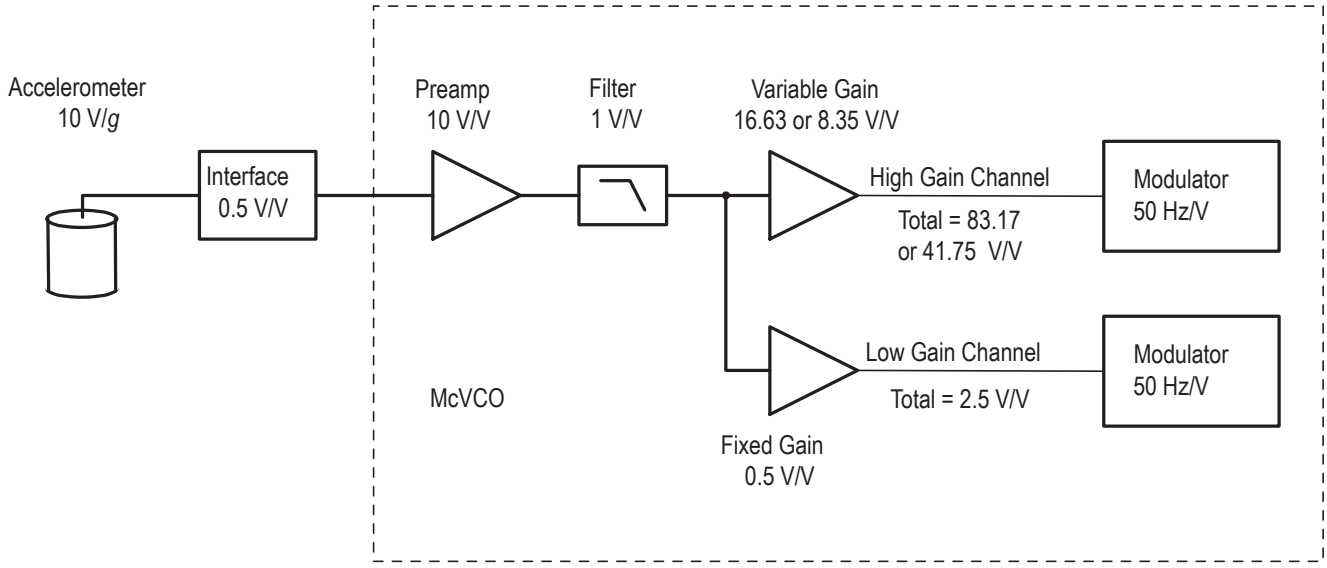

Figure 5. Dual-gain model of spider accelerometer. Additional gain and response terms result from demodulation and digitization. McVCO, microcontroller-based mimic of analog voltage-controlled oscillator.

later interfaces, is cancelled by the attenuation caused by the impedance match between interface and VCO, so the net gain of all interface stages is 0.5 V/V.

The input amplifier in the McVCO usually has a gain of 100 V/V. This was reduced to 10 V/V with jumpers on the input stage (McChesney, 1999, p. 31). After filtering (4th-order Butterworth, low-pass, 30-Hz filter) the signal splits into low- and high-gain channels. The low-gain channel is modified to have a gain of 0.5 V/V after the filter; consequently the total gain is 2.5 V/V from the interface input to the low-gain channel output. The maximum input signal swing of the channel's analog to digital converter is 2.5 V. A signal of 1 V from the sensor (0.1 *g*) produces a full-scale measurement on the low-gain channel.

The amplification of the high-gain channel after the filter stage depends on the gain switch setting and the microcontroller program version (McChesney, 1999, p. 15, p. 30–31). The high-gain channel after the filter stage was initially set for 16.63 V/V for a total gain of 83.17 V/V from the interface input to the high-gain channel output. As stated previously, this was reduced to 8.35 V/V for a total gain of 41.75 V/V for the deployments from AHAB onward (see table 3).

The McVCO modulator sensitivity is 50 Hz/V (McChesney, 1999, p. 30–31). The sensitivity of the discriminators used for demodulation was 0.02 V/Hz. The digitizer sensitivity was 819.2 counts/V. Where the total response to input excitation is the quotient of output counts divided by acceleration input, the scale factor for each channel voltage gain is shown in table 4.

Table 4. Scale factor for accelerometer channel gains.

Channel gain, V/V	Scale factor, counts/*g*
2.5	20,480
41.75	342,016
83.17	681,329

The "Marv Lander" Platform

We discovered a significant noise problem caused by spider vibrations during the first NED deployment. Later testing showed that soft tapping anywhere on the spider generated high levels of noise as long as the accelerometer was mounted on it. Our solution was to put the sensor on a separate platform, the "Marv lander," named for its developer, Marvin Couchman.

Previous experience with seismic installations at Mount St. Helens had shown that it was not always necessary to bury a seismometer to get good coupling and good noise performance. The installation at SEP before October 2004 was such an example. At the SEP site, warm temperatures a few centimeters below ground had caused rapid failures of several Sercel L4-C seismometers before a surface installation solved the problem. This approach was continued with the Sercel L22-3D installation at SEP on November 4, 2004. Other experiences with installations on rock, where digging was impossible, had also produced favorable results. In all these cases, isolation from surface noise was achieved by surrounding the seismometer with a rock pile, bags of sand, or concrete. We reasoned that a seismometer platform for remote deployment should provide significant mass around the sensor. Consequently the lander body is a 20-kg barbell weight (45 lb) with the piezoelectric sensor sealed with epoxy in the center hole (fig. 6).

The platform is coupled to the ground through three short legs formed by the eyebolts used to attach the rigging between it and the spider. Most of the spider sites had some ash cover, and, although we could not closely observe most of the platforms on the ground, we believe that the combination of tripod legs and weight helped root them in the ash and avoid tipping instability. The barbell weight also provided thermal mass, isolating the piezoelectric sensor from temperature changes rapid enough to produce an inband signal.

The lander rigging includes a 5-m length of 5-mm ($^3/_{16}$ in.) stainless steel cable attached to the spider's instrument box with a ring and thimble that protect the cable from wear during the helicopter flight (fig. 7). At the other end, a 10-mm ($^3/_8$ in.) rope harness attaches the lander to the cable. Soft rope is used to isolate the cable from the lander, eliminating cable vibrations as a source of seismic noise. Polypropylene rope was used for the first lander. When the instrument was retrieved after an explosion, one of the three leads was burned through, and hot rock was found embedded in the others. Subsequently, nylon rope was used because of its higher melting point and superior strength.

Separating the sensor from the spider body created some electrical problems. When the seismic spider is set down by the helicopter, the lander makes first contact with the ground. This can produce a strong static discharge between the lander

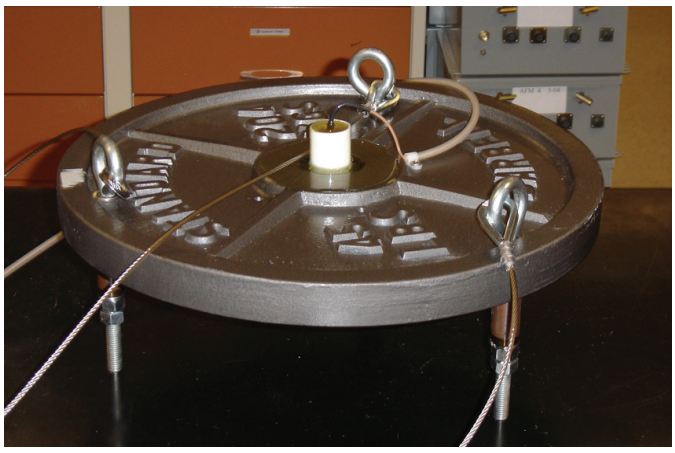

Figure 6. Marv lander under construction. Barbell weight stands on three legs formed by eyebolts that connect with rigging. Accelerometer is potted with epoxy inside the plastic pipe, which is cemented into center of the weight. USGS photo by M.R. Couchman, December 2, 2004.

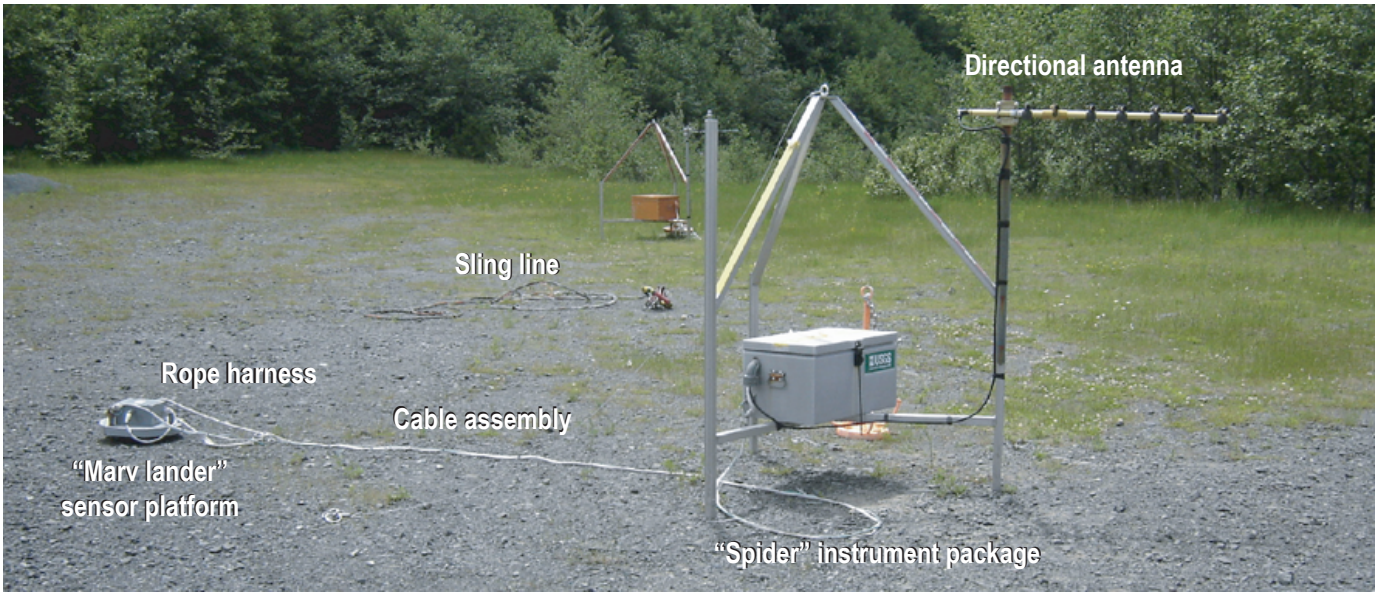

Figure 7. Seismic spider laid out at staging area. Instrument box is approximately 70x40x40 cm. USGS photo by S.C. Moran, June 20, 2006.

and the spider that can damage the sensor and electronics. To provide a low-impedance discharge path, a grounding wire connects one of the lander's legs to the spider body. Discharge through the signal-cable shield is avoided by grounding it only at the spider end, and the sensor case is isolated from the lander body by potting it with epoxy inside a short length of PVC pipe (fig. 6). The signal cable is vulnerable to thermal and mechanical damage. Consequently, the two-pair shielded cable (Belden type 8723) is enclosed in thermal sleeving. Grounding wire and sensor cable are tied to the lander rigging.

The performance of an accelerometer mounted on the lander is illustrated in figure 8. The top trace is from the piezoelectric accelerometer installation at SEP shortly before it was replaced by a three-component velocity seismometer (Sercel L22-3D) on February 24, 2006. The bottom trace is from the L22 and shows an earthquake from February 26, 2006. The two earthquakes were chosen because signals from other stations indicated that they were very similar, having approximately the same magnitude, location, and source mechanism. The accelerometer data were integrated to produce a velocity response and then filtered (2 Hz, Butterworth high-pass filter) to remove long-period noise and produce an instrument response comparable to the L22. Despite the fact that the two sensor locations differed by ~15 m, their seismic traces share many similarities, particularly at the onsets. More to the point, the comparable signal-to-noise ratios show the effectiveness of the lander coupling.

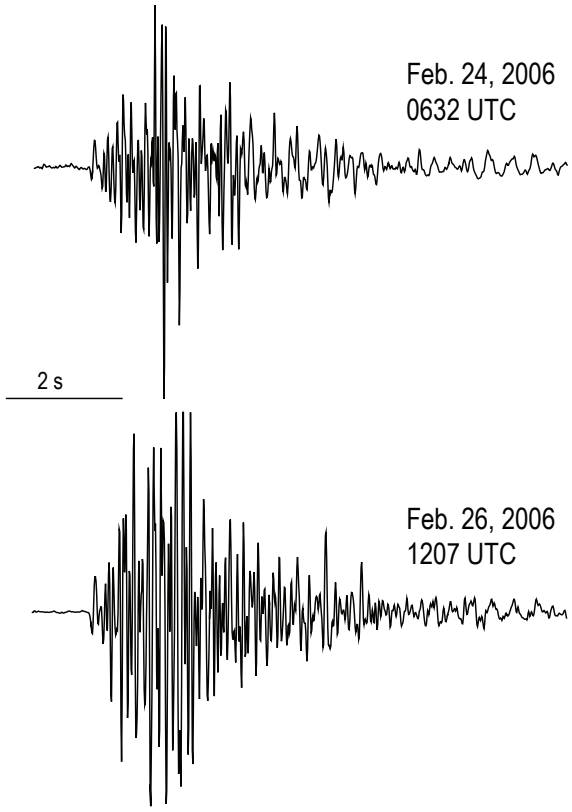

Figure 8. Comparison of numerically integrated response of piezoelectric accelerometer (top) and velocity seismometer (bottom) for similar earthquakes at station SEP. Accelerometer data were integrated to produce a velocity response and then filtered to remove long-period noise and produce an instrument response comparable to the velocity seismometer.

Summary

Even though Mount St. Helens was regarded as a well-monitored volcano, the September 2004 unrest exposed weaknesses in the seismic monitoring network. The explosion of October 1,

2004, removed our near-field monitoring capacity when station SEP was lost, reducing the quality of hypocenter determinations. One or more additional close-in stations would have increased the chance that near-field monitoring could survive a small explosion. Deployment of broadband seismometers before the start of volcanic unrest would have supplemented the short-period network by making up for its limited dynamic range and, if positioned within 4 km, could have detected any very long period events.

Once the eruption started, near-field sites quickly became too dangerous for fieldwork. However, with the seismic spider, we were able to improvise a solution that allowed us to establish close-in sites in comparative safety. The spider package not only enabled us to place a telemetered seismometer close to the vent but also to retrieve it for service or redeployment. This portability facilitated short-term studies such as AHAB on spine 4, and portability allowed us to adapt to changing field conditions during this prolonged eruption. A different choice of sensor and telemetry technology for remote deployment might have emerged from a less-hasty development process, but, given the advantage of strong signals in the near-field, both the sensor and analog telemetry were more than adequate for the task. We were particularly pleased with the performance of the Marv lander. It eliminated the spider platform noise and produced good coupling for the sensor. With the possible exception of the glacier site (WESG), there were no signal problems caused by poor sensor installation in 10 deployments.

Seismic spiders are not substitutes for well-established seismic stations because they lack the sensitivity to detect small earthquakes, unless they happen to be in the near field, or to detect the long-period earthquakes that may well mark the start of volcanic unrest. However, once unrest has begun, they can be used to supplement an existing network where additional near-field monitoring is desired. These portable, remotely deployed stations can be built in advance, allowing a very rapid response to events. The seismic spider is a new tool for monitoring erupting volcanoes, a tool that can be used in dangerous places with comparative safety.

Acknowledgments

The authors would like to thank Richard P. Hoblitt for suggesting the piezoelectric accelerometer used in the seismic spider and supplying them during the first deployments. His perceptive review of this paper greatly increased its coherence. Thomas L. Murray's review gave us a new perspective on the seismic spider design; this resulted in a more balanced paper and allowed us to avoid several shortcomings. Finally, we would like to thank Anthony Qamar for his initial calculation of the peak acceleration that a near-field sensor would measure and his many discussions of instrument response. Because of Tony, seismic spider data were "on scale" and calibrated.

References Cited

Allocca, J.A., and Stuart, A., 1984, Transducers—theory and applications: Reston, Va., Reston Publishing Company Inc., 497 p.

Ewert, J.W., Guffanti, M., and Murray, T.L., 2005, An assessment of volcanic threat and monitoring capabilities in the United States; framework for a National Volcano Early Warning System: U.S. Geological Survey Open-File Report 2005–1164, 62 p.

Horton, S.P., Norris, R.D., and Moran, S.C., 2008, Broadband characteristics of earthquakes recorded during a dome-building eruption at Mount St. Helens, Washington, between October 2004 and May 2005, chap. 5 *of* Sherrod, D.R., Scott, W.E., and Stauffer, P.H., eds., A volcano rekindled; the renewed eruption of Mount St. Helens, 2004–2006: U.S. Geological Survey Professional Paper 1750 (this volume).

LaHusen, R.G., Swinford, K.J., Logan, M., and Lisowski, M., 2008, Instrumentation in remote and dangerous settings; examples using data from GPS "spider" deployments during the 2004–2005 eruption of Mount St. Helens, Washington, chap. 16 *of* Sherrod, D.R., Scott, W.E., and Stauffer, P.H., eds., A volcano rekindled; the renewed eruption of Mount St. Helens, 2004–2006: U.S. Geological Survey Professional Paper 1750 (this volume).

McChesney, P.J., 1999, McVCO handbook 1999: U.S. Geological Survey Open-File Report 99–361, 48 p. [http://wrgis.wr.usgs.gov/open-file/of99-361/, last accessed Dec. 26, 2006].

Moran, S.C., 2004, Seismic monitoring at Cascade volcanic centers, 2004; status and recommendations: U.S. Geological Survey Scientific Investigations Report 2004–5211, 28 p.

Moran, S.C., Malone, S.D., Qamar, A.I., Thelen, W.A., Wright, A.K., and Caplan-Auerbach, J., 2008a, Seismicity associated with renewed dome building at Mount St. Helens, 2004–2005, chap. 2 *of* Sherrod, D.R., Scott, W.E., and Stauffer, P.H., eds., A volcano rekindled; the renewed eruption of Mount St. Helens, 2004–2006: U.S. Geological Survey Professional Paper 1750 (this volume).

Moran, S.C., McChesney, P.J., and Lockhart, A.B., 2008b, Seismicity and infrasound associated with explosions at Mount St. Helens, 2004–2005, chap. 6 *of* Sherrod, D.R., Scott, W.E., and Stauffer, P.H., eds., A volcano rekindled; the renewed eruption of Mount St. Helens, 2004–2006: U.S. Geological Survey Professional Paper 1750 (this volume).

Schloss, F., 1993, Accelerometer noise: Gaithersburg, Md., Wilcoxon Research, Inc., Sound and Vibration instrumentation reference issue, March 1993, 2 p. [http://www.wilcoxon.com/knowdesk/accelnoise.pdf, last accessed Dec. 26, 2006].

Schloss, F., 1998, Piezoelectric accelerometer specifications and specmanship: Gaithersburg, Md., Wilcoxon Research, Inc., Sound and Vibration, February 1998, 2 p. [http://www.wilcoxon.com/knowdesk/piezo_spec.pdf, last accessed Jan. 8, 2007].

Scott, W.E., Sherrod, D.R., and Gardner, C.A., 2008, Overview of 2004 to 2006, and continuing, eruption of Mount St. Helens, Washington, chap. 1 *of* Sherrod, D.R., Scott, W.E., and Stauffer, P.H., eds., A volcano rekindled; the renewed eruption of Mount St. Helens, 2004–2006: U.S. Geological Survey Professional Paper 1750 (this volume).